"Microstructure, Oxidation & Mechanical Properties of As-sprayed and Annealed HVOF & VPS CoNiCrAlY Coatings"

Saman Saeidi

Thesis submitted to the University of Nottingham
for the degree of Doctor of Philosophy

December 2010

Abstract

Three HVOF and a VPS CoNiCrAlY coating were sprayed using Praxair CO-210-24 and Sulzer Metco Amdry 9951 powders. All coatings were subject to vacuum annealing treatments at different temperatures for different exposure times in order to achieve equilibrium microstructures in all test samples. Both HVOF and VPS, as sprayed and heat treated coatings were oxidised at 850℃ and 1100℃ for periods of up to 250 hours. Scanning electron microscopy (SEM), energy dispersive X-ray analysis (EDX), transmission electron microscopy (TEM), X-ray diffraction (XRD) and laser diffraction powder size analyses were used in order to analyse the powder particle size distribution and characterise the microstructure of the as-received powders, as-sprayed coatings and annealed and oxidised coatings. Thermogravimetric analysis (TGA) was carried out on as-sprayed and heat treated HVOF and VPS coatings at 1100℃ for 96 hours in order to compare the oxidation rate of HVOF and VPS coatings and investigate the effect of microstructure and heat treatment on the oxidation rate of both types of coatings. Furthermore, micro hardness, nano hardness and dynamic mechanical analysis (DMA) with a 3-point bend clamp were used in order to study the hardness and Young's modulus of as-sprayed and annealed HVOF and VPS coatings. The Eshelby inclusion model and image analyses were used in order to further investigate the effect of microstructure on the mechanical properties of these coatings.

It was observed that heat treatment prior to oxidation will change the dual oxide layer observed for the as-sprayed oxidised coatings to a single alumina layer for the heat treated and oxidised coatings. Furthermore, it was observed that microstructural features such as porosity and oxide stringers have an effect on the oxidation rate of coatings. A model was presented indicating the role of oxide stringers and porosity on the resulting heat treated microstructure and oxidation rate. It was also understood that the beginning stage of oxidation can play an important role on the oxidation behaviour (oxidation rate and different oxides present) of both HVOF and VPS coatings.

It was observed that annealing will change the microstructure of the coatings and affect their mechanical properties. It was seen that annealing reduced the hardness of the thermally sprayed coatings while it had increased the Young's modulus of the coatings. It was also observed that features such as porosity levels and β volume fraction have an effect on the mechanical properties of the coatings.

Acknowledgments

I wish to express my appreciation to Dr. Katy Voisey and Prof. Graham McCartney for their supervision, advice and encouragement throughout my PhD. I would also like to thank the staff and technicians, Mr Keith Dinsdale, Mr Tom Buss, Dr Nigel Neate, Mr Martin Roe, Mr Rory Screaton, Mr Graham Malkinson, Dr David Furniss, Dr Deen Zhang and all others who have helped me throughout my stay in Nottingham. A special thanks goes to Hassan for his time and help and all other friends and colleagues in the Wolfson building who have made my stay in Nottingham enjoyable.

I would also like to take this opportunity to thank my parents for their continual love and support, financially and emotionally, throughout this time. Finally I would like to thank my wife, Bahar, whose love and support has made this all worthwhile.

Contents

CHAPTER 1

Introduction

Oxidation, hot corrosion, interdiffusion and thermal fatigue are different surface related problems in gas turbine applications. The severity of the problems are different for aircraft engine, land based powder generation and marine engines. However, what is similar in all cases is that, the surface related problems have become more severe as higher and higher operating temperatures have been used. In spite of the significant improvements in the base material, moving from wrought alloys to directionally solidified alloys and single crystal alloys, the use of appropriate coatings is unavoidable. It should be noted that the emphasis in this work is on turbine aircraft engines.

Coating deposition is utilised in engineering design and manufacture to modify the properties of the surface, i.e. to combine the optimum bulk properties with the required surface protection. Different methods of surface coating exist which differ in the manner in which the coating is applied, i.e. coating thickness, materials used, temperature of coating material, temperature of the material being coated, etc. However, whichever method used for the deposition of the coating(s), they must offer protection within a specified period of service life time against destructive attacks such as high temperature oxidation, corrosion and erosion.

A typical coating used for high temperature applications, oxidation and corrosion resistance, involves an oxidation resistant coating and a thermal barrier. However, in today's technology a variety of different coatings (layers) could be applied to the surface of the blade in order to protect the blade from its destructive environments.

Thermal barrier coatings (TBC) are one of the highly advanced material systems used in high temperature environments. These coatings are composed of three essential layers: (i) ceramic top coat, typically made of yttria stabilised zirconia (YSZ) which is desirable for having very low thermal conductivity, (ii) a thermally grown oxide (TGO) layer, preferably the dense stable α-Al_2O_3, (iii) metallic bond coat, usually an aluminide (AlNi, Al_2Ni_3) diffusion coating or a MCrAlY (where M= Co, Ni or combination of both) overlay coating.

However, over the past few years, other layers such as an AlNi layer beneath the bond coat, have been added to the thermal barrier coating systems for inhibition of diffusion and lost of the protective Al in the bond coat, making the TBC system even more complex and more expensive. The decision to use particular extra layers depends upon the capabilities and limitations the extra layer(s) provides and the benefit versus cost analysis of the coating applied.

The MCrAlY overlay coatings are commonly utilised to protect the blades surfaces against oxidation and hot corrosion. Beside their good oxidation and corrosion behaviour, they act as good underlying layer for the deposition of the ceramic top coat, and hence are also known as bond coats.

The MCrAlY coatings can be deposited using different thermal spraying techniques; amongst which high velocity oxy fuel (HVOF) process has shown very encouraging results due to the low oxygen content and low porosity of the coating layer. However,

low pressure plasma spraying (LPPS) and vacuum plasma spraying (VPS) are the methods used commercially to apply MCrAlY coatings. Since, the cost associated with the vacuum in the mentioned processes is high, more attention has been paid to HVOF which is an atmospheric pressure process. Thus, evaluation of MCrAlY coatings applied by HVOF has been the subject of some research. Most of the research has focused on the oxidation and hot corrosion characteristics of coatings produced using different spraying parameters and on different substrates. However, insufficient understanding of differences between HVOF, VPS and LPPS coatings and also characterisation of the coating layer by itself and without the effect of substrate has not been deeply investigated.

The overall aim of this research project is to evaluate the microstructure and phase constituents of CoNiCrAlY layers produced by HVOF and VPS processes. Also the phase transformations and microstructural changes of free standing HVOF and VPS coatings, during vacuum annealing, is investigated. Furthermore, the oxidation behaviour of as-sprayed and heat treated coatings over a range of temperatures and exposure times are investigated. Mechanical properties such as hardness and Young's modulus of these coatings are of great interest for modelling work, in order to be able to predict the behaviour and life of thermal barrier systems; as such, mechanical property measurements of free standing coatings has been carried out at different testing temperatures and as a function of annealing temperature in order to provide a map of these properties across a wide range of temperatures. Finally a further investigation, using the Eshelby inclusion model, on the Young's modulus of these coatings has been carried out in order to analyse the effect of phase constituents and porosity on the Young's modulus of the MCrAlY coatings.

This thesis consists of 8 chapters. A literature review is presented in chapter 2. The experimental methods and techniques used throughout this research work are presented in chapter 3. The results are presented in chapters 4, and 5. The investigation and characterisation of as-received powders and, as-sprayed and annealed (different temperatures and exposure times) HVOF and VPS free standing coatings have been reported in the first part of chapter 4 and the mechanical behaviour investigation of as-sprayed and annealed free standing HVOF and VPS coatings is reported in the second part of chapter 4. The oxidation behaviour of as-sprayed and heat treated HVOF and VPS free standing coatings oxidised at 1100℃ and 850℃ for various exposure times is presented in chapter 5. A summary, conclusions and future work for this research is presented in chapters 6 and 7 respectively.

CHAPTER 2

Literature Review

2-1- Introduction

The history of gas turbine goes back to 1791 [1], and many endeavours have been made since then. However, today gas turbines are used widely in various industries to produce mechanical power. The performance and satisfactory operation of gas turbines are of great importance to the industries varying from civil and military to power generation and also oil and gas exploration and production [1].

A gas turbine basically consists of gas generator and power conversion sections. The gas generator section consists of a compressor, combustion chamber, and turbines.

For a turbine to produce power, it must have a higher inlet pressure than that at the exit [1]. Compressors are thus used to enhance the pressure difference across the turbine. The compressed air is than mixed with fuel and burnt in the combustion chamber. The resultant hot gases at high temperature and pressures are then passed through sets of turbine blades (e.g. high pressure turbine blades, low pressure turbine blades), extracting sufficient power to drive the compressor as well as shafts through which mechanical power is extracted [2]. For aero-gas turbines the hot gases are expanded through nozzles to create some of the thrust.

The drive to improve engine combustion efficiency, while reducing emissions, has meant that the operating temperature within the turbine engines has increased

significantly over the last 30 years [3]. The mean temperature of gas at turbine entry, for aero engines, has increased from 1200K to 1800K [1]; under industrial and marine service conditions temperatures are a little lower, 1100-1200K, but more severe environments are encountered. The pressure ratio of the compressor has grown significantly as well. The gas temperature at a turbine entry is the most important parameter determining the specific power and efficiency of gas turbine. Working at higher temperature, combined with the desire to reduce weight, particularly of the rotating components, has resulted in the progressive changes of various materials used in the engine (see Figure 2-1).

In fact the growth of the gas turbine in the recent years has been brought about most significantly by several factors [4]:

1. Metallurgical advances that have made possible the employment of higher temperatures in the combustor and turbine components.

2. The cumulative background of aerodynamic and thermodynamic knowledge.

3. Coatings technology which has had a great influence in increasing gas temperatures.

4. The utilisation of computer technology in the design and simulation of turbine airfoils and combustor and turbine blade cooling configurations.

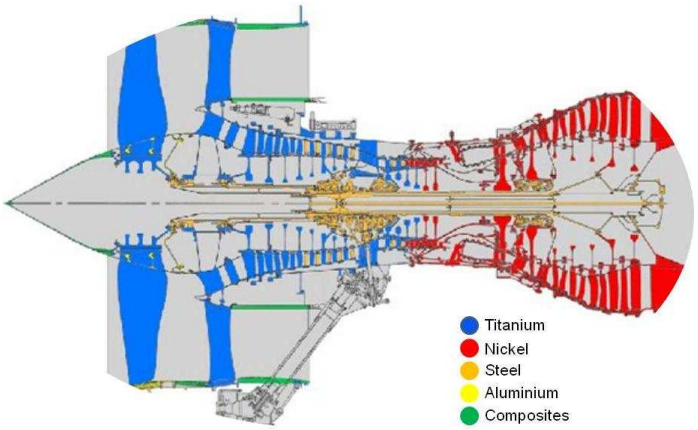

Figure 2-1. Combination of different materials used in a Rolls-Royce jet engine, Rolls-Royce Corporation.

2-2- Turbine blades

Of all the components in an engine, high pressure turbine (HPT) blades operate under the most arduous conditions of high temperature and pressure [5]. Not only do the HP blades experience the high temperature but also high stresses (due to centrifugal forces) and rapid temperature transients at different points of the flight cycle are experienced. Figure 2-2 illustrates a Rolls Royce jet engine showing the different stages and the pressure and temperature profiles along the engine.

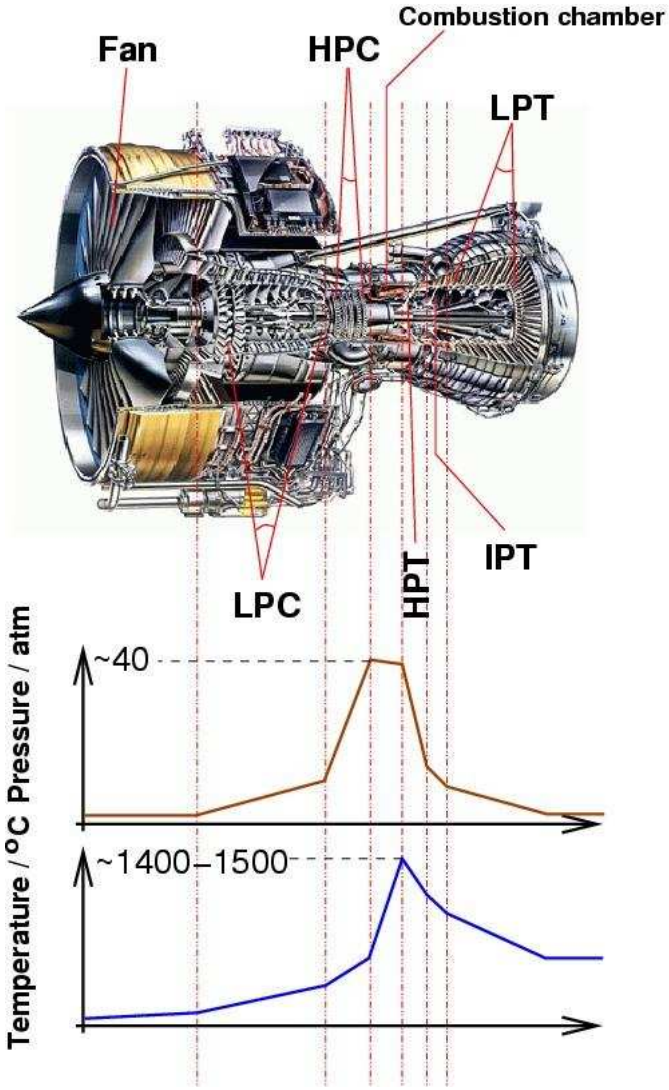

Figure 2-2. A jet engine showing different stages (intermediate pressure compressor, ICP, high pressure compressor, HPC, high pressure turbine, HPT, intermediate pressure turbine, IPT, low pressure turbine, LPT) and pressure and temperature profiles along the engine. Diagram after Micheal Cervenka, Rolls-Royce Corporation.

The hot gases surrounding the blade are highly oxidising, and contain contaminants such as chlorides and sulphates which can lead to hot corrosion, and also may contain erosive media. Erosion may be caused by sand which can be ingested during take-off and landing. Figure 2-3 presents the temperature contour of an HPT blade in the 1980s. Considering the increases in gas temperature at the turbine entry these values are now considerably higher, though the patterns of temperature variation will remain the same.

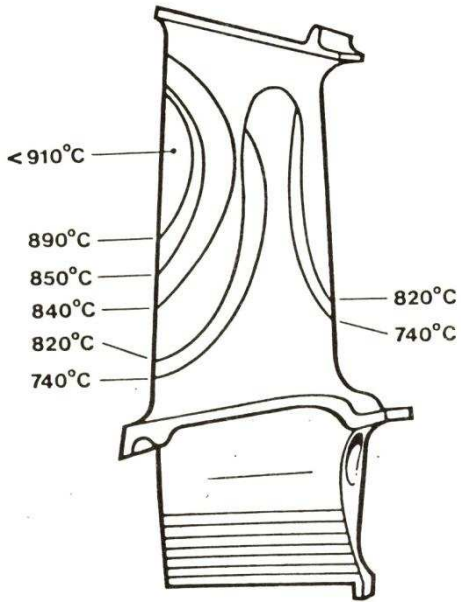

Figure 2-3. Temperature contours of a HPT blade [6].

The combination of the high temperature and the stresses applied to the blades gives rise to creep while the temperature transients can cause thermal fatigue. Dimensional changes due to creep may result in blades fouling housings and fatigue crack growth which both directly lead to blade failure.

As the aim for turbine engines is higher engine efficiency, higher and higher turbine inlet temperatures are required (which in today's engines is over 250°C above the melting point of the superalloy used to produce the blade [7]). Higher temperatures result in higher oxidation, corrosion and mechanical failure rates.

2-3- Materials used in turbine engine

Since the beginning of the use of gas turbines, considerable progress has been made in the metallurgical field in the search for alloys which are mechanically resistant at high temperatures. As for maximum efficiency the gas should enter the turbine at higher

temperatures which is limited to the capacity of the material used in the component parts to withstand the effect of such temperatures.

The desire for higher efficiency combined with reduction in weight (particularly of the rotating components) has resulted in progressive changes in the proportions of various materials used in an engine as improved material have been developed. Figure 2-4 illustrates the trend of different materials used in younger generation jet engines. It must be noted that the figure shows the general trend in material usage rather than indicating the precise material make-up of a gas turbine at any one time. A similar trend is expected for more recent years, i.e. a further decrease in the amount of steel and Al alloys used at the cost of higher share of Ti alloys and superalloys.

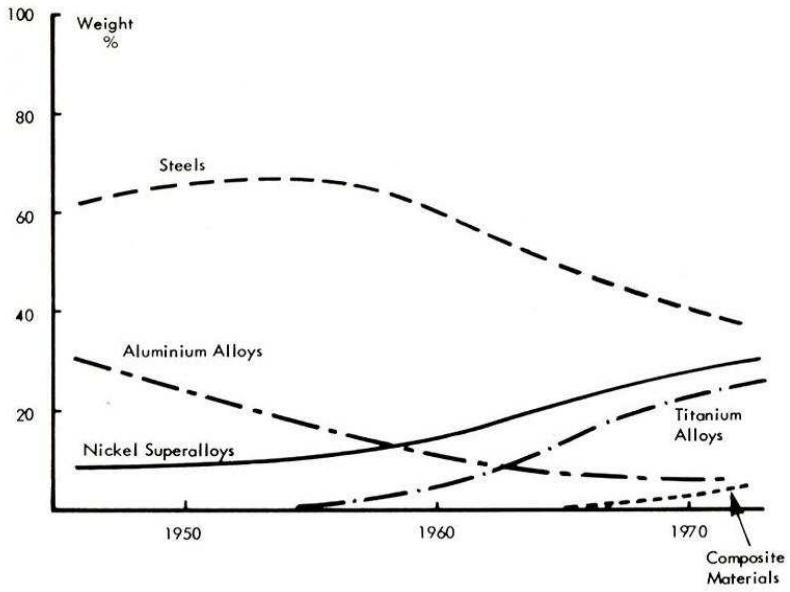

Figure 2-4. Trend in jet engine material usage [5].

As the working conditions for first generation gas turbines were not very severe the early jet engines used a significant amount of aluminium alloys for impellers, compressor blades, etc. However, apart from the use of steels and cobalt base alloys in some American engines, turbine blades were mostly been fabricated from nickel

base superalloys [5]. As can be seen in Figure 2-4, it was not until the mid 1950's when the superior specific strength of early titanium alloys resulted in their application in compressor blades and casings. The subsequent development of Ti alloys with increased temperature capabilities had resulted in further reduction of utilisation of denser materials.

In the selection of a material system it is important to know the requirements determined by the function of component (such as mechanical properties, environmental resistance, temperature capabilities).

From the mechanical point of view the main factors are creep and thermal fatigue as well as the requirement for sufficient strength to withstand the loads experienced. In the case of turbines it is known that creep and thermal fatigue are the limiting factors for the first stage blades, while for the second stage blades it is mainly creep [6].

Since the environment of the components consists of combustion gases resulting from the combustion of fuel and air and contains pollutants such as chloride and phosphates, the environmental factors are oxidation (T>1000°C), high temperature hot corrosion, hot corrosion type I (T>800°C) and low temperature hot corrosion, hot corrosion type II (T=650 to 750°C) [6].

Furthermore, fabrication methods such as forging, casting, directionally solidified and single crystal castings can affect the microstructure of the component and, as a result, improve its mechanical properties at higher temperature. For example single crystal blades show higher creep resistance compared to directionally solidified and wrought casting blades. Figure 2-5 shows the increase in operational temperatures of turbines as a function of different fabrication methods.

From what has been mentioned above it can be stated that materials developed for such applications must exhibit [6]:

- High mechanical strength at elevated temperatures
- Resistance to creep, thermal and mechanical fatigue
- High microstructural stability
- High temperature oxidation and high temperature corrosion resistance

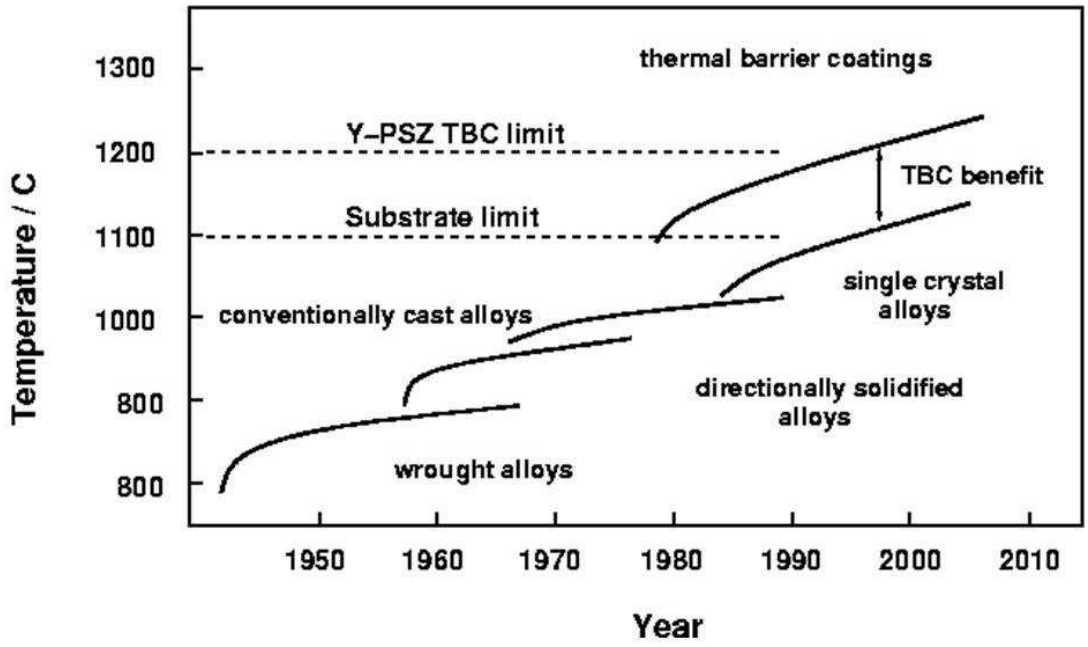

Figure 2-5. Affect of different fabrication processes on operational temperatures [4].

The appearance of superalloys in the early 1950's, considerable amelioration in casting technologies and, in the 1960's, the cooling system for turbine blades were all major steps forward, each allowing the service temperature to be increased by 20°C or more.

Over the last 20-30 years, alloy improvements, directional and single crystal solidification have contributed significantly, but as demand for higher efficiency and thus higher temperature exists and the damage to blade surfaces caused by oxidation and hot corrosion results in considerable deterioration of mechanical properties and shortens blade life, the emphasis has been shifted towards coating systems which have allowed an increase of gas temperature of up to 110°C (coated turbine blades boost service lives of 2 to 5 times those of their uncoated counterparts) [8].

2-4- Superalloys

Superalloys are a class of materials for which is difficult to create an exact definition. However, the definition used somewhat 14 years ago has proven reasonably acceptable [9]: "a superalloy is an alloy developed for elevated temperature service, usually based on group VIII A elements, where relatively severe mechanical stressing is encountered, and where high surface stability is frequently required".

Superalloys are generally divided into three classes of nickel-base, cobalt-base and iron base superalloys. Gas turbines have been the prime driving force for the existence and development of superalloys. More details on the background of superalloys can be found in [9].

The outstanding strength of superalloys over a wide range of temperatures at which gas turbine components operate is the main reason for the existence of these alloys. The close-packed face centred cubic (FCC) structure of these alloys has the capability to maintain high tensile, rupture, creep and thermo-mechanical fatigue properties that are much higher than equivalent body centred cubic (BCC) structures [9]. Furthermore, superalloys have the capability to develop high temperature strength

through solid solution strengthening (Ni lattice has a large solubility for many other elements), which gives them the capability to be used at temperatures as high as 0.7 of the absolute melting temperature.

Microstructure of the superalloys is generally consisted of the following phases, γ, γ', β-(NiAl), σ, and α-Cr. The phases available in the microstructure of a superalloy depend on the composition of the alloy. Different alloying elements can stabilise different phases. The processes which these alloys undergo can also have an effect on their microstructure. For example Durand-Charre [10] has mentioned that the most controversial point in the microstructure of the superalloys is the nature of the reactions between γ-Ni, γ'-Ni_3Al and the liquid, and between γ, β and the liquid. Several studies have shown that the temperature interval between these reactions (γ/γ'/L & γ/β/L) is about 2°C [10]. Considering this narrow temperature range, it can be seen that a slight difference in the composition or solidification conditions could modify the nucleation process in favour of one or the other of these reactions.

High pressure turbine (HPT) rotator blades are one of the greatest challenges ever faced by engineers, as today they must withstand gas temperatures higher than the melting point of the metal of which they are made of [11]. This phenomenon would not have been possible if it wasn't for the ultimate strength of superalloys and development of coatings. The idea of applying protective layers to the surface of turbine blades was first practiced in the 1960's and found wide application. Since then, protective coatings have been used on aero engine and land based turbine blades.

2-5- Coatings for turbine blades

Due to the extreme conditions experienced by the components in a turbine engine, whether in aircraft, marine or power plants, protection against adverse effects is required in order to maintain component integrity and overall engine performance. As a result, an extensive use of surface engineering is required in order to combine the optimum bulk properties with the required surface protection. Such coatings are normally applied to higher strength structural alloy substrates.

Surface engineering plays an important role in the operation of all high temperature components in a turbine engine. In its simplest form it improves the environmental resistance of the components; as the improvement in mechanical properties of the structural alloys was made at the expense of the environmental resistance.

Any coating deposited on a turbine blade must offer protection within a specified period of service life against destructive attacks of high temperature corrosion, oxidation and erosion; having this in mind the coating must meet the following requirements [6, 8]:

- It must withstand hot corrosion, oxidation, and erosion when placed into a flow of gas whose parameters are similar to those of turbine gases.
- It must safely withstand the static and alternate stresses applied to the blade surface
- It must show good stability and not be destroyed by interaction with the substrate.
- It must not degrade the blade material mechanical properties.

- Compatibility with the substrate alloy in terms of chemistry and expansion coefficient.

The selection of a suitable treatment or coating for a given application depends on complex interplay of surface, coating and substrate related properties that are defined by the specific application. Table 2-1 illustrates a summary of the desirable features and forms the frame work around which the design requirements of a coating for a good oxidation/corrosion resistance can be discussed.

Table 2-1. Desirable features of an oxidation / corrosion resistance coating [12].

Coating Property	*Requirement*	*Location coating*		*Coating/substrate interface*
		Surface	**Bulk**	
oxidation/corrosion resistance	Low rates of scale formation	√		
	Uniform surface attack	√		
	A thermodynamically stable surface oxide	√		
	Ductile surface scales	√		
	Adherent surface scales	√		
	High concentration of scale forming elements within the coating to act as reserve for scale repair	√	√	
Interface stability	Low rate of diffusion across interface at operating temperatures			√
	Limited compositional changes across interface			√
	Absence of embrittling phase formation during service			√
Good adhesion	Matched coating and substrate properties to minimise coating mismatch & stress generation at coating / substrate interface		√	√
	Optimum surface condition before coating			√
	Growth stresses during coating formation should be minimised		√	√
Mechanical strength	Coating must withstand all stress (creep, fatigue & impact loading) that is generated at component surface during service		√	
	Well matched surface expansion coefficients between coating & substrate to minimise thermal stressing & thermal fatigue		√	√

The primary aim of coating or surface treatment for high temperature operating components is the ability to form thermodynamically stable, slow growing surface oxide capable of separating the coating alloy and the environment [12]. This is why most coatings contain the three key elements of aluminum, chromium and silicon [12]. However, not only oxidation and corrosion resistance are important but also mechanical properties, adhesion and metallurgical stability must be kept in mind when designing a coating.

The numerous variants of high temperature coatings that are in use today fall into three generic types [12]:

- Diffusion coatings
- Overlay coatings
- Thermal barrier coatings (TBCs)

2-5-1- Diffusion coatings

Diffusion coatings are formed by surface enrichment of an alloy with other element(s). In the case of coatings for oxidation resistance the elements used are either aluminum (aluminides), chromium (chromised) or silicon (siliconised) [12]. Combination of these elements are also possible, i.e. chrome-aluminides, silicon-aluminides.

Extensive research carried out in the 1960s on different properties of various diffusion coatings, showed that diffusion aluminide coatings had the best protective properties on turbine blades made of nickel superalloys [8]. Having properties such as high oxidation resistance, high stability when deposited on superalloys and a favorable combination of physical and mechanical properties made the diffusion aluminide coatings the predominant type of aircraft engine turbine blade coating used for several decades (1960's to 1980's) [8].

However, poor resistance of these coatings in environments containing sulfur compounds led to further development of the coatings. Increasing the chromium content in the outer layer of the diffusion coatings (chromising-aluminising method) had found application in the protection of the blades suffering from hot corrosion.

Also, alloying aluminide coatings with silicon turned out to be another technique that allowed the improvement of coating resistance to hot corrosion and oxidation.

The studies aimed at modifying diffusion aluminide coatings are ongoing as the design of new engines with increased inlet temperatures result in the shortening of the surface lives of the blades protected with diffusion coatings. The low ductility of the diffusion coatings and high stresses generated in cooled blades cause the formation of numerous thermal fatigue cracks in the outer layer of diffusion coatings.

The ductility of the diffusion aluminide coatings was increased by the gradual decrease of the aluminium content of the coatings from 34-36 % (typical of the coatings used in the 1960s) down to 20-24% (typical of the coatings used in the 1970s). This trend however, resulted in a decrease in oxidation resistance.

The process was also altered by moving towards gas aluminising methods which allowed less employment of powder mixtures and higher efficiency of gas transfer of aluminium to blade surfaces. The latest development in the diffusion coating deposition was the use of electric arc evaporation of aluminium alloys and their transfer to the blade surface in the form of plasma. In this technique the need for the use of halides and powder components is eliminated completely [8].

2-5-2- Overlay coatings

Overlay coatings are deposited onto the component surface. Overlay coatings used in gas turbines are a family of corrosion/oxidation resistant alloys specifically designed for high temperature surface protection and are often referred to as M-Cr-Al-Y, where M is the alloy base metal, usually nickel, cobalt or a combination of both [12].

Compared with diffusion coatings, one of the main advantages of overlay coatings is that the composition of the coating can be controlled in a wide range and is almost independent of the substrate composition. Hence, the composition of overlay coatings can be specifically designed to match the particular environmental conditions [13].

The first commercial MCrAlY alloy was an iron based FeCrAlY formulated by Pratt and Whitney [14]. As stated by Nicholls [12], Talboom [15] published the first paper on the electron beam physical vapour deposition (EB-PVD) of a number of cobalt based MCrAlYs (CoCrAlY) in 1970.

Electron-beam physical vapour deposition (EB-PVD) was the first method used to deposit MCrAlY coatings [14]. However, due to cost considerations, coating manufacturers soon developed techniques such as air, vacuum and low pressure plasma spraying (APS, VPS and LPPS) and high velocity oxy fuel (HVOF) deposition techniques. These processes will be explained in more detail in the following sections.

MCrAlY overlay coatings are also frequently used as bond coats where they are applied to increase adherence of the outer ceramic layer of thermal barrier coatings (TBC) to the substrate superalloy. However, it should be noticed that although these coatings do enhance the bonding between alloy and TBC, their primary function is to increase the high temperature oxidation and corrosion resistance of the underlying structural alloy.

2-5-3- Thermal barrier coatings (TBC)

A different approach to using coatings with high oxidation resistance is to design and develop coating systems that lower the metal surface substrate temperature. TBCs work in this way. The great difference in the thermomechanical properties of metals and ceramics would seem to prevent their use in composite structures subjected to large changes in temperature and thermal stresses. Nevertheless, thermal barrier coatings (TBCs) which are made of low thermal conductivity ceramics are being used widely as thermal insulation to metallic components from the hot gas stream in gas turbine engines. In fact the use of TBCs along with internal cooling of the underlying superalloy component provides a reduction of up to 200K of the superalloy operating temperature [12, 14, 16]. This enables modern gas turbine engines to run at gas temperatures above the melting temperature of the superalloy and hence improve the engine efficiency. Furthermore, such a drop in temperature of a component surface would have the effect of reducing oxidation rates by an order of magnitude and reduce the components propensity to creep [12].

TBCs have a structure which consists of three different layers on top of a substrate which can be observed in Figure 2-6. Having such a structure results in different physical, thermal and mechanical properties which make it an even more complex system compared to components that are all metallic or all ceramic. As a matter of fact, TBC systems are perhaps the only system where a complex interplay of all the following phenomena does occur [16]: diffusion, oxidation and phase transformation, elastic and plastic deformation, creep, thermal expansion, thermal conduction, fracture and fatigue.

The ceramic top coat of a TBC system is the layer which provides the thermal insulation and is typically made of Y_2O_3 stabilised ZrO_2 (YSZ) [16]. The TGO and the bond coat provide the oxidation protection and the alloy sustains the structural loads [17]. The ceramic top coat provides a combination of desirable properties that make it the material of the choice for the top coat. Some of these properties are as follows [16]:

- One of the lowest conductivities of all ceramics at elevated temperature (~2.3W/mK at 1000℃ for a fully dense material)
- High thermal expansion coefficient (~11×10^{-6}°C^{-1}) → reduces thermal expansion mismatch between the ceramic top coat and the underlying metal to some extent
- Low density (~6400kg/m^3)
- High hardness (~14GPa) → improves resistance to erosion and foreign body impact
- High melting point (~2700°C) → suitable for high temperature applications
- Resistant to ambient and hot corrosion

Although many various methods are used for depositing ceramic coatings, APS and EB-PVD are the most important methods used for deposition of YSZ top coat. These two methods produce characteristic microstructures with certain desirable attributes that are discussed in reference [16].

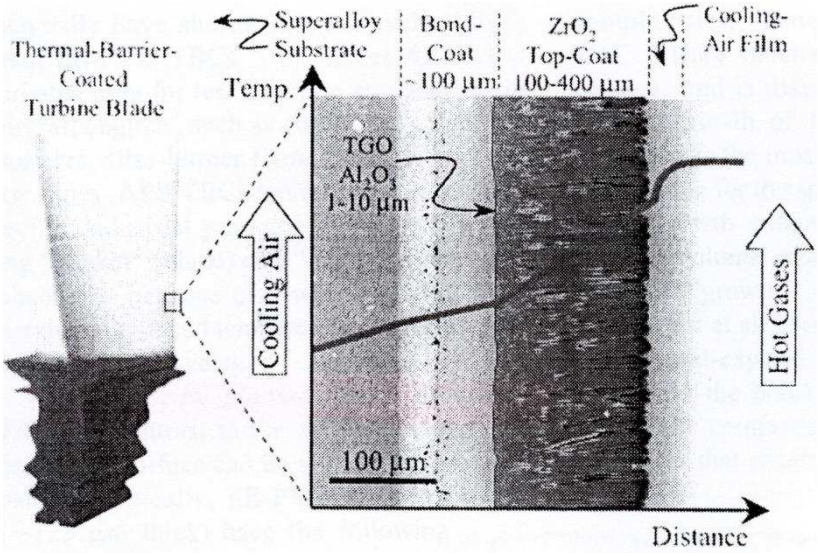

Figure 2-6. Cross sectional SEM micrograph of an EB-PVD TBC, imposed onto a schematic diagram showing the temperature reduction provided by the TBC. The blade contains internal hollow channels for air cooling, whereas the outside surface is TBC coated, setting up a temperature gradient across the TBC system [16].

However, having said all the good properties about the TBC top coat, the inter-connected porosity which always exists in the top coats produced by APS, allows easy ingress of oxygen from the engine environment to the underlying material [16]. Moreover, even for fully dense top-coats, produced using EB-PVD, the extremely high ionic diffusivity of oxygen in the ZrO_2 based ceramic tends to make it oxygen transparent [16]. This oxygen transparency, which increases the thermally grown oxide thickness, along with the thermal expansion mismatches leads to the most important failure mechanisms of TBCs, which is spallation.

This thesis is concerned with overlay MCrAlY coatings that may be used as TBC bond coats.

2-6- Metallurgy and application of MCrAlY coatings

MCrAlYs (where M= Ni, Co) were initially developed in the 1960s based on a FeCrAlY system [7, 14]. Unlike the diffusion coatings which by the nature of their formation, imply a strong interdependence on substrate composition –i.e. the composition of the coating is dependent on the substrate and is not flexible, the overlay coatings (MCrAlYs) provide increased flexibility of design with compositions tailored specifically for different applications. MCrAlYs can be divided into several groups depending on the metal used as "M" (the base metal). Some of the more important groups are: NiCrAlY, CoCrAlY, CoNiCrAlY, NiCoCrAlY. In each group the metal which is presented first, e.g. cobalt in CoCrAlY, is the base metal and has the highest percentage in the composition. However NiCrAlY coatings are generally the most oxidation resistant, while CoCrAlY systems provide better hot corrosion resistance [18]. Generally, under high temperature oxidising conditions NiCrAlYs & NiCoCrAlYs outperform the cobalt base systems. This is illustrated schematically in Figure 2-7.

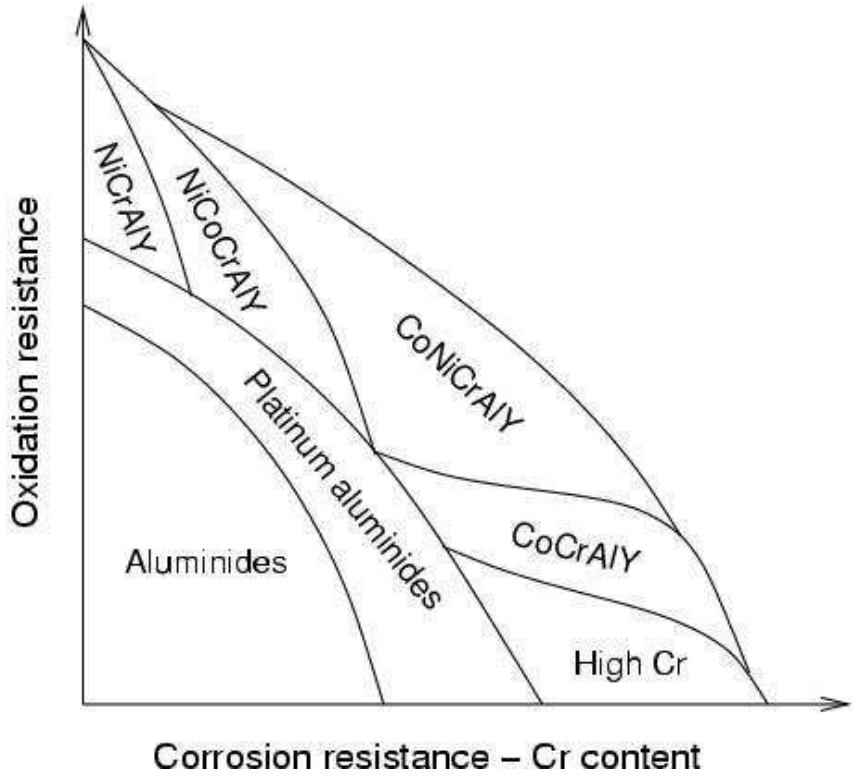

Figure 2-7. Relative oxidation and corrosion resistance of high-temperature coating systems [12].

MCrAlYs are considered as superalloys due to the high percentage of Ni or Co in their composition.

Hot corrosion (type I & type II) and high temperature oxidation are the difficulties MCrAlY coatings are facing. Overlay coatings of classic design with 18-22% chromium and 8-12% aluminium, generally perform better at higher temperatures (>900°C) where oxidation is the dominant failure mode [12]. At lower temperatures (650-800°C) where type II hot corrosion predominates, corrosion rates for the NiCrAlY and NiCoCrAlY coatings can be relatively high; hence Co base MCrAlYs with high Cr contents show better performances.

To have a better understanding of the differences in performance of Co base and Ni base MCrAlYs, it is essential to understand the role each element plays in these coatings. With the help of diagrams like the one in Figure 2-7 and better

understanding of the behaviour and roll of each element in the coating, better designs and composition of MCrAlYs are possible (composition of the MCrAlY system is selected to give a good balance between oxidation and corrosion resistance, and coating ductility).

2-6-1- Role of alloying elements

MCrAlY overlay coatings typically contain four elements or more. The role of these alloying elements is described as follows:

Aluminium (Al): Has the greatest effect on the oxidation resistance. It forms the stable α-Al_2O_3 which is a slow growing protective oxide. This effect of Al generally increases with its concentration. However, too much increase in its content can result in significant reduction of ductility of the MCrAlY, nevertheless it should be sufficiently high enough to develop and maintain an alumina layer and prevent subsequent breakaway oxidation [19]. Aluminium contents of 10-12 wt.% are typical. Aluminium, alloys with Co or Ni to form β-(Co,Ni)Al which readily forms the protective α-alumina scale and provides a reservoir from which the alumina scale can be replenished.

Chromium (Cr): Not only does it improve hot corrosion resistance, it also increases the activity and diffusivity of aluminium meaning less aluminium is required for forming and maintaining the protective alumina oxide scale. This will result in an increase in ductility. Chromium also effectively reduces oxygen diffusion into the alloy by lowering the oxygen activity at the oxide scale-alloy interface [20] and is also found to stabilise α-Al_2O_3 in preference to γ-Al_2O_3 [19]. It should be noted that Cr_2O_3 decomposes into volatile CrO_3 at temperatures above 900℃ [21].

Cobalt (Co): Generally the oxidation resistance increases as the cobalt concentration decreases [20]. It alloys with aluminium producing the β-CoAl and provides improved sulphidation resistance. It can be readily substituted for nickel.

Nickel (Ni): Forms a series of high melting point phases such as γ-Ni, γ'-Ni_3Al and oxidation resistant β-NiAl. It has also been reported that adding nickel to a ternary alloy of Co-Cr-Al can possibly reduce the process of interaction between the coating and the superalloy [8].

Boron (B): Boron has a strong detrimental effect on oxidation resistance. It encourages NiO scale formation rather than Al_2O_3 [20].

Titanium (Ti): this is one of the essential alloying elements in Ni base superalloys. It helps generation of the γ' phase which causes elevated temperature strength. However, it can be detrimental to the oxidation resistance as it leads to the formation of TiO_2 crystals which can break the alumina layer.

Yttrium (Y): The presence of yttrium improves the adherence of Al_2O_3 as well as Cr_2O_3 scales to alloy substrates [20, 22]. It has been reported by Peng et al. that the presence of yttrium prevents interfacial cavity formation [23]. Moreover, it has been reported that adherence of the thermally grown oxide layers (TGO's) are crucially dependent on the yttrium reservoir [24], a high yttrium reservoir leads to a high growth rate of the TGO which is basically detrimental for oxide adherence. Toscano et al. [24] have reported that an optimum yttrium content exists to obtain a compromise between the beneficial effect on oxide adherence without enhancing the growth rate of the oxide. However, in defining this optimum yttrium content, it is necessary to take into account the actual yttrium reservoir in the material i.e. the yttrium content for obtaining optimum TGO growth rate and adherence in a 100μm

thick layer will differ from that in a 200μm layer. The extent of yttrium reservoir required is directly proportional to the coating thickness. A thin coating has a low yttrium reservoir and hence a low TGO adherence while a thick coating has a high yttrium reservoir and hence good TGO adherence but due to the high yttrium reservoir higher locally accelerated oxide growth paths exists resulting in higher locally TGO growth rates [25].

Oxygen reactive elements (REs): Elements such as Hf, La, Zr etc are known as oxygen reactive elements as their oxides are generally more stable than the oxide scales formed on most alloys when exposed to high temperature oxidising environments [20]. A number of mechanisms have been proposed to explain the beneficial effects of REs which are as follow [20]:

- REs mechanically key the oxide scale to the alloy by forming oxide pegs at the oxide-alloy interface.
- REs segregate at the interface and increase the bond strength of the oxide scale to the alloy.
- REs suppress the formation of void by acting as a vacancy sink.
- REs tie up sulphur, which can segregate to the oxide-alloy interface and reduce the bond strength of the oxide scale.
- REs alter the growth mechanism of alumina and chromia from a combination of outward diffusion of Al or Cr and inward diffusion of oxygen to predominantly inward diffusion of oxygen.

However, it should be mentioned that all of the mechanisms may not be operating for all of the REs when added as elements or oxides.

Considering the role of REs has made MCrAlY coatings more complex and recent coatings are based on the MCrAlX system where M is Co, Ni or combination of both elements and X is an oxygen active element such as Y, Si, Ta, Hf, or even precious metals such as Pt, Pd, Re, etc. [3]. This system has led to the modification of the overlay coatings and coating systems such as Pt-aluminide MCrAlY coatings have been developed where a thin layer of Pt-aluminide is deposited before the deposition of the MCrAlY bond coat.

2-7- Deposition of MCrAlY coatings

MCrAlY coatings were initially deposited by EB-PVD [3, 14] and were very successful in enhancing the oxidation and hot corrosion resistance of the components. However, due to high capital cost considerations, techniques such as air, vacuum and low pressure plasma spraying (APS, VPS, LPPS) have found wide acceptance and more recently, coating manufacturers have developed a new technique, high velocity oxyfuel (HVOF) [3, 14].

2-7-1- High Velocity Oxy Fuel (HVOF)

The HVOF process was developed in the 1980s as a lower cost alternative to the detonation-gun (D-Gun) and had a dramatic influence on the thermal spray industry. At first designed for spraying wear resistant cermets such as WC-Co, however, now the process has evolved into a key thermal spraying process and is used for spraying many types of materials including metals, alloys, ceramics, composites and even polymers as well as the initial cermet materials [26].

The purpose of the HVOF design, as is the same for any other thermal spray process, is to transfer energy in kinetic and thermal form to the powder particles with a high degree of efficiency. In the past decades the major trend in thermal spraying processes has been to reduce the temperature of the spraying process and increase the velocity of the powder particles so that there is less melting and thus less vaporisation and oxidation of the material during spraying and more mechanical bonding to the substrate. One of the most successful processes in this trend has been the HVOF spraying system. A schematic of a HVOF device is shown in Figure 2-8.

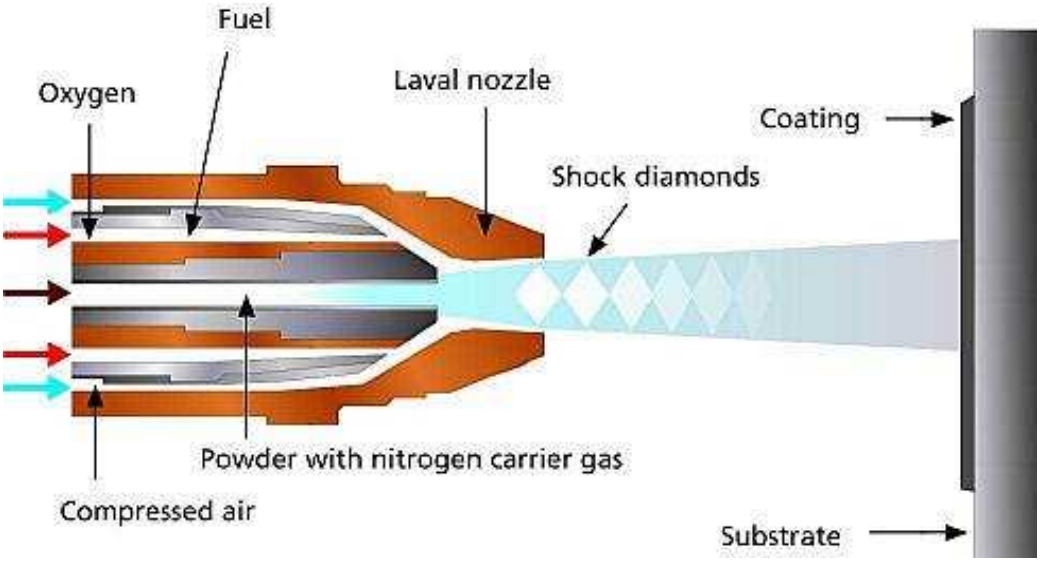

Figure 2-8. Schematic diagram of a Sulzer Metco Diamond Jet gun [26].

In the HVOF process, a blend of fuel in the form of gas (e.g. propane, propylene, hydrogen) or liquid (e.g. kerosene) and oxygen are injected under high pressure into a combustion chamber where they are burned. The maximum temperature attained in this process is around 2700-3200K [27]. The hot burning gases are then allowed to expand and flow through special nozzle which allows the gas to accelerate to speeds as high as 2000m/s. The appropriate combination of the gas and oxygen generates hypersonic exhaust gas velocities. In this method the powder to be deposited is

injected into a stream of carrier gas, usually argon or nitrogen, into the combustion chamber, where they are heated and accelerated by the expanding gases along the nozzle. Particle velocities may reach 800m/s. Particles are ejected from the gun as a stream of fully or partially melted particles, the latter being frequently the case in HVOF. On impact, a large enough stress is produced to significantly deform the particles and build up the coating. This is enhanced by the heating process which softens the particles.

The high kinetic energy (due to a high particle velocity) of the powder particles play an important role in HVOF spraying. It supplies a mechanical force which helps bond new particles onto previously deposited mass. As the particles impact on the substrate the thermal energy is rapidly and uniformly absorbed by the substrate which results in rapid solidification of the molten regions of the coating. The high kinetic energy stored in each particle and the corresponding higher stresses experienced on impact are the main reasons why HVOF coatings have a higher density and bond strength than most other thermal spray coatings [28].

By utilising the correct operating parameters, coatings with high bond strength (up to 70MPa) and low porosity (<1%) can be achieved. The coating thickness is usually in the range of 0.05-0.5mm. However, thicker coatings can be formed from some materials. A powder size range of 15-45μm is typical for HVOF spraying. Like any other spraying process HVOF also has some advantages and disadvantages which are illustrated in Table 2-2.

Table 2-2. Advantages & disadvantages of HVOF spraying over other thermal spraying methods [26].

ADVANTAGES		DISADVANTAGES	
Characteristic	**Comment**	**Characteristic**	**Comment**
Low level of through-porosity (about 1-2vol.%)	Improved corrosion protection	A line of sight process	Difficult to spray on internal surfaces of small cylindrical components or other restricted access surfaces
Low oxide content (in the range of 1-2wt.%)	Due to less in-flight exposure time		
Higher hardness	Improves the wear resistance		
Retention of powder chemistry	Caused by a reduced time at temperature		
Higher coating adhesion	Higher particle velocity on impact Low levels of residual stress, can be in compression	Small powder particle sizes and narrow size distribution	High consumable costs
Thicker coatings (up to 2mm)	Self peening effect of impacting particles		
Lower levels of residual stresses-can be in compression			

2-7-1-1- Types of HVOF guns

The first commercial HVOF spray gun was the Jet-Kote, this was developed in the 1980s [7, 28] and is the basis of many HVOF thermal spray systems in production today. Different manufacturers have developed several different spraying guns which mainly differ by fuel type (liquid or gas), water or air cooled, axial or radial powder injection, combustion chamber configuration and nozzle design and length. Operational differences comprise combustion pressure, fuel and gas flow rates, and

powder feed rates. Powder particle heating time, temperature and velocity are determined by these parameters.

The common spraying guns used commercially are as follows, the manufacturer is indicated in brackets:

- Jet Kote II (Deloro Stellite)
- Diamond Jet (Sulzer Metco)
- Top Gun/HV-2000 (Praxair)
- JP-5000 (Tafa)
- Met-Jet II (Metallisation)

Since the Met-Jet II was used to spray the coatings studied in this work, a short description of this specific gun is as follows.

Met-Jet II (Metallisation)

There are two classes of high velocity combustion spray devices, dividing according to their combustion chamber pressure. The first class, known as high velocity, is characterised by chamber pressures exceeding 241kPa (35psi) and heat inputs of ~527MJ. However, the second class would be better termed hypervelocity, operating nominally at 620 to 827kPa (90 to 120psi) with ~1GJ heat input and is typically fuelled with kerosene [29].

The Met Jet gun is considered as being in this second class and uses kerosene as its fuel. Kerosene and oxygen are premixed and injected axially into the combustion chamber where they burn. The hot gas jet then passes through a converging-diverging

throat, which accelerates the gas stream. The powder is fed into the hot gas jet downstream of the throat. It is observed that coatings produced with this gun comprise partially melted powder particles rather than fully melted splats [26]. Figure 2-9 illustrates a schematic diagram of this gun.

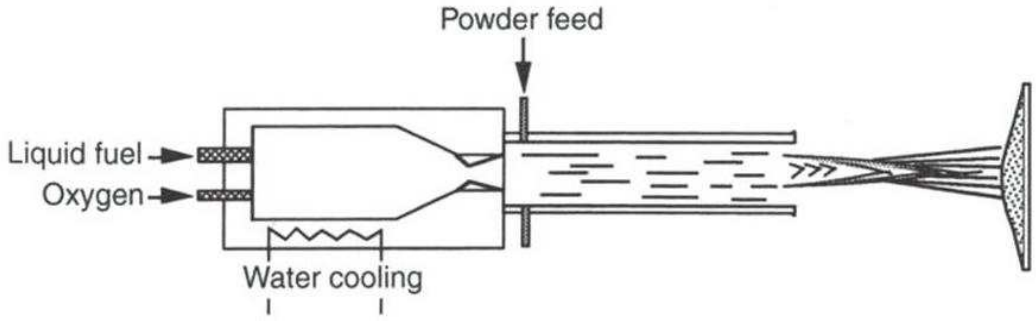

Figure 2-9. Schematic diagram of a Met Jet type gun [29].

Typical values for fuel flow rate, oxygen/fuel ratio and spraying distance for different spraying systems are shown in Table 2-3.

Table 2-3. Typical spraying parameters for different HVOF systems [30].

System	Fuel type	Fuel flow (m^3h^{-1})	Oxygen flow (m^3h^{-1})	Oxygen / Fuel ratio	Powder feed rate ($g.min^{-1}$)	Spray distance (mm)
Jet Kote	Hydrogen	25.5	12.8	0.5	32-40	250
	Propane	3	18	6	30-40	
	Ethylene	4.8	28.4	5.9	30-40	
Top Gun	Hydrogen	26	13	0.5	30-40	250
	Propane	3	15	5	30-40	
	Ethylene	4.7	14.1	3	30-40	
DJ 2600	Hydrogen	38.2	12.8	0.45	60-70	230-250
DJ 2700	Propane	4.1	14.5	4.6	60-70	230-250
	Ethylene	6.8	15	2.9	60-70	
JP-5000	Kerosene	20.8	53.6	4.3	80	350-380

2-7-1-2- HVOF process variables

Although HVOF spraying is a relatively simple process, there are still number of parameters which need to be controlled. These process variables include: fuel type (gas or liquid), fuel to oxygen ratio, gas pressure, powder feed rate, nozzle length, stand off distance, composition of the fuel, etc [31]. It has been shown that spraying distance, fuel/oxygen ratio, fuel plus oxygen mass flow rate and powder feed rate exert a major influence on microstructure and oxygen content [32]. For example, changes in spraying distance can affect the time in flight and thus result in different percentages of particle melting; oxygen to fuel ratio can affect the flame temperature and thus result in different percentages of melted particles. Further details on the affect of spraying parameters can be observed in [32-35].

2-7-2- Plasma Spraying

Plasma spraying is a well established thermal spraying technique which has been around for several decades and is used to produce thick coatings. The process was first invented by Thermal Dynamic Corp (Lebanon) in 1957 [36]. This process employs the high temperature of the plasma ranging from 6000 to 15000°C [29] in order to melt any material which does not decompose before melting. Even high melting point ceramics such as alumina and zirconia may be deposited using plasma spraying.

There are two main plasma spraying methods, atmospheric plasma spray (APS) and vacuum plasma spray (VPS).

2-7-2-1- Air Plasma Spraying

In atmospheric plasma spray, also known as conventional plasma spray, the plasma is generated by allowing a flow of, usually, argon gas between a tungsten cathode and a water cooled copper anode. At this point an electric arc is initiated between the two electrodes using a high frequency discharge and then sustained using dc power. This arc heats up the gas which expands in the atmosphere forming a jet ,the velocity at the nozzle exit can reach 600-800m/s [27, 37]. The powder is usually introduced to the gas stream, via a carrier gas, either just outside the torch or in the diverging exit region of the nozzle. The molten/semi-molten powder particles are accelerated towards the prepared substrate by the initial expansion of the gas and form the coating. A schematic of a typical APS gun is illustrated in Figure 2-10.

The porosity of the APS coating is usually in the range of 1-7% [37], and could be intentionally made greater. The thickness of these coating are typically in the range of 300-1500µm [37]. The operating parameters not only include the gas flow, power levels, powder feed rate, and carrier gas flow but also the standoff distance and the angle of deposition.

High porosity levels and oxidation rates are some of the main disadvantages of APS. The cathode life is also shorter in APS compared to other methods due to the high enthalpy of oxygen plasma [7]. Furthermore, due to the direct contact of the high temperature gas stream to the substrate, high substrate temperatures are generated.

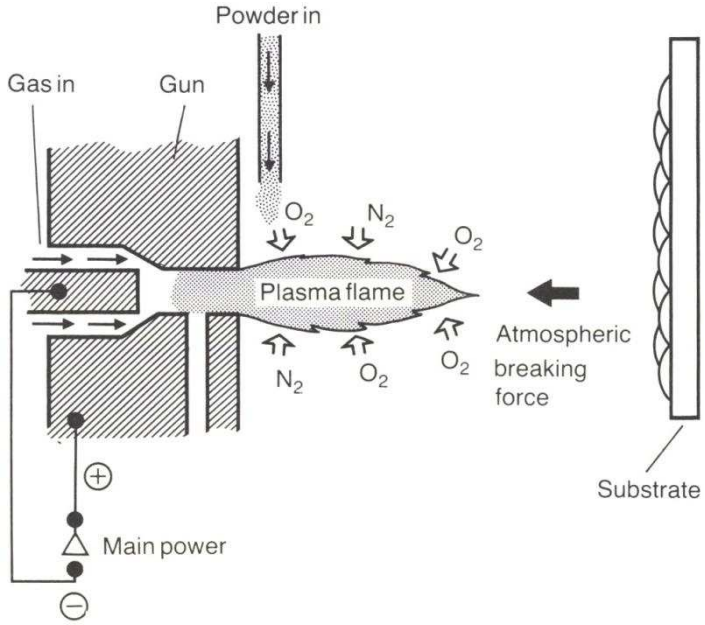

Figure 2-10. A schematic diagram of the APS system [38].

2-7-2-2- Vacuum Plasma Spraying (VPS)

The second type of plasma spraying is vacuum plasma spraying which is also known as low pressure plasma spraying (LPPS). The principle of this technique is based on the APS method, where a plasma source is generated in order to heat and accelerate the powder particles towards the preset substrate. However, since the APS process is carried out in normal atmospheric air, during the APS process there is a chance of air entrapment. This can lead to the oxidation of the coating material. Moreover, since the temperatures are extremely high in plasma spraying, and APS is carried out in air; there is a high oxidation rate of the in-flight particles.

The desire to minimise oxide content of the plasma sprayed coating led the process to be carried out in a lower pressure or vacuum and the development of vacuum plasma spraying (VPS). LPPS or VPS reduced the problems associated with APS by spraying in a vacuum or a low pressure inert gas environment (typically 10-100 mbar). In

addition to overcoming the problems of entrainment of air in the plasma stream, it is possible to transfer the arc which allows both preheating of the component and sputter cleaning to remove contamination and surface oxide prior to coating deposition. This improves the adherence of the coating to the substrate.

Also because of the reduction in the atmospheric braking force, the plasma flame is longer in VPS compared to APS which can cause overheating of the substrate. This can be seen in Figure 2-11 and Figure 2-12. However, despite the increase in plasma length, the jet and therefore the injected particles have greater kinetic energy in VPS, which can lead to inadequate melting of the powder particles due to reduced dwell time. To compensate for the effect of reduced dwell time the torch to work piece distance is increased from ~50mm in APS to 300mm in VPS. The powder particle size is also reduced for VPS, from 20-70μm for APS to 5-25μm for VPS to ensure full melting despite the reduced dwell time. Figure 2-13 shows a schematic diagram of a VPS system.

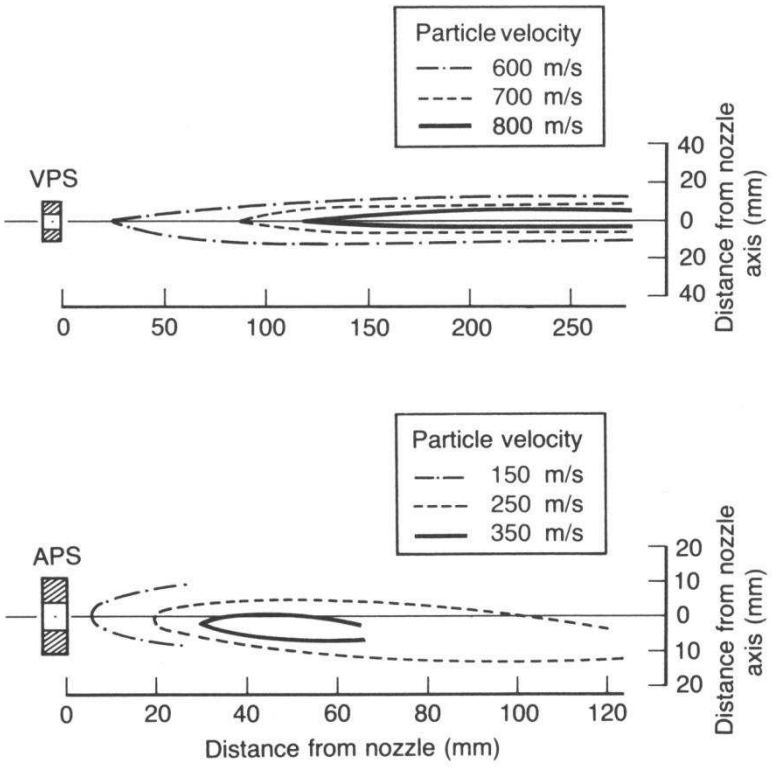

Figure 2-11. Particle velocity profiles for VPS & APS alumina [38].

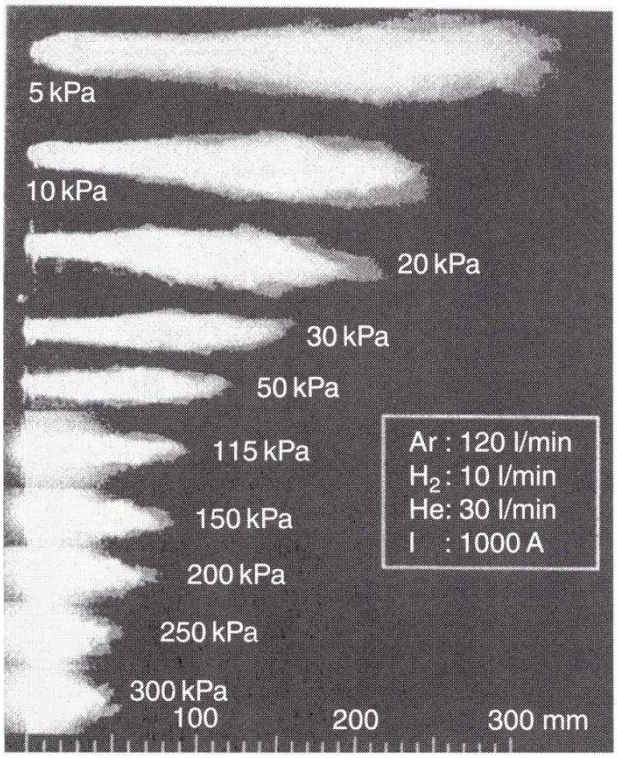

Figure 2-12. Length of plasma plume as a function of chamber pressure [20].

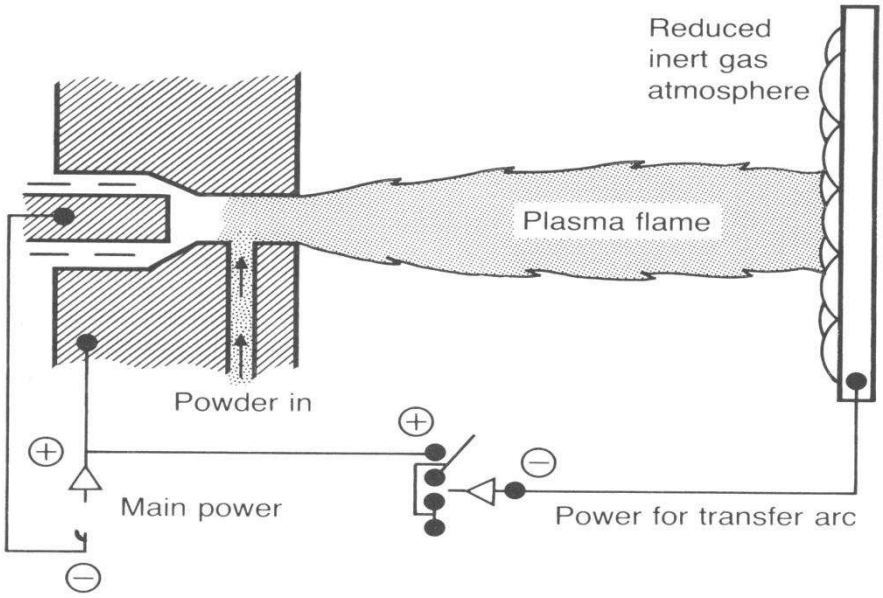

Figure 2-13. Schematic diagram of a VPS gun [38].

The operating parameters in VPS not only include the gas flow, power levels, powder feed rate and carrier gas flow, but also the stand-off distance (distance from the torch to the substrate) and the angle of deposition.

As in HVOF, stand-off is of substantial importance since adequate distance must be provided for heating and accelerating the powder, however, if this distance is too high it will allow the powder to cool and lose velocity because gas stream is rapidly expanding, cooling and slowing. Standoff distances in the range of 300 to 400mm are typical [39]. The size and morphology of the powder particles strongly influence their rate of heating and acceleration and hence the deposition and the quality of the coating. Table 2-5 shows some typical VPS parameter values.

Table 2-4. Typical values for VPS spraying parameters [37].

Working gas composition	Ar mixed with H_2, He or N_2
Flow rate (slpm)	90-200
Electric power input (kW)	80
Powder particle size (µm)	5-20
Stand-off distance (mm)	300-400
Spray atmosphere (Pa)	1.3 (before spraying) 655-13300 (dynamic pressure at spraying)

As there is a cost associated with the advantages of different thermal spray techniques, one must weigh the benefits obtained against the high cots associated with the technique. A comparative gas temperature, particle velocity and cost for different thermal spray processes are illustrated in Figure 2-14.

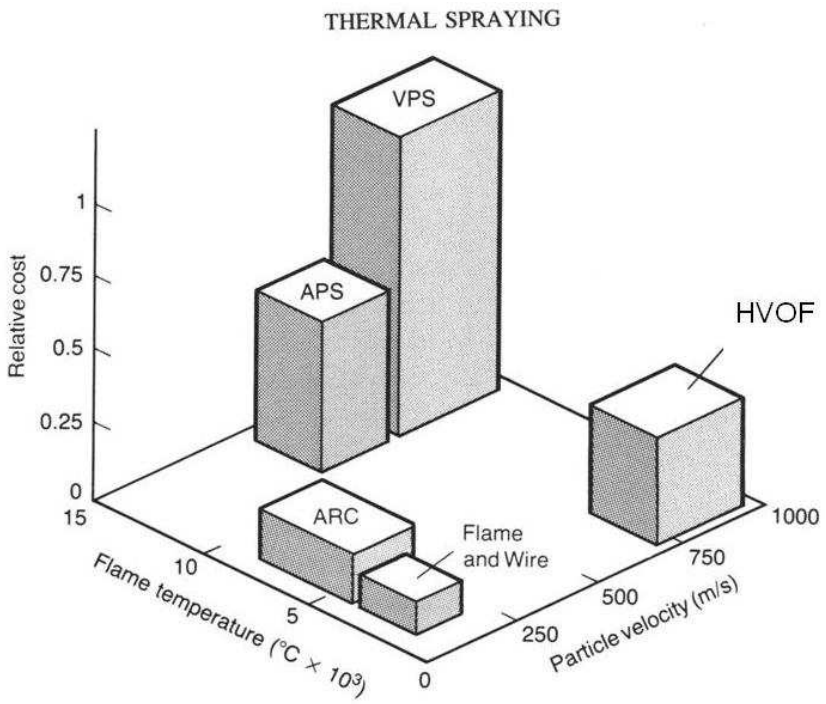

Figure 2-14. Comparison of the flame temperature, particle velocity & cost of the major thermal spray processes [38].

2-8- Constitution of thermally sprayed MCrAlY coatings

MCrAlY alloys typically exhibit a two phase microstructure of γ+β as shown schematically in Figure 2-15.

The γ phase is face centred cubic (FCC) and is a solid solution of Co, Ni, Cr, etc with a lattice parameter close to 0.354nm. The β phase is a (Co,Ni)Al, which results from CoAl, NiAl phases and is an ordered body centred cubic (BCC) phase with a lattice parameter close to 0.286nm. It is the amount of the β phase that is most essential for the coating protection. In fact, the β phase acts as a reservoir for aluminum to form protective Al_2O_3. This is why the cyclic oxidation life of the coating is directly related

to the amount of β phase present in the coating. The β phase occurs in different morphologies, which have been related to the different cooling rates associated with different sized powder particles during spraying. Figure 2-16 shows TEM images of a VPS as-sprayed CoNiCrAlY coating which illustrate different morphologies of β phase [40]. "Elongated laths of β phase inside γ grains (Figure 2-16a) and small grains of β located in the boundary between γ grains (Figure 2-16b) were associated with rapid cooling of small droplets on deposition or in the plasma spray. Larger grains of β (Figure 2-16c) were more common and were associated with larger, slow cooling particles" [40].

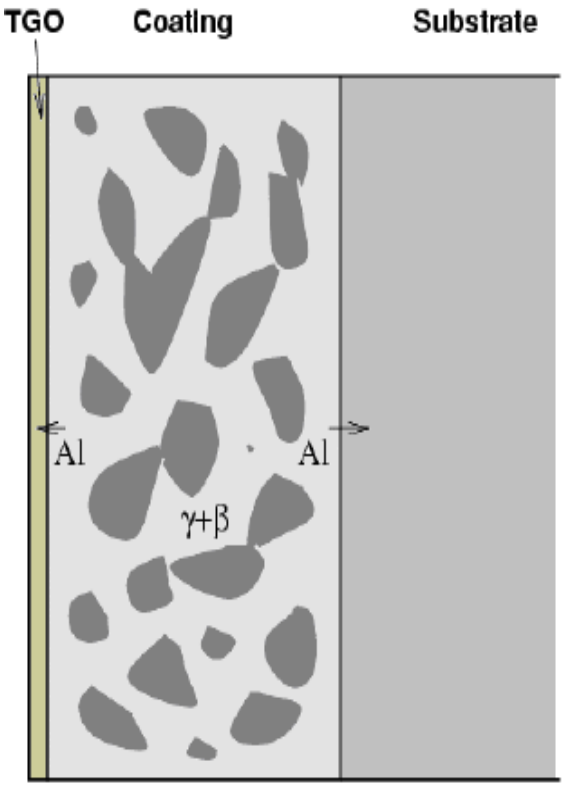

Figure 2-15. Schematic illustration of MCrAlY microstructure.

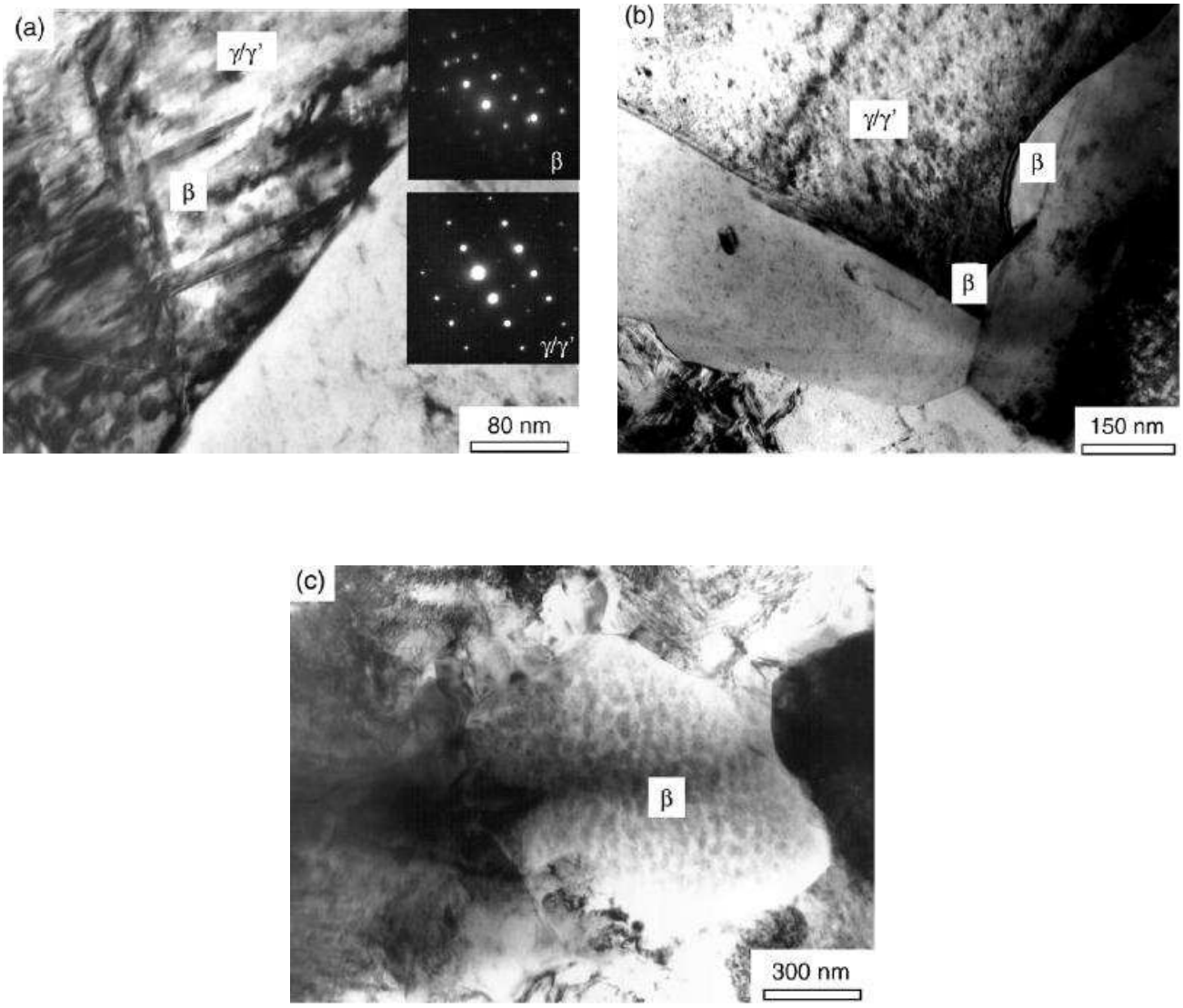

Figure 2-16. Distribution of β phase over the as-sprayed coating microstructure of a VPS sprayed CoNiCrAlY, a) Elongated laths of β phase inside a γ grain, b) small grains of β located in the γ grain boundaries, c) large grain of β surrounded by the γ matrix [40].

However, phases other than γ and β will form depending on temperature and the composition of the MCrAlY alloy. Table 2-5 and Table 2-6 show the chemical and phase constituent of a wide range of CoNiCrAlY and NiCoCrAlY alloys respectively.

Table 2-5. Chemical compositions & phase constituent of CoNiCrAl alloys [8].

		Chemical composition, wt%					
No.	**Alloy**	**Co**	**Ni**	**Cr**	**Al**	**Y**	**Phases at 20℃**
1	Co10Ni15Cr6AlY	Base	10.6	15.1	6	0.3	γ, β
2	Co30Ni15Cr6AlY	Base	30.8	14.9	5.9	0.3	γ, β
3	Co10Ni30Cr6AlY	Base	10.8	29.8	6	0.3	γ, β
4	Co30Ni30Cr6AlY	Base	30.6	30.2	6.2	0.3	γ, β
5	Co10Ni15Cr12AlY	Base	10.6	15	11.8	0.3	γ, β
6	Co30Ni15Cr12AlY	Base	30.6	15.1	11.8	0.3	γ, β, σ
7	Co10Ni30Cr12AlY	Base	10.7	29.8	12	0.2	γ, β, σ
8	Co30Ni30Cr12AlY	Base	29.7	29.2	11.8	0.6	γ, β, σ
9	Co10Ni22Cr9AlY	Base	12.6	22.5	9.3	0.7	γ, β, σ
10	Co30Ni22Cr9AlY	Base	31	22.4	9.2	0.2	γ, β, σ
11	Co20Ni15Cr9AlY	Base	22.4	14.3	9.1	0.2	γ, β
12	Co20Ni30Cr9AlY	Base	22.2	30	9.2	0.1	γ, β, σ
13	Co20Ni22Cr6AlY	Base	17.2	23.5	6.9	0.1	γ, β, σ
14	Co20Ni22Cr12AlY	Base	21.2	22.6	11.8	0.3	γ, β, σ
15	Co20Ni22Cr9AlY	Base	20.4	22.6	9.3	0.3	γ, β, σ
16	Co20Ni22Cr9AlY	Base	20.6	22.5	9	0.1	γ, β, σ
17	Co20Ni22Cr9AlY	Base	17.8	22.6	9.3	0.5	γ, β, σ
18	Co22Cr9AlY	Base	—	22.6	9.2	0.3	γ, β, σ

Table 2-6. Chemical composition & phase constituent of NiCoCrAl alloys [8].

		Chemical composition, wt%					
No.	**Alloy**	**Ni**	**Co**	**Cr**	**Al**	**Y**	**Phases at 20℃**
1	Ni10Co15Cr8Al	Base	11.3	15.5	8.9	0.04	γ, γ', β
2	Ni30Co15Cr8Al	Base	27.5	14.4	9.3	0.05	γ, γ', β
3	Ni10Co30Cr8Al	Base	10.1	28.5	7.8	0.11	γ, γ', β, α
4	Ni30Co30Cr8Al	Base	29.4	29.6	7.8	0.1	γ, γ', β, σ
5	Ni10Co15Cr14Al	Base	10.5	15.1	13.5	0.07	γ, γ', β, α
6	Ni30Co15Cr14Al	Base	27.5	15.2	13.6	0.08	β, α
7	Ni10Co30Cr14Al	Base	10.6	30.0	14.1	0.06	β, α
8	Ni30Co30Cr14Al	Base	29.7	29.7	14.1	0.08	β, σ
9	Ni10Co15Cr8AlY	Base	11.2	15.2	8.2	0.04	γ, γ', β
10	Ni30Co15Cr8AlY	Base	30.2	14.7	8.1	0.45	γ, γ', β
11	Ni10Co30Cr8AlY	Base	11.1	29.3	8.0	0.2	γ, γ', β, α
12	Ni30Co30Cr8AlY	Base	28.8	29.5	8.1	0.33	γ, γ', β, σ
13	Ni10Co15Cr14AlY	Base	10.4	14.6	13.6	0.04	γ, γ', β, α
14	Ni30Co15Cr14AlY	Base	29.5	15.9	13.8	0.25	β, α
15	Ni10Co30Cr14AlY	Base	10.5	28.8	13.8	0.32	β, α
16	Ni30Co30Cr14AlY	Base	29.9	29.7	14.1	0.46	β, σ
17	Ni10Co22Cr11AlY	Base	10.1	22.2	10.6	0.30	γ, γ', β, α
18	Ni30Co22Cr11AlY	Base	29.8	22.2	10.9	0.23	γ, γ', β, σ

If the Ni to Co ratio is high enough then γ'-Ni_3Al phase may also form [41]. Presence of this phase (γ') in NiCoCrAlY has been reported in several papers [8, 22, 31, 42, 43]. However, it has been reported that alloying the NiCrAl system with cobalt reduces thermal stability of γ', decreases its quantity and converts the NiCoCrAl system into the state based on γ+β [8]. Fritscher and Lee [43] have mentioned that the γ'-Ni_3Al phase tends to vanish as soon as a Ni:Co ratio exceeds 2:1.

The γ' phase has not been observed in Co base MCrAlYs (CoNiCrAlY) [8, 41, 42]. The reason for the absence of γ' has been reported by some researchers [44, 45] who state that Co tends to reduce the fraction of γ' and increases that of the γ-phase due to an increased equilibrium Al-activity in the γ-phase. However, it has been stated by Cheruvu et al. and Mobarra et al. [46, 47] that inward and outward diffusion of Al, into the underlying substrate and the oxide layer (for the replenishment of the oxide layer) forces the transformation of the β-NiAl into γ'-Ni_3Al. Poza et al [40] have also reported traces of γ'-Ni_3Al near the coating-substrate interface due to the diffusion of Co and Cr to the substrate and the replacement of Co by Ni which stabilises the γ' phase.

2-9- Effect of thermal exposure

2-9-1- Heat treatment

As mentioned previously the high temperature strength of the superalloys is due to the fact that they have a stable FCC matrix combined with either precipitation strengthening and/or solid solution strengthening. Superalloys owe their precipitation strengthening to the formation of γ′ intermetallic (Ni_3Al,Ti). Furthermore, second phase strengthening from γ″ (Ni_3Nb) intermetallic formation could also help further

strengthening the superalloy. However, non-hardenable alloys rely on solution strengthening. Considering what has been mentioned above, heat treatment of these alloys is an important aspect.

Due to confidentiality, industries do not declare their exact heat treatment processes carried out on specific alloys and components. However, as a rule of thumb, superalloy substrates with the MCrAlY bond coat go through a solution heat treatment followed by an ageing treatment. The solution heat treatment carried out for Inconel superalloys is usually within the temperature range of 980℃ to 1150℃ for exposure times of up to 2 hours [48].

Hence, heat treatment is required for solution strengthening and ageing, better adhesion of coating to substrate through interdiffusion, reducing porosity levels within the coating, etc.

2-9-2- Phase changes

Phase transformations in the MCrAlY bond coats can have a profound effect on the TBC lifetime. These transformations are associated with a volume change resulting in expansion [25]. This volume change will further affect the TGO and its adherence is deteriorated and TBC lifetime is shortened. Hence the investigation of these phase transformations is of great importance and should be considered when designing the bond coat chemical compositions [25].

The microstructure of MCrAlY coatings at T<1000°C may be more complex as it often contains large volume fractions of σ-(Co,Cr) and α-Cr phases [44, 49]. The σ phase is a topologically close packed (TCP) intermetallic phase which is rich in Ni, Co, and Cr and has been observed to form after prolonged exposure at temperature

[50]. This undesirable phase is generally characterised by its hardness, brittleness and crystallographic arrangement, sigma has 30 atoms per body centred tetragonal unit cell [50]. σ can form either in a discrete blocky morphology at the grain boundaries or as needle or plates which span grain boundaries and grow into the matrix. The platelike σ phase precipitation dramatically degrades the ductility of alloy and also results in localised depletion of the solid solution strengthening elements in the adjacent γ matrix [8, 50]. The instability of the σ-(Co,Cr) phase in a NiCoCrAlY coating above 880°C has been reported by Toscano et al. [42]. They showed that the chromium released due to the disappearance of this phase (σ), leads to an increase of the α-Cr phase. Contrary to the σ-(Co,Cr), the α-Cr remains stable even at 1100°C [42]. This relationship is illustrated in Figure 2-17.

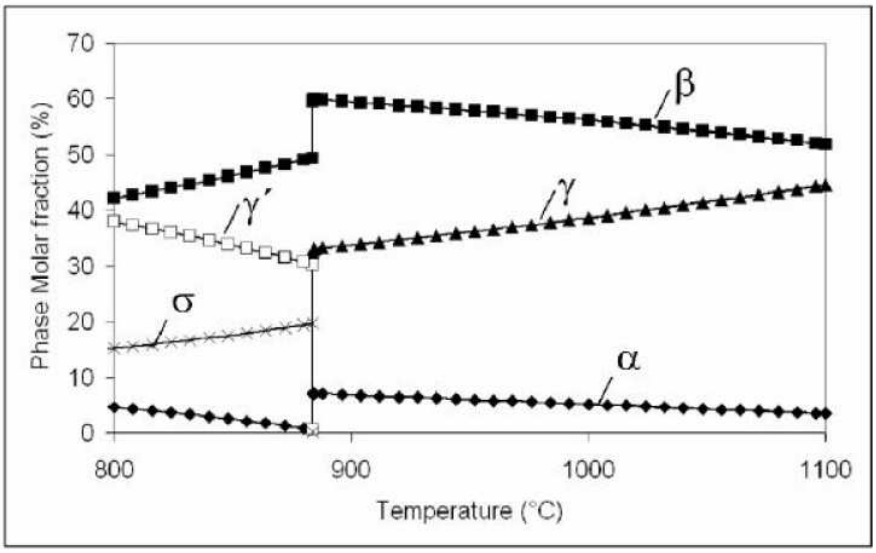

Figure 2-17. Molar fraction of the phases in a temperature range 800-1100°C calculated by ThermoCalc software for a NiCoCrAlY coating [42].

Thermal stability of σ phase for a CoNiCrAlY coating is also shown in Figure 2-18 where it is shown that stability of σ phase decreases at temperatures higher than 800°C and it disappears at 1100°C.

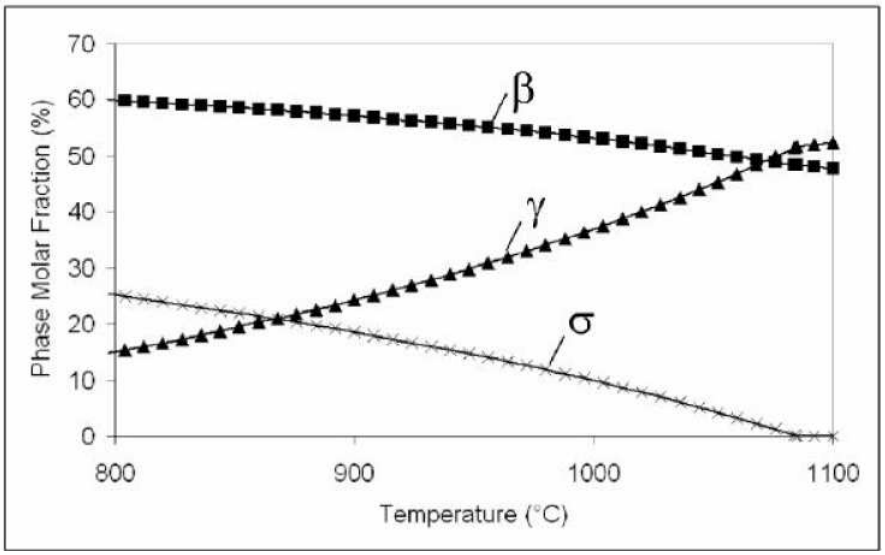

Figure 2-18. Molar fraction of the phases in a temperature range 800-1100°C calculated by ThermoCalc software for a CoNiCrAlY coating [42].

Figure 2-19 shows a SEM micrograph of a NiCoCrAlY after 25hr of exposure in air at 1100°C in which isolated precipitates of α-Cr in addition to γ & β phase could be observed.

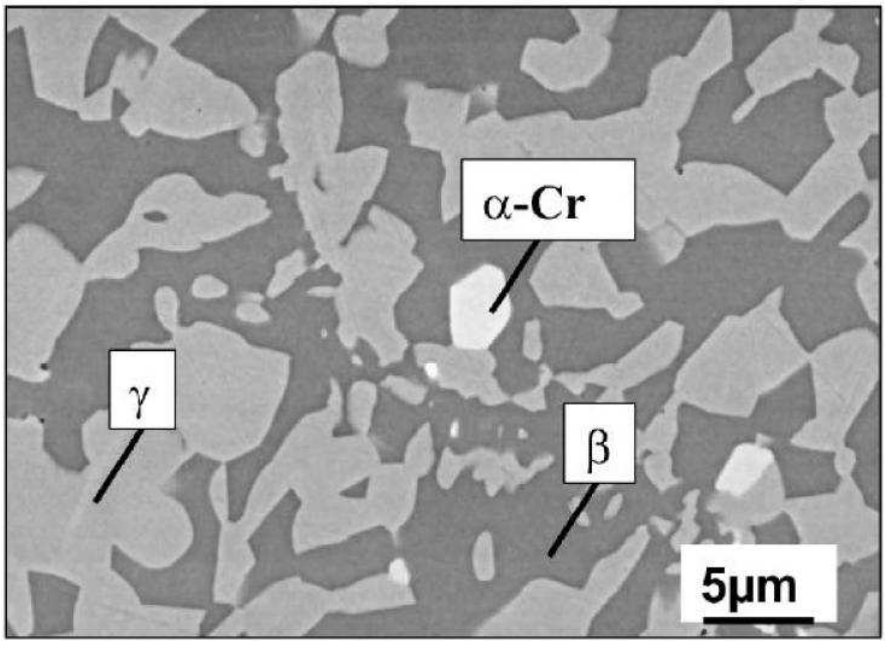

Figure 2-19. SEM micrograph of a NiCoCrAlY coating after 25hr isothermal air exposure at 1100°C and subsequent water quenching [42].

After homogenisation and precipitation annealing of a NiCoCrAlY coating, Brandl et al. [22] identified (using TEM/EDS) a Ni_5Y intermetallic phase in addition to γ, γ'-Ni_3Al, β-NiAl, and σ-(Co, Cr). However they have stated that these particles (Ni_5Y) are very small and their identification by XRD was impossible due to the low amount of the phase in the coating. Toscano et al. [42] have also reported that in their annealed CoNiCrAlY coating at 1100°C, in addition to the predominant γ and β phase, particles corresponding to a Ni-Y intermetallic phase were observed. It was concluded that the observation of Ni(Co)Y intermetallic phase in the CoNiCrAlY, and not in the NiCoCrAlY coating can be an indication that the Ni(Co)Y compounds are stabilised by higher Co concentrations [42]. However, at 1000°C, the NiY phase was also observed in the microstructure of the NiCoCrAlY coating containing less Co. This was due to the fact that the Y solubility limit in the γ and β was exceeded at this temperature, contrary to 1100°C [42].

2-9-3- Interdiffusion

Until recently with the interest in the MCrAlY alloys as bond coats, interdiffusion with the substrate has not been considered a major failure mode of overlay coatings [12]. However, even with MCrAlX systems and more advanced overlay coating concepts, diffusion of elements between the substrate and the coating and loss of Al to the oxide can have a major influence on coating performance. Some of these interdiffusion effects are of benefit to the overlay coating and some are not; for example it has been observed that Hf diffusion from a Hf modified MM200 has been found to improve the hot corrosion resistance of CoNiCrAlY coatings [12]. However at the same time the diffusion of other elements from the substrate (e.g. tungsten and molybdenum) to the coating may well be detrimental to corrosion or oxidation resistance or even cause microstructural instability of the superalloy substrate.

Nicholls [12] has reported that diffusion stability can be considered a life limiting factor if coatings are operated at temperatures greater than 1000°C for prolonged periods of time. Therefore it is necessary to develop diffusion barrier coatings which can minimise the interdiffusion between the coating and the substrate to provide long term stability. Extensive efforts have been made in this regards by carburising or nitriding of the superalloy substrate or using diffusion barrier layers such as TiN or Al-O-N thin film layer. Among the various diffusion barrier candidates, α-Al_2O_3 has been reported to be an effective diffusion barrier to suppress the interdiffusion between MCrAlY coating and the superalloy substrate [51].

However, some interdiffusion is necessary to provide, for example, good adhesion, therefore the diffusion barriers must be tailored to limit the movement of particular elements [3]. Diffusion barrier coatings must limit the diffusion of Cr from the coating to the substrate, since diffusion of Cr to the coating can increase the likelihood of forming the sigma phase within the alloy below the coating and hence reduce its properties [3]. They must also inhibit the diffusion of Al from the coating to the substrate since this will result in loss of the β phase which is essential for oxidation resistance [52].

However, it must be noted that in this research work free standing coatings have been investigated where no interdiffusion between coating and substrate can occur.

2-9-4- Oxidation and corrosion

High temperature alloys derive their protection against oxidising environments by forming a thin oxide layer commonly called thermally grown oxide (TGO) layer. This layer acts as a barrier between the coating and the atmosphere and prevents further oxidation. The growth of the TGO occurs by outward diffusion of metal ions or by

inward diffusion of oxygen ions through the oxide layer [14]. Generally the inward diffusion of oxygen through the TGO controls the further TGO growth, but in some cases this is controlled by outward diffusion of metallic ions (e.g. Al, Cr, etc) leading to a formation of the new TGO at the TGO/topcoat interface, TGO exposed surface or at the α-Al_2O_3 grain boundaries within the TGO [16].

Hot corrosion problems (type I, 800-950°C, and type II, 600-800°C) are a direct result of salt contaminants such as Na_2SO_4, NaCl, and V_2O_5 which in combination produce low melting temperature deposits that dissolve the protective surface oxides [12]. These corrosion processes can be separated into initial and propagative stages. In the initial stage the corrosion rates are very low since the breakdown of the oxide surface occurs. Once the oxide surface is broken and the repair is no longer possible (α-Al_2O_3 is no longer capable of replenishing itself) the propagation stage results in the rapid consumption of the alloy [12]. This stage often results in catastrophic corrosion rates.

2-9-4-1- Oxidation during spraying

Oxidation during thermal spraying can have a significant effect on the phase composition, microstructure, properties and performance of the sprayed coatings. Ideally it would be better to understand and control or predict the extent of oxidation.

During HVOF thermal spraying there are three areas where oxidation can occur [34]:

- Oxidation of the powder while in the combustion chamber or barrel
- Whilst powder particles are in flight
- After impact on the substrate surface until they are covered by subsequent particles

The turbulent mixing of the spray jet with the surrounding atmosphere can have a significant influence on the oxide content of the coatings.

However, since the amount of the oxides formed during HVOF spraying is low (can be <5%) and they are usually localised to the surface area of the powder particles or splats, techniques such as X-ray diffraction (XRD) can not easily detect the presence of these oxides. Brandl et al. [22] have found two types of oxide present in a NiCoCrAlYRe coating sprayed by HVOF using transmission electron microscopy (TEM). These oxides have been proven to be alumina and aluminium yttrium oxides.

2-9-4-2- Oxidation in service

Oxidation is an environmental phenomenon in which metals or alloys exposed to oxygen or oxygen containing gases at elevated temperatures convert some or all of the metallic elements into their oxides [20]. The oxide formed can act as a protective scale if it remains adherent and so reduce further oxidation. However, if the oxide scale formed continually spalls off, it will expose fresh metal and thus results in progressive metal loss.

When the total chemical equation for the chemical reaction between a metal and oxygen gas to form the metal oxide is considered, oxidation of metals may seem to be among the simplest chemical reactions. However, the reaction path and the oxidation behaviour of a metal can depend on a variety of factors, and reaction mechanisms may as a result prove complex.

$$aMe + \frac{b}{2}O_2 \rightarrow Me_aO_b \qquad (2\text{-}1)$$

Oxidation is generally studied by controlled exposure of metals to oxidising atmospheres such as O_2, CO_2, H_2O, NO_2 or air at high temperatures for a various lengths of time. The purpose of oxidation experiments is generally to assess the reaction kinetics and the mechanism of oxidation of a metal or alloy under a set of exposure variables such as temperature, pressure, or gas composition.

The rate of formation of an oxide on a metal according to the reaction in equation (2-1) can be investigated by several methods [53]:

- The amount of metal consumed: in practice this may be assessed by observing either the mass loss of the sample or the residual metal thickness.
- The amount of oxygen consumed: This may be assessed by observing either the mass gain or the amount of oxygen used.
- The amount of oxide produced: This may be assessed by observing the mass of oxide formed or by measuring the oxide thickness.

When representing oxidation kinetics any of the above variables can be used and can be measured as a function of time, since they all result in an assessment of the extent of reaction.

2-9-4-3- Oxidation process

A metal will oxidise if the free energy ($\Delta G°$) associated with its reaction is negative. However, the free energy for a reaction is affected by a number of parameters which are as follow:

- Temperature
- Partial pressure
- Composition

The effect of temperature and oxygen partial pressure on the free energy of different material can be seen in the Ellingham diagram of Figure 2-20. Composition also has a big effect on the free energy associated with an oxidation reaction, as it is usually assumed that the thermodynamic activity of metal(s) in a reaction is one ($a_{Me}=1$). However, in the case of alloys, this is not true as the thermodynamic activity of different elements varies within an alloy.

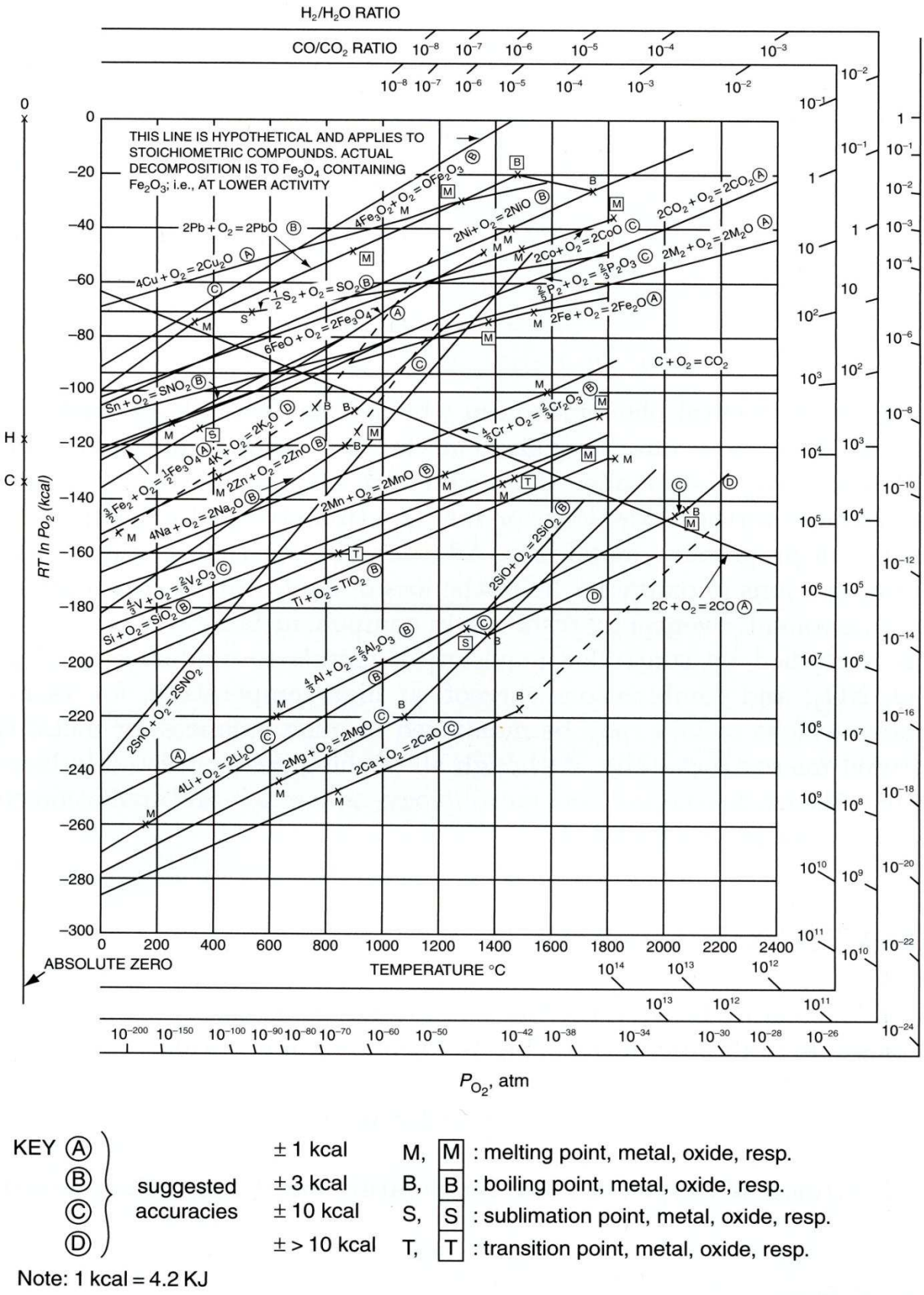

Figure 2-20. Ellingham diagram of free energy of formation of oxides as a function of temperature [20].

Although it is essential to know the thermodynamic consideration of free energy change to determine the occurrence of an oxidation reaction, the kinetics of the reactions is also important. It has been found experimentally that several rate laws can be identified. The principal laws are as follow [54]:

- The linear law: the rate of reaction is independent of time, is found to refer predominantly to reaction whose rate is controlled by a surface reaction step or by diffusion through the gas phase.

$$\frac{\Delta m}{A} = K_p t$$

- The parabolic law: the rate is inversely proportional to the square root of time, is found to be obeyed when diffusion through the scale is the rate determining process.

$$\left(\frac{\Delta m}{A}\right)^2 = K_p t$$

- The logarithmic law: refers to the formation of very thin films of oxides, which are between 20 to 40 angstroms thick at low temperatures.

Some systems, however, under certain conditions might show a composite kinetics (e.g. niobium oxidising in air at about 1000°C initially conforms to the parabolic law but later becomes linear) [53].

2-9-4-4- Oxidation of alloys

Since some part of this research work is based on oxidation; some background to the oxidation of alloys is brought forward.

From the consideration of equation (2-1) it is obvious that the solid reaction product will separate the two reactants as shown below:

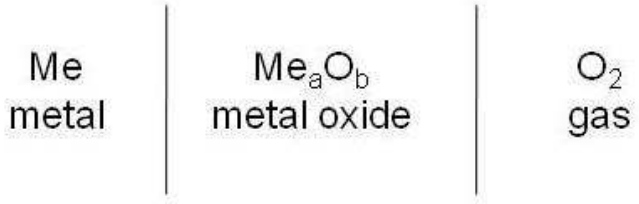

It is clear that for the reaction to proceed further, one or both of the reactants must penetrate the scale. Therefore, the mechanisms by which the reactants may penetrate the oxide layer are an important part of the mechanism by which high temperature oxidation occurs. Since all metal oxides are ionic in nature it is not practicable to consider the transport of neutral metal or non-metal atoms through the reaction product [53]. Several mechanisms are available to explain the transport of ions through ionic solids which have been explained in details in references [53-55].

Since pure metals are seldom used in load-bearing applications, metals are strengthened by appropriate alloying. However, the basic mechanisms operating in the oxidation of pure metals are also operative in the oxidation of alloys with added complexity such as formation of multiple oxides, mixed oxides, internal oxides, and diffusion interaction within the metals [20].

To better understand the effect of oxidation in alloys, a binary AB model where A is the major component and B is the minor component is considered. Two distinct possibilities exist:

1. Element A is more noble and B is more reactive.

2. Both A and B are reactive to oxygen with BO more stable than AO.

In the 1st situation where element A is considered to be more noble and B to be more reactive, at atmospheric pressures of oxygen A does not form AO, whereas B converts to BO. Depending on the concentration of B in A; (i) the alloy is dilute in B, (ii) the alloy is concentrated in B.

Where the alloy is dilute in B, oxygen will diffuse internally to oxidise and form dispersed precipitates of BO in A. Because there is not enough B available a continuous BO scale does not form. In the case where the alloy is concentrated in B, there is sufficient B available and thus a continuous BO layer forms. This is shown schematically in Figure 2-21.

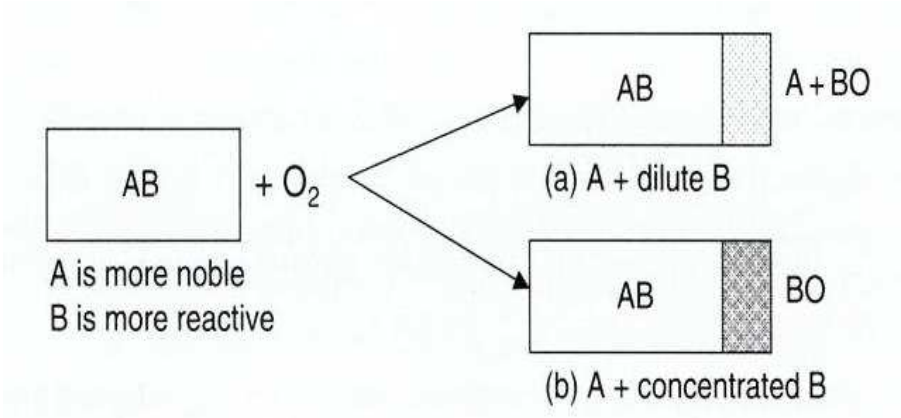

Figure 2-21. Binary alloy oxidation, component A is more noble and B is more active [20].

In the 2nd situation where A and B are both reactive to oxygen with BO being more stable than AO; the concentration of B again dedicates the oxide morphologies. (i) the alloy is dilute in B, (ii) the alloy is concentrated in B.

If the alloy is dilute in B a stable oxide AO forms as the outer scale. Bellow this scale at the AO-alloy interface, the oxygen activity is high enough to oxidise B into BO precipitates. If the alloy is concentrated in B, the concentration of B exceeds the critical level required to form a continuous BO scale. This is shown schematically in Figure 2-22.

The latter case is the basic model for creating oxidation resistant alloys and coatings (the process is known as selective oxidation where there is a preferential attack by oxygen on one of the components in the material). The oxide growth rate is parabolic, and the actual rate of oxidation depends on how protective the BO scale is and on the presence of additional alloying elements [20].

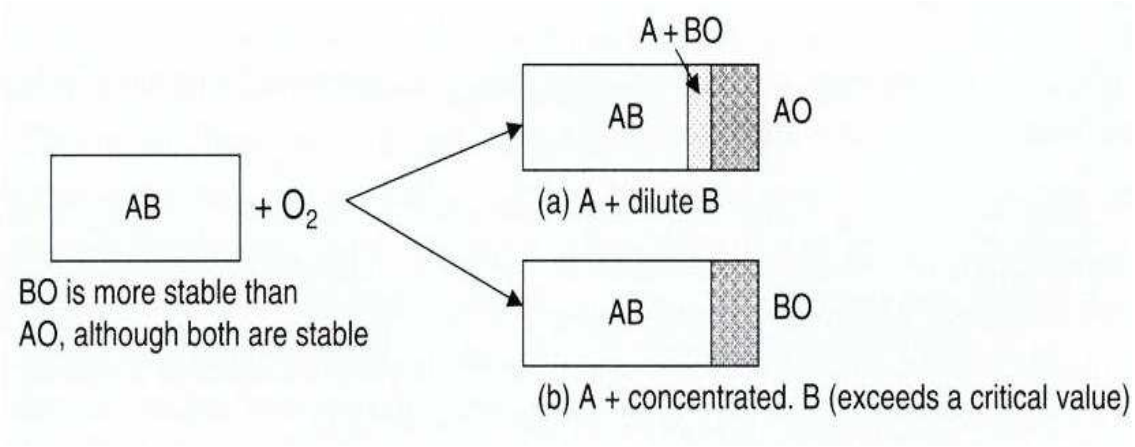

Figure 2-22. Binary alloy oxidation, component A & B form stable oxides but BO is more stable than AO [20].

Discussion of the oxidation of the Ni-Cr alloy has been investigated widely, e.g. [53, 56, 57]. Low Cr alloys in this system have shown the formation of Cr_2O_3 islands within the matrix of almost pure Ni in the early stages of the oxidation. As time progresses the formation of NiO outer scale occurs, as discussed in the first case of Figure 2-22 (where A is Ni and B is Cr). As time progresses, the Cr_2O_3 oxides surrounded by NiO result in a solid state reaction to form $NiCr_2O_4$ ($NiO + Cr_2O_3 = NiCr_2O_4$); this results in an oxide scale comprising both NiO and $NiCr_2O_4$, see Figure 2-23. Oxygen availability to the underlying alloy is not impeded at any time due to the inability of $NiO+NiCr_2O_4$ layer to restrict oxygen diffusion [57]. In addition to this, Ni diffuses outward and reacts at the surface to form NiO as the outer oxide, resulting in an increase in oxide thickness. However, much slower cation diffusion through the $NiCr_2O_4$ spinel layer has been reported as compared to NiO [53], resulting in the spinel islands acting as diffusion blocks for outward migration of Ni ions. As the Cr content in the alloy increases, the increasing volume fraction of spinel reduces the Ni flux through the scale and the oxidation rate constant begins to fall. As the Cr content increases further, to approximately 10wt.% at 1000℃, the mode of oxidation changes to give a complete external scale of Cr_2O_3, as discussed in the second case of Figure 2-22. At this and higher chromium compositions, the oxidation rate falls to values more typical of Cr than Ni, see Figure 2-24. However, at high temperatures, 900-950℃, scale thinning by CrO_3 evaporation can occur [21]. In this situation because of the Cr depleted area under the oxide layer, the formation of fast growing NiO and spinel oxides can resume.

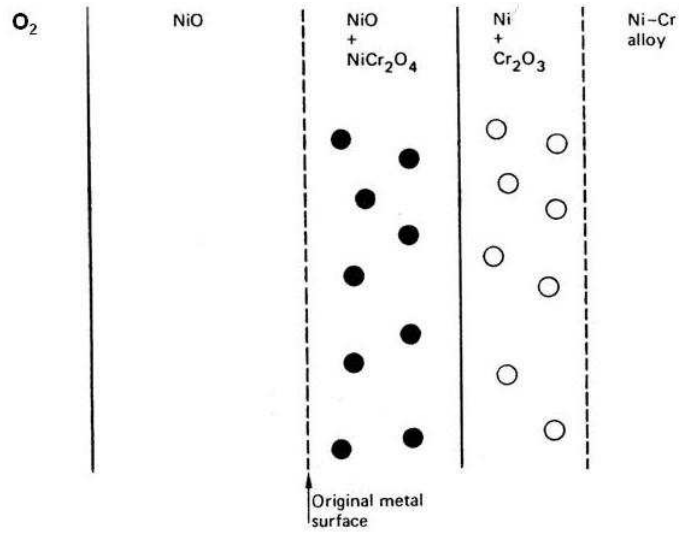

Figure 2-23. Schematic diagram of the oxidation morphology of dilute Ni-Cr alloys [53].

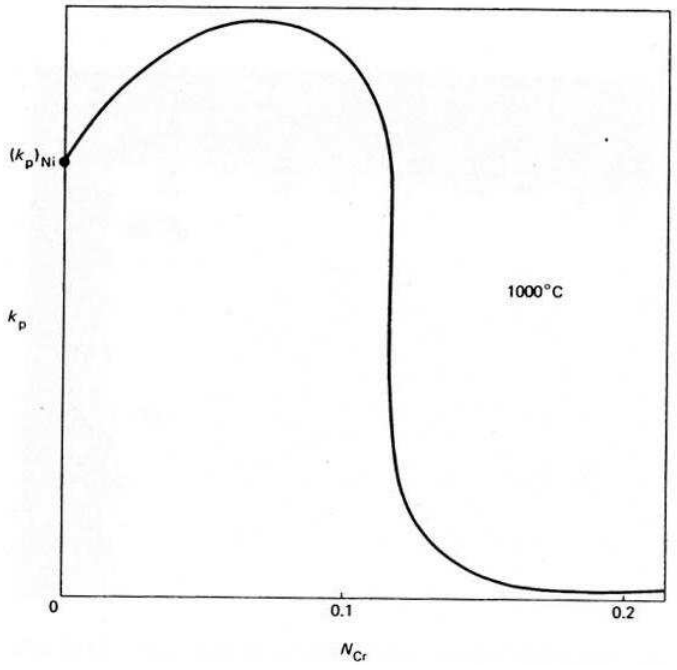

Figure 2-24. Dependence of the parabolic rate constant for the oxidation of Ni-Cr alloys on Cr content [53].

Furthermore, Giggins and Pettit [58] have investigated the oxidation of Ni-Cr-Al alloys in the temperature range of 1000 to 1200℃ where a protective alumina layer can be formed. They analysed a range of Ni-Cr-Al alloys with different Cr and Al

contents, and found that a continuous external layer of Al_2O_3 formed on a Ni-Cr-Al alloy at lower aluminium concentrations than would be necessary if Cr was not present in the alloy [58]. However, a sufficiently high amount of Al is required in order to form the continuous alumina layer. This has been reported to be in the range of 10 to 12 wt.% [19]. Higher Al content results in higher oxidation resistance. On the other hand, high Al contents can lower the ductility of the alloy. Hence, in order to have a high Al content for good oxidation protection and at the same time keeping the excellent mechanical properties, coatings such as MCrAlYs have been utilised. The composition of MCrAlY coatings (particularly the Al and Cr content) ensures they are chosen to be alumina formers, protecting the substrate from oxidising environments whilst maintaining the excellent mechanical properties of the superalloy substrate.

2-9-4-5- Oxidation observations in MCrAlY coatings

MCrAlY alloys were originally designed as high temperature oxidation resistant coatings. Research has been carried out considering the oxidation behaviour of these coatings at different conditions. Like any other coating designed for oxidation resistance, MCrAlYs are capable of developing a thermodynamically stable, slow growing and adherent oxide layer (e.g. Al oxide) [27]. It is this Al_2O_3 layer which inhibits continued ingress of active oxygen and other species [40]. Since the scale failure due to cracking and spallation depends strongly on the oxide thickness, it is desirable for the oxide to be slow growing (so a thinner oxide layer will develop at a given time) [59]. It is preferred that this oxide scale be a continuous, dense α-alumina, since it protects the coating from further oxidation due to the low diffusivity of oxygen and metallic elements through the α-alumina layer [60]. The presence of elements such as Y in the coating is beneficial because they inhibit the Al_2O_3 growth and improve its adherence [40].

Tang et al. [61] have studied the effects of surface oxidation during HVOF spraying on the primary stage oxidation of a CoNiCrAlY coating. They observed that the oxide scale grown on the as-sprayed samples is quite different from that of polished coatings. While an almost pure alumina scale (α & θ-alumina) was formed on the polished coating; on the as sprayed samples a duplex oxide scale, consisting of a mixture of spinel-type oxide and Cr_2O_3 in the upper scale and α-alumina in the subscale, was formed (Figure 2-25). The reason for the difference between the oxide scales grown on the as-sprayed and polished coatings was reported not to be the surface roughness. This conclusion was made on the basis of their (Tang et al. [61]) observation which stated that during HVOF spraying the particle surface oxidises (the type of oxide was not mentioned), this oxide(s) promotes the formation of spinel-type oxide in the subsequent oxidation of the coating. In the as-sprayed coating, the oxides which had formed during spraying promoted the formation of the spinel-type oxides on the coating surface prior to the formation of alumina in the primary stage of the oxidation and resulted in the duplex oxide layer. This is while in the polished coating only the top surface was polished and the oxides, formed during spraying, of the top surface were removed. When the cross section of the polished and oxidised coating was observed, spinel type oxides were only seen on the particle boundaries, where the oxides which were formed during spraying were not removed due to polishing. Hence the conclusion was made that the difference between the oxide scales grown on the as-sprayed and polished coating does not appear to be due to surface roughness but is instead due to the prior presence of oxides.

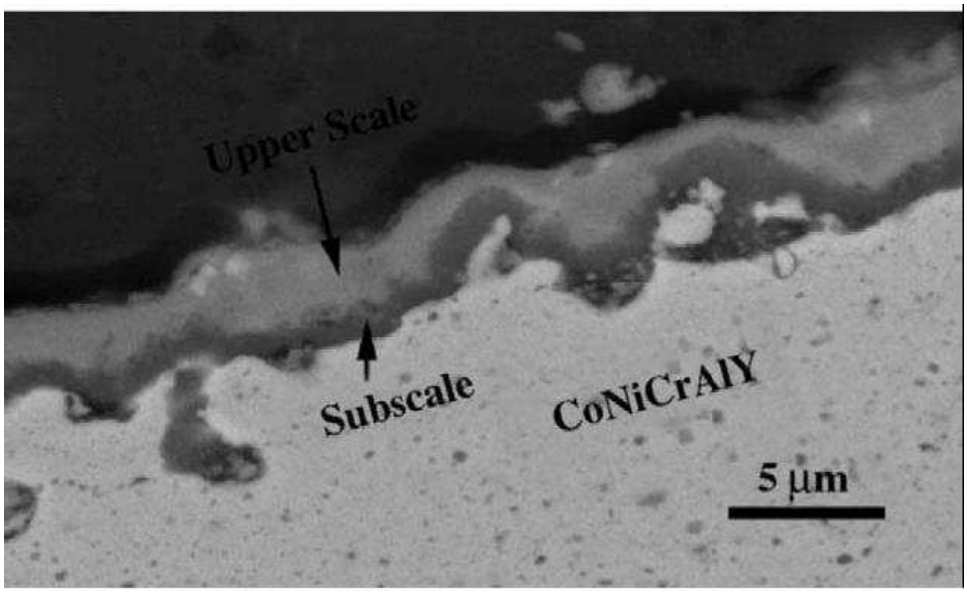

Figure 2-25. BSE image of an oxide scale grown on as-sprayed HVOF CoNiCrAlY coating after oxidation [61].

Tang et al. [62] have mentioned elsewhere, that the critical value of the effective aluminium concentration needed to form a pure Al_2O_3 scale on an alloy can be estimated as a function of factors such as the diffusion coefficient of Al, and oxygen permeability in the alloy. In a work done by Tang and his team [62], a MCrAlY coating with higher oxygen content had higher content of Al-rich oxides. As a result the Al available for oxide formation was decreased (the Al activity is decreased), thus in this stage the coating falls into a region where the oxide formation is sensitive to the oxygen activity. Spinel oxides grow when the oxygen activity is higher than a certain level [17]. This relationship can explain the duplex oxide scale formation seen on some MCrAlY coatings (Figure 2-25). The upper scale consisted of spinel, because the oxygen activity is higher at the top surface. The oxygen activity decreases with increasing depth into the oxide scale, finally going below the critical value where the formation of the Al_2O_3 subscale is promoted.

Fossati et al. [63] have studied the oxidation behaviour of two HVOF sprayed CoNiCrAlY coatings with similar chemical compositions but different starting reactivity toward oxygen. They have reported better oxidation resistance and adhesion for the coating with higher starting reactivity towards oxygen in comparison with the coating with lower starting reactivity towards oxygen. They have ascribed this behaviour to the formation of alumina precursor nuclei on the splat surface which promotes adherent and good quality oxide scale growth.

Brandl et al. [31] have also reported the existence of α-alumina in the oxide scale after 300hr oxidation at 950°C. However, in longer exposures (1000 & 1500hrs) Cr_2O_3 and $NiAl_2O_4$ were also observed. They have reported that at higher temperatures, 1050°C, the oxide scale is consisted of α-alumina and spinels $NiAl_2O_4$ and $CoAl_2O_4$, but they have not reported any trace of Cr_2O_3. The reason for the absence of Cr_2O_3 was mentioned to be due to the presence of α-alumina in the HVOF coatings before the oxidation. These small α-alumina particles were mentioned to be localised along the grain boundaries around the β-NiAl [31]; these particles hinder the diffusion of Cr, Co, and Ni along the grain boundaries. The grain boundary diffusion coefficient of Al in the α-Al_2O_3 is higher than Cr, Ni, and Co; the difference between these diffusion coefficients is considerably higher at higher temperatures, and thus it explains the absence of Cr_2O_3 in oxide scale at 1050°C.

Di Ferdinando and his colleagues [64] have studied the oxidation behaviour of a CoNiCrAlY coating sprayed by different spraying methods (APS, VPS and HVOF). A better oxidation resistance for the HVOF coating compared to VPS and APS coatings has been reported. They have also reported the presence of a major alumina layer on their CoNiCrAlY coatings oxidised at 1000℃ for periods of up to 3000

hours. The coatings, however, had gone through a vacuum interdiffusion treatment at 1150℃ for 2 hours prior to oxidation. Their judgment for the better performance of HVOF coatings compared to the other processes was based on the presence of some β particles after 3000 hours of oxidation for the HVOF coating (the VPS and APS coating were completely depleted of β). However, they had mentioned that the reason for the presence of the β phase in the HVOF coating was due to the formation of oxide stringers on particle surfaces during the spraying. This does not seem like a good reason as oxide stringers are also present on the surface of the particles sprayed by APS.

Richer et al. [65] have recently studied the oxidation behaviour of a CoNiCrAlY coating deposited by APS, HVOF and cold gas dynamic spraying (CGDS). They too have reported a better oxidation resistance for HVOF coating as compared to other deposition techniques. They have attributed the better performance of the HVOF coating to be due to the limited existence of oxide stringers present in the HVOF coatings as compared to CGDS where no oxide stringers had been detected (due to the process being carried out at low temperatures).

TGO growth rate and its effects on the TBC lifetime have been investigated by several researchers [66-69]. Naumenko et al. [25] have reported that oxidation rate can be influenced by temperature, reactive element contents in the coating and coating thickness. Yuan et al. [69] have studied the oxidation rate of a NiCrAlY bond coat sprayed by HVOF and detonation gun with the presence of a YSZ ceramic top coat. They have reported a lower oxidation rate for the HVOF coating oxidised at 1100℃ (K_p= 1.5×10^{-12} $g^2/cm^4/s$).

Table 2-7 illustrates some oxidation rate (K_p) values for different MCrAlY coatings sprayed by different processes, where the oxide growth rate has been fitted to parabolic growth behaviour.

Table 2-7. Some oxidation rate (K_p) values for different MCrAlY coatings sprayed by HVOF & plasma processes.

Spraying method	Coating	Time (hr)	Temp. (°C)	Condition	K_p* ($g^2.cm^{-4}.s^{-1}$)	Notes	Ref.
LPPS	NiCoCrAlYRe	100	950	Polished surface	3.5×10^{-13}	—	[70]
			1000		7.6×10^{-13}		
HVOF	CoNiCrAlY	50	950	As-sprayed	3.96×10^{-13}	Free standing coatings	[71]
		100			1.16×10^{-13}		
		50		Ground	14.33×10^{-13}		
		100			6.71×10^{-13}		
		50		Polished	11.83×10^{-13}		
		100			4.55×10^{-13}		
		50		EB-remelted	0.44×10^{-13}		
		100			0.27×10^{-13}		
HVOF	NiCoCrAlYRe	330	1050	In synthetic air	6.60×10^{-14}	Free standing coatings	[31]
		1500			5.83×10^{-14}		
VPS		330			2.83×10^{-13}		
		1500			1.8×10^{-13}		
VPS	CoNiCrAlY	6	1050	Heat treated	4.11×10^{-10}	Free standing coatings	[66]
	NiCoCrAlY				3.74×10^{-10}		
HVOF	NiCrAlY	100	1000	—	4.80×10^{-13}	—	[69]
			1050		8.83×10^{-13}		
			1100		1.50×10^{-12}		

*K_p is the parabolic growth law constant.

By comparing the K_p values in Table 2-7, it can be seen that they generally vary in the range of 10^{-12} to 10^{-14} $g^2.cm^{-4}.s^{-1}$. However, there are two values (4.11×10^{-10} and 3.74×10^{-10} $g^2.cm^{-4}.s^{-1}$) which seem very large as compared to the other reported K_p values. These two K_p values are related to the coatings produced by VPS. The main reason for such a high value could be the fact that the K_p has been measured after a very short time of 6 hours. This amount of time is not sufficient for oxidation rate measurements as the initial parts of the mass gain vs time graphs are usually related to the transient oxidation period were high oxidation rates are observed. The K_p values measured for the 6 hours oxidation period are suspected to be highly affected by the

transient oxides formed at the beginning stage of oxidation and hence a much higher K_p has been measured.

2-10- Mechanical properties of MCrAlYs

In service thermal barrier coating systems may fail by spallation of the ceramic top coat originating from the formation and growth of micro-cracks at the bond coat/TGO or TGO/top coat interface. The main reasons for damage are oxidation of the bond coat and thermally and mechanically induced stresses in the coating system [72]. Coating failure may further be affected by coating stiffness of the TBC as well as creep and stress relaxation of the bond coat and the ceramic top coat [72].

The three different sources which contribute to the development of stresses in a TBC system are as follows [73, 74]:

i. Coefficient of thermal expansion (CTE) mismatch

ii. Oxidation and growth of the TGO and its associated volume change

iii. Externally applied load, i.e. imposed strain

Creep of the layers acts as a stress relieving mechanism above the ductile-brittle transition temperature (DBTT). Young's modulus will, only when deformation is elastic, determine the stress arising from imposed strains, below DBTT when $\sigma < \sigma_y$ or σ_F. Hence it is important to understand and study the mechanical behaviour of the MCrAlY coatings (such as creep, elastic modulus and DBTT) in order to prevent the catastrophic failures.

2-10-1- Young's modulus

Elastic modulus is important as it determines the stresses that result from the imposed strain during elastic deformation. Different measurements of the elastic modulus using different techniques (e.g. 3-point bend, 4-point bend, tensile test, indentation, etc) and different materials have been reported in the literature. For example it has been reported [8] that the dynamic modulus (ratio of stress to strain under vibratory conditions) of elasticity has been measured using cylindrical cast sample for NiCrAl, NiCoCrAl, CoNiCrAl alloys at a range of temperatures which can be observed in Table 2-8.

It was mentioned that the NiAl base alloys feature the lowest values of elastic modulus whereas the maximum elastic modulus is demonstrated by the alloys whose phase composition corresponds to γ-solid solution and γ' phase with low Cr content [8]. Al tends to reduce the value of elasticity modulus due to the higher volume formation of NiAl. Cobalt has been reported to have an even greater effect, especially if the Al content is high [8]; this has been explained by a rise in atom interaction energy when the Ni base γ-solid solution is alloyed with these elements [8].

Similar values for the elastic modulus of vapour deposited samples to the cast alloys have been reported in [8], this is while Kuroda et al. [75] have reported that the Young's modulus of thermally sprayed metallic deposits is one third that of dense materials.

Table 2-8. Elastic modulus (E) of NiCrAl, NiCoCrAl and CoNiCrAl cast alloys [8].

	E, GPa				
alloy	**20°C**	**200°C**	**300°C**	**400°C**	**500°C**
NiCrAl system					
Ni14Cr3AlY	178	171	166	160	154
Ni18Cr5AlY	174	168	161	156	150
Ni16Cr9AlY	166	160	156	151	147
Ni21Cr9AlY	157	152	148	144	139
Ni22Cr11AlY	170	167	164	161	158
NiCoCrAl system					
Ni10Co15Cr8Al	156	150	146	146	139
Ni30Co15Cr8Al	170	164	159	153	148
Ni10Co30Cr8Al	166	160	157	154	149
Ni30Co30Cr8Al	186	180	175	170	166
Ni10Co15Cr14Al	131	131	130	129	127
CoNiCrAl system					
Co10Ni15Cr6AlY	207	187	181	174	166
Co30Ni15Cr6AlY	189	180	174	165	160
Co10Ni30Cr6AlY	196	186	179	170	162
Co30Ni30Cr6AlY	182	172	168	160	155
Co10Ni15Cr12AlY	196	184	178	170	164

Different models such as Spriggs' Equation, Hashin-Hasselman Equation, the Zhao model and the Eshelby equivalent homogenous inclusion model exist which relate the elastic modulus of a coating to its microstructure [75-77]. Azarmi et al. [76] have used some of these models to calculate the modulus of Inconel 625 coating and compare it with the measured modulus. They observed discrepancies between the models and the measured values: much higher values were obtained for the predicted results compared to experimentally measured modulus, see Table 2-9. They claimed that the discrepancies are due to the failure of the models to account for the effect of non

visible microstructural characteristics such as weak bonding across splat boundaries [76].

2-10-1-1-Spriggs' equation

This is a commonly used empirical model which suggests an empirical expression for the porosity dependency of the elastic moduli of polycrystalline material with a uniform distribution of spherical pores in the form of an exponential relationship [78].

$$E^* = E_s \exp(-bp) \tag{2-2}$$

Where p is the volume fraction of all pores, cracks and splat interfaces. E_s is the elastic modulus of the alloy and E* is the elastic modulus of the porous material. The empirical constant b varies according to the fabrication method and perhaps method of modulus measurement [78]. Spriggs [78] has mentioned that b ranges from 4.08 to 4.35 for hot pressing, from 3.44 to 3.55 for cold pressing and sintering and for casting and sintering is 2.73. Azarmi et al. [76] have suggested the value 5.16 for the constant b for air plasma spraying (APS) of Inconel 625. However, the exact significance of the constant b is not fully understood.

E^* has been calculated for an Inconel 625 by Azarmi et al. [76] using the Spriggs' equation and result is given in Table 2-9.

Although Azarmi et al. [76] have reported disagreement between the model and the measured values, Spriggs [78] has reported a good agreement between the model and the experimentally measured values particularly for Al_2O_3 oxide prepared by different techniques and for various methods of modulus measurement.

2-10-1-2-Hashin-Hasselman equation

Hasselman [79] disagreed with Spriggs' equation and has reported that the disadvantage of Spriggs' equation becomes immediately evident as it does not satisfy the boundary conditions. He has mentioned that "setting p equal to unity in equation (2-2) does not yield the condition that E* is equal to zero as required. Not satisfying the boundary conditions will affect the actual values of E_s and b obtained from the experimental data" [79]. It should of course be noted that if p is set to unity, there will be no material for its E to be affected as this corresponds to 100% porosity.

However, Hasselman tried to generate an equation of different form based on the solution of elastic moduli of heterogeneous system given by Hashin [80].

A straight line relation between $1/E^*$ and p/(1-p) is used as an theoretical equation to estimate the elastic modulus of a porous material [79, 80].

$$E^* = E_0\left[1+\frac{Ap}{1-(A+1)p}\right] \tag{2-3}$$

Equation (2-3) can be rearranged into [81]:

$$\frac{1}{E^*} = \frac{1}{E_0} + B\frac{p}{1-p} \tag{2-4}$$

Where $B = -\left(\frac{A}{E_0}\right)$, A is a constant, p is the volume fraction of all pores, cracks and splat interfaces, and E_0 is the elastic modulus of the dense material. The unknown parameters, E_0 and A, are to be determined statistically from the experimental data. Hasselman [79] has reported that "the constants can be calculated most conveniently

using the numerical analysis technique of Scarborough and the pseudomatrix technique of Moore, which result in a matrix inversion and multiplication operation" given as:

$$\begin{bmatrix} E_0 \\ \\ A \end{bmatrix} = \begin{bmatrix} \sum_{i=1}^{n} \frac{1}{E_i^2} & \sum_{i=1}^{n} \frac{p_i}{E_i(1-p_i)} \\ \sum_{i=1}^{n} \frac{p_i}{E_i(1-p_i)} & \sum_{i=1}^{n} \frac{p_i^2}{(1-p_i)^2} \end{bmatrix}^{-1} \begin{bmatrix} \sum_{i=1}^{n} \frac{1}{E_i} \\ \sum_{i=1}^{n} \frac{p_i}{1-p_i} \end{bmatrix} \quad (2\text{-}5)$$

Where n is the number of data points.

The estimated E^* value for an Inconel 625 using Hashin-Hasselman equation has been reported by Azarmi et al. [76] and is given in Table 2-9, the constant A used is -33.4.

A comparison of the Spriggs' and Hashin-Hasselamn equation has been carried out by Wang [81] on porous alumina.

2-10-1-3-Eshelby inclusion model

The Eshelby model was originally derived by J.D Eshelby in the 1950's and allowed the elastic strain field of an ellipsoidal inclusion to be determined [82]. However, the key point to consider is that an ellipsoid of any aspect ratio has a uniform stress at all points with in it, and thus the variation of a uniform stress field in a material can be determined when it is distributed by an ellipsoidal inclusion. The effect of inclusions or pores within composites, coatings or foamed material has been modelled by Eshelby [75, 77, 82, 83].

The Eshelby homogenous inclusion model has been used for thermally sprayed coatings to analyse the effect of porosity and the aspect ratio on the coating stiffness

[75, 84, 85]. The aspect ratio of a pore is defined as the width, x, divided by the length, y, as shown in Figure 2-26. It was found that pores with an aspect ratio of one (spherical pores) have only a small effect on the overall elastic modulus where as pores with aspect ratios of ~0.01 have a greater effect in the reduction of the coating elastic modulus. For further information on the Eshelby model refer to [77, 82, 83].

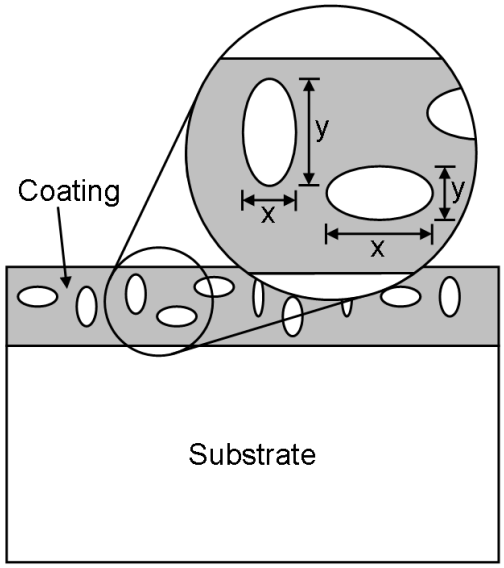

Figure 2-26. The aspect ratio of a given pore is defined as the width (x) divided by the length (y).

2-10-1-4-Zhao model

Different studies have indicated that coatings exhibit different mechanical behaviour in directions perpendicular and parallel to the coating planes [86, 87]. Zaho et al. have presented a hybrid that combines the Mori- Tanaka and Eshelby's solution for an ellipsoidal inclusion to solve for the effective mechanical properties of an ellipsoidal array in porous media [87]. The model presents equations that estimate elastic moduli of a coating in both parallel (transverse) and perpendicular (longitudinal) directions relative to the coating plane. A schematic of the microstructure of a thermally sprayed

coating defining directions parallel and perpendicular to the coating plane is illustrated in Figure 2-27.

For materials with elliptical pores, the two dimensional elastic moduli in the longitudinal (E_L) and transverse (E_T) directions can be estimated using the following two equations [87-89].

$$E_L = \frac{E_m(1-p)}{1+2\pi\rho} \quad (2\text{-}6\text{-a})$$

$$E_T = \frac{E_m(1-p)}{1+2\pi\rho\alpha^{-2}} \quad (2\text{-}6\text{-b})$$

Where E_m is the elastic modulus of the dense material, p the porosity, ρ ($=\Sigma a_i/A$) the crack density, and α ($=\left(\sum a_i^2/\sum b_i^2\right)^{1/2}$) the average pore aspect ratio, where A is the total area and a_i and b_i are the major and minor axes respectively, of the i^{th} pore.

The reason for the aspect ratio not to be present in E_L has been reported to be that the cross section of the pores will be circular in planes parallel to the coating plane [76].

However, only when the number of ellipsoidal pores with the defined aspect ratio is great, with respect to the total porosity, is the model valid for the estimation of the modulus of porous material [76, 87]. E_L and E_T have been calculated for an Inconel 625 by Azarmi et al. [76] and the results are illustrated in Table 2-9. More on Zhao model can be found in [87, 88].

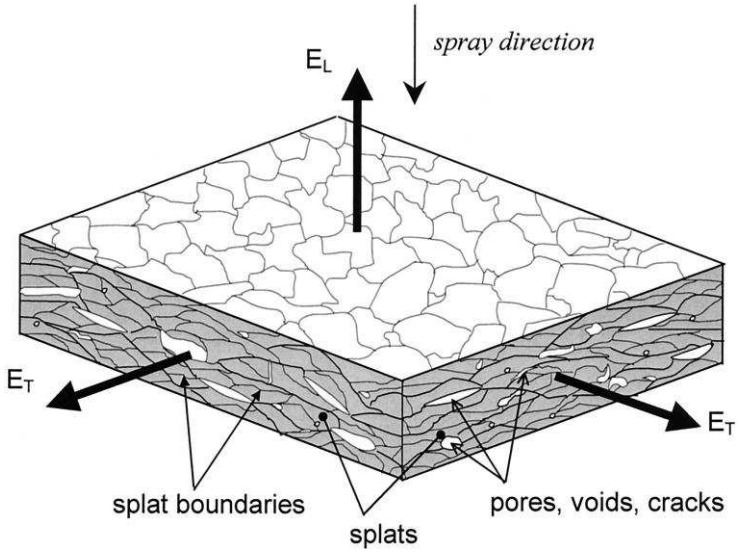

Figure 2-27. A schematic of the microstructure of a plasma sprayed coating (directions of elastic modulus along the spray direction (E_L) and transverse direction (E_T) are indicated by heavy arrows) [87].

Table 2-9. Estimation of Young's modulus of Inconel 625 in as-sprayed (APS) and bulk conditions, using different models [76].

Method	Volume fraction of all pores (p)	Modulus of alloy 625 (GPa)*	Modulus of coating (alloy 625) (GPa)
Spriggs' equation	0.04	205	166
Hashin-Hasselman equation	0.04	205	85
Zhao model	0.04 α =1.5	205	E_T=141 E_L=105
Experimentally measured *		205	20±1

* Measured through the ratio of the stress to strain in the linear elastic region of the stress-strain curves, obtained by tensile testing.

CHAPTER 3

Experimental Procedure

In this work the overall aim was to achieve an understanding of the microstructural development of free standing CoNiCrAlY coatings deposited by HVOF (Met Jet II gun) and VPS systems. Different treatments such as annealing and oxidation were carried out on the free standing thermally sprayed coatings. These treatments were carried out at different temperatures for different exposure times. The coatings were subsequently examined by optical microscopy, scanning electron microscopy, transmission electron microscopy, X-ray diffraction. Vickers micro-hardness and Young's modulus of the coatings were also determined.

Free standing coatings were used throughout this work in order to analyse the microstructural development of the CoNiCrAlY coating discretely and without the interference of the Inconel substrate. This will contribute to better understanding of the microstructure, microstructural development and properties of the CoNiCrAlY alloy as a single material rather than a complex coating/substrate system where, interdiffusion plays an important role and similar behaviours might not be observed (due to interdiffusion). Furthermore, for development or modification of similar coatings, understanding of the coating and its properties as a single material is essential and will help to better understand the coating/substrate system, i.e. for development of new coatings, the coating properties and the coating/substrate

properties should match respectively. This chapter gives details of the experimental methods used.

3-1- Raw materials

3-1-1- MCrAlY powder

Two commercially available gas atomised Co based MCrAlY (CoNiCrAlY) powder supplied by "Praxair" (CO-210-24) and "Sulzer Metco" (Amdry 9951) were used. HVOF and VPS spraying was carried out using both the Amdry and Praxair powders. The nominal size range of the powders were specified as -45+20μm with a mean particle diameter, D(v, 0.5), of 34μm for the CO-210-24 powder and -38+5μm with a mean particle diameter, D(v, 0.5), of 20μm for the Amdry 9951 powder. This was verified with Malvern analyses (Figure 3-1), a laser particle size analyser which will be explained in detail in section 3-4-1, and scanning electron microscopy (SEM). The nominal composition of the powders is given in Table 3-1.

Table 3-1. CO-210-24 & Amdry9951 nominal powder composition (wt%).

Elements → **Powder ↓**	**Co**	**Ni**	**Cr**	**Al**	**Y**
CO-210-24 Supplier chemical analysis	balance	31.70	20.80	8.10	0.47
Amdry9951 Supplier chemical analysis	balance	31.74	20.83	7.98	0.40

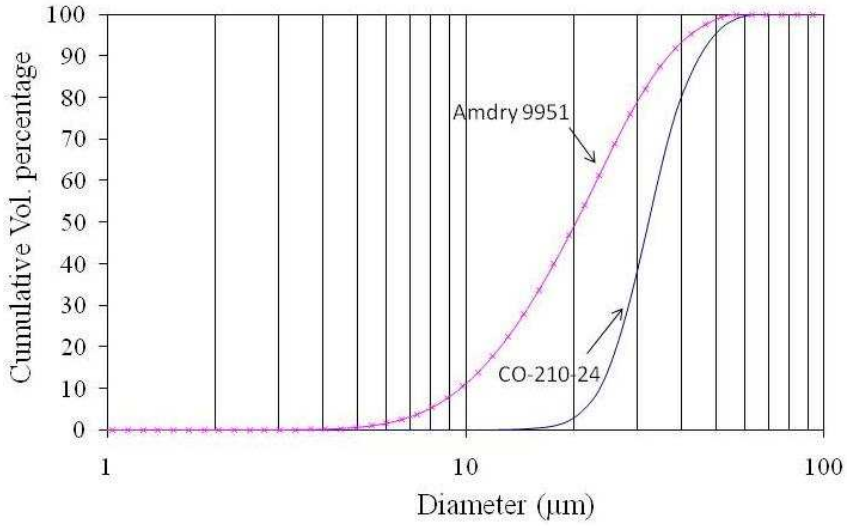

Figure 3-1. Plot of cumulative volume percent versus particle diameter for the as-received Praxair CO-210-24 & Sulzer Metco Amdry 9951 powders.

3-1-2- Substrates

Mild steel substrates were used for both forms of spraying, 60 × 25 × 1.8 mm substrates were used for HVOF, and slightly smaller, 60 × 20 × 1.8 mm substrates were used for VPS. Prior to spraying the substrates were cleaned with ethanol and ground with 800 grade SiC paper, rather than being grit blasted, in order to enable coating detachment after spraying.

3-2- Thermal spraying

3-2-1- HVOF spraying

HVOF spraying was carried out using a commercial MetJet II (Metallisation) gun. Kerosene was used as fuel and nitrogen as the carrier gas. In this gun the specified ratio of fuel and oxygen is burnt in the combustion chamber. The resultant hot gases then pass through a converging diverging throat and along a, in this case 100mm nozzle, before emerging as a free jet. Powder is radially injected downstream of the throat.

Compressed air jets were used to cool the samples during and after spraying. The substrates were mounted on a rotating sample holder while the spray gun traversed vertically. Figure 3-2 illustrates a schematic set-up of the HVOF spraying system.

Considering the large number of variables which must be taken into account when spraying HVOF coatings (see section 2-3-2), and the graph illustrated in Figure 3-3 (which will be discussed in the following section) three sets of spraying were carried out in order to obtain three different coatings. For ease of reference, from this point onwards the coatings produced using the first set of spraying parameters are called HVOF1, the coatings produced using the second set of spraying parameters are called HVOF2 and the coatings produced using the third set of spraying parameters are called HVOF3. It should be noted that HVOF1 and HVOF2 were sprayed using the CO-210-24 powder and HVOF3 was sprayed using the Amdry 9951 powder. These three set of HVOF spraying parameters can be seen in Table 3-2. The specific parameters used were chosen as preliminary experiments, indicated they would generate different microstructures, 1 and 2 with small differences and 3 being completely different.

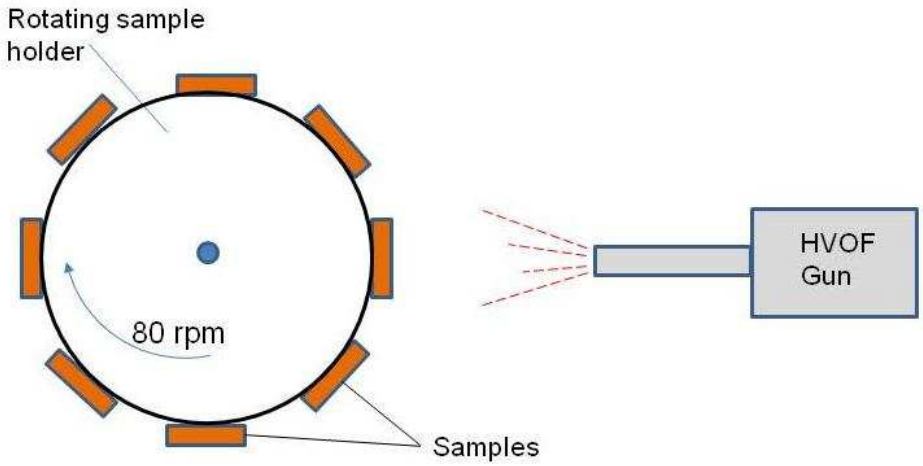

Figure 3-2. A top view of the setup arrangement for the HVOF spraying system.

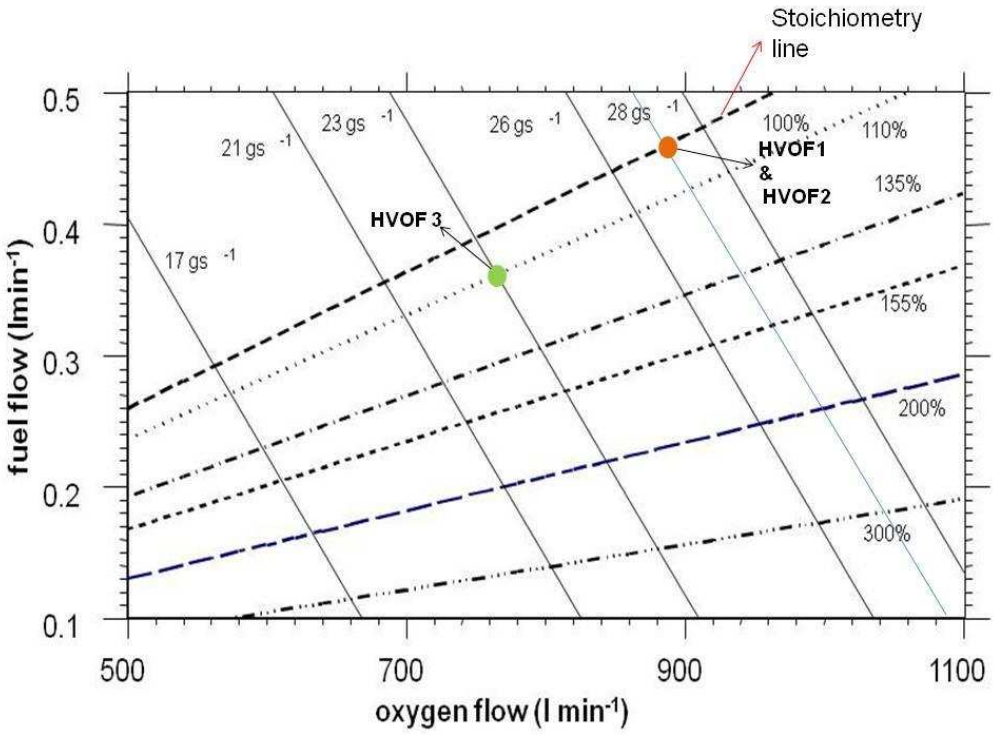

Figure 3-3. Stoichiometric chart for HVOF spraying system. The dotted lines indicate the oxygen to fuel ratio whereas the solid lines specify the total mass flow rate. Conditions associated with three HVOF sprayings are also illustrated.

Table 3-2. HVOF1, HVOF2 & HVOF3 spraying parameters.

	HVOF1	**HVOF2**	**HVOF3**
Powder used	CO-210-24	CO-210-24	Amdry 9951
Spray distance (mm)	356	356	356
N_2 carrier gas flow rate (l/min)	5.5	4.3	5.5
O_2 gas flow rate (l/min)	890	890	771
Kerosene flow rate (ml/min)	470	470	361
Nozzle length (mm)	100	100	100
Powder feed rate, rpm [g/min]	186 [64]	186 [66]	186 [68]
Number of passes	30	30	30
Stoichiometry	98%	98%	110%

The graph in Figure 3-3 is the stoichiometric chart pointing out the fuel to oxygen flow conditions used in HVOF sprayed coatings. Moving across the stoichiometry lines, from a higher percentage to a lower percentage, leads to a decrease in the excess oxygen of the flame which respectively, results in increase in flame temperature, and thus higher percentage of particle melting. In a similar manner moving across from lower percentages to a higher percentages, introduces more oxygen than required leading to a lower flame temperature due to excess gas that is not taking part in combustion. It is important to notice that the lowest oxygen to fuel ratio is the 100% line and at all times the spraying is carried out at or above the stoichiometric conditions (i.e. always at or >100% line). This is because points lower than the 100% line mean excess fuel is used and is a waste in fuel and this has greater economic implications than the waste of oxygen in oxygen rich mixtures. Moving across the total mass flow rate lines also has an impact on the flame temperature but to a lesser extent.

3-2-2- VPS spraying

The first set of VPS coatings were manufactured by a Plasma TECHNIK VPS unit at University of Cambridge. For ease of reference this set of coatings will be referred to as VPS1 from this point onwards. The VPS chamber was evacuated to exclude oxygen and then back filled with Ar to a preset pressure to ~130 mbar. A total number of 5 passes were sprayed and waiting times of 20 seconds per pass were allowed.

The second set of VPS coatings were manufactured at Cranfield University. For ease of reference this set of coatings will be referred to as VPS2 from this point onwards. The precise VPS parameters can be seen in Table 3-3.

Table 3-3. The spraying parameters for the VPS coatings.

	VPS1	VPS2
Powder used	CO-210-24	Amdry 9951
Spray distance (mm)	280	300
Current (A)	600	550
Voltage (V)	63	42
Power (kw)	40	—
Air flow (l/min)	50	80
H_2 flow (l/min)	10	5
Nozzle diameter (mm)	8	—

3-2-3- Coating detachment

Following the spraying process, both HVOF and VPS coatings were detached from their substrates by bending the substrate. Due to the large deposited coating thickness (~600 μm) and the fact that the substrates were ground to an 800 grit finish prior to spraying, bending the substrate was sufficient to detach the coating (Figure 3-4).

Figure 3-4. Detachment of a coating from the substrate by bending the substrate using a wrench tool.

3-3- Thermal exposures

3-3-1- Heat treatment

A Carbolite box furnace was used in order to carry out the heat treatments. Free standing coatings of each spraying systems were dried in an oven at a temperature of ~80°C. The dried coatings were then placed inside silica quartz tubes and connected to a rotary and diffusion pumps where they were pumped down to approximately 8.5×10^{-3}mbar. The tubes were then sealed using an oxy-fuel torch. The vacuum tubes were subsequently placed inside the furnace and heat treated at 1100°C for a period of 3 hours followed by furnace cooling, a typical heat treatment for coatings of this type [1-3].

3-3-2- Annealing

Isothermal annealing of the free-standing coatings (~7×25mm and ~7×20mm), rather than coated superalloy specimens where interdiffusion can affect the equilibria, were carried out in vacuum at four different temperatures. The exposure times were increased with decreasing temperatures in order to achieve equilibrium microstructures in all test samples, i.e. at 1100°C for 4h, 1000°C for 24h, 900°C for 90h and 800°C for 840h. The specimens were subsequently quenched in water (samples not removed from quartz tubes) to preserve their high temperature microstructure (quartz tubes did not break after placed into water). Considering the fact that the sample are in vacuum and that only a small area of the samples are in contact with the quartz tube (the tip of the samples), radiation can be assumed to be the main heat transfer mechanism during quenching. Hence, the heat transfer can be estimated assuming blackbody behaviour and radiation as the heat transfer mechanism. With the use of equation (3-1) and assumption of an emissivity of 0.7 for

MCrAlY coatings [4], the heat loss from the coatings at 1100℃ is estimated to be approximately 49W equivalent to 140Ks^{-1} (considering a C_p of 0.445kJ/kgK for nickel [5]).

$$q = \varepsilon\sigma\left(T_h^4 - T_c^4\right)A \tag{3-1}$$

Where q is heat transfer (W), ε is emissivity, σ is Stefan-Boltzmann constant of 5.6703×10^{-8} (W/m^{2}K^4), T_c and T_h are cold surrounding absolute temperature (K) and hot body absolute temperature (K) respectively and A is surface area (m^2).

Furthermore, the annealing times were calculated by means of $x \approx \sqrt{Dt}$, where x is diffusion distance, D is diffusion coefficient and t is time and by considering the diffusion calculation based on the diffusion of Cr in Ni, since chromium controls the kinetics. This is because the powder studied in this work was a Co base powder and as diffusion coefficient for Co, i.e. Ni in Co (D_{Ni}^{Co}), was not available in the handbook and also because the Ni content was close to Co (38.5%wt.Co & 32%wt.Ni), and since the biggest atom down the line (after Ni) was Cr, the calculations were based on the diffusion coefficient of Cr in Ni (D_{Cr}^{Ni}); this value for the temperature of 1373K is 4.67×10^{-15} m^2/s. The value used for diffusion distance is 8μm. Furthermore, a safety factor of 2 has been applied in the calculations, i.e. double the time has been given to ensure equilibrium is reached.

3-3-3- Isothermal oxidation

As-sprayed and heat-treated HVOF and VPS free standing coatings were subjected to isothermal oxidation at 1100°C and 850°C in air for time periods of 1, 50, 75, 100 and 250 hours. The samples (~6×25mm for HVOF and ~6×20mm for VPS) were either

entered into a furnace at temperature or entered into a rapid heating Carbolite furnace which took 7.5min to get to 850°C and 13min to get to 1100°C from room temperature (25°C). The latter furnace was usually used for the samples which were harder to handle and needed to be inserted into the furnace at low temperatures. After oxidation, specimens were removed from the furnace at temperature and cooled in laboratory air to room temperature.

Thermogravimetric analysis (TGA)

Continuous weight measurement of as-sprayed and heat-treated samples during oxidation was also carried out using a SDT Q600 TA Instruments thermogravimetric analyser (TGA). A base line was obtained before each temperature run, to ensure any machine artefacts could be identified and eliminated from analysis. Samples of approximately 3×3mm were put in pre-heated alumina crucibles, top surface facing up. At the beginning of the test, the furnace was set to equilibrate at 50℃ while the data storage was off. Following this the data storage was turned on and the furnace was ramped 50℃/min to 1100℃ and isothermally stayed at 1100℃ for 96 hours.

For the oxidation rate measurements the parabolic oxidation law was assumed. Monceau et al. [6] have stated that "since the classic work of Tammann and Bedworth the oxidation rate of metals and alloys determined from TGA were commonly described through a parabolic law of":

$$\left(\frac{\Delta m}{A}\right)^2 = K_p t \qquad (3\text{-}2)$$

Where m is mass in grams, t is time in seconds and K_p is parabolic rate constant in $g^2/cm^4/s$.

However, the initial conditions of Δm=0 at t=0 and a constant temperature required for using the above equation is quite difficult to achieve experimentally. For example before the test temperature is reached to the desired temperature and stabilises, the specimens can be oxidised during the initial heating period. Even in the case of non-oxidising atmospheres the introduction of the oxidising gas can disturb the temperature and measurement of mass changes for several minutes leading to a systematic error for the starting point of mass gain curves. Furthermore, for the oxidation of alloys, where a transient oxidation period occurs when the oxidation of more noble component occurs simultaneously with the oxidation of less noble and more protective component (e.g. alumina forming alloys), the initial starting point of Δm=0 at t=0 is difficult to meet. Thus, the mentioned initial conditions usually can not be applied. Hence, to account for the transient oxidation period of non-parabolic kinetics, the initial condition could be $\Delta m=\Delta m_i$ at $t=t_i$. So the (3-2) equation can be re-written as [6]:

$$\frac{\Delta m^2 - \Delta m_i^2}{A^2} = K_p\left(t - t_i\right) \tag{3-3}$$

by assuming that the oxide layer grown at $t>t_i$ has the same protective properties as the scale grown at $t<t_i$. For further condition of when the oxide layer grown at $t>t_i$ does not have the same properties of the oxide layer grown at $t<t_i$, i.e. un-protective first oxide layer see reference [6].

In this research work the parabolic rate constants (K_p) were determined by plotting the square of the mass gain per unit area against time ($\left(\frac{\Delta m^2 - \Delta m_i^2}{A^2}\right)$ vs. $\left(t - t_i\right)$), and finding the gradient of the best straight line fit to the results by the means of equation

(3-3). In this regards the initial starting points were set to 500 minutes (t_i=500 min) where a stabilised temperature and oxide layer was available.

It should be noted that for the K_p measurements only the area of one side of the samples, the top surface which was facing up, was taken into account as the side sitting on the crucible was not oxidised much and the majority (more than 50%) of the oxide layers formed were on the top surface (surface facing up) of the sample.

In order to check the measured K_p values using equation (3-3); equation (3-4) [7] was used to calculate the oxide thickness of the coatings from their measured K_p and comparing the calculated oxide thicknesses with the measured oxide thicknesses (from SEM images).

$$h^2 = K_p t \tag{3-4}$$

Where h is surface density in g/cm^2. In order to extract the oxide thickness from h, the density (g/cm^3) of the oxide layer is required. Dividing h by the density gives the oxide thickness. However, if a dual oxide layer exists (the case for the as-sprayed oxidised coatings in this work) then the oxide density will be a function of the individual oxide thicknesses, i.e. oxide density depends on the thickness of individual layers; and a weighted average of the density of the existing oxide layers has to be taken into account. For example if the thickness of the spinel to alumina is 3/2 than this ratio has to be considered when averaging the spinel and alumina densities. In the calculation carried out in this work, since the thickness of the individual layers were approximately the same, an average of the density of spinel and alumina was considered as the density required to extract the oxide thickness from K_P.

3-4- Characterisation

3-4-1- Laser diffraction powder size analyses

This technique is based around the principle that particles passing through a laser beam will scatter light at an angle that is dependent on their size; as the particle size decreases, the observed scattering angle increases. The observed scattering intensity is also dependent on particle size. Large particles scatter light at narrow angles with high intensity, whereas small particles scatter at wider angles but with low intensity. Figure 3-5 demonstrates a typical measurement system consisting of a laser, a sample presentation system, and a series of detectors.

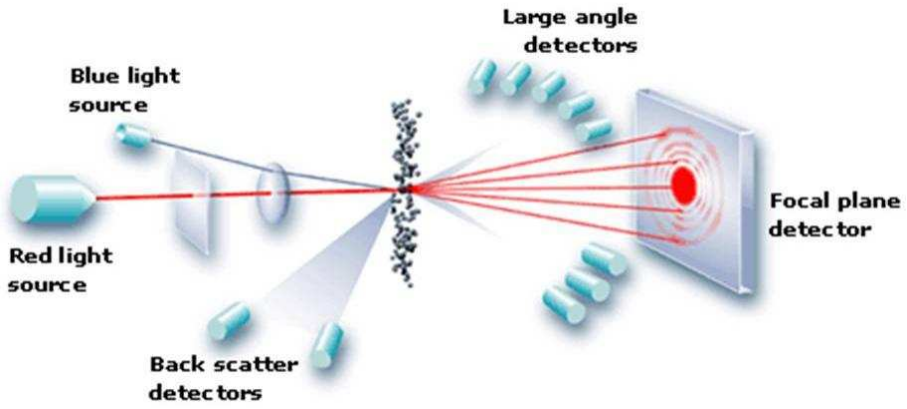

Figure 3-5. A typical primary measurement laser diffraction system.

In this study a Malvern Master size S (Malvern Instruments Ltd, UK) was used for measuring the particle size distribution of the feed stock powder. The powder was pre-wetted, suspended in a liquid medium and fed through the measuring zone. The test was carried out several times in order to verify reproducibility and accuracy.

Selection of an appropriate dispersant is an important aspect of the laser diffraction analyser, as it must [8]:

- Be transparent to the laser beam, ensuring the feasibility of light scattering measurements
- Wet the particle, but not dissolve the material being measured
- Stabilise the particles following dispersion to prevent re-agglomeration

To comply with the requirements above, ethanol was chosen as the optimal dispersant.

3-4-2- X-Ray Diffraction (XRD)

A Siemens D500 X-ray diffractometer (Siemens Analytical X-ray Instruments) combined with a DIFFRAC PLUS (by Bruker-AXS) software was operated at 40kV and 25mA using a Cu-Kα source with a wavelength of 0.15406nm. 2θ diffraction angles of 10°-100° with step sizes of 0.01° and 0.02° and step times of 4 and 2 seconds respectively were used for determining phases present in the powder and coatings. The phases present in the spectra were identified with the aid of JCPDS diffraction files.

In the case of the as-sprayed and oxidised coatings the XRD analysis was performed on the top surface of the samples. However, in the case of the annealed samples, they were ground and polished using 800 grade SiC paper and 6μm polishing pads in order to conduct the analysis in areas away from the surface to avoid any possibility of any existing surface oxide layer(s).

3-4-3- Scanning Electron Microscopy (SEM)

A Philips XL-30 scanning electron microscope (SEM) fitted with a tungsten filament was used for the analysis of external morphology and cross section of coatings and

powder particles. Where very high magnification and resolutions were required an environmental scanning electron microscope (ESEM-FEG XL30) fitted with a FEG source was used.

The microscopes were primarily operated at an acceleration voltage of 20kV, spot size of 4-6, and working distance of 10mm in both secondary electron (SE) and backscattered electron (BSE) imaging modes. Secondary electron imaging was mainly used for analysing powder and coating morphologies and particle size measurements. Backscattered electron imaging was carried out for the analysis of different phases available in the powder and coatings (heat treated, annealed and oxidised); since the BSE imaging mode relies on the differences in the mean atomic number of the existing phases. This results in the phases with higher mean atomic number to appear brighter than the phases with a lower mean atomic number.

Sample preparation

The morphology of the powder was examined by sprinkling the powder particles on an adhesive carbon tab which was than directly inserted into the SEM chamber. Cross sections of the powder particles were investigated by sprinkling the powder particles on the mounting stage followed by adding the hot mounting powder (Metprep conductive), using a Buehler Metaserv automatic mounting press. The mounted samples were than ground and polished to 1μm finish using the standard metallographic procedure.

Coatings cross sections were analysed by sectioning the required samples using a Struers Accutom-5 Cut-off machine fitted with a SiC discs operating at 3000rpm and a cutting rate of ~0.03-0.05mms^{-1}. Cross-sectional samples were then hot mounted using a Metprep conductive mount and a Buehler Metaserv automatic mounting press.

The mounted samples were than ground and polished to a 1μm finish using the standard metallographic procedure.

3-4-4- Energy dispersive X-ray analysis (EDX)

Energy dispersive X-ray analysis was used to analyse different elements existing and examine the elemental content of different phases in the samples. An Oxford instrument Link ISIS-3000 energy dispersive X-ray detector was used in combination with the XL-30 SEM. For elemental quantification of coatings, an area of approximately 2×2μm was considered. Furthermore, quantification was carried out using ZAF correction for atomic number absorption and fluorescence, using peak profiles from elemental standards measured.

3-4-5- Transmission Electron Microscopy (TEM)

Microstructural investigations of free standing coatings were performed using a JEOL 2100F FEG TEM at 200kV (located in the Nottingham Nanotechnology and Nanoscience centre) equipped with Gatan Orius camera for imaging and Gatan Tridium imaging filter for spectroscopic analysis. Bright field (BF) and dark field (DF) imaging, selected area electron diffraction techniques and microanalysis (using an Oxford instruments INCA EDX system) were employed as part of the characterisation.

TEM samples for the JEOL 2100F were prepared using a FEI Quanta 200 3D FIB-SEM (located in the Nottingham Nanotechnology and Nanoscience centre) lift out which had a tungsten emission gun for the electron source and a Ga ion beam source. In this technique after identifying the desirable phase, using BSE imaging mode and EDX (an Oxford instruments INCA EDX system) analysis, a thin membrane suitable for TEM analyses is made. An Omniprobe model 100.7 in-situ nano-manipulator was

used to attach the membrane to (see Figure 3-6). The last part of the membrane was then cut free from the rest of the sample. The membrane was then attached to an Omniprobe Cu grid, and the probe cut free. Any additional final thinning is then carried out. The prepared TEM sample was then placed on a Gatan double tilt beryllium holder for TEM observations and analyses.

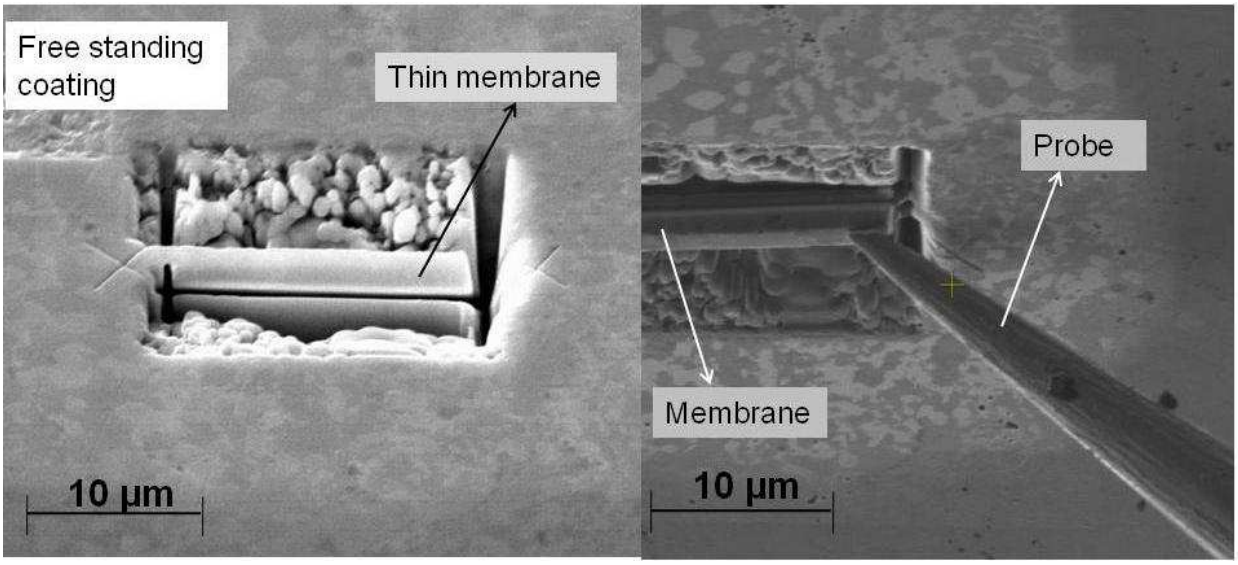

Figure 3-6. SEM micrographs presenting a thin membrane to be used as a TEM sample and an Omniprobe attached to the membrane (image on the right) for the lift out, SE mode.

3-4-6- Dynamic Mechanical analyser (DMA)

Young's modulus of as-sprayed and annealed free standing coatings as a function of temperature was measured using a TA Q800 DMA equipped with a 3-point bend clamp.

The fundamental measurement of the DMA is the sample stiffness (K). Sample stiffness is defined as the force applied to the sample divided by the deformation. This is measured in Newtons per meter in the international system of units (SI). Using the sample stiffness one can calculate the Young's modulus of the material.

In the DMA machine a controlled force and rate mode was used. With this mode one could control the force being applied to a sample directly, or affect the rate at which the sample may be deformed in terms of displacement or strain. Provided the stiffness of the material is within the limits of the machine (10^2-10^7N/m), the modulus of elasticity can be evaluated.

Like any other technique, sample preparation is one of the most important factors in achieving accurate and reproducible modulus values. Rectangular shape samples without any buckles and malformation were produced with a uniform thickness across the sample. The thickness of the sample should be 1/10 to 1/32 of the length of chosen 3-point bending sample supports (5, 10, 15, 20 or 50mm). Considering the coatings thickness (0.5-0.7mm), GF factor (described later on) and the stress produced within the sample (needs to be adequate for the sample to elastically deform without going into plastic region) a sample support length of 15mm was chosen. The maximum thickness allowed is 7mm and thickness accuracy of 0.02mm is required across the sample. It is important to have a uniform thickness for the sample and that the sample is accurately measured as the cube of the sample thickness is used in the modulus calculation; therefore, a 3% error in the thickness became a 10% error in the calculated modulus. Considering the accuracy required for the thickness, thermally sprayed coatings which are produced by deposition of a layer by layer of the powder particles have a major advantage, resulting in good measurements of the Young's modulus using the DMA. Furthermore, due to this required accuracy for thickness measurement, sheets of materials (such as stainless steel) with known moduli could not be used as a standard reference material and hence each time the tests were ran a previously tested sample was ran as a reference material in order to check on any changes in machine calibration.

To ensure if the sample size chosen are correct or whether the sample dimensions should be changed, a graph displaying the modulus range versus the possible sample size range was used (see Figure 3-7). The possible sample sizes are calculated as a geometry factor (GF) shown in equation (3-5).

$$GF = \frac{L^3}{48I}\left[1+\frac{12}{5}(1+\upsilon)\left(\frac{t}{L}\right)^2\right] \qquad (3\text{-}5)$$

$$I = \frac{wt^3}{12}$$

Where:

L= sample length (mm)

I= sample moment of inertia (mm^4)

t= sample thickness (mm)

w= sample width (mm)

υ= Poisson's ratio

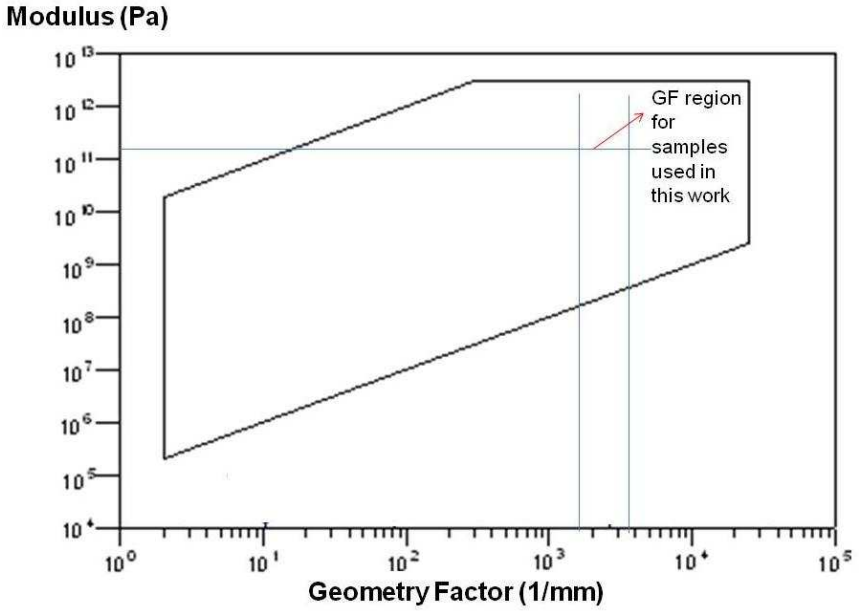

Figure 3-7. Geometry factor vs. modulus diagram, used for sample size.

Having checked with the GF diagram, rectangular samples with a thickness of 0.5-0.7mm and width of ~2mm were prepared and a 15mm long 3-point bending sample support was used. Some of the prepared samples were then annealed at 900°C, 1000°C and 1100°C (see section 3-3-2 for more details). As-sprayed and annealed samples were then tested at different temperatures (25°C, 100°C, 200°C, 300°C, 400°C and 500°C) at least three times in order to ensure a good reproducibility. The samples were held at temperature for approximately 3-5 minutes before the test was carried out, in order to achieve a constant temperature throughout the sample.

After each test the result was presented in the form of a graph, displacement as a function of applied load, the slope of which presents the measured stiffness. This value was then used in order to calculate the Young's modulus using equation (3-6).

$$E = K_s \times \frac{L^3}{6I}\left[1 + 0.6(1+\upsilon)\left(\frac{t}{L}\right)^2\right] \qquad (3\text{-}6)$$

Where:
E= Elastic modulus (MPa)
L= sample length (one side) (mm)
t= sample thickness (mm)
I= sample moment of inertia (mm4)
υ= Poisson's ratio
K_s= measured stiffness (N/μm)

3-4-7- Micro hardness

Micro hardness test were carried out on cross sections of free standing coatings using a LECO M-400 microhardness tester with a 300 gf load. Indentations were carried out

on polished samples in the middle of the coatings with a 20μm space between the indents. At least 20 indents were carried out on each sample and an average was taken.

3-4-8- Nano-indentation

A MML Nanotest system manufactured by Micro Materials Ltd was used to carryout the nano-indentation for hardness and Young's modulus measurements. The indentation experiments were performed using a standard diamond Berkovich indenter. A 5mN load was used in order to produce a 10×10 grid in which indents were approximately 5μm apart. The indentation was carried out on polished cross sections of HVOF and VPS coatings annealed at 1100°C for 4 hours (these samples had the largest β phase due to annealing and hence an indent could be seen in individual phases). The indented samples were then observed using SEM and each indent was classified as either being in the γ, β or γ/β phases and Young's modulus of the individual phases were extracted. It should be mentioned that some of the data points from the 10×10 grid were ignored as the indents corresponding to these data points did not start at the surface of the sample leading to a rapid increase in recorded depth at the beginning of the loading cycle. An example of one incident is illustrated in Figure 3-8. This is most probably caused due to the surface roughness of the sample leading to the indenter not finding the surface correctly or a subsurface cavity giving way during the initial loading.

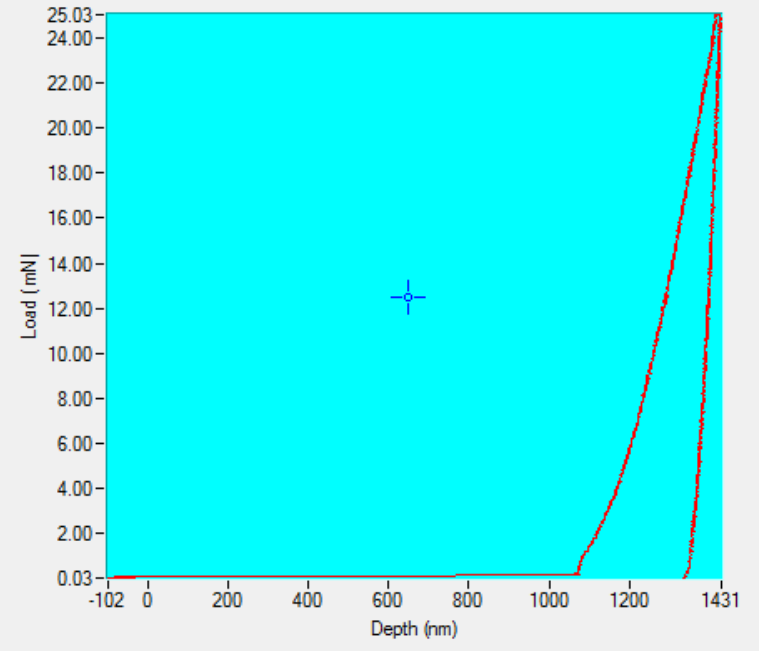

Figure 3-8. A 25mN indent demonstrating a rapid increase in recorded depth at the start of the loading cycle (jump in).

Furthermore, a 3N load was used in order to replicate the hardness measurement carried out using the micro hardness, on as-sprayed and annealed samples. 20 indents were made on each sample and an average of the results was taken. The hardness measurement was based on the hardness as a function of depth which was extracted using the load-displacement graphs, produced from each individual indent. Analysis of the load-displacement curves allows calculation of hardness (and elastic modulus) without the direct measurement of the contact area. The load and depth data (for 3N load) were then analysed using the Oliver and Pharr method [9] to determine the hardness.

The load-displacement graphs show an elastic-plastic loading followed by an elastic unloading (see Figure 3-9). The elastic equations of contact are then used in conjunction with the unloading data to determine the hardness (and elastic modulus) of the test material [10]. The hardness is calculated using equation 3-7.

$$H = \frac{P_{max}}{A} \tag{3-7}$$

Where A is the projected area of contact at peak load and P_{max} is the maximum load. Hence, in order to measure the hardness the contact area at peak load needs to be measured. This contact area is determined considering the geometry of the indenter and the depth of contact (h_c). The indenter geometry can be described by an area function F(h) which related the cross sectional area of the indenter to the distance form its tip. Given that an indenter does not itself deform significantly, the projected contact area at peak load can be calculated:

$$A = F(h_c) \tag{3-8}$$

In which the contact depth, measured from the total depth of penetration, is given by equation 3-9 [11].

$$h_c = h_{max} - \varepsilon \frac{P_{max}}{dp/dh} \tag{3-9}$$

Where h_c in the contact depth, ε factor depends upon the indenter shape and dp/dh is the unloading stiffness. Once h_c is known, A is found and hence hardness is calculated from equation (3-7).

It should be noted that the nano-indentation tests and Young's modulus data extraction were carried out at Micro Materials Ltd.

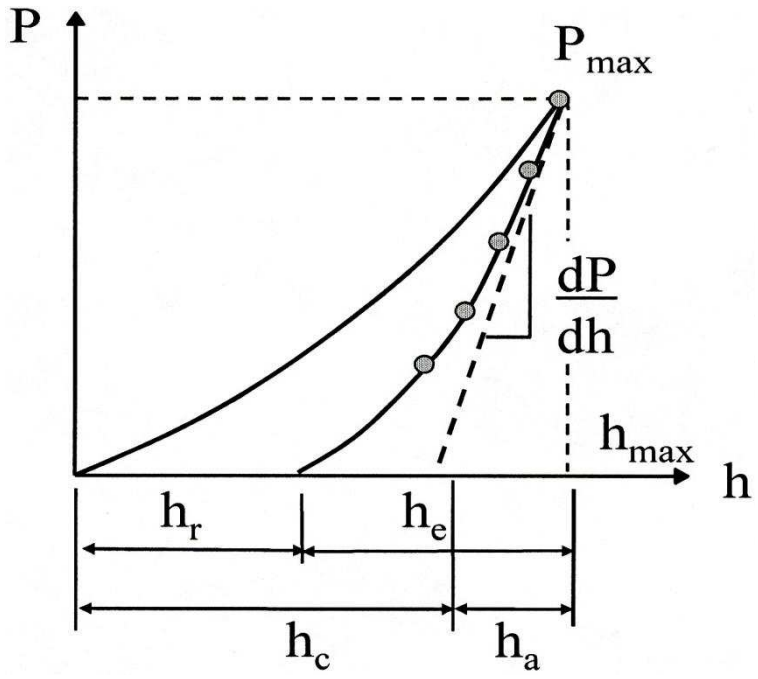

Figure 3-9. Typical load vs. displacement curve obtained from nano indentation [10].

3-4-9- Image analysis

Image analysis was used in order to carry out phase fraction quantification measurements (for γ and β) as a function of annealing temperature. The technique is based on difference in contrast in an image. Using threshold, one phase can be distinguished from another phase, and the surface area under the threshold can be calculated.

However, since it is based on a difference in contrast it is not a precise measuring tool for oxide and porosity. This is because both oxide and porosity look black in SEM images and it is very difficult to set a threshold to distinguish between the two.

For the phase quantifications as a function of annealing temperature, at least four typical SEM images at different magnifications (2000x, 4000x, 8000x and 16000x) for each coating and each annealing temperature were chosen for the image analyses.

For each coating and each annealing temperature, an average of the β volume fraction measured in the four different magnifications was taken and the value was reported as the β volume fraction for the particular coating and annealing temperature.

In the case of HVOF coatings where higher amount of internal oxides existed, a threshold was chosen in such a way that only the oxides / pores were taken into account; following this another threshold was chosen in such a way that this time the β particles were too taken into account. The volume fractions measured in both cases were than deducted from each other in order to reveal the β volume fraction.

3-4-10- Eshelby model

The Eshelby inclusion model, which treats porosity as randomly distributed ellipsoids with zero stiffness, has been used for thermally sprayed coatings to assess the effect of porosity and its aspect ratio on the coatings stiffness [12-15]. The aspect ratio of a pore is defined as the width (x) divided by the length (y) as shown in Figure 3-10. This approach to modelling the Young's modulus of the thermally sprayed coatings was justified on the basis that porosities perpendicular to coating surface and parallel to coating surface could be modelled as ellipses with low aspect ratio and high aspect ratio respectively.

For further information on the Eshelby model refer to [16-18].

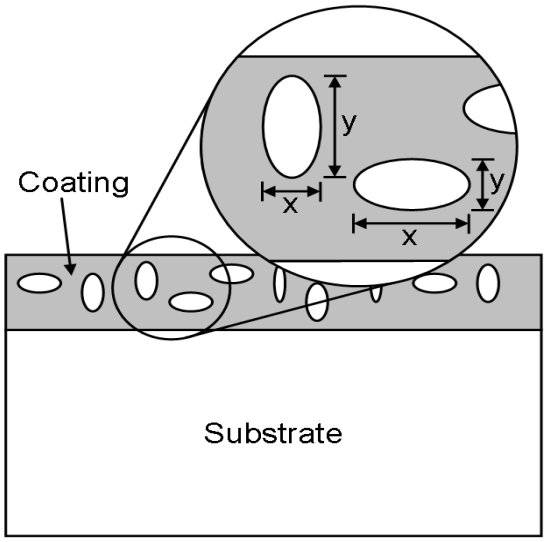

Figure 3-10. The aspect ratio of a given pore being defined as width (x) to length (y). On the basis of this definition pores perpendicular to the coating surface will have low aspect ratios and pores parallel to the coating surface will have high aspect ratios.

A computer programme produced by the group run by Bill Clyne in the Materials Science Department of Cambridge University which was released in January 1998 was used in order to predict the elastic modulus of the thermally sprayed coatings.

This programme calculates the elastic constants of a composite material; in this case the MCrAlY coating consisted of a dual phase structure, using the Eshelby equivalent homogeneous inclusion model. The reinforcements, the β phase in our case, are represented as a set of ellipsoids. Input data in the form of the Young's modulus and poisson ratio of the matrix and the reinforcement are required. For the purpose of this research work, the Young's modulus of the γ and β phases calculated using the nano-indentation technique was used as the input data. The aspect ratio of the reinforcement is also an input. This can be greater than one, equal to one or smaller than one depending on the shape of the reinforcement. In order to see the effect of the reinforcement aspect ratio on the Young's modulus a wide range of aspect ratios (0.001 to 100) were chosen for this research work. The maximum required value of

the reinforcement volume fraction and the number of values of this volume fraction for which calculation is to be carried out are also required as input data. The out put data, on the other hand, are given as a set of data pairs, which correspond to reinforcement volume fraction against Young's modulus. A summary of the data points used as the input data are illustrated in Table 3-4.

Table 3-4. A summary of the input data used in the Eshelby model software.

Input parameter	Reinforcement (second phase)	
	β phase	**Porosity**
Matrix Young's modulus (GPa)	231	215
Matrix poisson ratio	0.3	0.3
Reinforcement Young's modulus (GPa)	181	0
Reinforcements poisson ratio	0.3	0
Aspect ratio	Vary (from 0.001 to 100)	
Max. reinforcement volume fraction	0.6	0.15
Number of values of the volume fraction	100	100

CHAPTER 4

Microstructural Characterisation & Mechanical Properties

4-1- Microstructural characterisation

In order to evaluate and investigate the properties such as Young's modulus, hardness, oxidation behaviour, etc. and its relationship to the microstructure of thermally sprayed coatings, two different spraying systems, HVOF & VPS, were chosen. Furthermore, considering factors such as the degree of particle melting, porosity levels and in-flight oxidation level of powder particles three different HVOF coatings were chosen from different spray runs. HVOF1 and HVOF2 were sprayed with the same powder (Praxair Co-210-24) under very similar processing conditions whereas HVOF3 was sprayed with a powder of different size range (Amdry 9951) to produce a significantly different coating structure. Moreover, initially two different VPS coatings were examined from different sources but the majority of work concentrated on VPS1. The reason for this being, that all the experimental work carried out in this research was on free standing coatings, and as will be seen later on in this chapter, VPS2 did not have the required thickness to be detached, so as-sprayed characterisation was the only investigation carried out on this (VPS2) coating.

This chapter describes the microstructural characterisation of the as-received powders, as-sprayed and heat treated coatings as well as the mechanical properties of coatings.

4-1-1- As-received powder

4-1-1-1- Particle size measurements

The nominal size of the powders used for HVOF and VPS coatings given by suppliers is as follows: Praxair CO-210-24 -45+20µm; Sulzer Metco Amdry 9951 -38+5µm. Figure 4-1 illustrates the cumulative results obtained from Malvern analyses for Praxair and Amdry powders. The median particle size D(v, 0.5), calculated by Malvern analysis, for the Praxair CO-210-24 powder is ~34µm and for Amdry 9951 powder is ~20µm. Figure 4-2 shows SEM images illustrating samples of the Praxair and Amdry powders. As can be seen, both powders have spherical particles with small satellites attached to them. When compared to the Malvern analyses it is observed that the two methods are consistent with each other and with the nominal size distribution. Both methods show that the Amdry 9951 powder has a wider distribution range and a smaller median diameter.

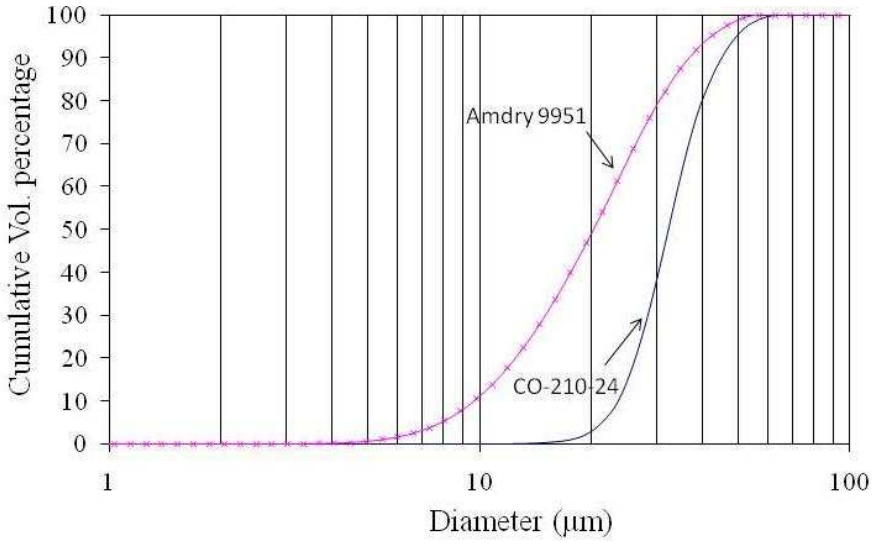

Figure 4-1. Plot of cumulative volume percent versus particle diameter for the as-received Praxair CO-210-24 & Sulzer Metco Amdry 9951 powders.

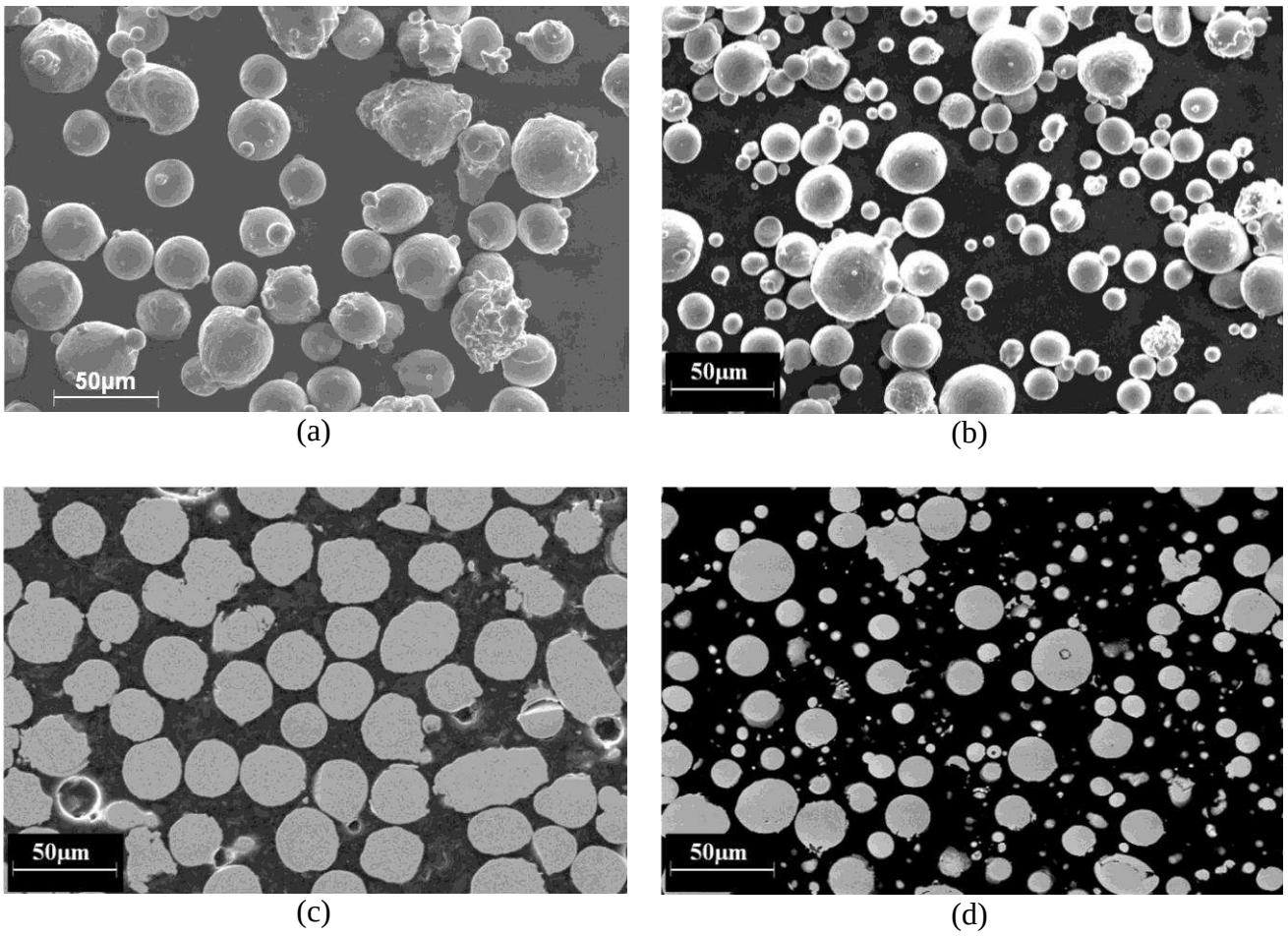

(a) (b)

(c) (d)

Figure 4-2. SEM secondary electron (SE) images of Praxair powder (a) & (c) and Sulzer Metco powder (b) and (d). (a) & (b) show surface morphology, (b) & (d) are powder cross sections. All images are at the same magnification.

4-1-1-2- Morphology and microstructure of powder particles

Figure 4-3 is a SEM image of powder particles in which some have small satellites and some have irregular shapes, which is due to impact of molten droplets on to already solidified particles during atomisation. An etched cross section of a Praxair CO-210-24 powder particle is shown in Figure 4-4. A fine scale dendritic structure is

visible. This results from the high cooling rate involved in the powder atomisation process, typically 10^3 to 10^5 Ks^{-1} [1].

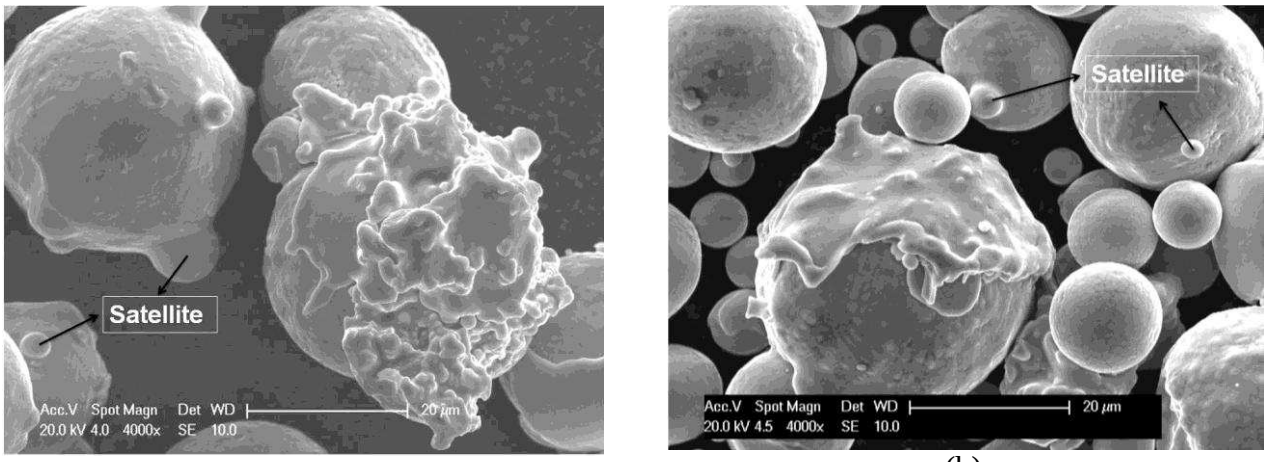

(a) (b)

Figure 4-3. Secondary electron SEM images showing external morphology of (a) CO-210-24 and (b) Amdry 9951 powder particles, illustrating satellites and irregular powder particles.

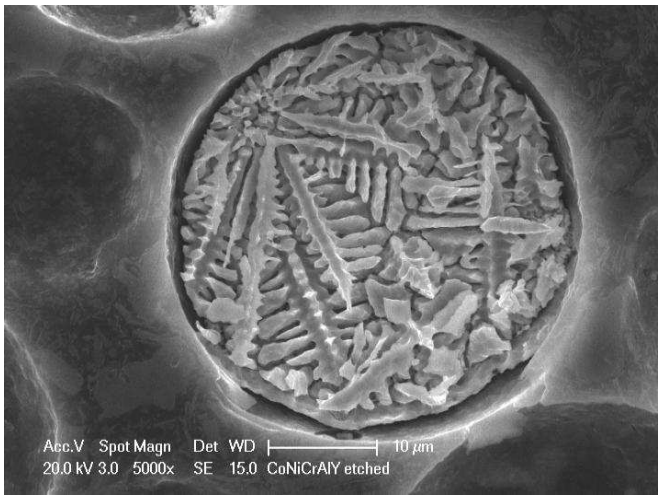

Figure 4-4. Secondary electron SEM image of the dendritic structure of a CO-210-24 powder particle.

As seen in Figure 4-5, in BSE mode, an atomic number contrast is clearly observed which indicates that the as-received powders have a two phase microstructure. Furthermore, the XRD pattern (Figure 4-6) of the powder particles revealed the presence of two phases, γ and β. γ is a FCC phase with a lattice parameter close to

0.358nm and β is a BCC phase close to that of NiAl / CoAl with a lattice parameter close to 0.286nm which have been measured using the Nelson-Riley method.

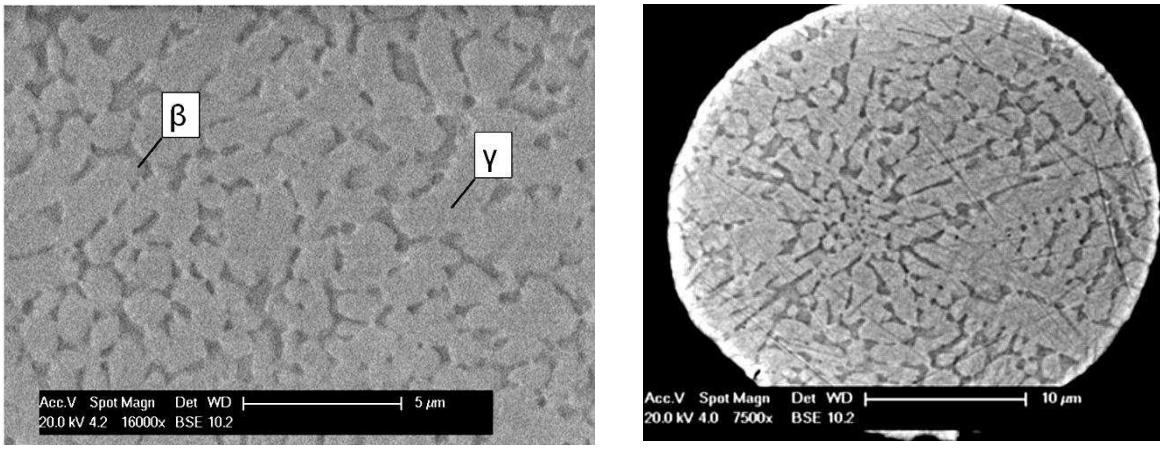

(a) (b)

Figure 4-5. SEM micrograph of (a) CO-210-24 & (b) Amdry 9951 powders, illustrating atomic number contrast due to a two phase structure. BSE mode.

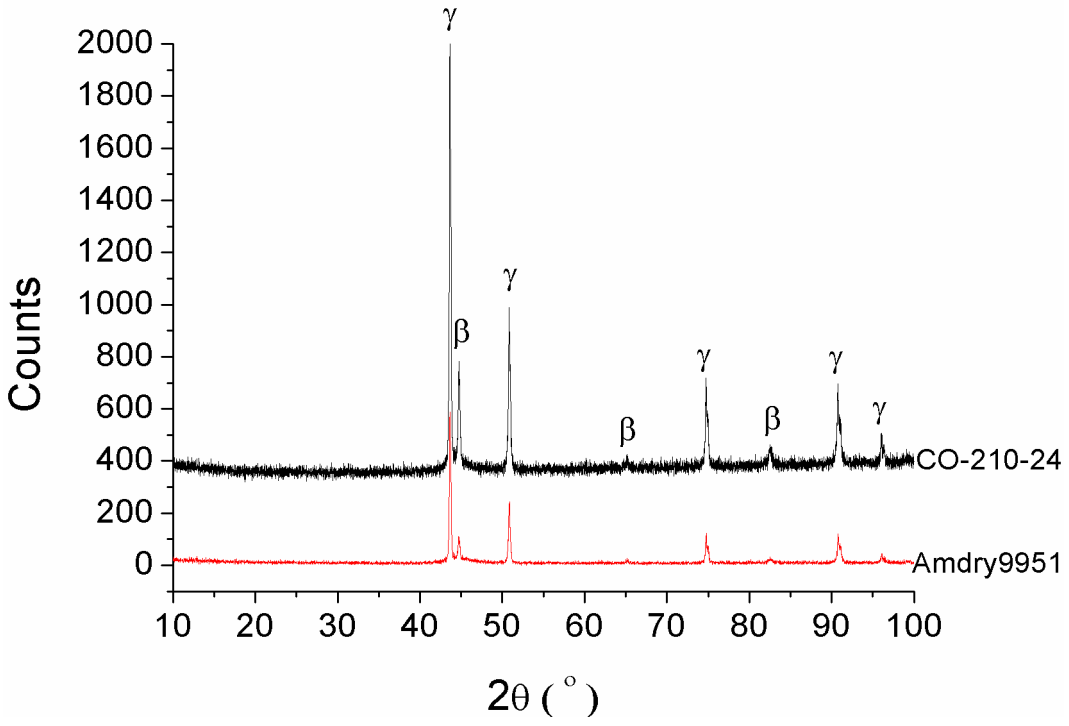

Figure 4-6. XRD patterns of CO-210-24 & Amdry 9951 powders. Patterns reveal a two phase, γ+β, structure for both powders.

Several area average EDX spectra were taken from cross sections of the powder particles themselves in order to compare the overall composition to the composition given by suppliers of each powder. A comparison of the nominal composition and EDX analyses is given in Table 4-1. A similar composition to the supplier's composition was obtained. Y could not be detected in the SEM by EDX.

Although the β phase is too small to allow for an accurate composition measurement by EDX, due to electron beam spreading, a compositional analysis was carried out to find an estimate of the composition of γ and β phases. Table 4-2 shows a comparison of the elemental composition of both phases, the values presented are an average of five different EDX measurements. The analysis revealed that the darker phase is enriched in Al whereas the brighter phase was enriched in Cr. Since the γ phase is a solid solution of Co, Ni, Cr, etc. and has a higher mean atomic number it appears brighter in BSE mode, hence the brighter phase is considered to be γ. The darker phase which has a lower mean atomic number in BSE mode is considered to be β-(Co,Ni)Al intermetallic. The γ phase is the major phase with β regions embedded.

Table 4-1. CO-210-24 & Amdry 9951 nominal & EDX powder composition (wt%). Error bars represent the standard errors in the mean.

Powder	Elements (wt%)				
	Co	Ni	Cr	Al	Y
CO-210-24 Supplier chemical analysis	38.93	31.70	20.80	8.10	0.47
CO-210-24, area EDX analysis*	36 ± 0.2	34 ± 0.7	23 ± 0.1	8 ± 0.4	—
Amdry 9951 Supplier chemical analysis	39.05	31.74	20.83	7.98	0.40
Amdry 9951, area EDX analysis*	37 ± 0.3	32 ± 0.2	23 ± 0.3	8 ± 0.3	—

* Values presented are average of five measurements.

Table 4-2. EDX elemental composition of γ & β phases in CO-210-24 as-received powder.

Element	Light phase (*γ*)		Dark phase (*β*)	
	wt%	**at%**	**wt%**	**at%**
Co	38	34	33	29
Ni	32	29	35	31
Cr	23	23	21	21
Al	6	13	10	18

4-1-2- As-sprayed coatings characterisation

4-1-2-1- HVOF coatings

XRD patterns (Figure 4-7) of all three HVOF coatings confirmed the presence of a two phase, γ+β, structure for the coatings, where γ is a FCC phase, with a lattice parameter close to 0.359nm for HVOF1 coating measured using the Nelson-Riley method, and β is a BCC phase (lattice parameter was not measured due to lack of peaks in the as-sprayed coatings). However, as can be seen HVOF3 shows a smaller peak height for the β phase indicating a smaller proportion of the β precipitates in HVOF3 as compared to the other two HVOF coatings.

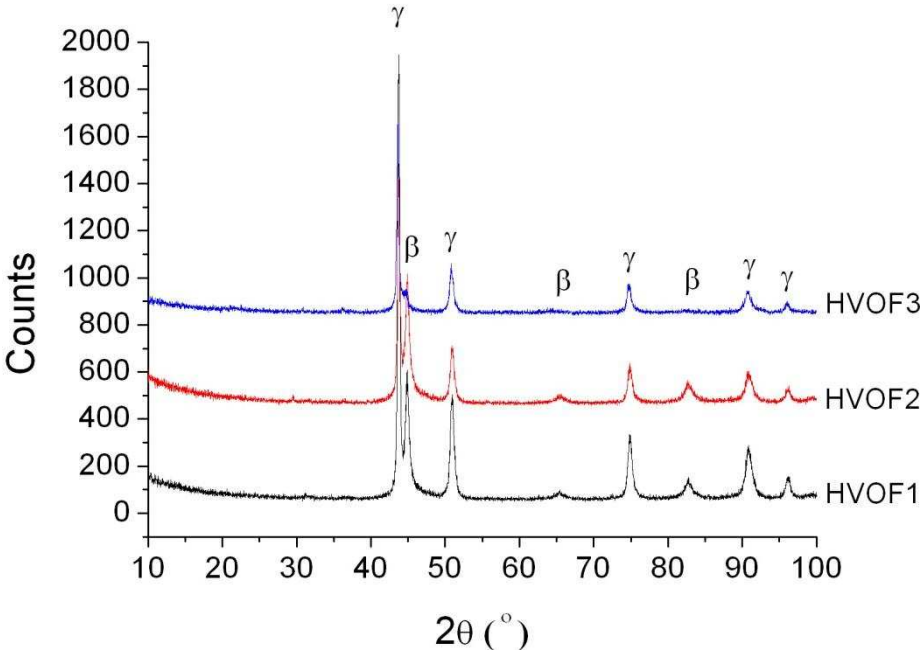

Figure 4-7. XRD patterns of all three HVOF coatings. The patterns illustrate a γ+β two phase microstructure.

Figure 4-8 shows the thickness of different HVOF coatings measured by SEM. A summary of the thickness values have been given in Table 4-3, each value is an average of several measurements (at least 6 measurements).

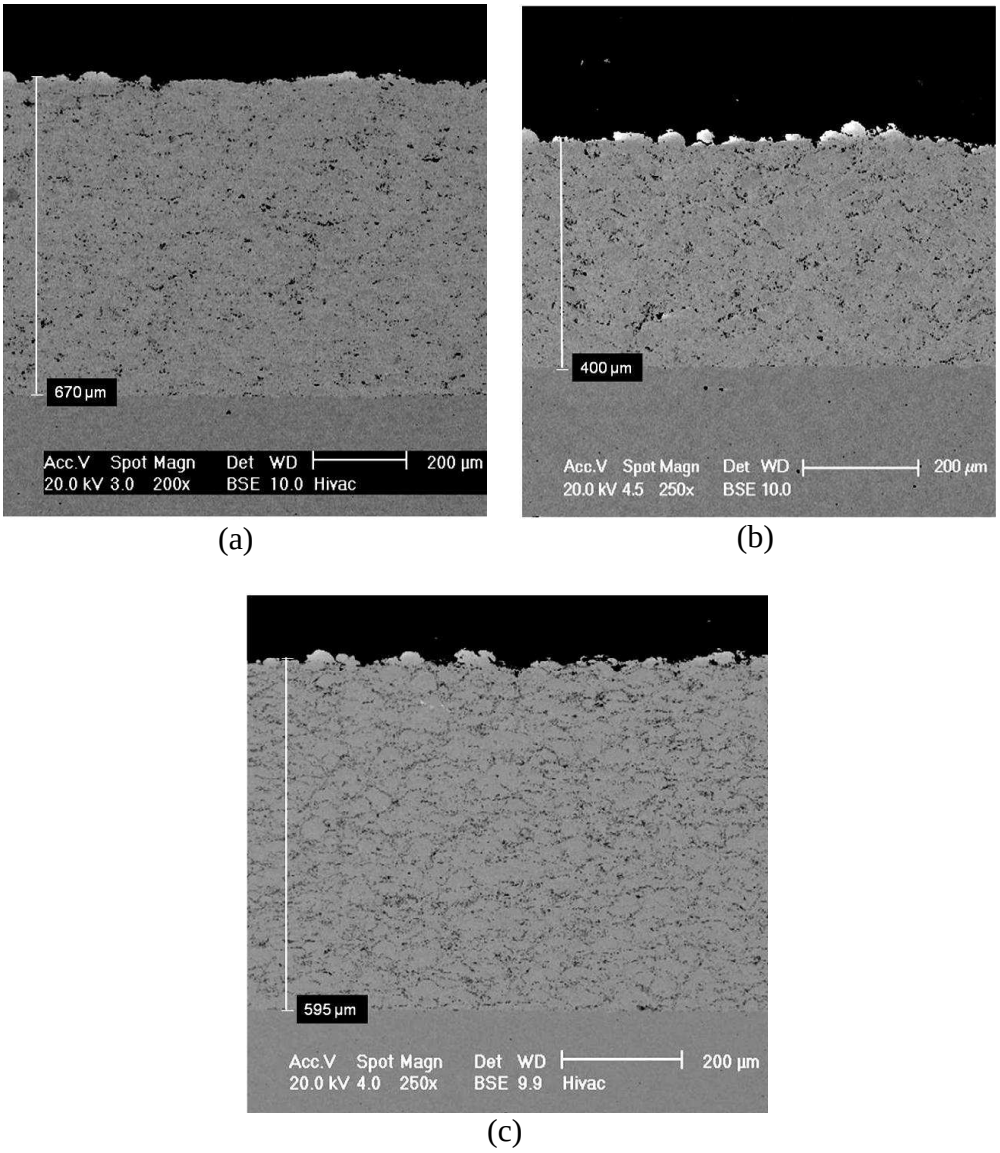

Figure 4-8. SEM (BSE) images of as-sprayed HVOF coatings. (a) HVOF1, (b) HVOF2 & (c) HVOF3.

Table 4-3. Coating thickness for HVOF sprayings.

	HVOF1	**HVOF2**	**HVOF3**
Thickness (µm)	590±22	405±5	650±6

When looked at in more detail, it was observed that the structure of all three coatings contained pores and oxides. Also, fully melted and resolidified, and incompletely melted powder particles could be observed in all three HVOF coatings. Figure 4-9 is an example showing the above mentioned characteristics in a HVOF2 coating. The

resolidified regions of powder particles are usually featureless due the rapid solidification of the molten material. This is seen more clearly in Figure 4-10; also as seen in Figure 4-9 and Figure 4-10 the un-melted regions of incompletely melted powder particles have a retained two phase (γ+β) structure of the as-received powder.

EDX analysis of the matrix phase revealed the presence of Co, Ni, Cr, etc. with higher Cr content as compared to the precipitates and the EDX analysis of the precipitates revealed the presence of Al, Co and Ni with higher Al content as compared to the matrix. Hence the matrix phase was revealed to be the solid solution FCC γ phase whereas the darker precipitates were revealed to be the BCC β-(Co,Ni)Al phase.

The EDX area analysis of un-melted particle regions and large areas (~20×20μm) of the coatings revealed a similar composition to that of the as-received powder presented in Table 4-1. This observation indicates no significant loss of individual low melting point elements, such as Al, during spraying.

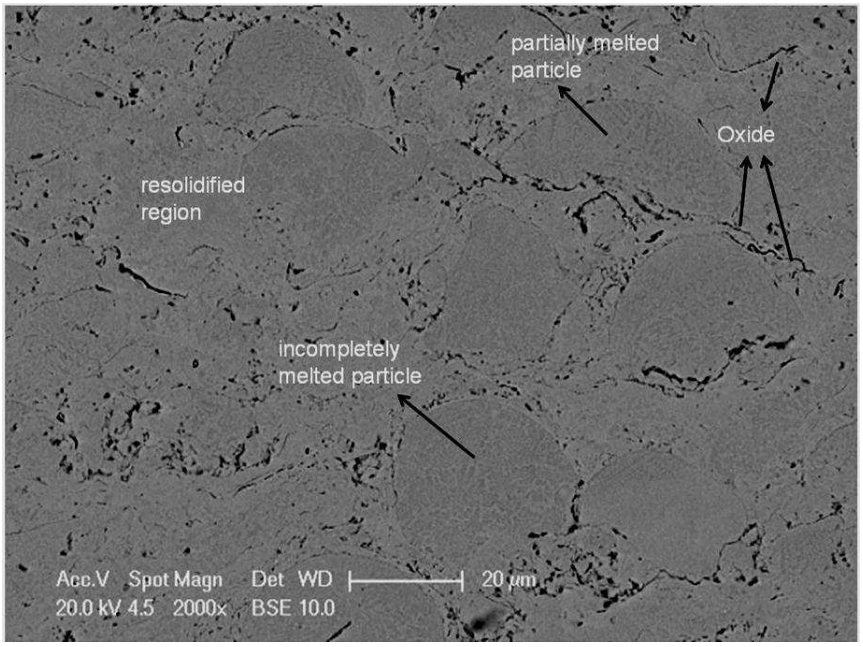

Figure 4-9. Back scattered electron SEM micrograph of HVOF2 coating illustrating oxides, melted and incompletely melted powder particles.

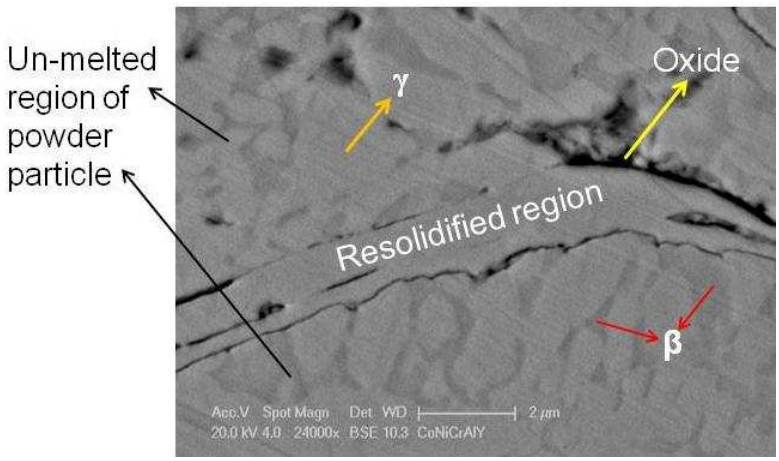

Figure 4-10. Back scattered electron SEM micrograph of HVOF1 coating illustrating a two phase structure for un-melted region of powder particle and a featureless structures for resolidified region.

Figure 4-11 illustrates an oxygen map for a region of HVOF3 coating. As can be seen, the dark areas surrounding the incompletely melted powder particles are oxygen rich. Oxides and pores are seen black in SEM images (BSE mode). Considering Figure 4-11 it can be stated that the black areas around the powder particles are usually oxides. This correlates well to the fact that for incompletely melted powder particles, during spraying the surface of the particle reaches higher temperatures and partially melts and during flight a thin oxide layer can form on the surface which will appear as a string (oxide stringer) in SEM cross section images. Furthermore, chemical analysis was used in order to measure the oxygen content of the coatings. Moreover, an attempt was made in order to measure the porosity and oxide content of the coatings using image analysis. However, as there are no significant differences in oxide and pore contrasts, the porosity plus oxide levels were measured. Table 4-4 illustrates the oxygen and oxide weight percents (assuming all oxide is Al_2O_3) and the porosity plus oxide level of the as-sprayed HVOF coatings.

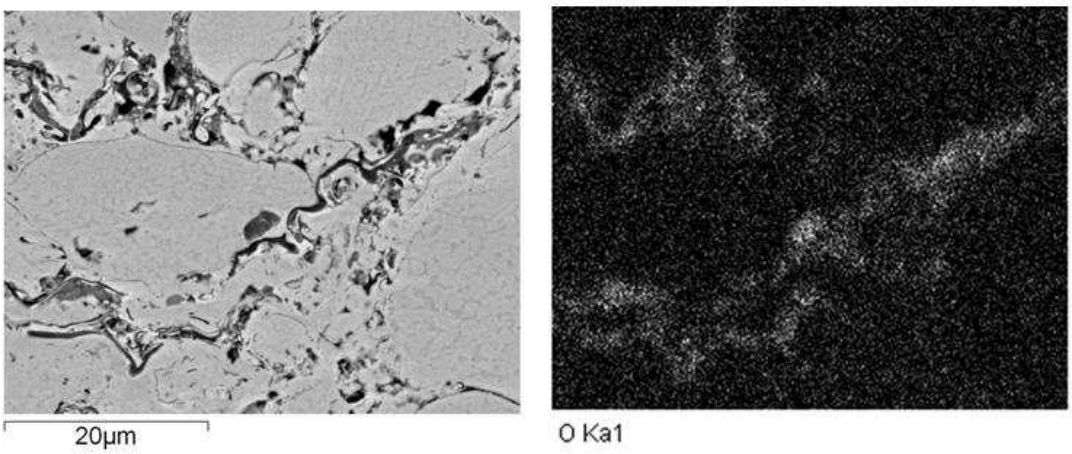

Figure 4-11. Oxygen map for as-sprayed HVOF3 coating. The black areas around the powder particles are oxygen rich.

Table 4-4. Oxygen content & porosity plus oxide level for as-sprayed HVOF coatings. Results obtained from chemical analysis & image analysis respectively.

	HVOF1	HVOF2	HVOF3
Oxygen (wt.%)	0.40	0.36	1.62
Oxide (wt.%)	0.85	0.76	3.44
Oxide* (vol%)	1.6	1.4	6.2
Oxide + porosity (vol%)	4	4	8

* See Appendix 1 for calculation method and assumptions used.

Figure 4-12 illustrates images of the top surface and Figure 4-13 illustrates cross sectional images of each HVOF coating. Although image analysis shows similar amount of pore and oxide for HVOF1 and HVOF2 coatings, a higher amount of incompletely melted powder particles can be seen sitting on the top surface of HVOF2 coating (~41 as compared to ~16 for HVOF1), see Figure 4-12; this is an indication of reduced heating. The cross sectional images (Figure 4-13) also shows more distinct particles for HVOF2 compared to HVOF1, indicating more extensive amount of melting for HVOF1 during spraying. However, a much higher amount of

melting is observed in HVOF3 coating, as compared to other two HVOF coatings, see Figure 4-13. As can be seen from Figure 4-13 and Table 4-4, HVOF3 coating has the highest amount of oxides and pores among all three HVOF coatings. This is due to the smaller powder particles used for HVOF3 coating.

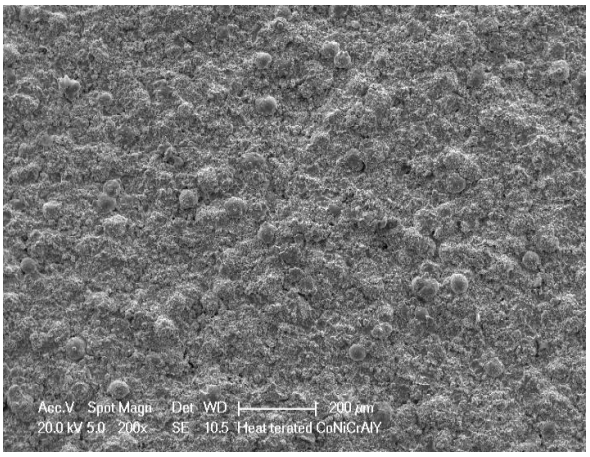

(HVOF1)

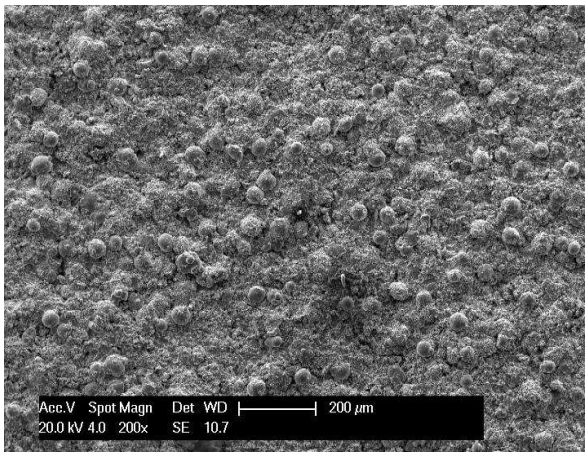

(HVOF2)

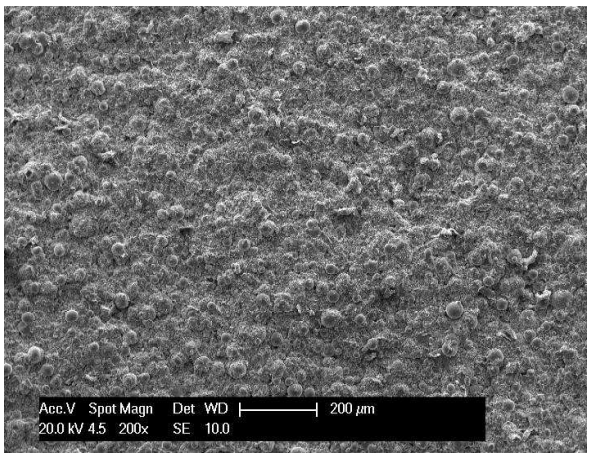

(HVOF3)

Figure 4-12. Secondary electron SEM micrographs of the top surface of as-sprayed HVOF1, HVOF2 &HVOF3 coatings. Number of incompletely melted powder particles clearly seen on the top surface, for: HVOF1 ~16, HVOF2 ~41 & HVOF3 ~20. All images are at the same magnification.

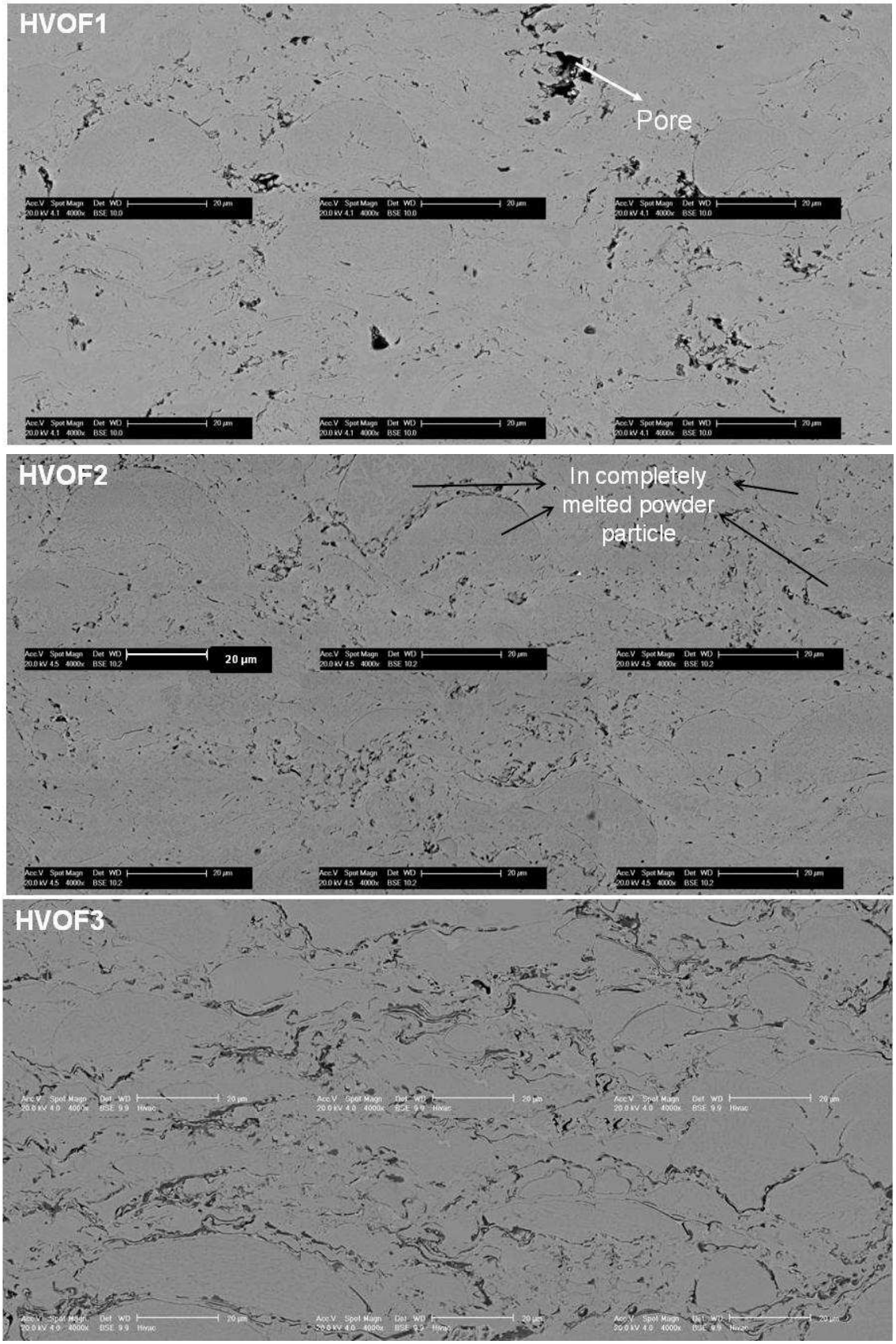

Figure 4-13. Back scattered electron SEM micrographs of as-sprayed HVOF1, HVOF2 & HVOF3 cross sections. Degree of melting: HVOF3 > HVOF1 > HVOF2. All images are at the same magnification.

4-1-2-2- VPS coatings

Figure 4-14 illustrates the XRD pattern of the VPS coatings. As can be seen, the XRD pattern of VPS coatings do not show a clear β phase peak when compared with XRD patterns of HVOF coatings (Figure 4-7).

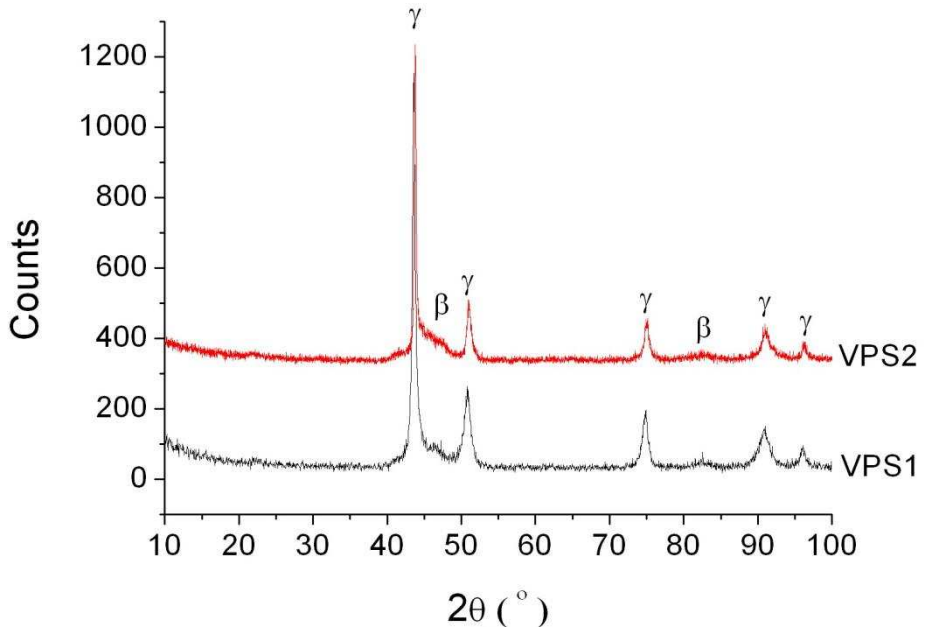

Figure 4-14. XRD patterns of as-sprayed VPS1 &VPS2 coatings.

The thicknesses of the different VPS coatings have been measured from SEM images. Figure 4-15 shows a general view of the coating microstructure and the relative thicknesses. The thickness of each VPS coating is given in Table 4-5 where each value is an average of several measurements (at least 6 measurements). Furthermore, a higher amount of porosity can be seen for VPS1 as compared to VPS2, see Figure 4-15.

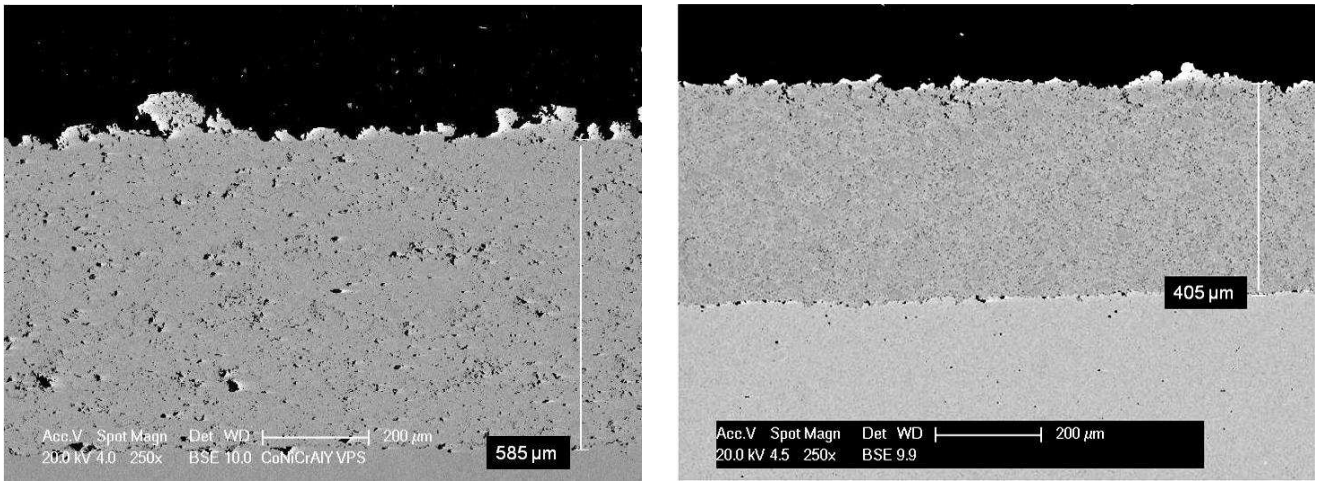

(a) (b)

Figure 4-15. Back scattered electron SEM micrograph of (a) VPS1 and (b) VPS2, illustrating an overall view of the coatings and coating thickness. Both images are at the same magnification.

Table 4-5. Coating thickness of VPS sprayings.

	VPS1	**VPS2**
Thickness (µm)	591±7	420±16

Like HVOF coatings the VPS coatings also had the typical thermal spray characteristics of melted and resolidified material, incompletely melted particles and pores. Figure 4-16 illustrates a SEM micrograph of VPS coatings showing the existence of melted and resolidified material, incompletely melted particles and porosity in the coating.

SEM images of incompletely melted powder particles revealed that these particles have retained the γ+β structure of the as-received powder whereas the resolidified regions only had a single γ phase structure, see Figure 4-16. This is due to the rapid solidification of the molten powders and formation of a single phase.

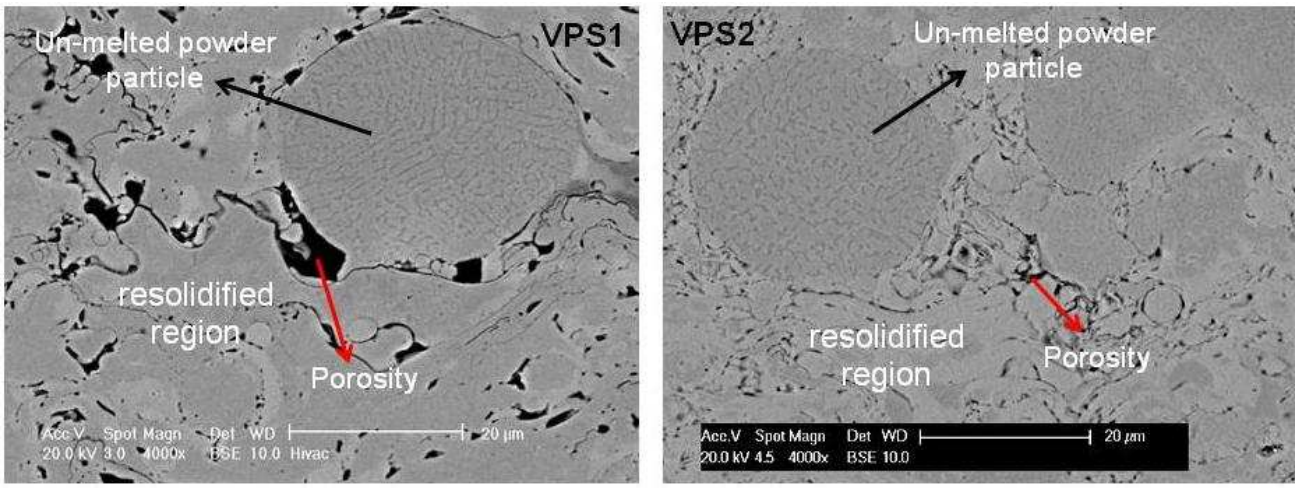

Figure 4-16. Back scattered electron SEM micrographs showing VPS1 & VPS2 characteristics such as un-melted powder particle, porosity and resolidified splats. Both images are at the same magnification.

Having said this, if VPS coatings are compared to HVOF, a higher amount of melted and resolidified material can be observed for VPS coatings. Comparison of Figure 4-17 and Figure 4-18 with Figure 4-12 and Figure 4-13 clearly shows a higher degree of melting for VPS coatings compared to HVOF. Since only the incompletely melted or partially melted particles have retained their two phase structure and VPS coatings tend to have fewer of the partially melted particles, compared to HVOF coatings, the VPS coatings do not show a clear β peak in their XRD spectra.

Furthermore, when VPS1 and VPS2 coatings are compared a higher degree of melting can be observed for VPS1 coating, see Figure 4-17 and Figure 4-18. This is whilst VPS2 coating has lower amount of porosity, see Figure 4-17.

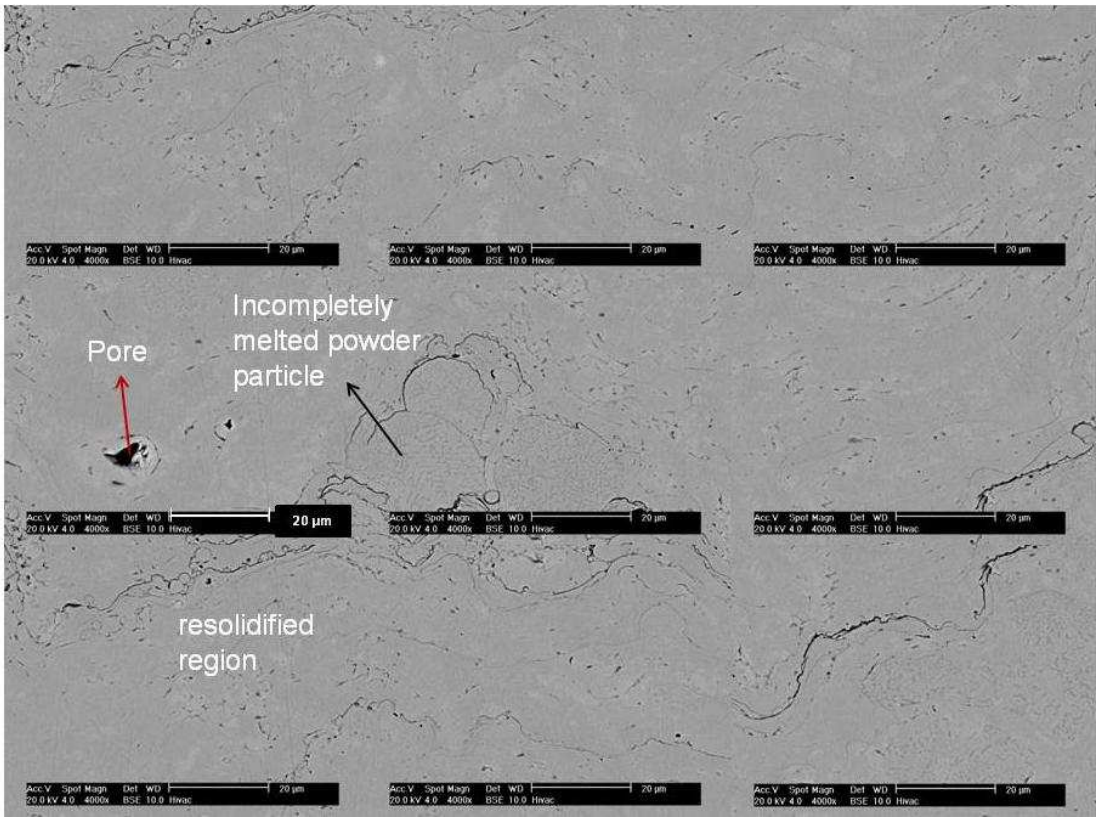

(VPS1)

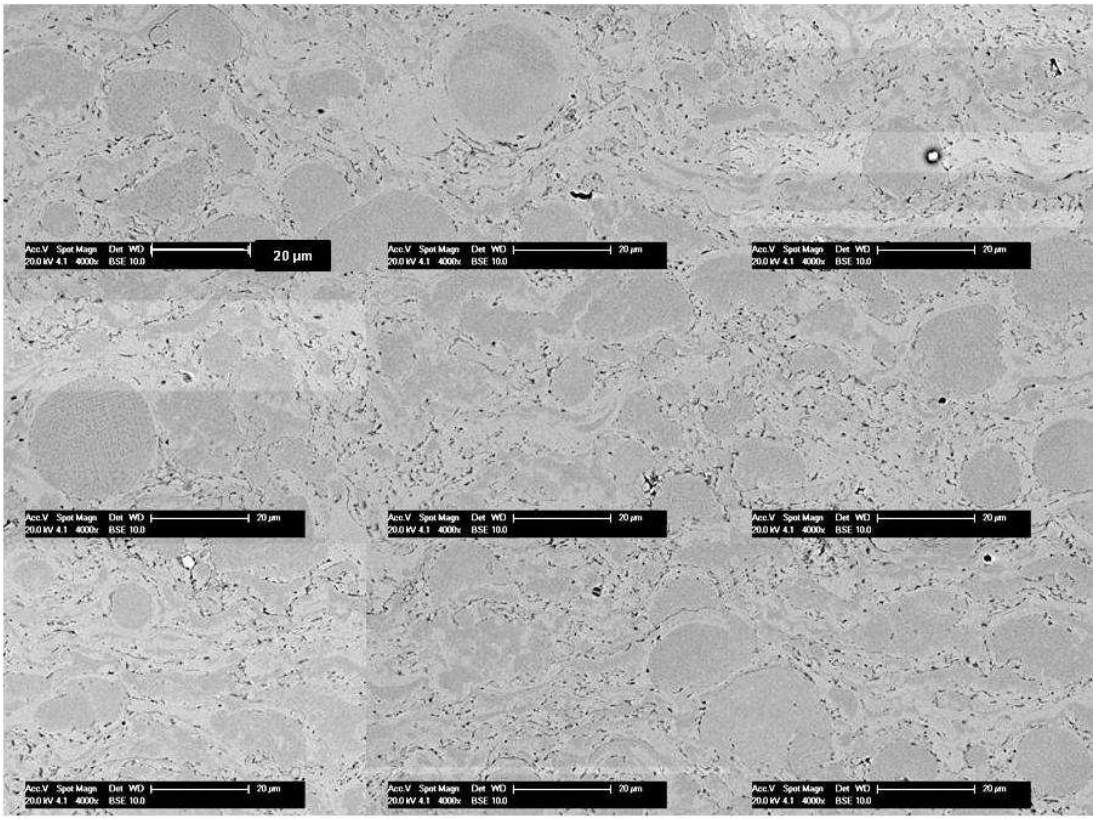

(VPS2)

Figure 4-17. Back scattered electron SEM cross sectional micrographs of (a) VPS1 and (b) VPS2 coatings, illustrating higher number of un-melted particles for VPS2 and higher amount of porosity for VPS1. Both images are at the same magnifications.

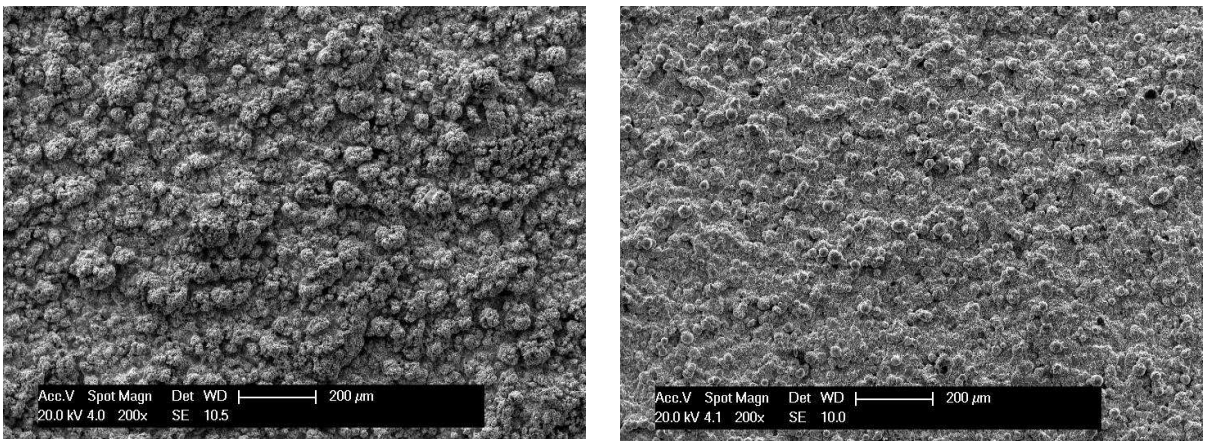

(a) (b)

Figure 4-18. Secondary electron SEM micrograph of the top surface of (a) VPS1 and (b) VPS2 coatings illustrating higher un-melted powder particles for VPS2. Both images are at the same magnification.

Chemical oxygen analysis of VPS1 as-sprayed coating revealed an oxygen content of 0.25wt.% equivalent to 0.53wt.% oxide content (assuming all oxides are alumina). Furthermore, this was equivalent to oxide volume percent of 0.5 (see Appendix 1 for calculation method and assumptions made). This value is lower than that of any of the HVOF coatings (see Table 4-4) as expected for a vacuum deposition process. Since the VPS spraying had been carried out under vacuum, generally it tends to have far fewer oxides compared to HVOF coatings. Furthermore, image analysis has also been carried out to measure the oxide plus porosity level of the as-sprayed coating. It was observed that the VPS1 as-sprayed coating had an oxide plus porosity level of ~5%. However, the chemical oxygen analysis result shows that the oxide level is ~0.5 vol% indicating a high porosity level in this coating. Figure 4-19 illustrates an oxygen map for the as-sprayed VPS1 coatings. It is clear from the map that only a small amount of oxide is available in the coatings (the black line in the SEM image). This image attributes well to the fact that the majority of the 5% measured is porosity.

Furthermore, by comparing the oxygen chemical analysis (for as-sprayed HVOF and VPS coatings) and comparison of Figure 4-13 and Figure 4-17, a lower oxide content for the VPS coatings compared to the HVOF coatings is clear.

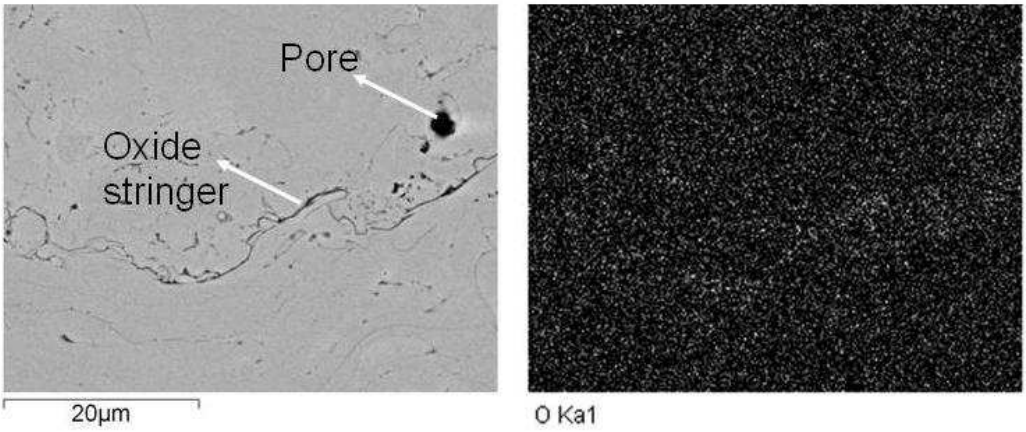

Figure 4-19. Oxygen map of as-sprayed VPS1 coating. A very low amount of oxygen is seen in the map.

4-1-3- Characterisation of heat treated coatings

HVOF and VPS free standing coatings were annealed at different temperatures for different exposure times where the exposure times were increased with decreasing temperature in order to achieve equilibrium microstructures in all test samples; details are given in chapter 3 section 3-3-2.

4-1-3-1- HVOF coatings

The microstructure of HVOF1 coating annealed at 900°C for 90h, can be seen in Figure 4-20. The first feature to be noted about the annealed coatings is that the annealing treatment has caused a reduction in the porosity level of the coating as compared to as-sprayed coatings.

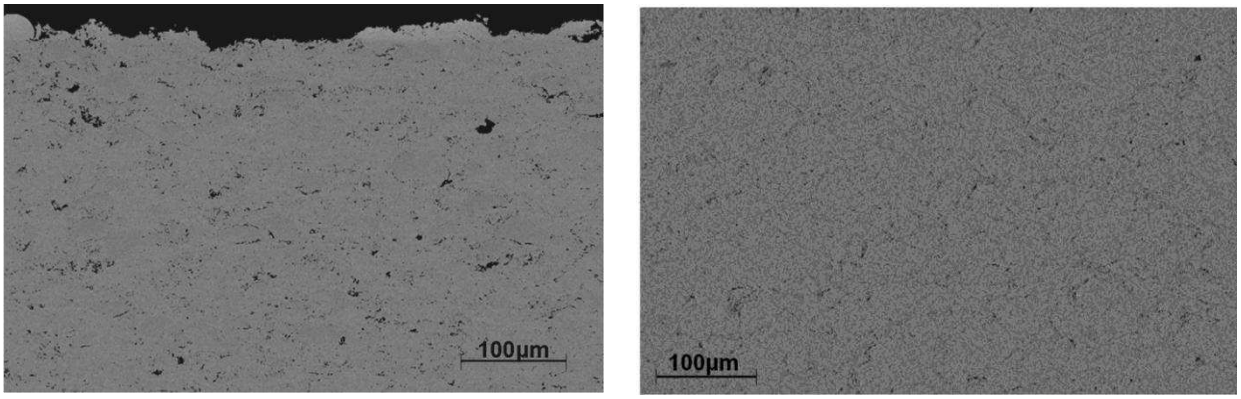

(a) (b)

Figure 4-20. SEM micrographs of (a) as-sprayed and (b) annealed at 900°C HVOF1 coatings. Annealing has decreased the porosity level. Both images are in BSE mode and are at the same magnification.

Furthermore, when investigated at higher magnification it is clearly seen that β-(Co,Ni)Al phase has became coarsened, see Figure 4-21, compared with Figure 4-13.

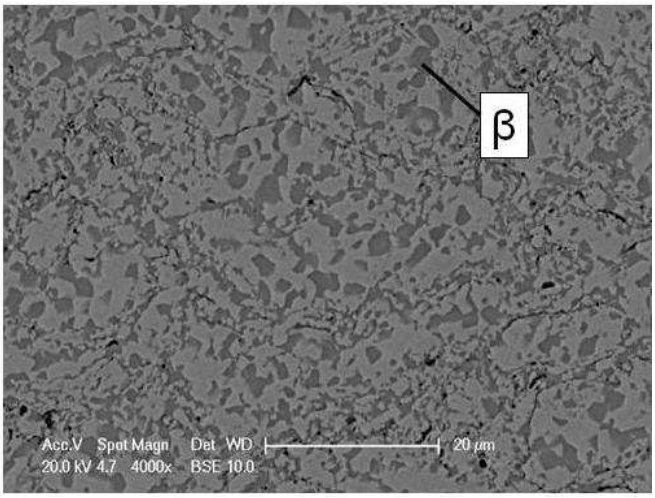

Figure 4-21. Back scattered electron SEM micrograph of HVOF1coating annealed at 900°C for 90 hours, illustrating coarsened β phase.

A comparison of the microstructure of HVOF1, HVOF2 and HVOF3 coatings annealed at 900°C, for 90h, can be seen in Figure 4-22. The presence of oxide stringers is clear in all three HVOF coatings, with HVOF3 having the highest amount of oxide stringers and HVOF1 having the lowest amount of oxide stringers.

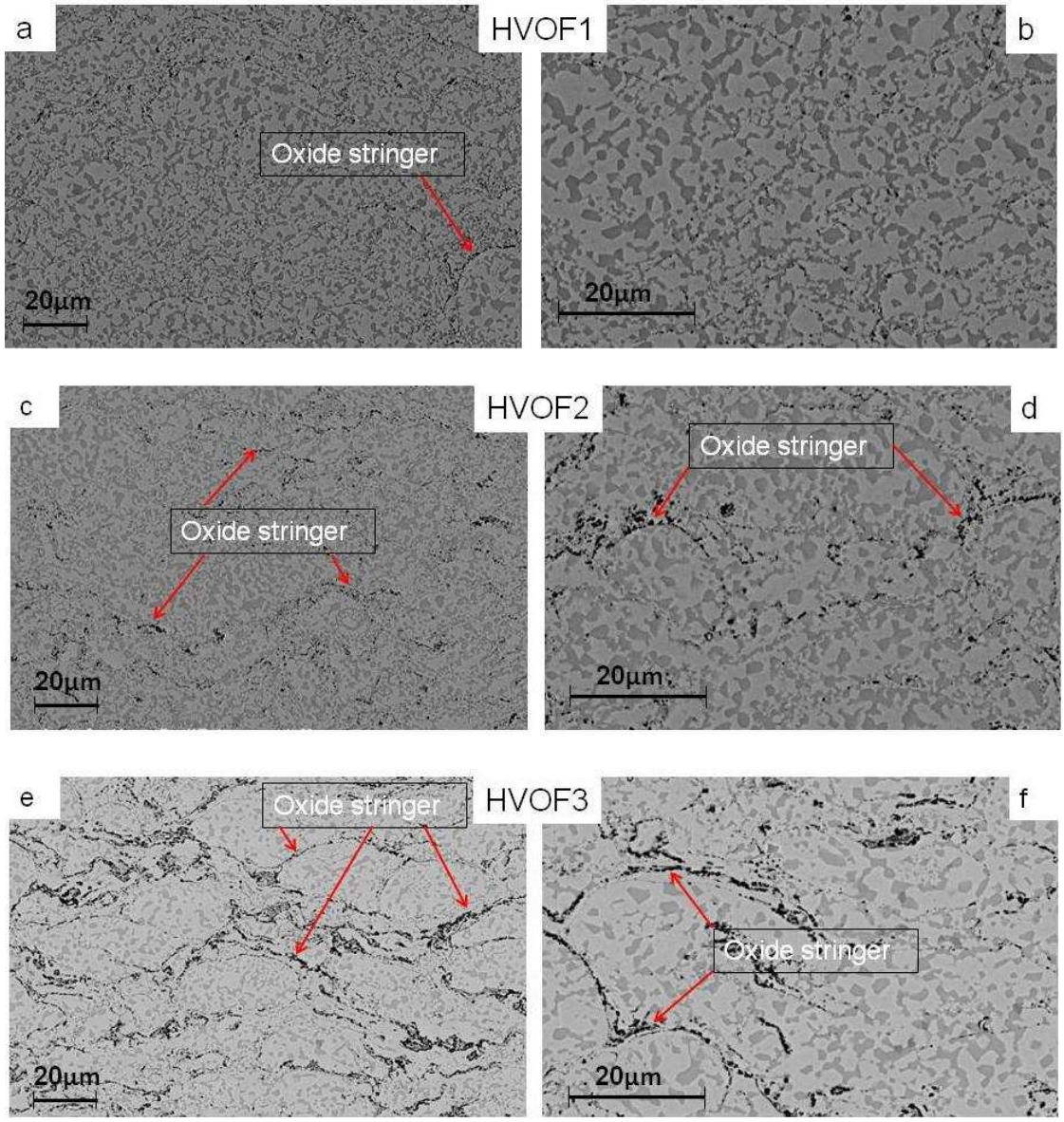

Figure 4-22. Back scattered electron SEM micrograph of HVOF1, HVOF2 & HVOF3 coatings annealed at 900°C for 90h. (b), (d) & (f) are higher magnifications of (a), (c) & (e) respectively.

Figure 4-23 shows the microstructure of HVOF1, HVOF2 and HVOF3 coatings annealed at 1000℃ and 1100℃ for 24h and 4h respectively. As seen the microstructure does not exhibit substantial differences from that observed at 900°C, Figure 4-21. Increasing the annealing temperature from 900°C to 1100°C has not resulted in a significant change in porosity level. Image analysis has been used in order to measure the porosity plus oxide content of the annealed at 1100℃ HVOF1, HVOF2 and HVOF3 coatings, see Table 4-6. Comparing these results with the results

in Table 4-4, also suggests a decrease in porosity plus oxides as a result of annealing treatment. Annealing has densified HVOF1 coating to a greater extent compared to HVOF2 and HVOF3, since there are far fewer internal oxides in HVOF1 compared to HVOF2 and HVOF3, see Figure 4-22 and Figure 4-23.

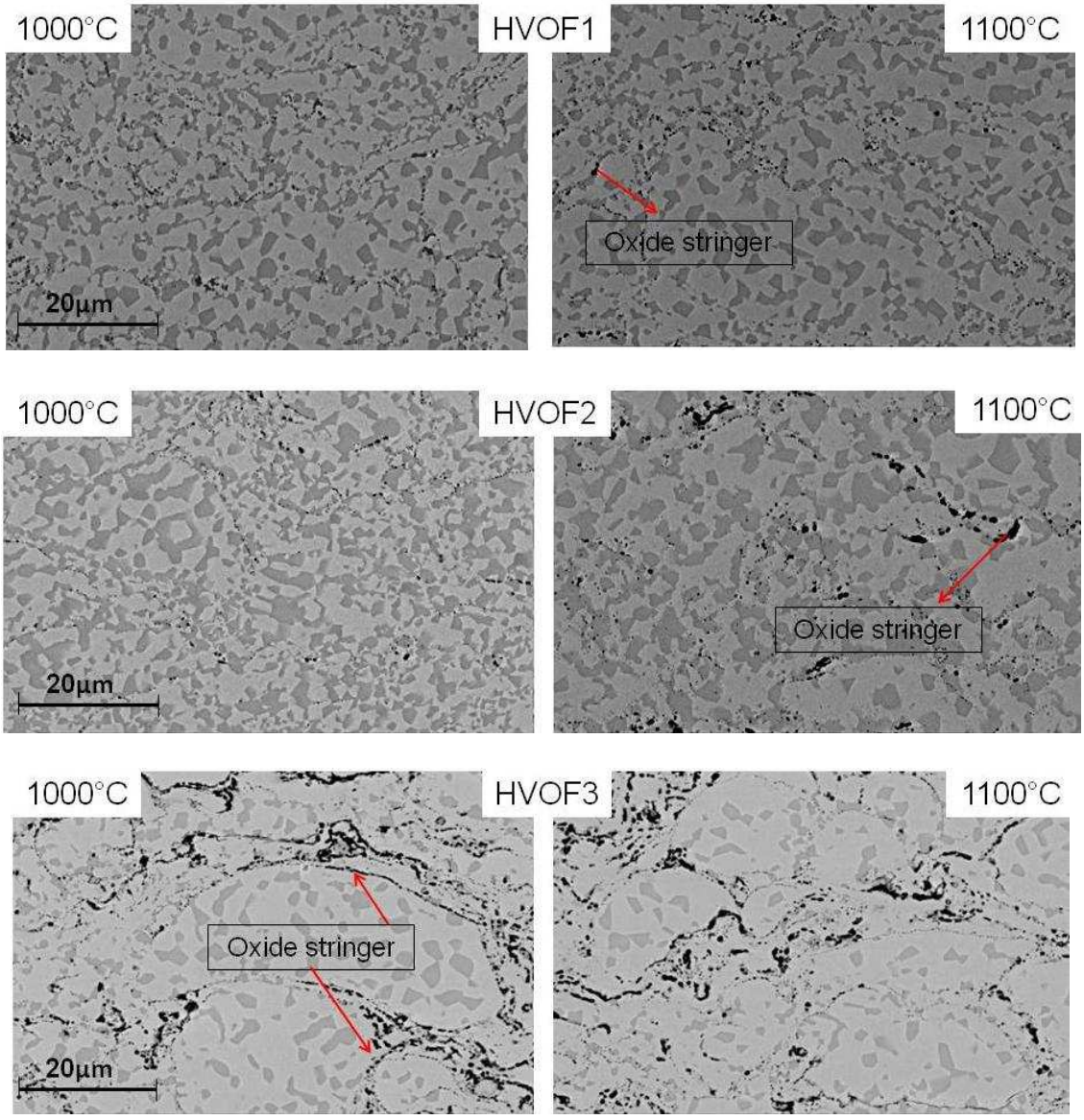

Figure 4-23. SEM micrographs of HVOF1, HVOF2 & HVOF3 coatings annealed at 1000°C & 1100°C for 24h and 4h respectively. A denser structure is seen for HVOF1 coating compared to HVOF2 & HVOF3. All images are in BSE mode and are at the same magnification.

Table 4-6. Porosity + oxide level for annealed at 1100℃ HVOF coatings. Results obtained from image analysis.

	HVOF1	HVOF2	HVOF3
Oxide + porosity (%)	2	3	5

Moreover, EDX analysis of the individual phases, γ and β, of the annealed HVOF1 at 1100℃ for 4h is illustrated in Table 4-7. Since the β phase had coarsened, due to the annealing treatment, the EDX analysis of the individual phases is more accurate.

Table 4-7. Elemental composition of γ & β phases for the HVOF1 coating annealed at 1100℃ for 4h. The values are averages of six measurements.

Element	Light phase (*γ*)		Dark phase (*β*)	
	wt%	at%	wt%	at%
Co	40	37	26	22
Ni	30	28	46	38
Cr	26	27	12	12
Al	4	8	16	28

4-1-3-2- VPS coatings

The microstructure of VPS1 coating annealed at 900°C for 90h can be observed in Figure 4-24. It is clearly seen that annealing has reduced the porosity level to a great extent. In fact, when compared with HVOF coatings, it can be seen that annealing has had a greater effect on reducing the porosity levels for VPS coating compared to HVOF, compare Figure 4-20 with Figure 4-24.

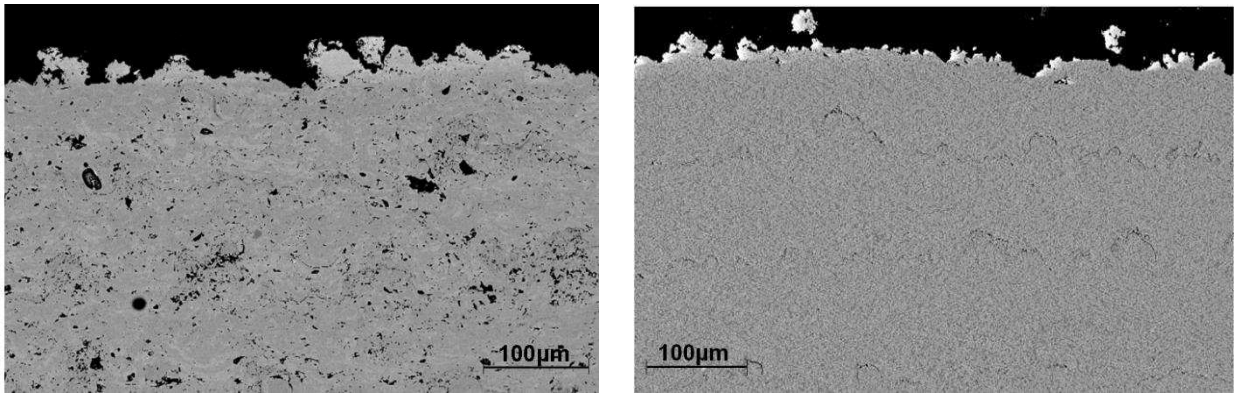

(a) (b)

Figure 4-24. SEM micrographs of (a) as-sprayed & (b) annealed at 900°C for 90h VPS1 coating. Annealing has decreases porosity levels. Both images are in BSE mode and are at the same magnification.

The microstructure of the VPS1 coating annealed at 900, 1000 and 1100°C for 90h, 24h and 4h respectively is illustrated in Figure 4-25. As seen, it can be stated that the microstructure of the annealed coatings are almost pore free. Increasing the annealing temperature from 900℃ to 1000℃ and 1100°C has not had a significant effect on changing porosity levels. Image analysis of the annealed at 1100℃ VPS1 coatings has revealed a porosity plus oxide content of ≤1%. Furthermore, compared to HVOF coatings there is not as much internal oxide in the structure of the annealed VPS coatings, compare Figure 4-25 with Figure 4-22 and Figure 4-23.

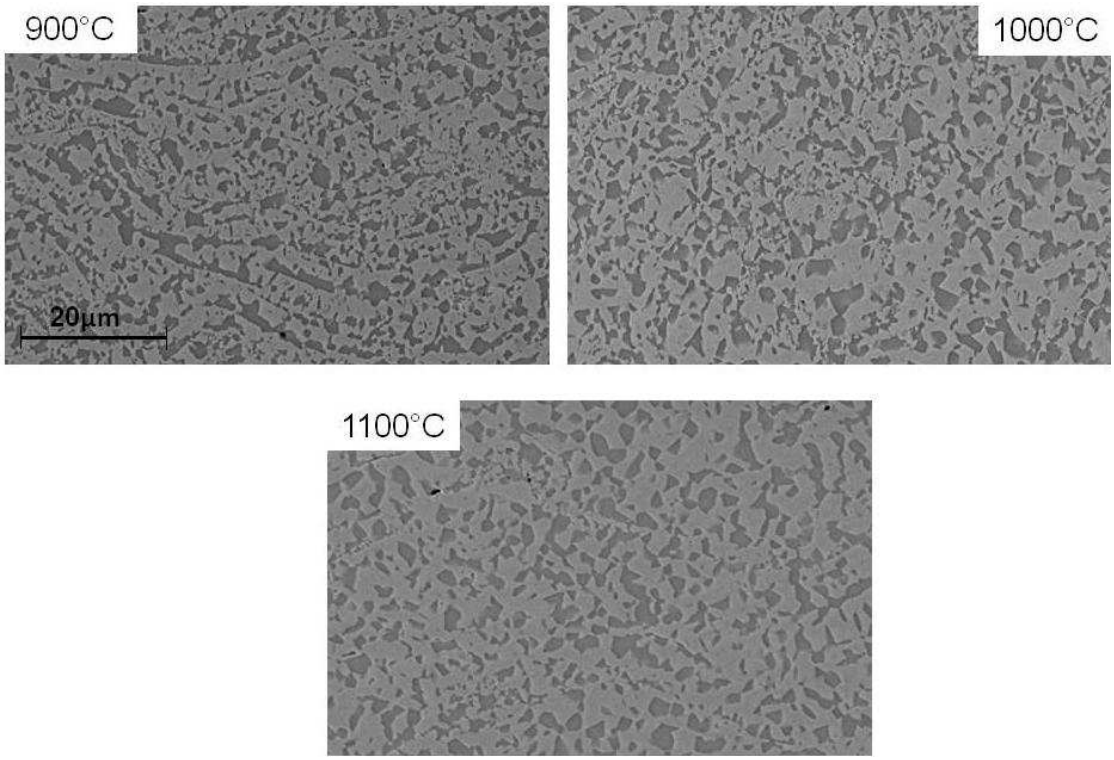

Figure 4-25. SEM micrographs of VPS1 coatings annealed at 900, 1000 & 1100°C for 90h, 24h & 4h respectively. The images show an almost pore free structure. All images are in BSE mode and are at the same magnification.

Furthermore, image analysis of the annealed HVOF and VPS coatings determined the β volume fraction of these coatings as a function of annealing temperature. The results are illustrated in Figure 4-26. As can be seen, as the annealing temperature increases the β volume fraction decreases for both HVOF and VPS coatings. Similar behaviour for γ/β volume fraction as a function of annealing temperature has been reported in [2].

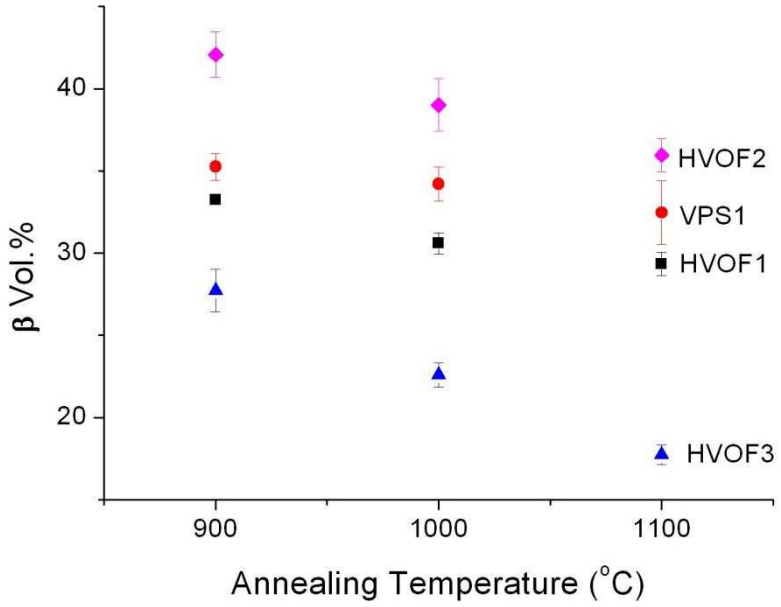

Figure 4-26. The effect of annealing temperature on the β volume fraction of HVOF and VPS coatings.

4-1-3-3- Formation of minor phases in HVOF1 & VPS1

The XRD patterns of the annealed HVOF1 and VPS1 coatings are illustrated in Figure 4-27. A clear β peak can be seen for the VPS annealed coatings, compare with Figure 4-14, suggesting the formation and presence of the β phase in the annealed VPS coatings. A lattice parameter close to 0.357nm and 0.286nm was measured for the γ and β phases of HVOF1 coating annealed at 1100℃ respectively. Compared to as-sprayed coating a slight decrease in γ lattice parameter can be observed as the result of annealing treatment.

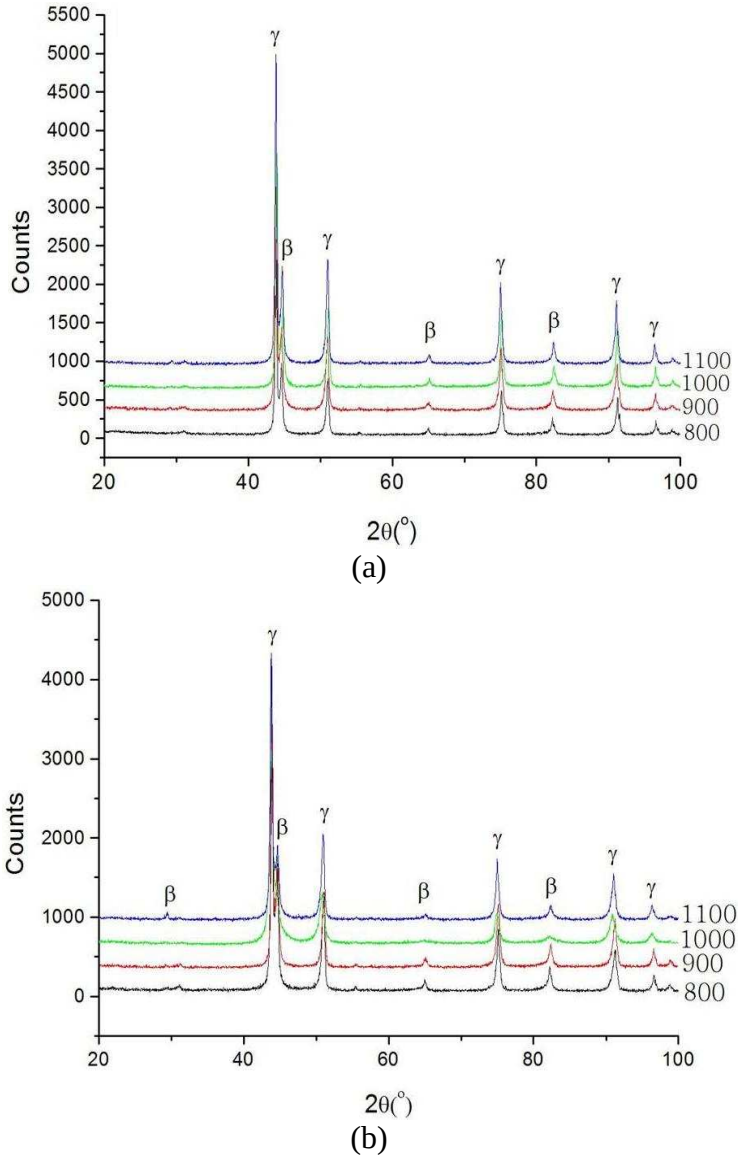

Figure 4-27. XRD patterns of (a) HVOF1 & (b) VPS1 coatings annealed at different temperatures for different times (the figure to the right of each pattern is the annealing temperature).

Figure 4-28 illustrates the microstructure of HVOF1 and VPS1 coatings annealed at 800°C for 840h. As suggested by XRD, the β-(Co,Ni)Al phase can be seen in the annealed VPS1 coating, compared with Figure 4-16 and Figure 4-17. Furthermore, when looked at in more detail, areas with slightly higher contrast and larger in size, compared to β precipitates, could be observed in both HVOF and VPS coatings, (Figure 4-28). EDX analysis of these areas revealed very high Cr contents. Elemental mapping (Figure 4-29) of these areas was also carried out, and this also confirmed the

presence of a Cr rich phase. Since the amount of Cr present in this phase was much higher than Co, a possible identity of this phase is α-Cr. However, this phase was not seen in high quantities (1-2%) and was not distributed evenly throughout the coating and thus no corresponding peaks were seen in XRD patterns, see Figure 4-27.

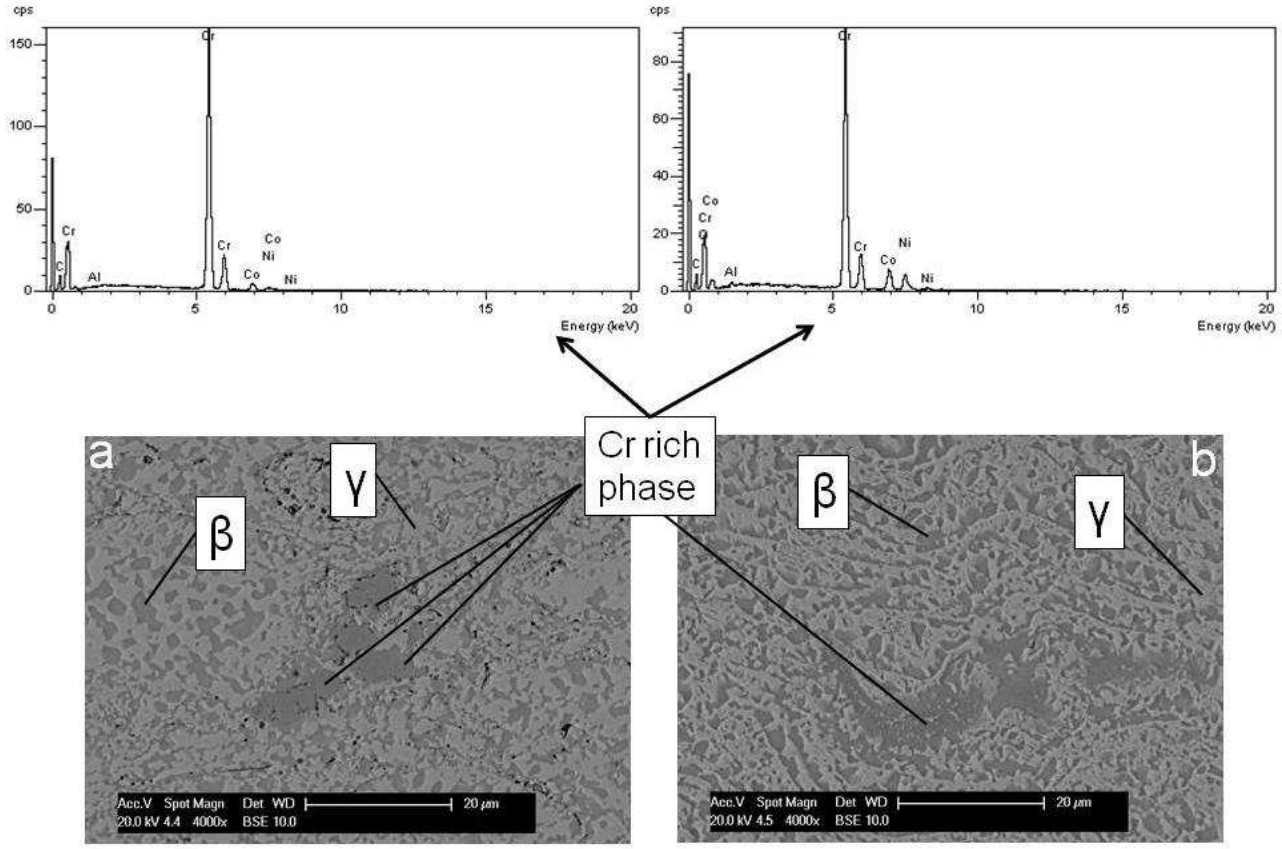

Figure 4-28. SEM micrographs of (a) HVOF1, (b) VPS1 coatings annealed at 800°C for 840h. The images show a three phase structure for both coatings.

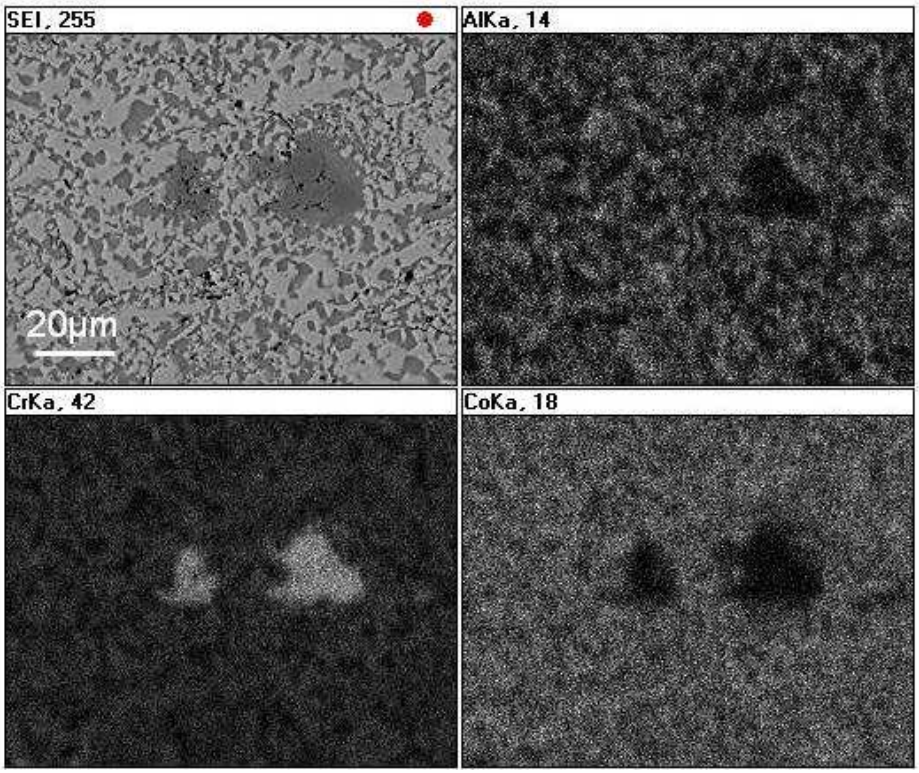

(a)

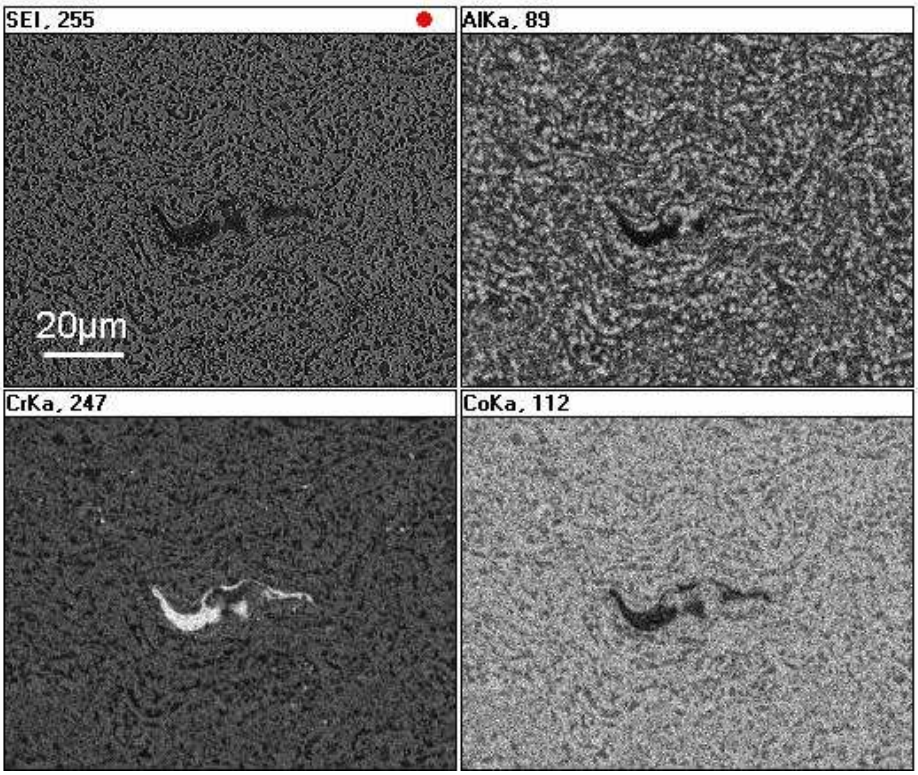

(b)

Figure 4-29. EDS elemental mapping of the Cr rich phase in annealed at 800 ℃ (a) HVOF1 & (b) VPS1 coatings.

The microstructure of the specimens annealed at 900°C and 1000°C for 90h and 24h respectively, can be seen in Figure 4-30. As seen the microstructure does not exhibit substantial differences from that observed at 800°C, Figure 4-28. The γ, β-(Co,Ni)Al and Cr rich phase were present in both HVOF and VPS coatings annealed at 900°C and 1000°C.

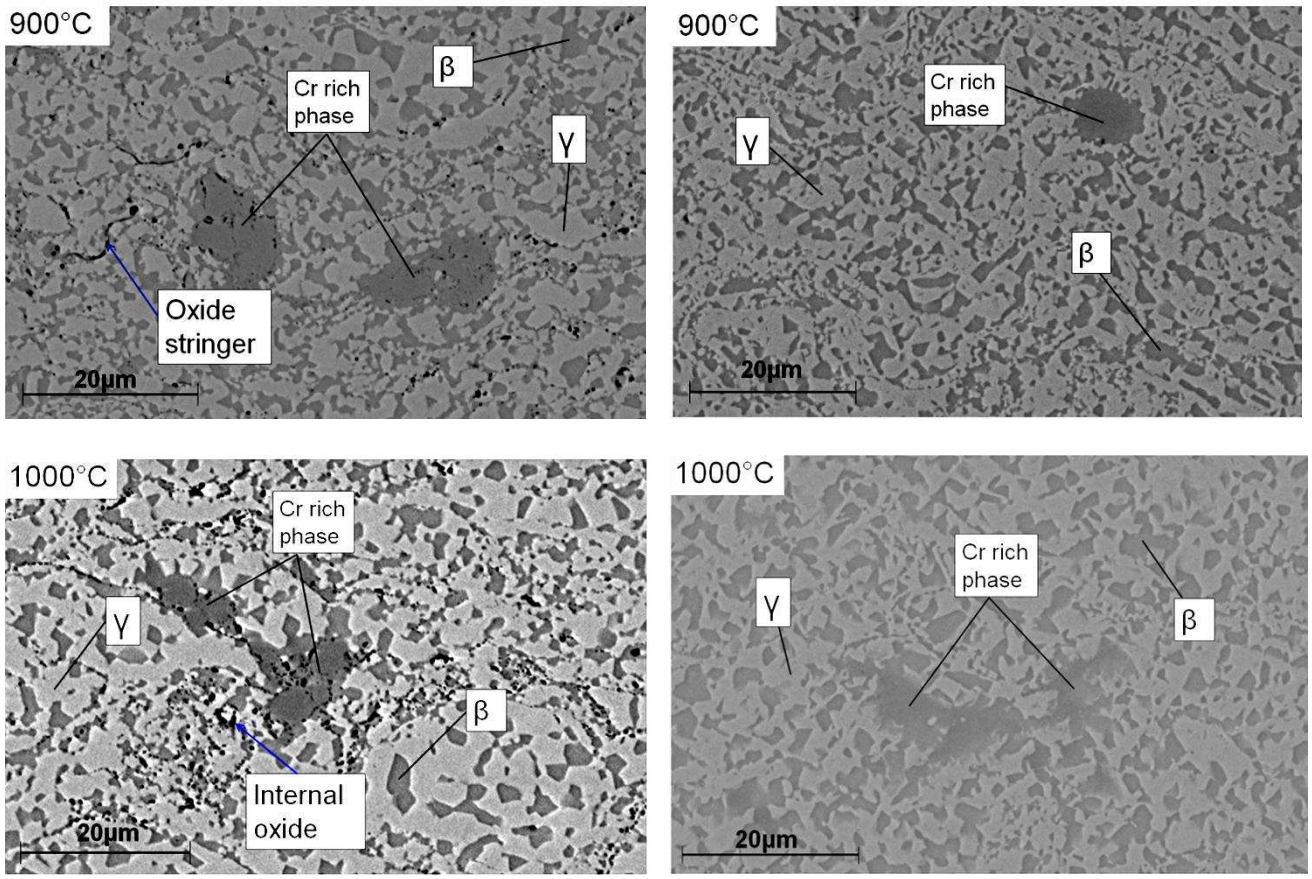

(a) (b)

Figure 4-30. SEM cross sections of (a) HVOF & (b) VPS specimens annealed at 900°C and 1000°C for 90h and 24h respectively. All images are in BSE mode and are at the same magnification.

A STEM elemental mapping was carried out for a region where the Cr rich phase was present in the HVOF1 annealed at 900℃ coating. Figure 4-31 illustrates the thin membrane (prepared using the FIB-SEM lift out) used to obtain the low magnification STEM element map seen in Figure 4-32. This membrane was cut from the region

where the Cr rich phase was observed with a β phase grain neighbour. Figure 4-33 illustrates a higher magnification of Figure 4-32. However, it should be noted that the images in Figure 4-33 are slightly to the right of the images in Figure 4-32 and that the line visible in the middle of the β grain in the dark field STEM image, Figure 4-33, is caused as the result of further milling of the selected area, i.e. the region to the left of the line is thinner than that to the right. From these images it is clear that the Cr rich phase is essentially Cr with negligible amount of other elements such as Al, Ni or Co. The composition of the Cr rich phase and the β phase can be seen in Table 4-8, data obtained from STEM analysis. The Cr rich phase therefore is assumed to be α-Cr.

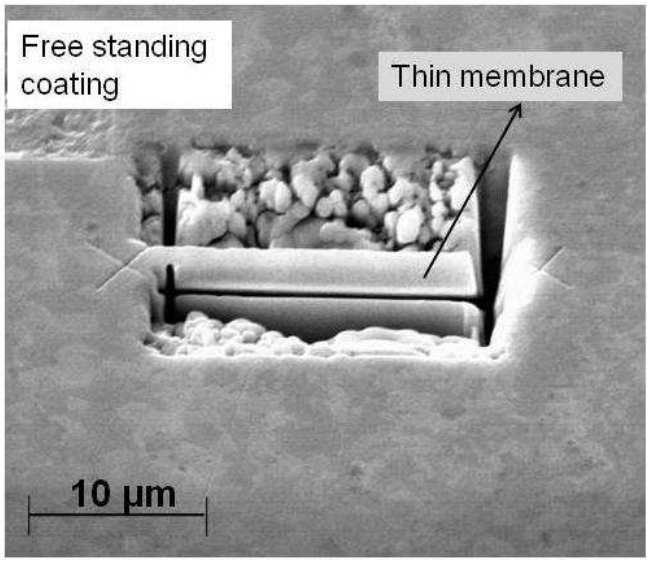

Figure 4-31. SEM micrograph presenting the thin membrane to be used as the STEM sample.

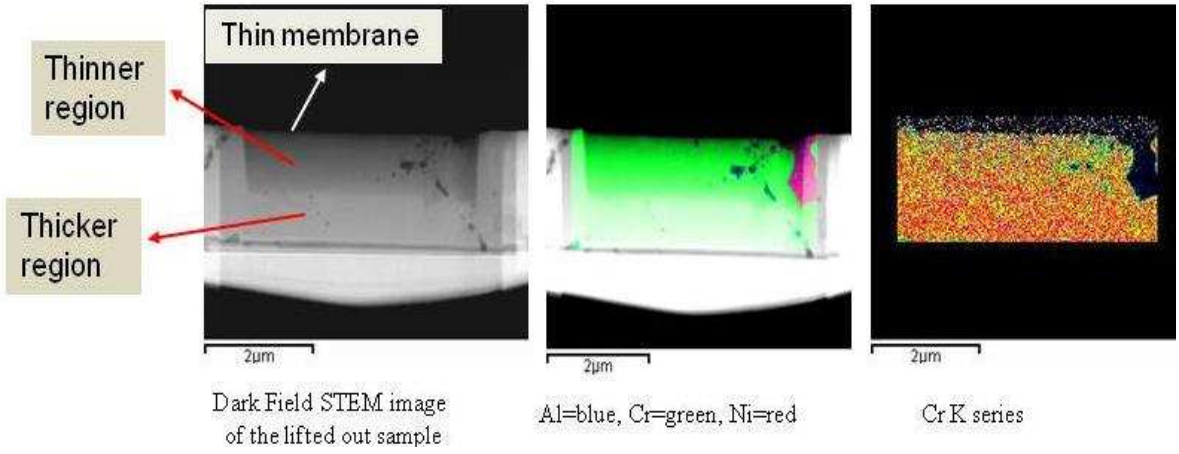

Figure 4-32. Low magnification, low resolution, STEM elemental mapping of HVOF1 coating annealed at 900℃ for 90h, illustrating the Cr rich & β phases. The darker region in the dark field mode is the region with less electron-sample interaction, i.e. thinner region.

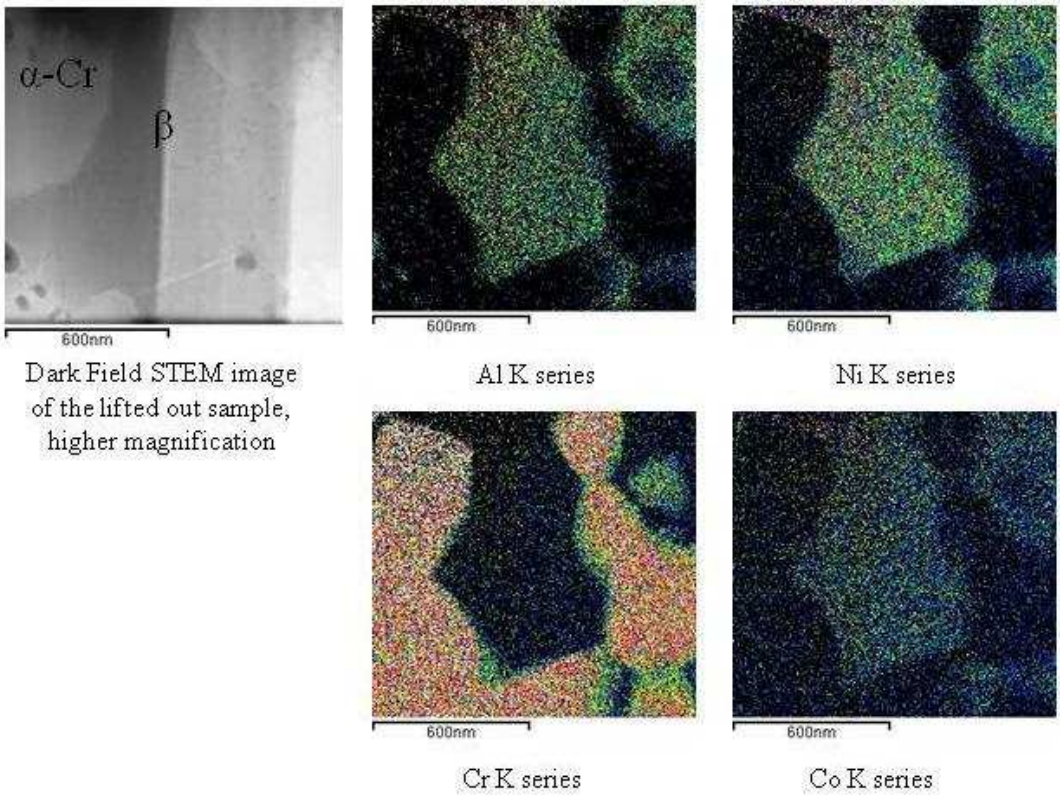

Figure 4-33. High magnification, higher resolution, STEM elemental mapping of the HVOF1 coating annealed at 900℃ for 90h.

Table 4-8. The composition of β-(Ni,Co)Al and Cr rich phase of HVOF1 coating annealed at 900°C. Results from STEM analysis.

Elements	Cr rich (wt%)	β (wt%)
Al	2	29
Cr	86	8
Co	7	20
Ni	4	42

The microstructure of the coatings annealed at 1100°C for 4hrs are presented in Figure 4-34. At this temperature there were no signs of the Cr rich phase in either of the coatings indicating that the α-Cr phase is not stable at this temperature. SEM and XRD analyses indicate that the only phases present at this temperature are γ, β and some oxides.

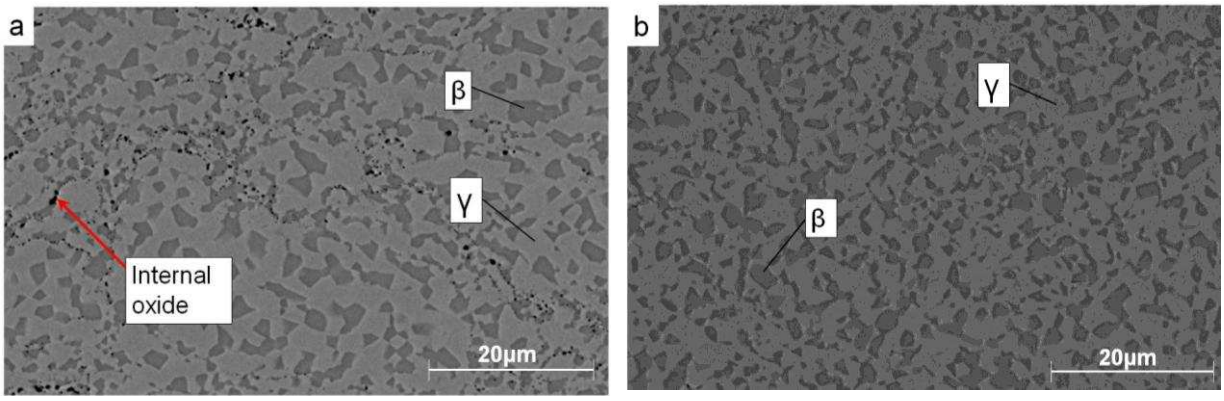

Figure 4-34. Back scattered electron SEM micrographs of (a) HVOF1 & (b) VPS1 coatings annealed at 1100°C. Both images are at the same magnification.

4-2- Mechanical properties

This section describes the experimental results on hardness and Young's modulus of HVOF and VPS coatings. Young's modulus was measured over a range of temperatures and both hardness and Young's modulus were measured for coatings subjected to different annealing temperatures. The Eshelby inclusion model is used to predict the effect of some microstructural variables on Young's modulus.

4-2-1- Hardness

Vickers hardness was measured on cross-sections of as-sprayed and annealed HVOF1, HVOF2, HVOF3 and VPS1 coatings. Figure 4-35 illustrates the hardness results as a function of annealing temperature. Annealing temperatures varied and are given in section 3-3-2 of chapter 3.

The hardness of both HVOF and VPS coatings drops after annealing and as the annealing temperature increases the hardness decreases. However, there seems to be relatively little change with annealing temperature, i.e. a large drop in hardness from as-sprayed to annealed at 800℃ and very little change thereafter. Nevertheless, a slight increase in hardness can be observed when moving from samples annealed at 1000℃ to those annealed at 1100℃ for HVOF1, HVOF2 and VPS1 coatings.

There is not a significant difference between the hardness of as-sprayed HVOF1, HVOF2 and VPS1 coatings. However, there seems to be a large difference in the hardness of HVOF3 compared to the other coatings. Also the hardness values of VPS1 coatings are always lower than HVOF1 and HVOF2 coatings with higher difference for annealed samples, whereas the hardness values of HVOF1 and HVOF2 coatings are very similar throughout the annealing temperature range.

Vickers hardness of other relevant materials (from literature) as a function of annealing temperature is given in Table 4-9. This is for comparison of the results obtained in this work with the results from similar materials obtained by other researchers [3-5].

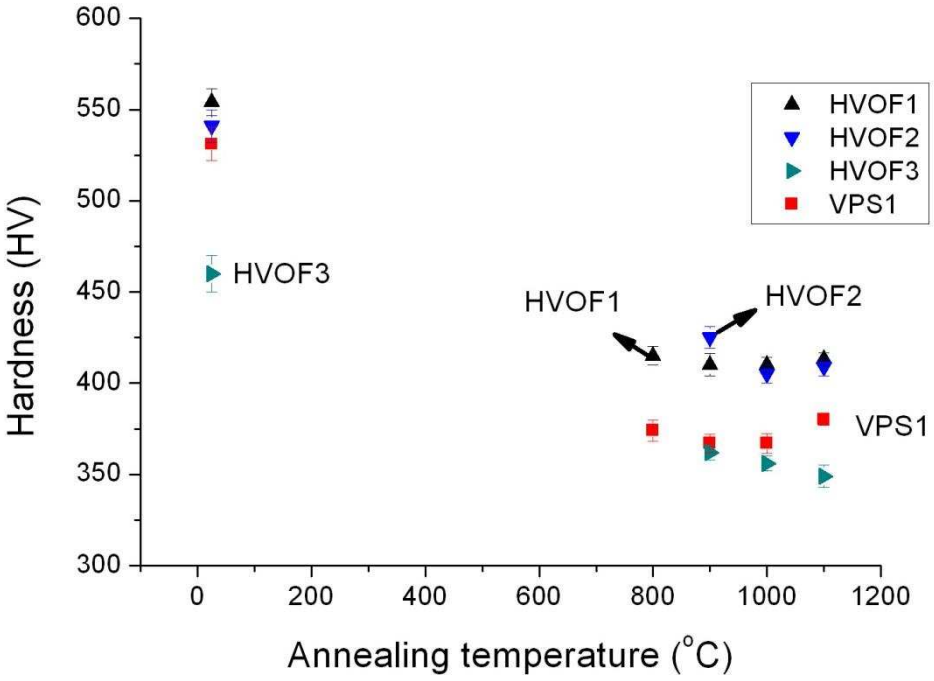

Figure 4-35. Vickers hardness for HVOF & VPS coatings as a function of annealing temperatures.

Table 4-9. Vickers hardness of single γ and β phases, results from nano-indentation, and hardness of different materials [3-5].

Material	Hardness (HV)	Comment	Microstructure
Alloy 625	213±38	As-rolled	γ
Alloy 625	118±43	Annealed	γ
Alloy 718	349	Bar	Not specified
Ni23Co17Cr12AlY	500	VPS sprayed	γ+β
Ni22Co17Cr12AlY	387	VPS sprayed than annealed	γ+β
Ni22Co17Cr12AlY	438	HVOF sprayed	γ+β
Ni22Co17Cr12AlY	475	HVOF sprayed than annealed	γ+β
Co32Ni21Cr9AlY	155±18	Plasma sprayed	Not specified
Co32Ni21Cr9AlY	418±31	HVOF sprayed	Not specified
Co32Ni21Cr8AlY	450	VPS sprayed	γ+β
*Co32.5Ni21Cr8AlY, γ phase	590±13	HVOF sprayed than vacuum annealed at 1100℃	γ+β
*Co32.5Ni21Cr8AlY, β phase	724±30	HVOF sprayed than vacuum annealed at 1100℃	γ+β
*Co32.5Ni21Cr8AlY, γ phase	552±17	VPS sprayed than vacuum annealed at 1100℃	γ+β
*Co32.5Ni21Cr8AlY, β phase	611±15	VPS sprayed than vacuum annealed at 1100℃	γ+β

* Results obtained as part of this thesis by nano-indentation.

4-2-2- Young's modulus

As detailed in chapter 3, section 3-4-6, a DMA machine was used in order to carry out a 3-point bend test on HVOF and VPS samples to determine the Young's modulus of the free standing coatings.

4-2-2-1- HVOF coatings

The Young's modulus of as-sprayed and annealed HVOF coatings was determined as a function of measurement temperature and annealing temperature. Figure 4-36 illustrates the Young's modulus of the HVOF1 coating. The measuring temperature and the annealing temperature both affect the Young's modulus. As the annealing temperature increases the modulus also increases, while as the measurement temperature increases the modulus decreases. However, when looked at in more detail, the modulus is approximately constant up to 200℃ then decreases with further increase in measuring temperature. All annealed coatings are stiffer than as-sprayed coatings.

It should be noted that for each new test at any one temperature a sample from a previous test at that temperature was tested again, in order to check for any machine artefact. For example before an annealed HVOF2 coating was tested at 100℃, the equivalent HVOF1 coating was tested at 100℃ to see if a similar result is obtained.

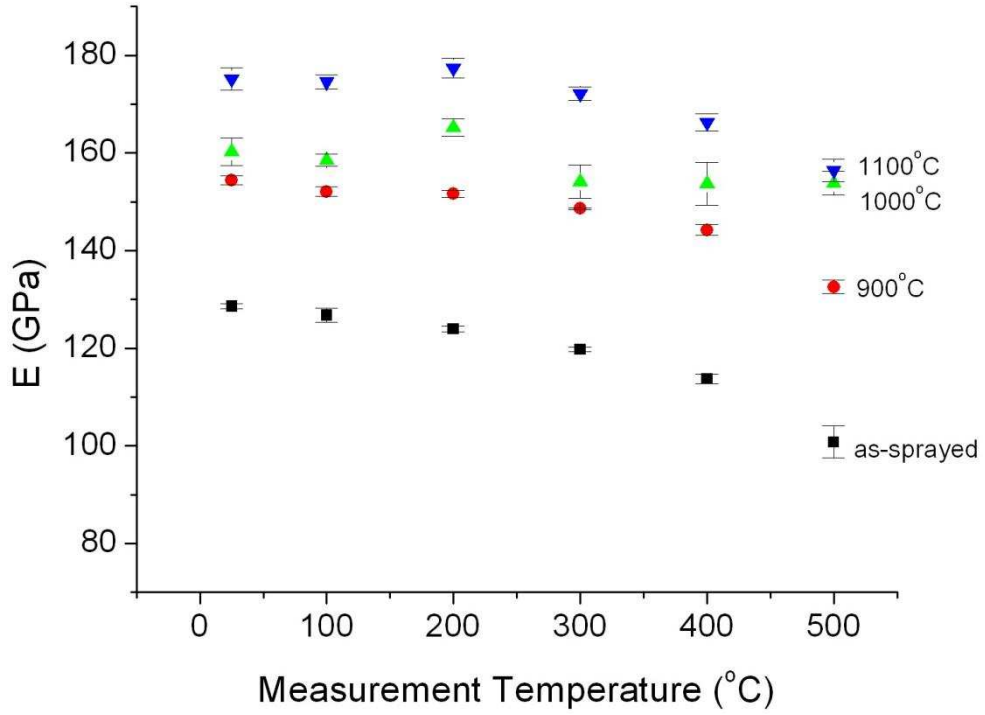

Figure 4-36. Young's modulus results from DMA testing as a function of measuring and annealing temperature for HVOF1 coatings. The temperatures to the right of the graph are annealing temperatures.

Similar trends have been observed for HVOF2 and HVOF3 coatings, illustrated in Figure 4-37 and Figure 4-38 respectively. As the annealing temperature increases the modulus also increases and as the measuring temperature increases the modulus decreases. Comparing the moduli of all three HVOF coatings, the absolute values for HVOF1 are greater than HVOF2 and HVOF3 coatings, and the HVOF2 coating has the smallest Young's modulus of them all. Also, it can be observed that the progressive increase in modulus as the annealing temperature increases makes smaller changes from 900℃ onwards for HVOF2 and HVOF3 compared to HVOF1 coatings, see Figure 4-36, Figure 4-37 and Figure 4-38.

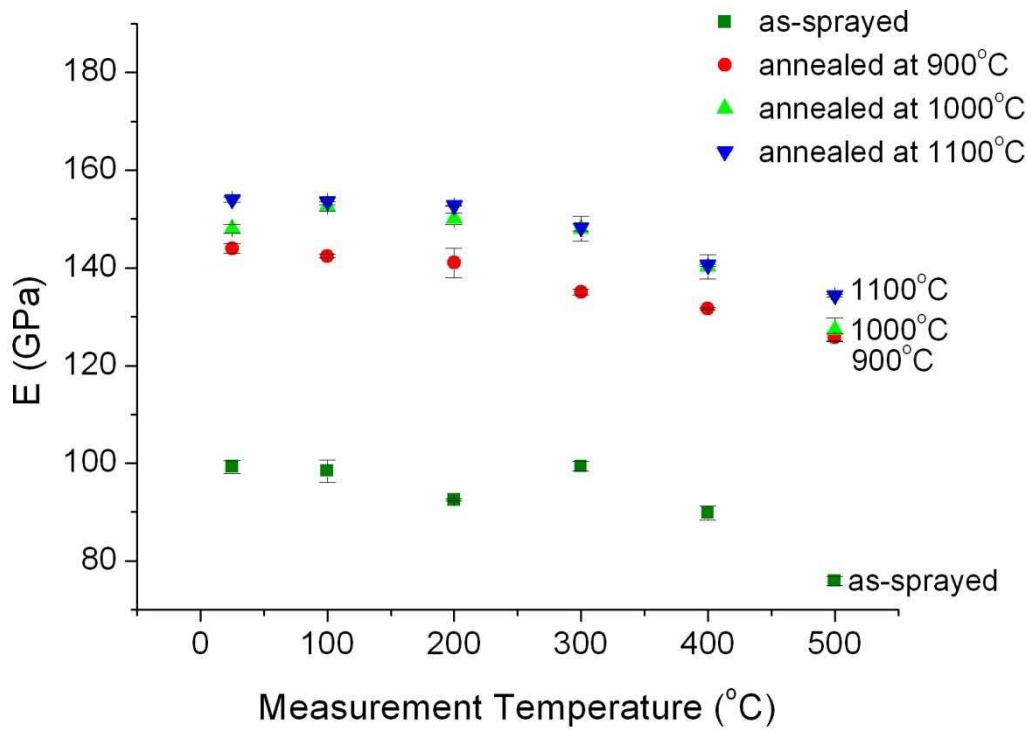

Figure 4-37. Young's modulus as a function of measuring temperature and annealing temperature for HVOF2 coating.

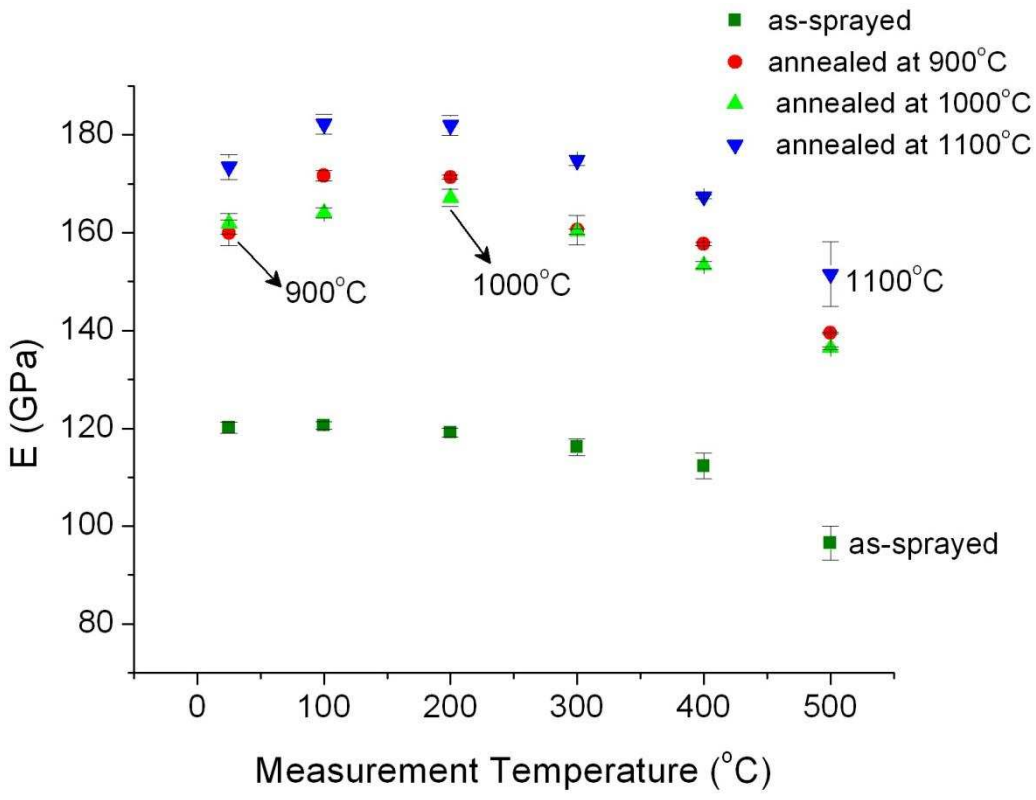

Figure 4-38.Young's modulus as a function of measuring and annealing temperature for HVOF3 coating.

4-2-2-2- VPS coating

The Young's modulus of the as-sprayed and annealed VPS1 samples was also measured as a function of measuring and annealing temperatures, using the DMA 3-point bending technique, Figure 4-39 illustrates the results. Similar trends to that of the HVOF coatings are observed for the VPS coating: as the annealing temperature increases the modulus of the coating increases while as the measuring temperature increases the modulus decreases.

When comparing the Young's modulus results of VPS1 coating with the results of HVOF1 coating (compare Figure 4-36 with Figure 4-39) it can be seen that while at lower annealing temperature the modulus of HVOF1 coating is slightly greater than that of VPS1 coating; as the annealing temperature increases the difference between the modulus of the two types of sprayed coating decreases.

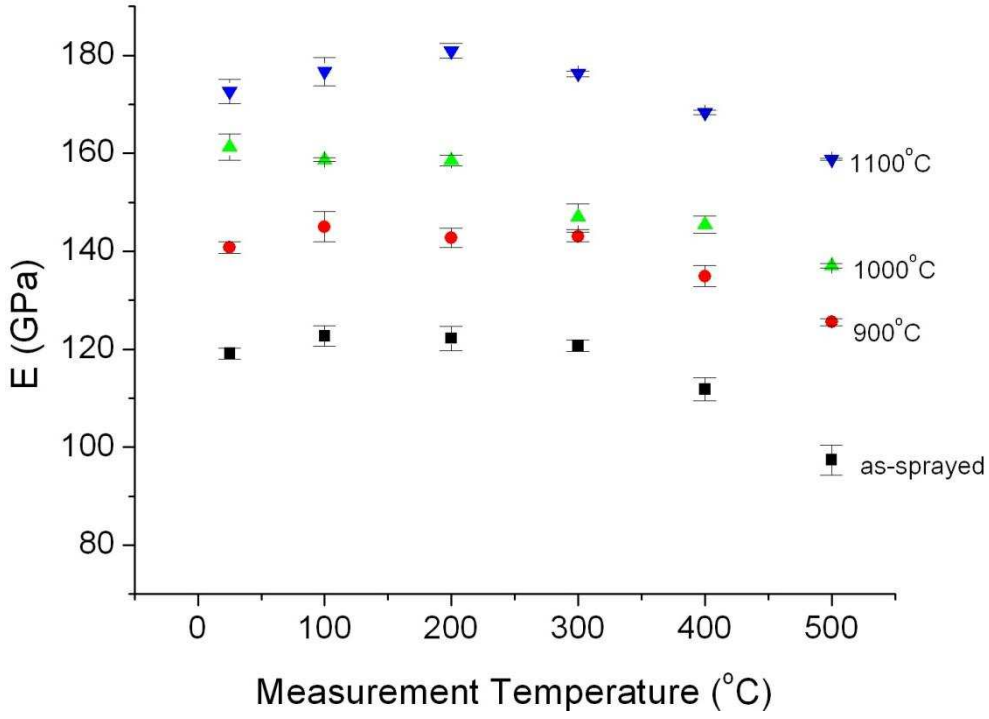

Figure 4-39. Young's modulus of VPS1 coating as a function of measuring and annealing temperature. The temperatures to the right of the graph are annealing temperatures.

4-2-2-3- Nano-indentation

Nano-indentation was carried out on HVOF1 and VPS1 as-sprayed and annealed samples in order to compare the hardness results with the results obtained from micro hardness. Figure 4-40 illustrates the comparison of the hardness determined from nano-indentation and Vickers micro hardness for both spraying methods. For both coatings the hardness values obtained from nano-indentation are higher than those obtained from microhardness.

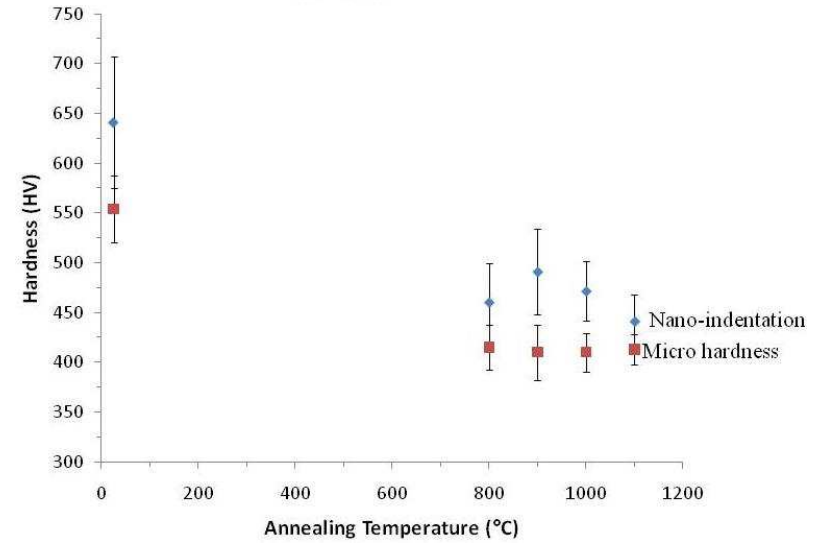

(a)

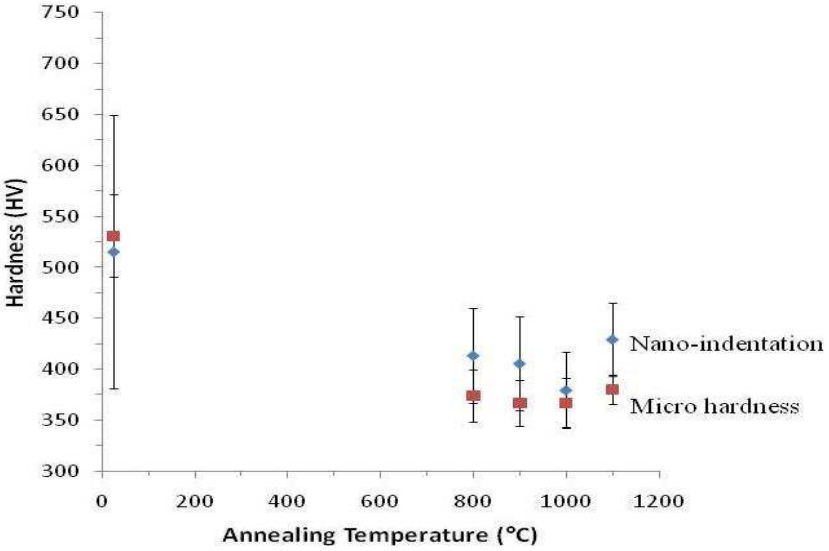

(b)

Figure 4-40. Hardness comparison between nano-indentation and conventional Vickers hardness, (a) HVOF & (b) VPS coatings

Furthermore, nano-indentation was carried out on HVOF1 and VPS1 samples annealed at 1100℃ using 10×10 indentation grid to determine modulus values. This is illustrated in the SEM micrograph of Figure 4-41. A cumulative distribution plot of all the indents carried out in both coatings is illustrated in Figure 4-42. The mean value, extracted from the plot, for the Young's modulus of the HVOF coating is 211GPa and for the VPS coating is 201GPa. The median number for the HVOF coatings is 208GPa and for VPS coating is 196GPa.

Looking at the 10×10 grid it is seen that while some of the indentations fall into a single phase, i.e. γ or β, others fall on or very near to a γ/β boundary. For HVOF coating approximately 8 indents fall onto the β phase and 15 indents fall onto the γ phase; whereas for the VPS coating 10 and 11 indents fall onto β and γ phases respectively. The Young's modulus values for the indents falling in the γ phase varied between 200-260 GPa and 177-263GPa for annealed at 1100℃ HVOF1 and VPS1 coatings respectively and the Young's modulus values for the indents falling in the β phase varied between 147-203 GPa for annealed at 1100℃ HVOF1 and 165-213GPa for annealed at 1100℃ VPS1 coatings. An average of the values where the indentations have fallen on a single γ or β phase was taken and the values are illustrated in Table 4-10. Considering the Young's modulus range for each of the phases (γ and β), there is no significant difference between the results from nano-indents on the HVOF and VPS coatings.

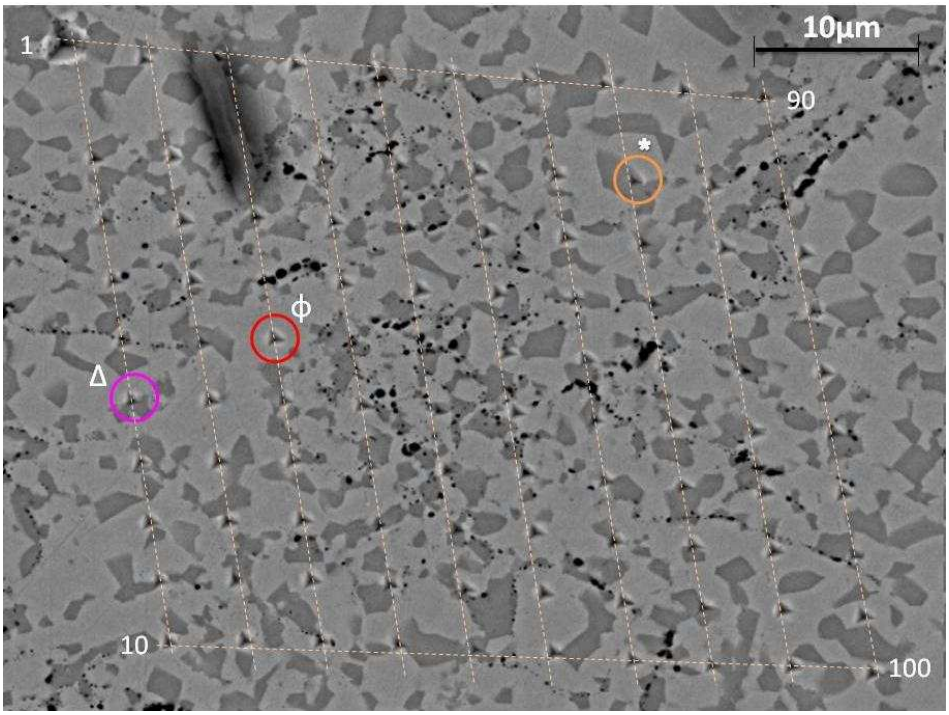

(a)

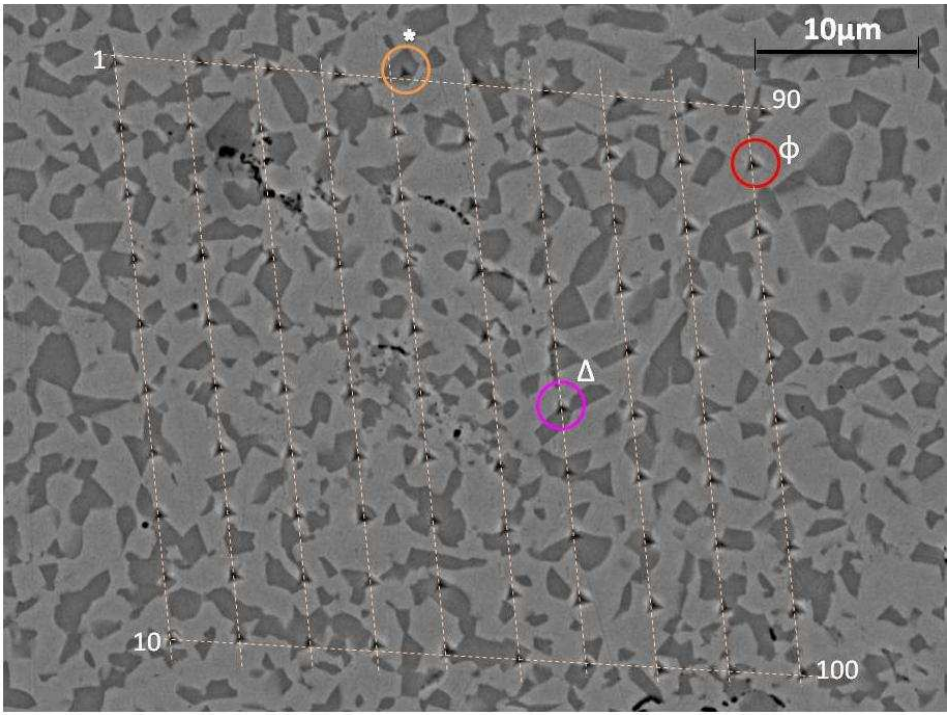

(b)

Figure 4-41. SEM micrograph illustrating the 10×10 indentation grid carried out using the nano-indentation, (a) 1100°C annealed HVOF1 sample, (b) 1100°C annealed VPS1 sample. The circle with the * symbol shows an indentation in a single β phase, ϕ symbol shows an indentation in a γ single phase and the circle with the Δ symbol shows an indentation in the γ/β boundary. Images are in BSE mode.

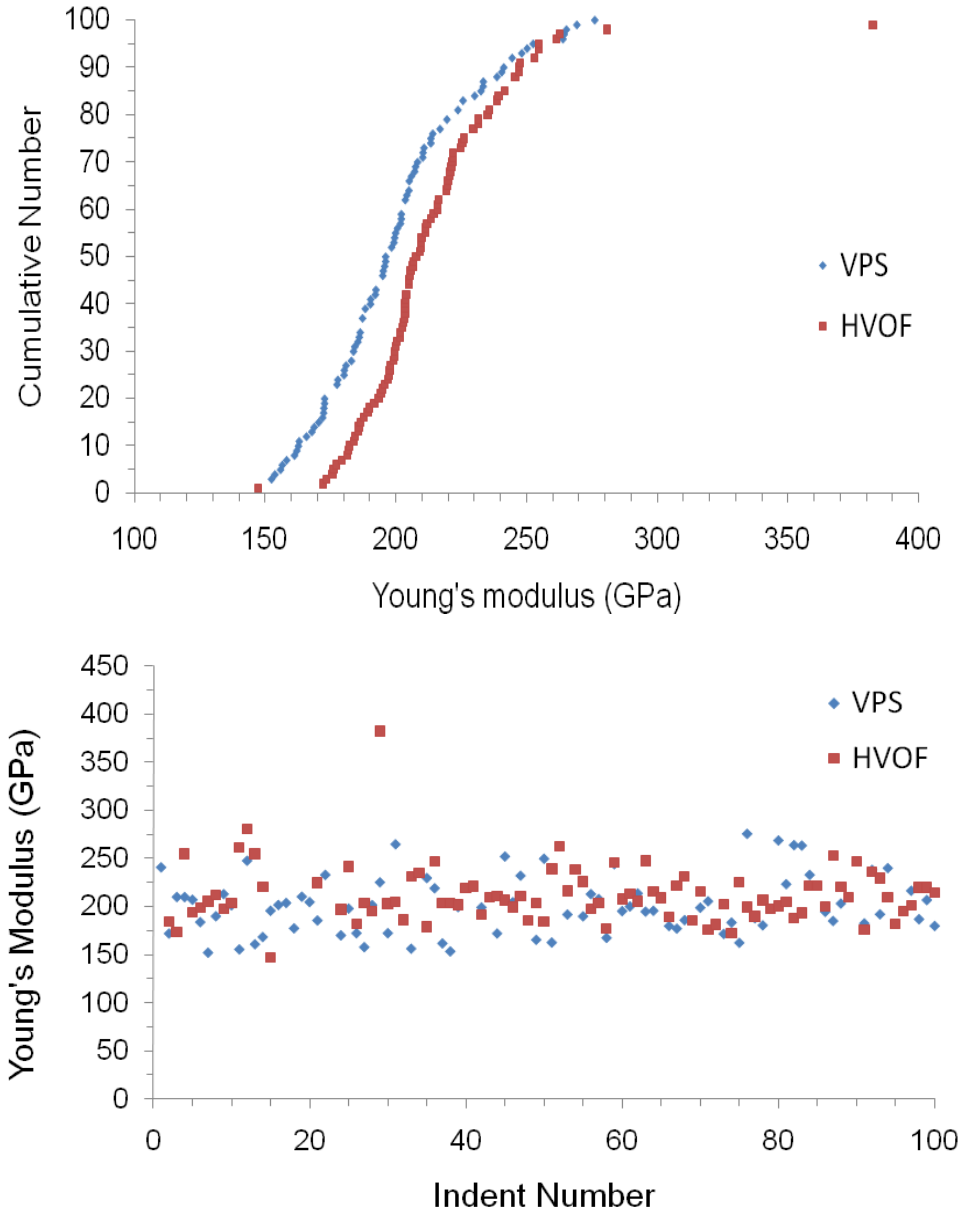

Figure 4-42. Cumulative distribution of the nano-indents carried out in HVOF1 and VPS1 coatings annealed at 1100℃.

Table 4-10. Young's modulus values for single γ & β phases. Results obtained from nano-indentation.

	E_γ (GPa)	E_β (GPa)
HVOF	231	181
VPS	213	182

4-3- Discussion

4-3-1- Microstructural characterisation

The SEM micrographs (Figure 4-4) revealed a dendritic structure for the spherical MCrAlY powder particles. Because the powder had been produced by the atomisation method and had gone through a fast cooling, a dendritic microstructure results. Furthermore, due to the fast cooling of the molten droplets the γ/β microstructure of the powder is very fine and homogeneous. This can be seen in Figure 4-5 where a distinct γ/β microstructure can be observed at a high magnification. It should be noted that the molten droplets in the atomisation method lose heat through convection and radiation and cooling rates of 5×10^{4} - $5\times10^{5}Ks^{-1}$ have been reported for gas atomised Co base superalloy powders of 20 to 50μm diameter [6].

The as-sprayed HVOF coatings had a two phase (γ+β) microstructure whereas the as-sprayed VPS coating essentially had a single phase γ structure since only the few un-melted powder particles had retained their dual microstructure. Shibata et al. [7] have also reported similar microstructures for HVOF and LPPS CoNiCrAlY coatings. The difference in the microstructure of HVOF and VPS is due to the different temperatures experienced by the powder in each spraying process. Powder particles are exposed to a flame temperature of ~2700-3200K for a relatively short time in the HVOF process. This results in incomplete melting of the feedstock powder, and thus the dual γ/β microstructure of the powder is retained. In VPS coatings, on the other hand, due to the high temperature of the plasma flame (>10000K) [3] and lower particle velocity, the feedstock powder is exposed to a higher temperature for a longer time. This results in complete melting of almost all powder particles. These molten particles will rapidly solidify on impact, not giving enough time for the β-(Co,Ni)Al

phase to precipitate out, resulting in the formation of a single γ phase. Solidification rates of up to $2\times10^{8}Ks^{-1}$ for plasma sprayed Nb particles on steel substrates have been reported [8, 9]. Cooling rates for solidification of plasma sprayed particles are higher than the highest of those encountered in gas atomisation ($5\times10^{5}Ks^{-1}$). The main reason for this phenomenon could be related to the fact that in the solidification of the plasma sprayed powder particles, in addition to convection and radiation, conduction has a major role in the heat loss process (contact of the hot particles with a cold substrate).

Since the highest flame temperature is achieved at 100% stoichiometry conditions and that HVOF1 and HVOF2 were carried out at 98% stoichiometry conditions, in order to obtain a higher degree of melting for HVOF3, an Amdry 9951 powder with smaller particle size but similar composition to the powder used in HVOF1 and HVOF2 was used. As a result of the smaller powder size, higher degree of melting was obtained. This resulted in the HVOF3 coating having the highest degree of melting among all other HVOF coatings, see Figure 4-13.

Annealing resulted in a reduction of porosity levels in both VPS and HVOF coatings. This reduction is due to diffusion occurring during annealing which heals some of the porosity via a sintering effect. However, annealing has a greater effect in reducing the porosity level for VPS coating compared to HVOF, see Figure 4-20 and Figure 4-24. It is generally accepted that VPS coatings are essentially oxide free [10], due to the process being carried out under vacuum, see Figure 4-19. In HVOF coatings on the other hand, a thin oxide layer is generated around each particle during spraying, see Figure 4-11. These oxides appear as oxide stringers in cross sections. These oxide stringers are not affected by annealing and hence are retained in the annealed HVOF coating. It is suggested that they act as obstacles to diffusion [11, 12], inhibiting the

porosity healing process (see Figure 4-22 and Figure 4-23). The above discussion also explains why the porosity plus oxide level had decreased from ~5% for as-sprayed VPS coating to less than 1% for annealed VPS coating. A similar effect and explanation has been previously reported [13].

Annealing had also coarsened the β-(Co,Ni)Al phase in the HVOF coating (compare Figure 4-13 with Figure 4-21). After annealing the formation of the β phase in the VPS coatings was also observed. The lack of time for the precipitation of β-(Co,Ni)Al phase, during spraying, due to the rapid solidification of the molten powder had caused the absence of the β phase in the as-sprayed VPS coating. However, since the coating had been held at 800°C for a long enough time to allow diffusion, the excess Al in the γ phase caused the nucleation and growth of the β phase and the system reached its equilibrium state.

Figure 4-26 illustrates the effect of annealing temperature on the β volume fraction of different coatings. It is clear from the image that as annealing temperature increases the β volume fraction decreases. A similar behaviour for β volume fraction as a function of annealing temperature has been reported elsewhere [14]. The reason for HVOF1 to have a lower β volume fraction compared to HVOF2 is suggested to be due to higher aluminium loss in HVOF1 coating, during spraying, compared to HVOF2. The HVOF2 coating has higher number of un-melted particles, indicating lower particle temperature which would be consistent with less extensive oxidation during deposition. Further reasons could be due to microstructural differences not visible in the SEM micrographs. As coatings obtained from a smaller powder particles tend to have higher oxide contents [15], the HVOF3 coating which has been sprayed using Amdry 9951 powder (smaller in size compared to CO-210-24 powder) is

expected to have the highest oxide content and hence higher loss of Al. This leads to the observed lower β volume fraction for this coating as compared to the other HVOF coatings. Furthermore, Thermo-Calc analysis for the CoNiCrAl alloy (Y is not available in the Ni database, TTNi7) is illustrated in Figure 4-43. Comparison of Figure 4-43 and Figure 4-44 (which is plotted as a result of converting the β volume fraction measured using image analysis to β wt.%) illustrates a similar behaviour for reduction in β phase as a function of annealing temperature. Furthermore, a good agreement is seen in the absolute values of the β wt.% measured for the HVOF1 coating, especially for the lower annealing temperatures (β wt.% of 31 at 900℃ and β wt.% of 28 at 1000℃) compared to the values given by Thermo-Calc (β wt.% of 33 at 900℃ and β wt.% of 29 at 1000℃). However, the value for the annealed at 1100℃ is higher than that of predicted by Thermo-Calc. Having a higher amount of β following annealing and cooling from a higher temperature (1100℃) could be due to the fact that the quenching of the samples from 1100℃ is not fast enough to prevent further β precipitation on cooling and hence the resultant microstructure has higher amount of β than predicted.

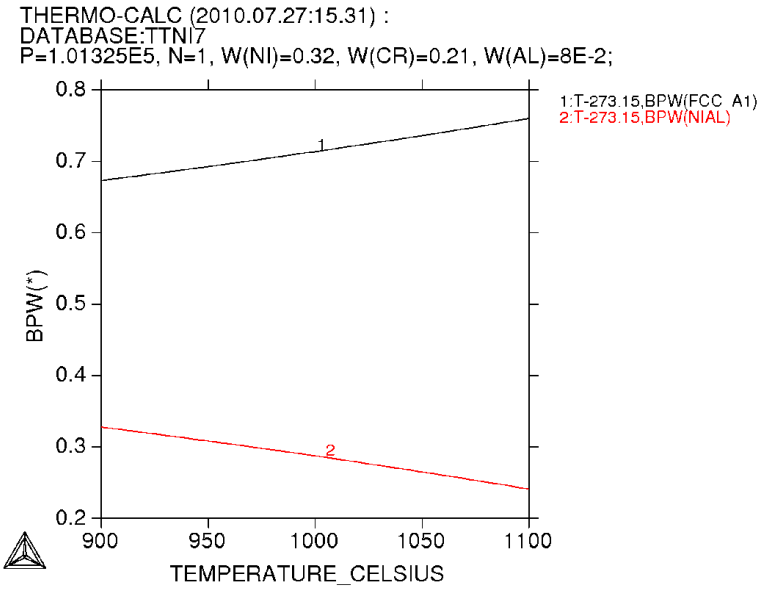

Figure 4-43. β mass fraction (BPW) as a function of temperature for Co32Ni21Cr8Al alloy. The black line (line number 1) is the γ phase and the red line (line number 2) is the β phase.

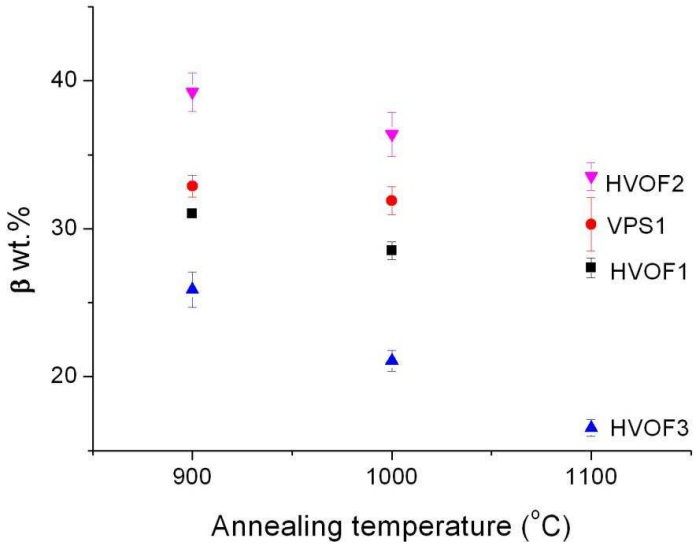

Figure 4-44. The effect of annealing temperature on β weight percent of HVOF and VPS coatings.

It should be noted, in order to convert the β volume fraction to β wt.% the following parameters are required: the densities of β, γ and the powder, β and γ compositions and lattice parameters. The powder's density was measured 7.46 g/cm^3 using a helium gas pycnometer. Furthermore, in order to calculate the γ and β densities the following assumptions were made: β is a BCC phase which has 2 atoms in its unit cell, γ is a

FCC phase which has 4 atoms in its unit cell and that the EDX spot analysis carried out on β phase is correct, considering the small size for β precipitates and the beam broadening effect.

Using the above assumptions the following formulae were derived for calculating the γ and β phase densities.

$$\rho_{\gamma} = \frac{\sum at_m \times A_m}{15.05a^3} = 7.94 \text{ g/cm}^3$$

$$\rho_{\beta} = \frac{\sum at_m \times A_m}{30.1a^3} = 6.96 \text{ g/cm}^3$$

where ρ is the density (g/cm^3), at_m is the atomic percent of element "m" in the required phase, A_m is the atomic weight of element "m" and "a" is the lattice parameter (angstrom) as determined by Nelson-Riley in section 4-1-3-3. Having the γ and β densities and the density of the alloy (powder) one can convert the volume fraction of the β phase to weight percent. Further more, an attempt was made by Sims et al. [16] and Meng et al. [17] to measure the density of the γ and β phase in a Ni base alloy, respectively. The density values reported are 8.9 and 5.9 g/cm^3 for γ and β respectively, which are in reasonable accord with the values derived above.

After annealing at 800°C both HVOF and VPS coatings had a γ+β microstructure. However, a third phase was also visible. EDX analysis of this phase revealed a very high quantity of Cr (see Figure 4-28). Toscano et al. [14] have reported the coexistence of the γ phase with the σ-(Co,Cr) phase in their annealed (800°C for 300h) samples sprayed with a CoNiCrAlY powder with a similar composition to the powder used in this work. However, since the amount of Co present in the third phase of the HVOF and VPS coating in this work was very low (very low Co to Cr ratio) it

was assumed that the third phase present is a α-Cr phase rather than the σ-(Co,Cr) phase since, higher Co content is present in the σ phase. Since the α-Cr phase had a contrast similar to β phase it is very difficult to determine how much is present, also the relationship between the annealing temperature and the quantity of this phase was not clear. However, a slightly higher quantity for this phase seemed to be present for HVOF coatings compared to VPS; this statement is based on optical microscopy observations.

One main reason for the dissimilarity between Toscano's observation and what has been observed in this work could be the fact that Toscano et al., had carried out their annealing process firstly in air and secondly on a coating/substrate system. Exposing a coating and its substrate to high temperatures can lead to a great amount of interdiffusion between the coating and the substrate [18-20] and hence change the composition of the coating. Also because they had carried out their annealing process in air, it will cause the oxidation of the coating and hence loss of elements such as Al, Cr, etc; which in general will change the composition of the coating. According to Achar et al. [19] even a minor modification in composition of the MCrAlY coating can have a substantial affect on its phase equilibria.

The α-Cr phase observed in the annealed HVOF and VPS coatings has a size of approximately 8-10μm and a similar colour (contrast) to the β phase. The reason for the α-Cr phase, to have a similar contrast to the β-(Co,Ni)Al phase is that there is very low amount of Co and Ni present in this phase compared to the amount of Cr (see Table 4-8). Since Cr has a lower atomic number compared to Co and Ni and there are very high quantities of Cr present in the phase, it is shown as the dark precipitates in the BSE mode; while the reason for the β phase to have a similar contrast is due to the

higher amount of Al compared to Cr in this phase. Toscano et al. [14] have reported the presence of the α-Cr phase in a NiCoCrAlY coating annealed at 1000°C for a period of 75 hr. The size of the reported α-Cr phase is approximately 2 to 3μm with much brighter contrast. Considering the atomic numbers of Co, Ni and Cr, it is not realistic to have such a contrast for α-Cr phase.

The microstructure of HVOF and VPS coatings annealed at 900℃ and 1000°C is similar to those annealed at 800°C. There were no signs of the σ-(Co,Cr) phase at these temperatures. This can be due to the fact that σ is a slow growing phase [14] and 90h exposure at 900°C might not have been sufficient for its formation. Also, Achar et al. [19] and Toscano et al. [14] have demonstrated that the σ phase (in a CoNiCrAlY coating) appears grey, similar to the γ phase, in BSE mode, due to the same average atomic number between σ & γ; which makes it more difficult to detect this phase. Similar to the specimens annealed at 800°C, the α-Cr phase was not distributed evenly throughout the coatings annealed at 900℃ and 1000℃, and as it was not present in large quantities, 1-2%, it was not detected by XRD.

The microstructure of the HVOF and VPS coatings annealed at 1100°C showed only the presence of the γ+β phases. It seems that no other phases are stable at this temperature and hence the dissolution of the α-Cr phase must have occurred in the temperature range of 1000℃ to 1100℃. Shibata et al. [7] have reported that at this temperature only a γ/β microstructure is stable for a CoNiCrAlY coating sprayed with a powder of the same composition as the powder used in this work, and that Al contents of less than 6.8 wt% will transform the microstructure to a single γ phase structure.

Due to the low contrast between the α-Cr phase and the β phase, and also because of the scarcity of the α-Cr phase; it was not possible to find a relationship between the annealing temperature and the quantity of the α-Cr phase.

The absence of γ' in the annealed coatings at all temperatures agrees with the finding of other authors [7, 14, 19, 21] who reported that Co tends to reduce the fraction of γ' and increase that of γ. The high Co content in the powders used in this work, appears to be preventing γ' formation.

4-3-2- Mechanical properties

Generally the properties of thermally sprayed deposits are very different from those of fully dense materials, and hence it is of interest, though difficult to establish a relationship between microstructural and mechanical characteristics of deposited coatings. Features such as pores, splat boundaries, micro-cracks, un-melted particles, and un-wanted phases (i.e. oxides), which are characteristics of the microstructure of thermally sprayed coatings influence the mechanical properties of coatings [22].

Hardness values determined for both coatings indicated a higher hardness for HVOF compared to VPS. Different hardness values have been reported in the literature (see Table 4-9). Since hardness has a great dependence on the microstructure of the coating, even a slight change in, for example, porosity level or oxidation during spraying may have a large effect on the final hardness values. Hence, the microstructure of the coatings will have a great effect on the hardness and thus similar materials sprayed with the same spraying method could end up with different hardness values because of the difference in the coating microstructure, i.e. less internal oxides, pores, melted and un-melted particles, etc. This fact is seen clearly in

Figure 4-35 where the same material sprayed in HVOF3 has a much lower hardness compared to that of HVOF1 and HVOF2 due to a higher porosity and melting levels.

The results from this work are in good agreement with the results from literature, e.g. the hardness measured for as-sprayed VPS2 in this work is 487±13HV and the hardness reported in literature for a VPS sprayed CoNiCrAlY is 450HV; for further comparisons see Figure 4-35 and Table 4-9. However, there are some little differences between the hardness values measured here compared to those reported in literature, which are attributed to the microstructural variations as described earlier.

Zhang et al. [23], have reported a higher hardness value for VPS compared to HVOF coatings, however, they too have observed a decrease in hardness in their heat treated coatings. Conversely, Higuera et al. [3] and Scrivani et al. [24] have reported higher hardness values for HVOF compared to VPS. This conflict in results could simply be due to the different coating qualities, i.e. different porosity and oxide levels, different spraying temperatures resulting in different extent of melting, etc., produced using different spraying techniques by different researchers.

However, the higher hardness value for HVOF compared to VPS coatings observed in this work could be due to the presence of well distributed fine, hard β-(Co,Ni)Al phase (see Table 4-9) in the as-sprayed HVOF coating, see Figure 4-9 and Figure 4-10, compared to as-sprayed VPS where there was not a great amount of β phase present, see Figure 4-17 and Figure 4-16; the β phase is only seen in the un-melted/incompletely melted powder particles and there were not many of these present in the as-sprayed VPS coatings. Also, it has been reported that hardness is related to the temperature and the speed of the particles when they impact on substrate [3]; the lower temperature and higher speed of the HVOF projected particles [25] can

explain the coatings higher hardness, due to work hardening; the opposite, higher temperature and lower velocity, occurring with the VPS projected particles.

The annealing process had reduced the hardness significantly compared to the as-sprayed values; thereafter, the hardness values did not decrease as much with increase in annealing temperature. Due to the nature of thermal spraying and the impact effect of the projected particles, thermally sprayed coatings have residual stresses. The annealing process will cause the stress relieving of the coating and so plays an important role in decreasing the hardness. The fall in hardness can also have a contribution from the coarsening of the β phase. As mentioned earlier on, the β phase coarsened significantly in the samples annealed at 800°C compared to the as-sprayed coating, see Figure 4-21. The increase in coarsening is not as significant, as the annealing temperature increases from 800°C to 1100°C and this is why the progressive reduction in hardness is not as great for the higher annealing temperatures as it was for the beginning of the graph in Figure 4-35. Further more, as seen in Figure 4-26, annealing decreases the total amount of the β phase present and this could also have an effect in reducing the hardness of annealed coatings. In fact the reasons for a slight increase in hardness for samples annealed at 1100℃ could be due to solid solution strengthening [26]: the gamma phase in the sample annealed at 1100℃ has higher amount of β dissolved in it (higher amount of alloying elements such as Al, Co and Ni) compared to the gamma phase annealed at lower temperatures. Considering what has been mentioned in the above discussion, the reasons for HVOF3 coating to have the lowest hardness among all other coatings is due to the higher porosity levels, ~8%, and lower β volume fraction (Figure 4-26), as compared to other coatings.

For both coatings the hardness determined by nano-indentation is higher than those found using conventional Vickers test, see Figure 4-40. This can be attributed to the fact that for conventional Vickers hardness, hardness is determined by load over indent area (residual projected area), whereas for nano-indentation, hardness is determined by load over projected contact area at peak load, which is calculated using the load-displacement graphs produced by the nano-indentation. Since the projected contact area is smaller than the residual projected area used in conventional Vickers hardness the hardness values determined using nano-indentation are slightly higher than those obtained using conventional Vickers hardness [27]. Furthermore, the purely elastic contact assumption describing the elastic/plastic indentation process in the nano-indentation has also an effect on the differences seen in the Vickers hardness (plastic deformation) and the nano-indentation hardness. Moreover, smaller volume sampled used in nano-indentation can result in less likelihood of complicated defects being taken into account resulting in higher hardness values.

Figure 4-45 illustrates values and behaviour of Young's modulus as a function of measuring temperature for various related coating and bulk materials, data displayed from literature [21, 28]. The Young's modulus of the individual γ and β phases measured by nano-indentation (e.g. E_γ = 213GPs and E_β = 182GPa for VPS coating) is in a very good agreement with what has been reported in the literature, compare Table 4-10 with Figure 4-45. However, when comparing the absolute E values for the as-sprayed HVOF and VPS MCrAlY coating measured with DMA in this work with the modulus of the MCrAlY coatings deposited by PVD reported in literature [21]; it is seen that the modulus measured in this work is slightly lower than those reported in literature. It should be noted that it was not stated in the literature whether the modulus of the PVD MCrAlY's are for as-sprayed or annealed coatings. However, the

modulus of the annealed coatings, at all measuring temperatures, measured in this work not only follows the similar trend to those observed by others (see Figure 4-45), but also seems to be in a good agreement with those reported in literature (compare annealed values in Figure 4-36 to Figure 4-39 with Figure 4-45). The slight difference between the results observed in this work and those reported in literature could be due to the fact that the coatings have been sprayed using different spraying methods, PVD in literature, HVOF and VPS for this work, and hence different microstructures. Also as the E values reported in literature are close to those of the annealed samples in this work, it could well be that the coatings used in the literature have been annealed, and as can be seen in Figure 4-36, different annealing temperatures can result in different values for the Young's modulus. One further difference is that in contrast to the results obtained in this work, the results presented in Figure 4-45 do not seem to show an approximately constant value for the modulus for measuring temperatures of up to 200℃.

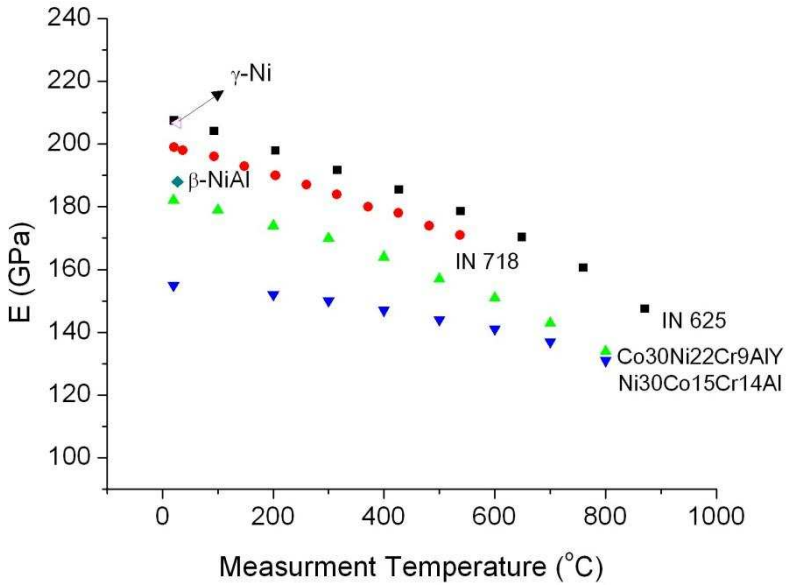

Figure 4-45. Young's modulus as a function of measuring temperature for different MCrAlY coatings (deposited by vapour deposition), Inconel alloys (bulk material) and γ-Ni & β-NiAl single phases [21, 28].

As can be seen in Figure 4-36, Figure 4-37 and Figure 4-38, the Young's modulus of HVOF1 coating is the greatest among all three HVOF coatings, followed by HVOF3 and than HVOF2 being the least. When comparing the E-T graphs of all three HVOF coatings, it can be seen that they all follow a similar trend; a large increase in modulus, when moving from as-sprayed to annealed at 900℃ and smaller progressive increase thereafter.

The reason for the HVOF coatings to have different Young's moduli could be correlated to the difference in microstructure of each coating. As seen in section 4-1, HVOF3 had the largest amount of melting, porosity and internal oxides among all three HVOF coatings which has resulted in HVOF3 having a lower modulus as compared to HVOF1. However, as can be seen in Figure 4-26, HVOF3 has a lower β volume fraction compared to HVOF1. As will be discussed later on (section 4-3-3), a lower β content should result in a higher Young's modulus; however, the higher porosity levels in HVOF3 have caused the absolute E values to be lower than that of HVOF1, regardless of its lower β volume fraction, as porosity has a greater effect on Young's modulus compared to β volume fraction, will be discussed later on in section 4-3-3.

On the other hand, as can be seen in Figure 4-37, the Young's modulus of HVOF2 coating is the lowest among all three HVOF coatings. It can also be seen that the progressive increase in the modulus from the sample annealed at 900℃ onwards is very small. The reason for the HVOF2 modulus to be lower than that of HVOF1 and HVOF3 is not quite known. However, Shen et al. [29] have reported that splat interfaces play a major role in defining the Young's modulus of coatings, in fact they have reported that splat interfaces account for 75-80% of the total reduction in the

Young's modulus of coatings compared to bulk material. This could be a reason for the lower modulus for HVOF2 coating; however, further microstructural investigations are required.

The Young's modulus of inhomogeneous, isotropic, and dense material is determined from the volume fraction of the phases present and their respective elastic moduli and is independent of its microstructural features; while, the elastic modulus of an anisotropic, non-homogenous, porous material is highly affected by its microstructural features [22].

The thermally sprayed coatings are non-homogenous, porous materials described above and hence the microstructural features will have a great effect on the Young's modulus. Furthermore, it has been reported that the difference between the modulus of a bulk material and that of a sprayed coating of the same material has been attributed, in qualitative terms, to defects within the coatings [30, 31]. These defects mainly include pores, secondary phases such as oxides (see Figure 4-9 and Figure 4-10) and weak bonding between splat boundaries, which in thermal sprayed coatings, contribute to reducing the elastic modulus of the coatings. This is because on application of load, pores have zero stiffness and will therefore lead to a reduction in the overall stiffness of the coating. Poor bonding between splats and between the coating and the substrate will also allow easier deformation of the system under a given stress resulting in a lower value of the Young's modulus, i.e. the strain tolerance of the coating is improved.

However, annealing of these coatings enhances cohesion between the individual lamella through diffusion and a sintering effect, resulting in elimination of fine porosity, see Figure 4-20. As seen in Figure 4-36, due to annealing, the modulus of

the coating increases. This increase is attributed to the reduction in porosity level as a result of annealing making the moduli become closer to that of the equivalent bulk material.

Also as a standard result, seen in Figure 4-36 to Figure 4-39, as the measuring temperature increases the modulus decreases. A similar trend in reduction of modulus as a function of measuring temperature is seen clearly in the results for all HVOF and VPS coatings tested in this work. However, when compared to the results from literature, the slope at which the modulus decreases as the measuring temperature increases in this work is different (less steep) to those from literature (for example compare Figure 4-36 with Figure 4-45).

Different models such as Spriggs' Equation, Hashin-Hasselman Equation, and Zhao model exist which relate the microstructure of a coating to the elastic modulus [32-34]. However, Azarmi et al. [22] have used these models to predict the modulus of thermally sprayed Inconel 625 coatings and have compared it with the measured modulus. They observed discrepancies between the models and the measured values: much higher values were obtained for the predicted results compared to experimentally measured modulus. They claimed that the discrepancies are due to the failure of the models to account for the effect of non visible microstructural characteristics such as weak bonding across splat boundaries [22].

Kuroda et al. [35] have reported satisfactory quantitative agreement of measured modulus with predicted values using Eshelby inclusion model and also Azarmi's [22] observation had given slightly better agreement between measured and predicted values when using Zhao model which is a combination of Mori-Tanaka method and Eshelby model [34]; hence, Eshelby model of inclusion was used in this work in order

to compare the predicted modulus with the measured modulus of the coatings and also to be able to discriminate between the effect of different parameters such as porosity and existence of a second phase on Young's modulus.

The change in the modulus due to annealing was thought to be due to two combined effects: (i) decrease in porosity levels, (ii) changes in β volume fraction as a result of annealing. The Eshelby model was used in this work in order to discriminate between these effects on the measured modulus as a function of annealing temperature.

4-3-3- Eshelby model

In the first part of the following section the effects of the β volume fraction and β aspect ratio on the Young's modulus of HVOF and VPS coatings have been studied using the Eshelby inclusion model. It should be noted that for this part of the prediction, a bulk material with a modulus that of γ phase, which has been measured by nano-indentation, and zero percent porosity was assumed.

Furthermore, as porosity is also known to have an effect on the modulus of coatings [22, 32, 33], the second part of the following section is correlated to the effects of porosity on Young's modulus of thermally sprayed coatings (HVOF and VPS) using the Eshelby inclusion model.

The e*ffect of β* phase *and its volume fraction on Young's modulus*

The β volume fraction of HVOF and VPS coatings was determined as a function of annealing temperature using image analysis, see Figure 4-26. As the annealing temperature increases the β volume fraction decreases for both HVOF and VPS coatings. A similar behaviour has been reported by Toscana et al. [14].

The Eshelby inclusion model was used in order to predict the effect of β volume fraction, as a second phase, on the Young's modulus of HVOF and VPS coatings. The single phase results used in Eshelby model are from the nano-indentation results, Table 4-10. It should be noted that the aspect ratio of a pore is defined as the width (parallel to coating substrate interface) by the length (perpendicular to the coating substrate interface), see Figure 3-9.

Figure 4-46 illustrates the predicted effect of β volume fraction (related to different annealing temperatures) on the Young's modulus of HVOF1 coating. As seen the increase in β volume fraction, which is a result of decrease in annealing temperature, is predicted to result in a decrease in modulus. Furthermore, the β aspect ratio also has an effect on the modulus. This is shown more clearly in Figure 4-47. However, this is only a slight effect, given that changing the β aspect ratio from 0.001 to 100 only changes the modulus by around 2GPa.

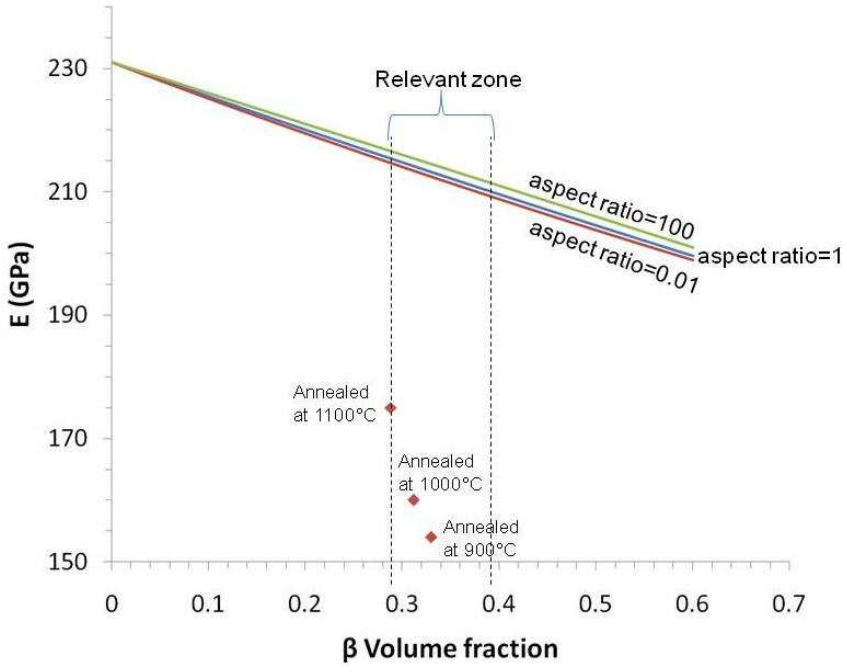

Figure 4-46. Effect of β volume fraction on HVOF1 Young's modulus. The initial point is the modulus of the γ phase measured by nano-indentation. Dotted lines indicate the region of interest. The individual data points are the modulus of HVOF1 coating measured using DMA.

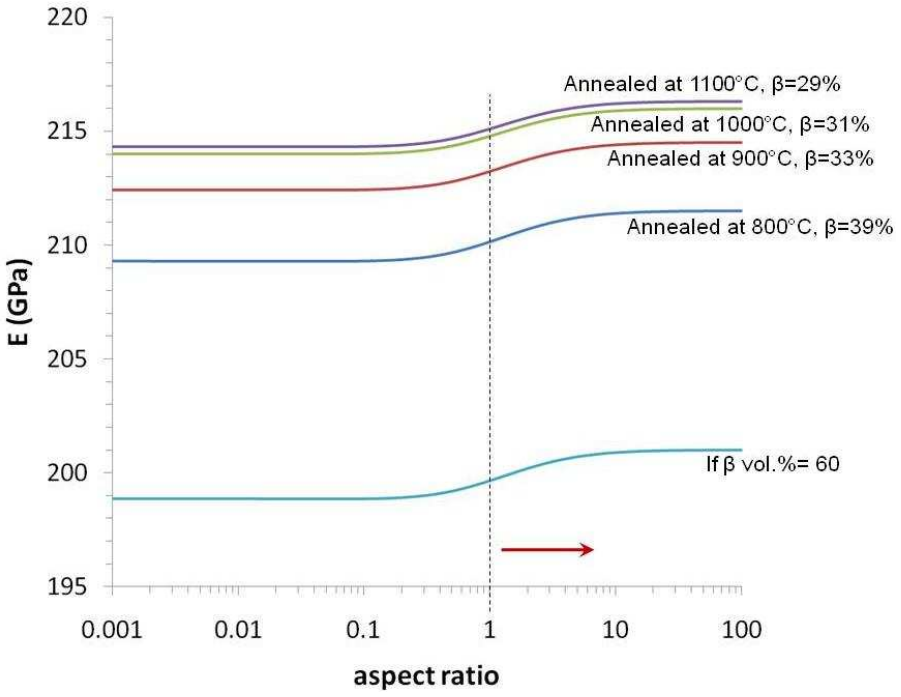

Figure 4-47. Young's modulus of HVOF1 coating as a function of β aspect ratio for different β volume fractions. The arrow and the dotted line show the area of interest, i.e. for β, aspect ratios of ~1.

Having said all the above regarding the effect of β volume fraction on the modulus of the HVOF coating, if the two extremes of the graph in Figure 4-47 are considered, i.e. E of 199GPa for a β volume percentage of 60% and E of 216GPa for a β volume percentage of 29% (related to 1100℃ annealed); the total effect which a 31% change in the β volume fraction has on the modulus of the coating (regardless of its aspect ratio) is something in the order of 8%.

The e*ffect of porosity on Young's modulus*

In this section a dual phase material, γ/β structure, was assumed and porosity was introduced in order to study the effect of porosity on the Young's modulus of the material.

Hence, a starting point modulus for a dual phase material (γ/β) with zero percent porosity was required in order to introduce the different levels of porosity. Based on the results obtained from the model in the previous section, a starting point of 215GPa was defined for the material, in order to understand the effect of porosity.

The value 215GPa was derived from Figure 4-47 under the following conditions;

- 29% β, since this is the β volume percent for the coating with the highest measured modulus, the annealed at 1100℃ coating (see Figure 4-36).
- β aspect ratio of 1, since this is the aspect ratio best describing the majority of the β particles in the coatings (see SEM cross-sectional images of annealed coatings).

Figure 4-48 illustrates the effect of different porosity levels, up to 15% which is much higher than any HVOF coating, on the Young's modulus. As can be seen, as the porosity level increases the modulus decreases. However, what can also be observed is that porosity with low aspect ratio (porosity perpendicular to coating layer) is predicted to have a much greater effect on the modulus compared to porosity with high aspect ratio (porosity parallel to coating layer), i.e. for a given porosity level low aspect ratio porosity leads to a lower modulus than the same extend of high aspect ratio porosity. This can be seen more clearly in Figure 4-49.

In Figure 4-48 and Figure 4-49 porosity aspect ratios of 1-10 and porosity levels of 1 to 8% (porosity plus oxide level) are marked as zone of interest for the coatings used in this work. This decision was made as the majority of the pores in the thermally sprayed coatings are pores which form parallel to the coating surface, due to the nature of deformation of powder particles in thermal spraying, and hence have aspect

ratios of one and greater (see SEM images of coatings cross section in section 4-1-2-1). Also, the maximum porosity level of 8% was chosen as an upper limit for the coatings, as in neither of the spraying methods used, HVOF and VPS, was such a porosity level achieved, i.e. HVOF3 which had the highest porosity plus oxide levels measured, using image analysis, revealed the value 8% for as-sprayed coating.

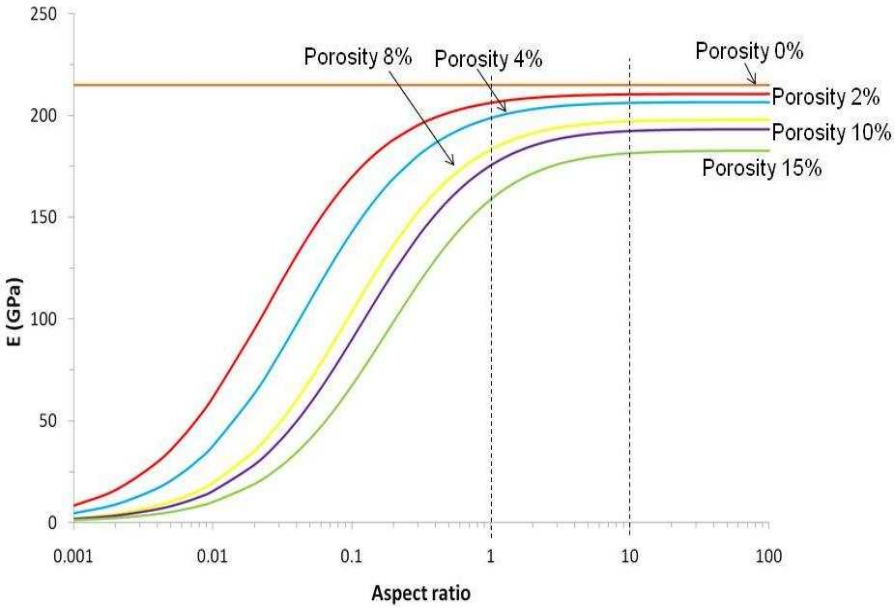

Figure 4-48. Young's modulus as a function of aspect ratio & porosity level for HVOF coating. Relevant to this work are aspect ratios of 1 to 10 and porosity levels of 1-8%.

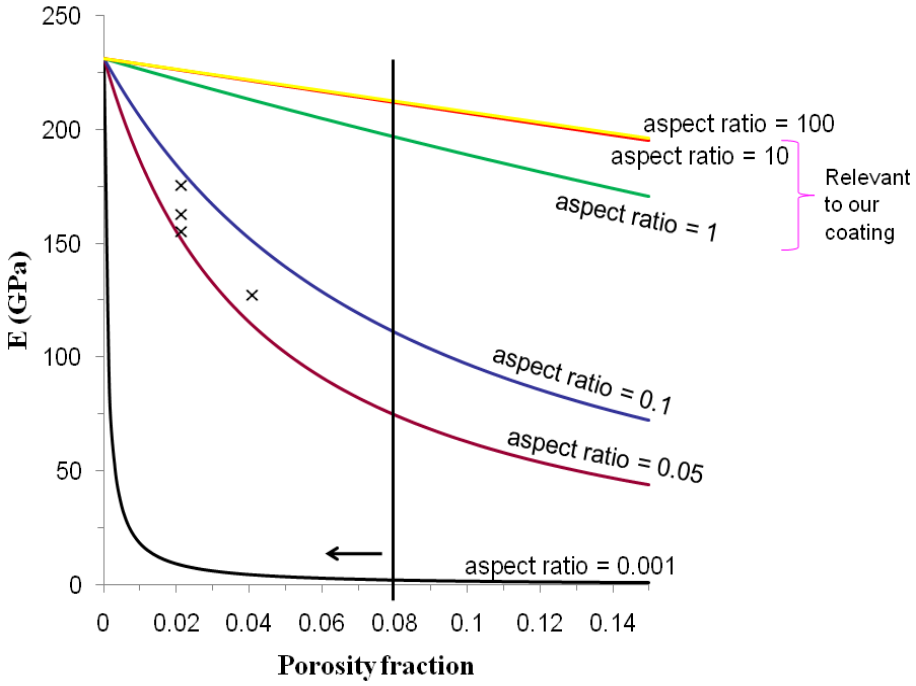

Figure 4-49. Effect of Porosity aspect ratio on the Young's modulus of HVOF1 coating. Aspect ratios relevant to this work are 1-10 for porosity levels of less than 8%. The crosses (×) in the graph are the values measure for the coating using the DMA for the annealed samples at porosity level of ~2% (the highest being annealed at 1100℃ and the lowest being annealed at 900℃) and for as-sprayed coating at porosity levels in the order of 4%.

What is also clear from Figure 4-49 is that aspect ratios greater than one do not seem to have any significant effect on the modulus of the coating. Indeed, for porosity levels smaller than 3%, the line for aspect ratios 1 to 100 are overlapping, and for any given porosity level aspect ratios greater than 10 have no further effect on the Young's modulus of the coating.

The increase in annealing temperature results in an increase in the modulus for both HVOF and VPS coatings, see Figure 4-36 and Figure 4-39. However, a larger increase in modulus (i.e. bigger step) can be observed when moving from as-sprayed coatings to the first annealing temperature (900℃) as compared to when moving from 900℃ to 1000℃ or from 1000℃ to 1100℃, see Figure 4-36 and Figure 4-39. Also, when comparing the porosity levels of different coatings, i.e. as-sprayed and annealed (comparing SEM micrographs of as-sprayed coatings with coatings annealed at

different temperatures in section 4-1-3-1, e.g. Figure 4-20, Figure 4-22 and Figure 4-23) a greater decrease in porosity can be observed when moving from as-sprayed to first annealing temperature coating compared to when moving from annealed at 900℃ to 1000℃ or annealed at 1000℃ to 1100℃, i.e. no significant changes in porosity levels are observed as the annealing temperature increase from 900℃ to 1100℃ contrary to the large decrease in porosity when moving from as-sprayed to annealed at 900℃. However, as can be seen in Figure 4-26, as the annealing temperature increases, the β volume fraction decreases. So, the large increase in Young's modulus is expected to be due to elimination of porosity and the progressive increase to be attributed to β volume fraction changes.

Using results obtained from the Eshelby model, the larger increase in the modulus at the beginning of the E-T graphs (Figure 4-36), moving from as-sprayed to the first annealing temperature, is attributed to the decrease in porosity; since changes in porosity levels have the major effect on the Young's modulus (from 6% to 4% porosity, i.e. 2% change, results in a ΔE of 5GPa), see Figure 4-49. Nevertheless, the following increases in the modulus as we go up in annealing temperature (which is smaller compared to the first increase) can be correlated to the changes in β volume fraction, as a large change in β volume fraction (from 29%β to 39%β, i.e. 10% change) only results in a small change in the modulus (ΔE= 6GPa), see Figure 4-46, and also because the porosity levels do not change significantly in this range (annealed at 900℃ to annealed at 1100℃) and the only factor changing is the β volume fraction.

Having said all the above, it has to be mentioned that increase in annealing temperature can also affect the porosity aspect ratios. Annealing can increase porosity

aspect ratio by healing up gaps formed between particles which act as cracks perpendicular to coating layer. These types of porosity, low aspect ratio, have the greatest effect on decreasing the modulus, see Figure 4-49. According to Figure 4-48 and Figure 4-49 any process (like annealing) capable of increasing the porosity aspect ratio, will result in an increase in the modulus. Hence throughout the discussion not only the porosity levels change but also porosity aspect ratio could increase as the annealing temperature increases and this could also add to the effect of porosity and the increase in modulus as the annealing temperature increases.

The trend or the behaviour of the results obtained experimentally is in good agreements with the trend of the results predicted by the Eshelby model. Furthermore, it can be stated that the results obtained experimentally are at the same order of magnitude as the results predicted by the model for the 0.05 aspect ratio (x to y ratio of 1 to 20). This aspect ratio is more likely to be observed in the splat boundaries of the coatings (especially coatings with higher amount of incompletely melted powder particles) at some angle to the tensile axis rather than parallel to the tensile axis. Such behaviour can be observed in Figure 4-9 and Figure 4-13. This phenomena is also similar to what has been reported by Shen et al. [29] which states splat interfaces play a major role in defining the Young's modulus of the coatings.

However, other variables such as existence of oxides, difference in composition (due to non-homogenise material or diffusion for coating and substrate systems) which have not been covered in this work by the Eshelby model, can also have an effect on the overall modulus of a coating. This could be a reason for the slight mismatches between the results obtained experimentally and the values predicted by the model for Young's modulus.

CHAPTER 5

Oxidation

This section describes the oxidation behaviour and characterisation of the oxide layer of as-received and heat treated HVOF and VPS coatings. As mentioned in chapter 3 section 3-3-3, free standing coatings were isothermally oxidised in air at 1100°C and 850°C for periods of up to 250h. Thermogravimetric analysis was also carried out in order to measure the oxidation rate of different coatings at an isothermal temperature of 1100°C.

5-1- Oxidation of as-sprayed coatings

5-1-1- HVOF coatings

Oxidation temperature of 1100°C

SEM micrographs in Figure 5-1 illustrate the oxide layer of HVOF1 coating after different exposure times. As seen an oxide layer has started to form as early as 1h thermal exposure. The existence of a dual oxide layer is clear from the micrographs. EDX analysis of these layers revealed the bright upper layer to be enriched in Co, Ni, Cr, Al and oxygen while the darker inner layer had high quantities of Al and oxygen. A β depleted zone is present at the sample surface (Figure 5-1). This is an indication of the consumption of the Al rich β phase to form Al_2O_3; β is regarded as an Al

reservoir. As expected and seen in Figure 5-1, as the exposure time increases the oxide thickness and β depletion zone also increases.

XRD analysis, Figure 5-2, of HVOF1 coatings exposed for different times revealed the existence of spinel oxides, α-Al_2O_3 and the γ solid solution. The presence of spinel and alumina peaks corresponds to the dual oxide layer structure of the oxidised coatings. Hence the brighter upper layer is attributed as being spinel oxide and the darker inner layer as α-alumina. The γ peaks are from the underneath coating.

Some spinel peaks in the XRD patterns were at slightly lower 2θ values than those expected for $NiAl_2O_4$ and $CoAl_2O_4$ and slightly higher than $NiCr_2O_4$ and $CoCr_2O_4$. EDX analysis showed that Co, Ni, Cr, Al and O were all present in the outer oxide layer. Therefore, while the precise spinel present can not be specified we can say that it is either a mixture of some/all of the spinel-type oxides ($NiAl_2O_4$, $CoAl_2O_4$, etc) or a substitutional solid solution $(Ni,Co)(Al,Cr)_2O_4$. A similar observation for HVOF sprayed CoNiCrAlY coatings oxidised at 1000℃ for up to 330 hours was reported by Tang et al. [1].

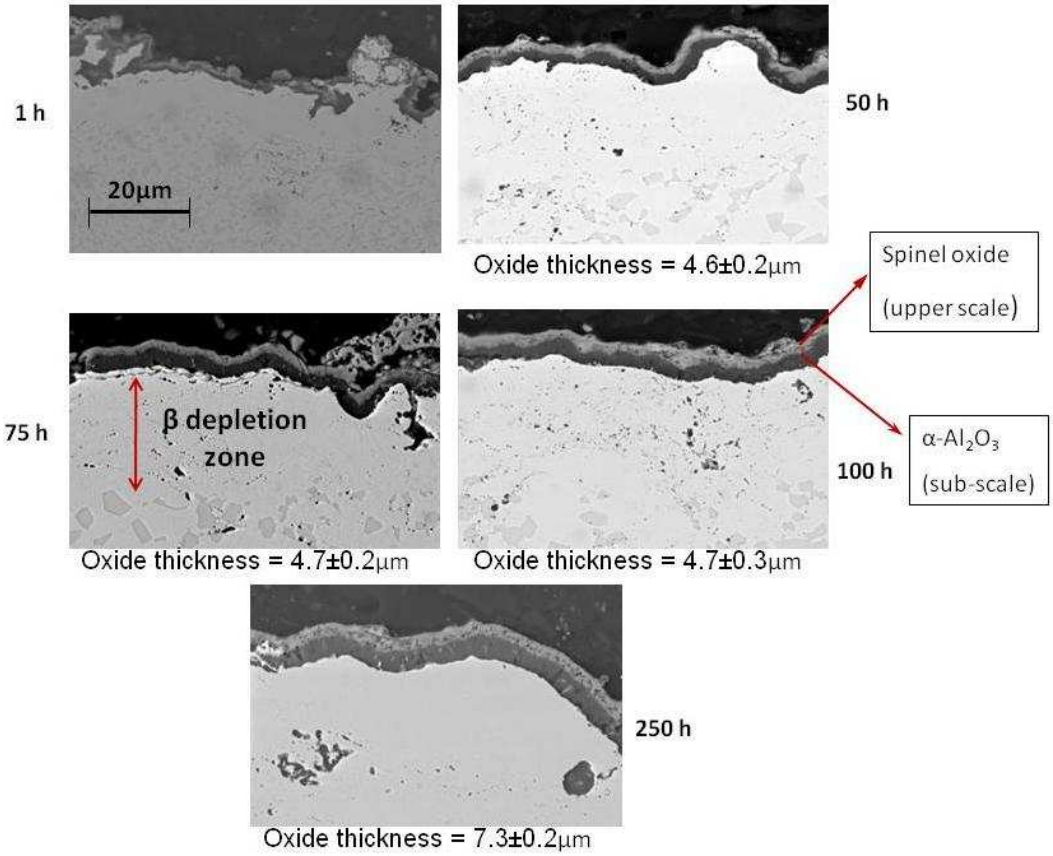

Figure 5-1. SEM micrographs of HVOF1 coating oxidised at 1100°C for different exposure times. A dual oxide layer is present at all exposure times. The upper scale is a spinel oxide and the lower scale is α-Al_2O_3. All images are in BSE mode and are at the same magnification.

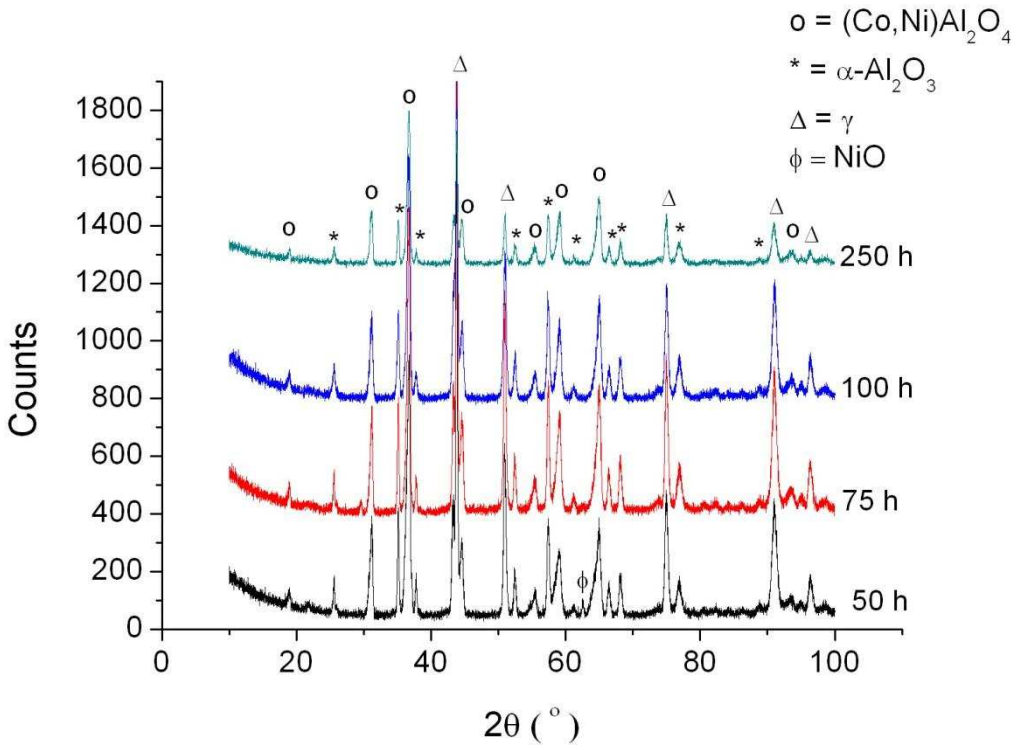

Figure 5-2. XRD spectra of as-sprayed oxidised surface of HVOF1 coatings for different oxidation times.

Table 5-1 illustrates an average of the extent of the β depletion zone for HVOF coatings as a function of exposure time.

Table 5-1. β depletion zone as a function of exposure time for HVOF coatings. Each value is an average of 15 measurements throughout the coating surface.

Exposure time (h)	β depletion zone (μm)		
	HVOF1	HVOF2	HVOF3
50	24±1	25±2	103±3
75	24±1	27±2	127±5
100	29±2	31±2	164±6
250	47±3	37±2	—

Figure 5-3 and Figure 5-4 illustrate a similar trend for as-sprayed oxidised HVOF2 and HVOF3 coatings. The oxidised surface of these coatings also presents a two layer oxide structure of an upper spinel layer and α-Al_2O_3 sub-scale. Although all coatings behave in a similar way, the HVOF3 coating has a much more extensive depletion zone compared to the other HVOF coatings, see Table 5-1. In fact almost the entire HVOF3 coating thickness was β depleted after the exposure time of 250hr.

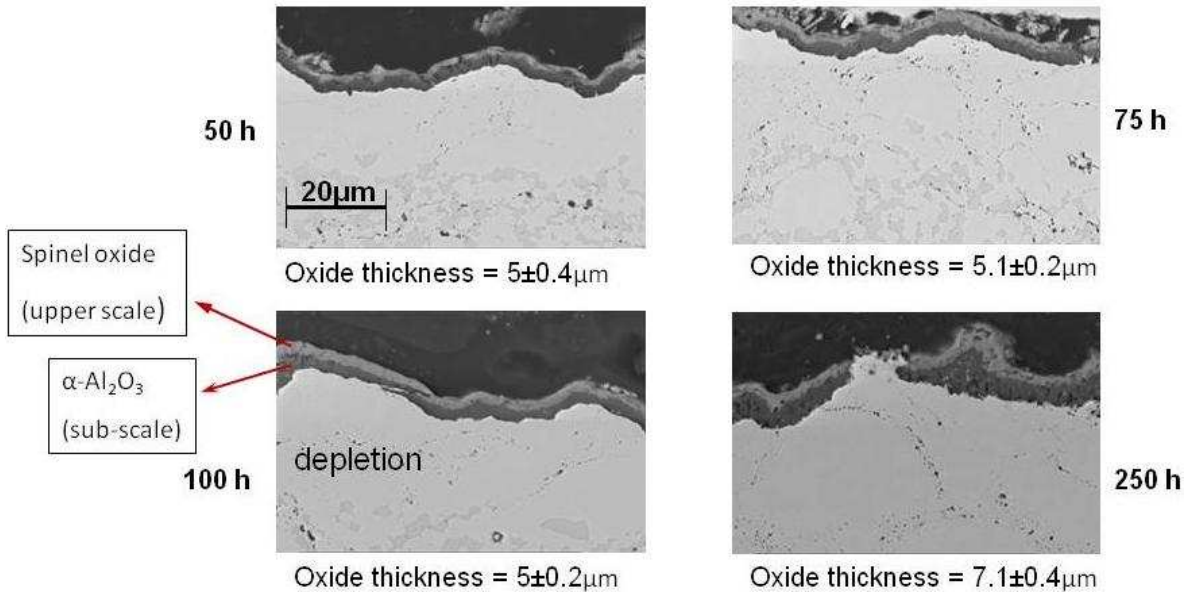

Figure 5-3. SEM micrograph of HVOF2 coating oxidised at 1100°C for different exposure times. A dual oxide layer is present at all exposure times. The upper scale is a spinel oxide and the lower scale is α-Al_2O_3. All images are in BSE mode and are at the same magnification.

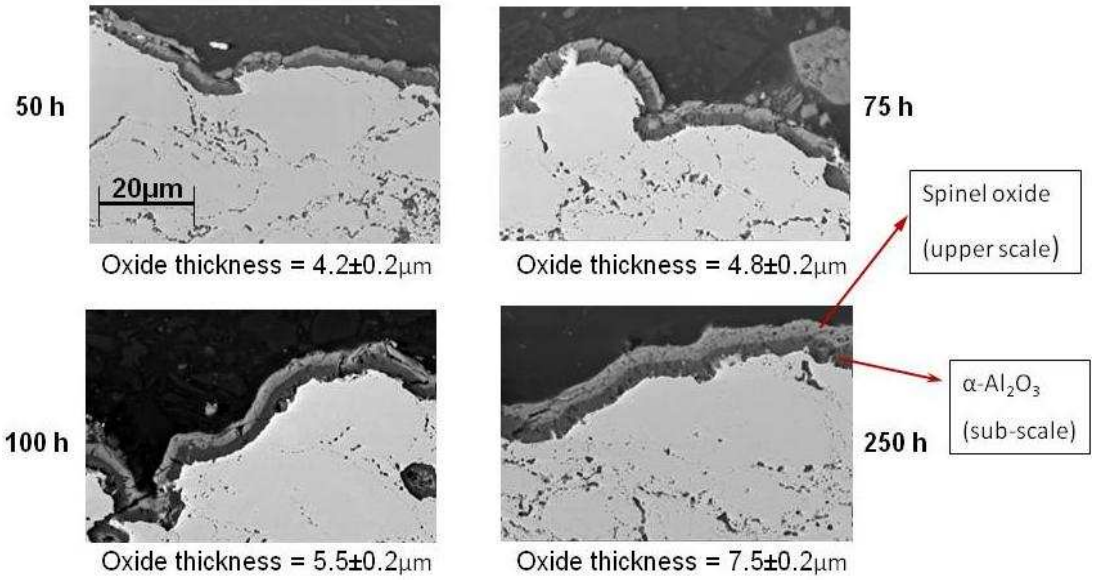

Figure 5-4. SEM micrograph of HVOF3 coating oxidised at 1100°C for different exposure times. A dual oxide layer is present at all exposure times. The upper scale is a spinel oxide and the lower scale is α-Al_2O_3. All images are in BSE mode and are at the same magnification.

Figure 5-5 and Figure 5-6 illustrate HVOF2 and HVOF3 XRD patterns for different exposure times. As can be seen, peaks related to spinel oxides such as $CoAl_2O_4$, $NiAl_2O_4$, etc and alumina can be observed. There are some peaks related to NiO in the XRD patterns of 75 and 100 hours exposure times. The presence of the NiO peaks is more clear in the XRD spectra of HVOF3 coating, Figure 5-6. Also when comparing the peak height of spinel and alumina for each of the patterns, it could be seen that as the exposure time increases the relative peak height for the oxides increases, consistent with an increase in oxide thickness. Furthermore, an increase in relative peak height, spinel to alumina, with increase in exposure time is seen especially in XRD pattern of HVOF3 coating which could be due to higher growth rates for spinel oxides as compared to alumina.

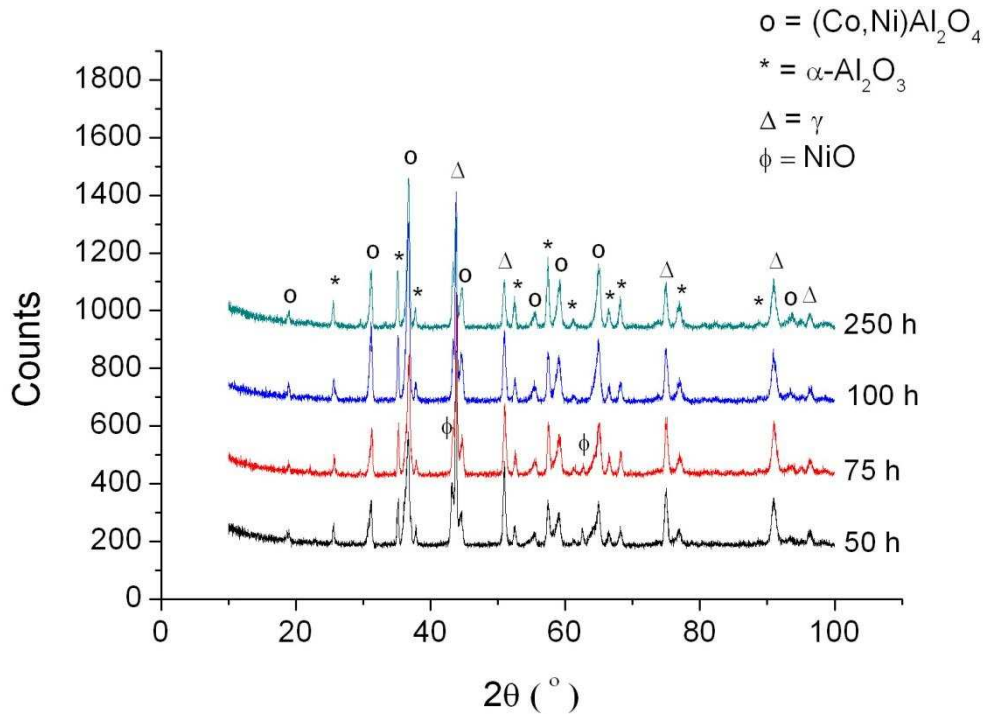

Figure 5-5. XRD pattern of as-sprayed oxidised HVOF2 coatings for different exposure times.

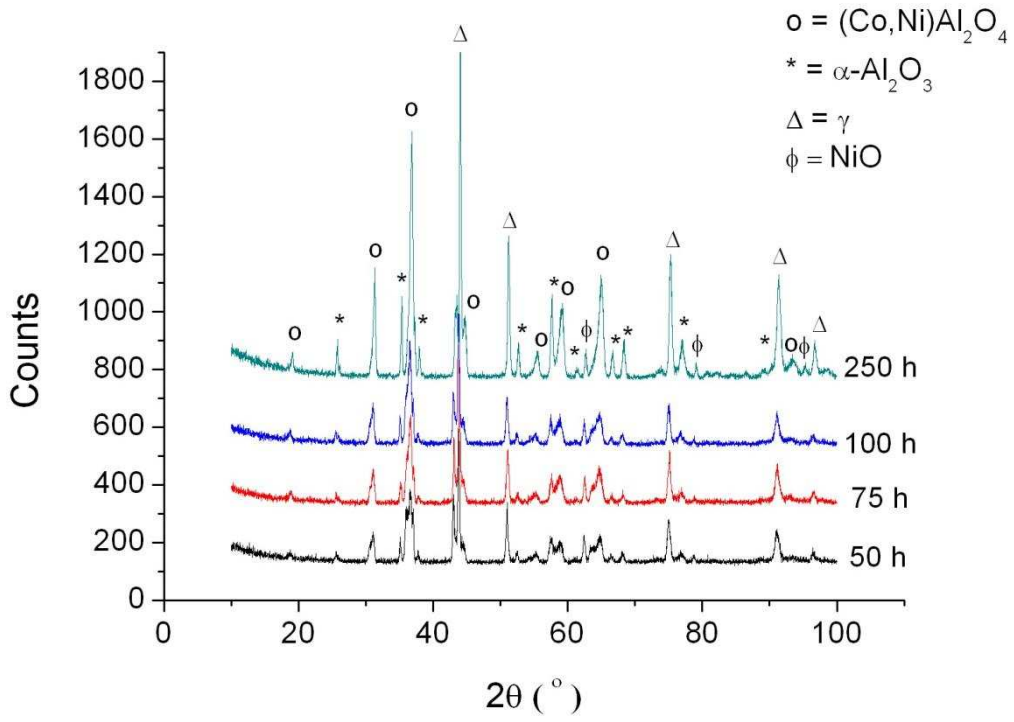

Figure 5-6. XRD spectra of as-sprayed oxidised HVOF3 coatings for different exposure times.

Internal oxidation of the coatings was also investigated. Figure 5-7 shows a typical SEM micrograph of the internal structure of all three as-sprayed oxidised HVOF

coatings. A higher degree of internal oxidation was observed for HVOF3 coating. Also, when looked at in more detail, it can be seen that HVOF3 oxidised coating has far fewer β particles compared to HVOF1 and HVOF2.

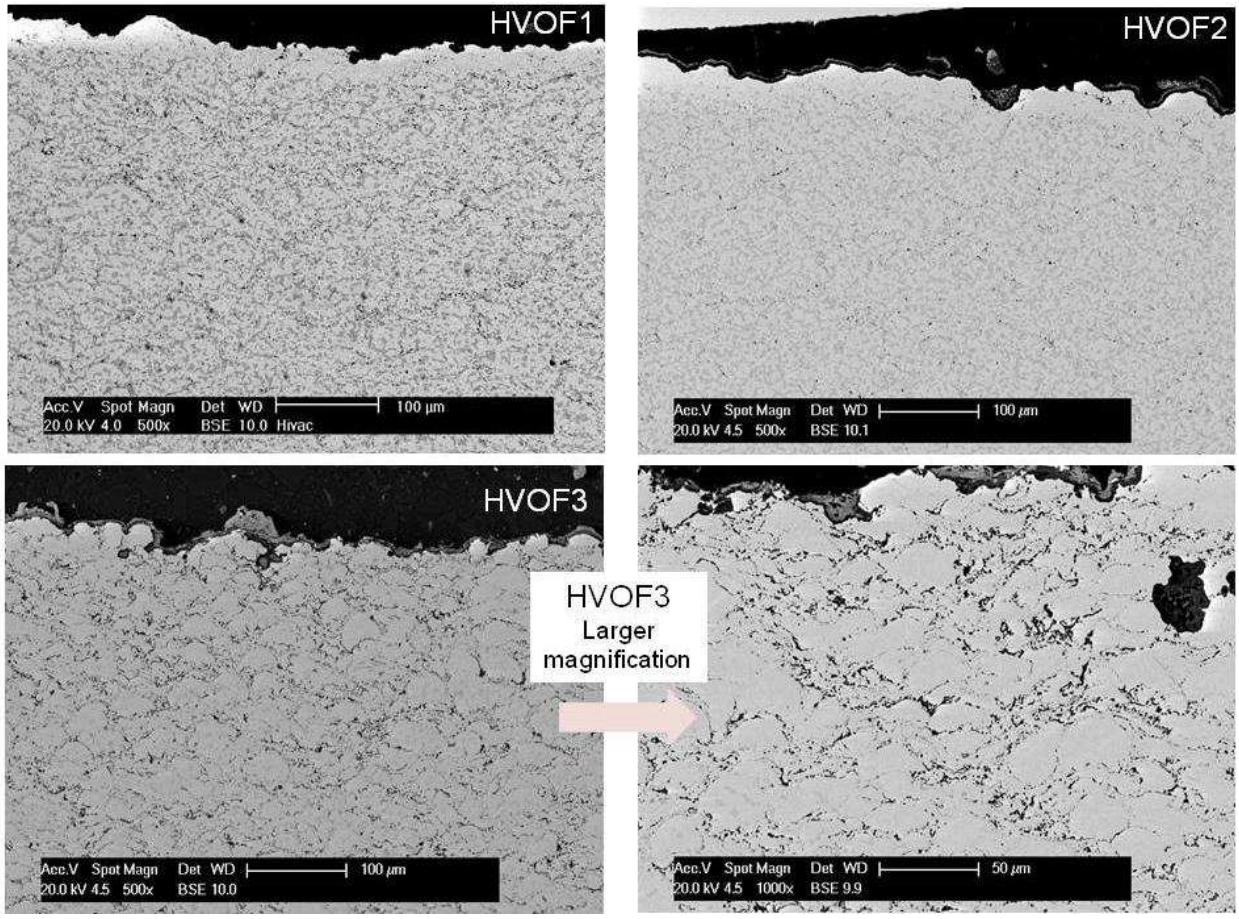

Figure 5-7. Typical SEM micrographs of internal oxidation of HVOF1, HVOF2 & HVOF3 as-sprayed oxidised (at 1100°C for 100h) coatings, illustrating a higher degree of oxidation for HVOF3. The larger magnification SEM micrograph of HVOF3 coating illustrates a very low amount of β phase left after a 100h oxidation duration. All images are in BSE mode and are at the same magnification (excluding HVOF3 larger magnification).

Oxidation temperature of 850°C

All coatings were oxidised at 850℃ for periods of 50 and 250 hours. Figure 5-8 illustrates the oxide layer of as-sprayed oxidised HVOF1 coating for both exposure times. As can be seen, only a single oxide layer exists, unlike as-sprayed HVOF coatings oxidised at 1100℃. Although, the oxide layer does not seem to be different

in thickness for different exposure times, the oxide layer for the 50 hours exposed sample seems to be smoother compared to the oxide layer for the 250 hours exposed sample. Due to the very low thickness of the oxide layer (submicron) EDX analysis of the layer, considering the beam size, was not achievable.

As expected, the β depletion zone for HVOF1 coating oxidised at 850℃ is far smaller than the depletion zone for HVOF1 coating oxidised at 1100℃, compare Figure 5-1 with Figure 5-8. This is consistent with the observed oxide thickness as; the coating with smaller β depletion has a thinner oxide compared to the coating with larger β depletion zone.

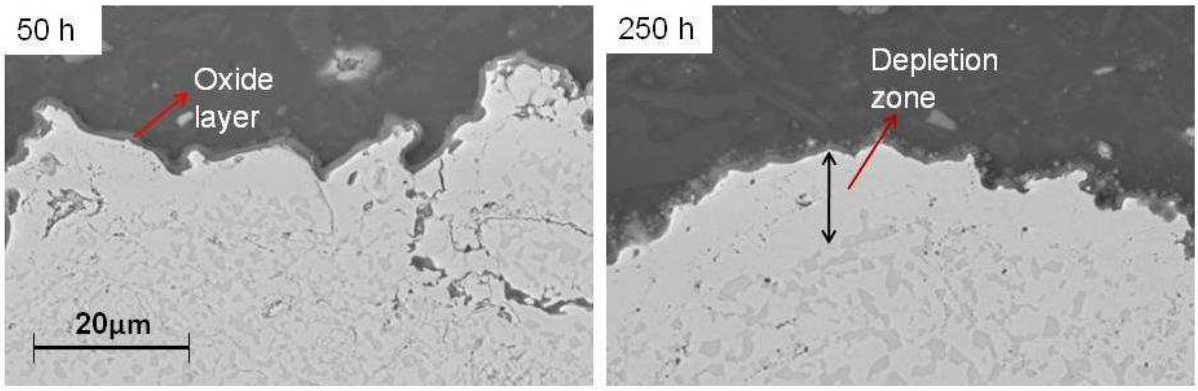

Figure 5-8. SEM micrograph of as-sprayed HVOF1 coating oxidised at 850℃ for periods of 50 and 250 hours. Only a single oxide layer is visible. Both images are in BSE mode and are at the same magnification.

The XRD pattern of the as-sprayed oxidised at 850℃ HVOF1 coating is illustrated in Figure 5-9. Unlike the as-sprayed HVOF coatings oxidised at 1100℃ where XRD analysis revealed peaks related to alumina and spinel oxides such as $CoAl_2O_4$, the XRD analysis of the HVOF coatings oxidised at 850℃ show peaks related to chromium oxide (Cr_2O_3), and alumina. Although EDX analysis of the oxide layer was not achievable, it is suggested that the bright spots seen after 250 hour exposure in

Figure 5-8 could be correlated to the chromium oxide peaks presented in XRD pattern of 250h exposure time. Furthermore, increase in relative peak heights of oxide peaks compared to the γ matrix with increase in exposure time is clear from the XRD pattern, see Figure 5-9, which indicates the growth of the oxide layer with time.

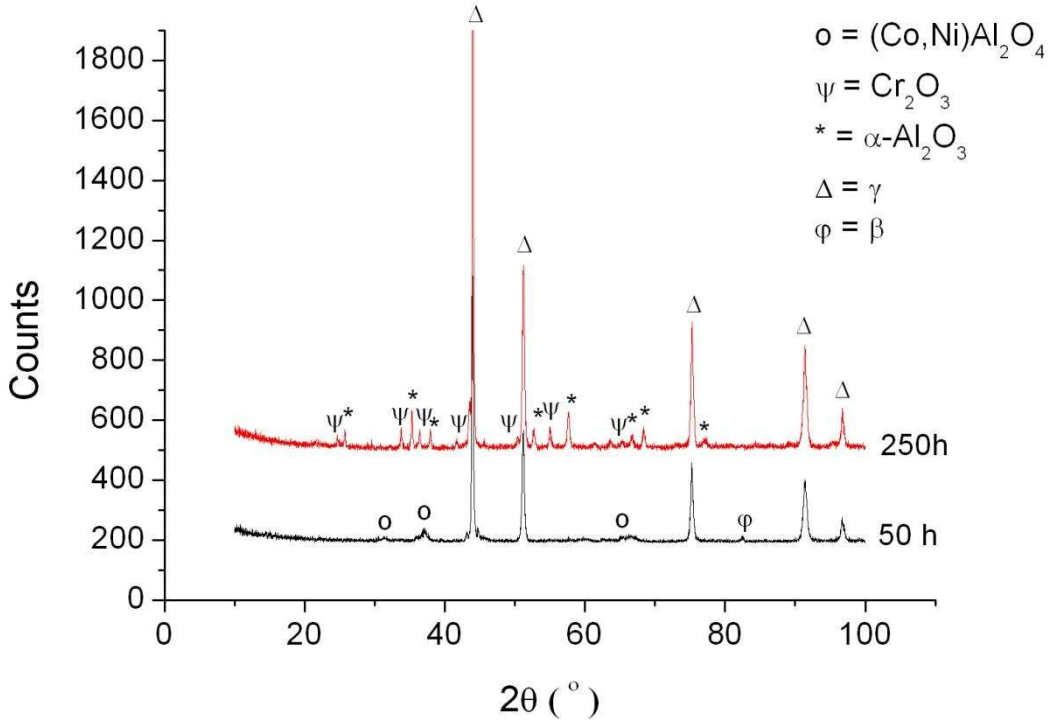

Figure 5-9. XRD spectra of as-sprayed HVOF1 coating oxidised at 850℃ for exposure times of 50 & 250 hours.

Similar behaviour was seen for HVOF2 and HVOF3 as-sprayed coatings oxidised at 850℃. Figure 5-10 and Figure 5-11 illustrate the oxide layer for the as-sprayed oxidised HVOF2 and HVOF3 respectively. Once more, a thin, oxide layer is visible. However, since the oxide layer is too thin it can not be determined if the oxide layer is a dual layer; although it does not appear to be. The XRD patterns of these coatings reveal a mixture of different types of oxides such as chromium oxide, alumina, spinel, NiO, etc, see Figure 5-12 and Figure 5-13. Moreover, an increase in relative peak height of XRD oxide peaks can be seen as the exposure time increases showing an

increase in oxide thickness. This observation is also in agreement with the SEM micrographs of individual coatings.

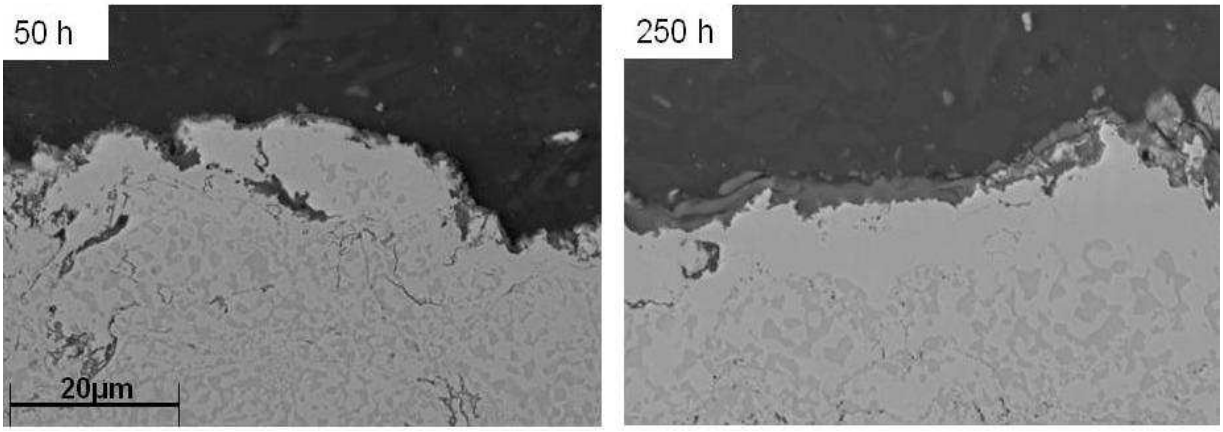

Figure 5-10. SEM micrograph of as-sprayed HVOF2 coating oxidised at 850 ℃ for periods of 50 and 250 hours. A thin single oxide layer is visible. All images are in BSE mode and are at the same magnification.

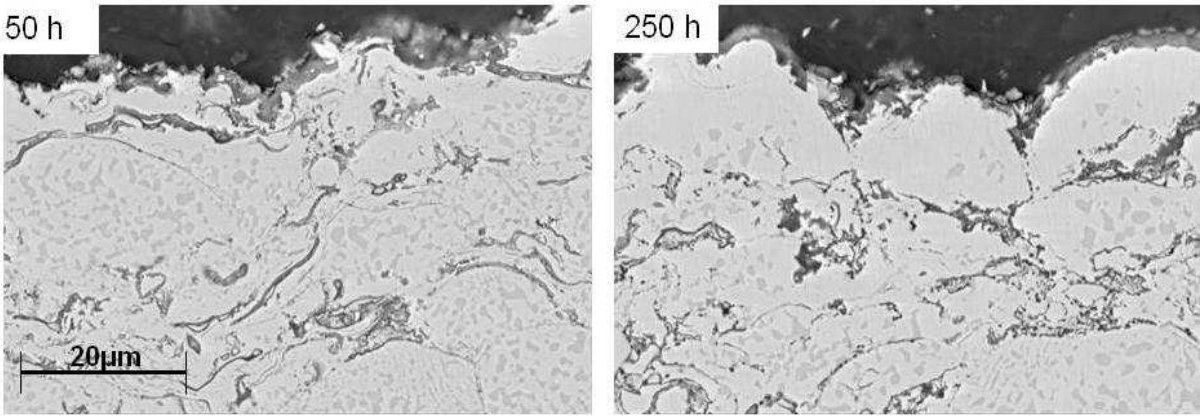

Figure 5-11. SEM micrograph of as-sprayed HVOF3 coating oxidised at 850 ℃ for exposure times of 50 and 250 hours. All images are in BSE mode and are at the same magnification.

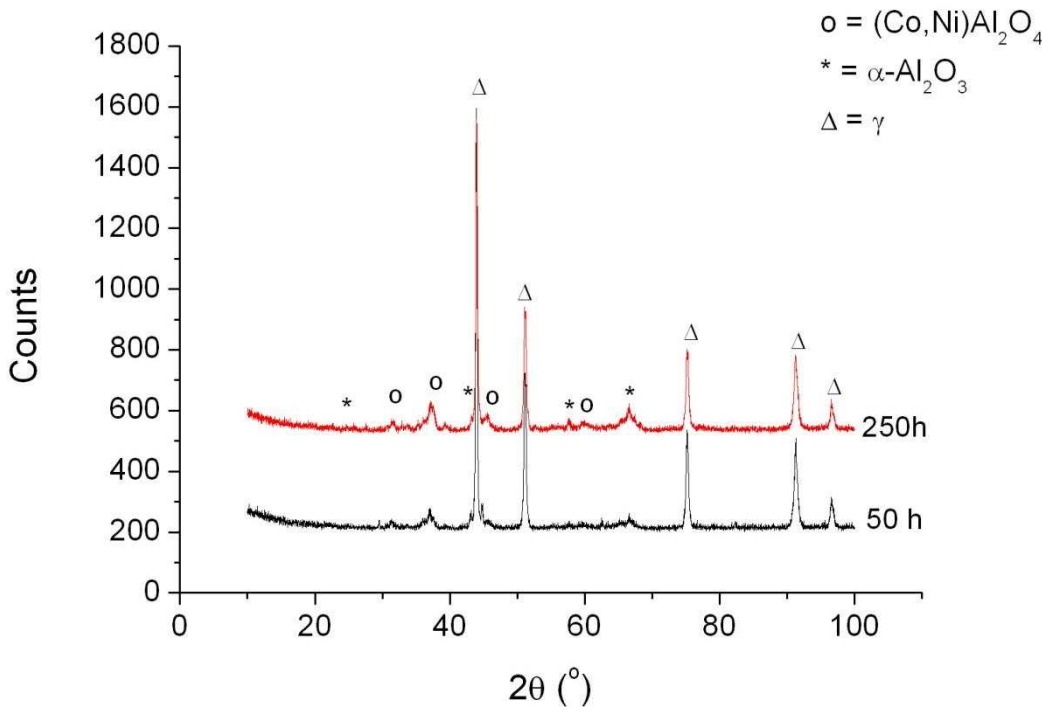

Figure 5-12. XRD spectra of as-sprayed HVOF2 coating oxidised at 850℃ for exposure times of 50 and 250 hours. Peaks related to alumina & spinel are visible.

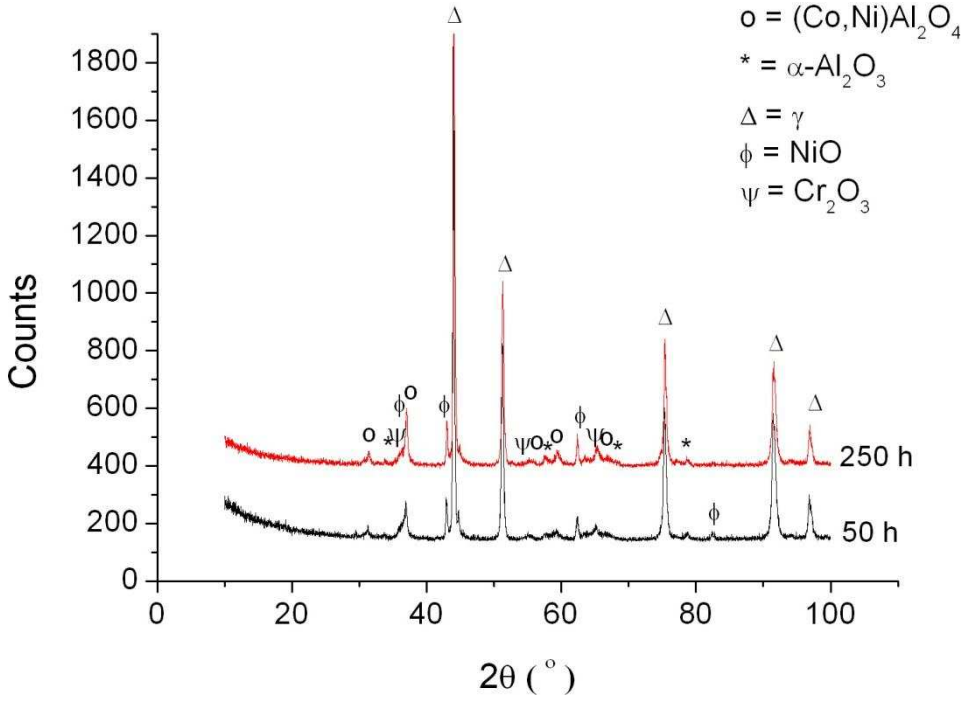

Figure 5-13. XRD pattern of as-sprayed HVOF3 coating oxidised at 850℃ for periods of 50 & 250 hours. The pattern reveals peaks related to Ni, Al & Cr oxides and spinel oxides.

5-1-2- VPS coating

Oxidation temperature of 1100°C

Figure 5-14 illustrates SEM micrographs of VPS1 coating oxidised at 1100°C for various exposure times. As for HVOF coatings, the VPS as-sprayed oxidised at 1100℃ coating also presented a dual oxide layer. EDX analysis of the upper brighter layer revealed the layer to be enriched with Co, Ni, Cr, Al and oxygen while the EDX analysis of the darker sub-scale revealed high quantities of Al and oxygen. However, as can be seen in Figure 5-14, oxides other than spinel and alumina such as NiO could also be seen, nevertheless, these mixed oxides were not seen very regularly and could mainly be observed at longer exposure times such as 250 and 100 hours. Furthermore, as can be seen in Figure 5-14 these oxide protrusions are voluminous. It is clear from the SEM micrographs that as time progresses the oxide thickness increases.

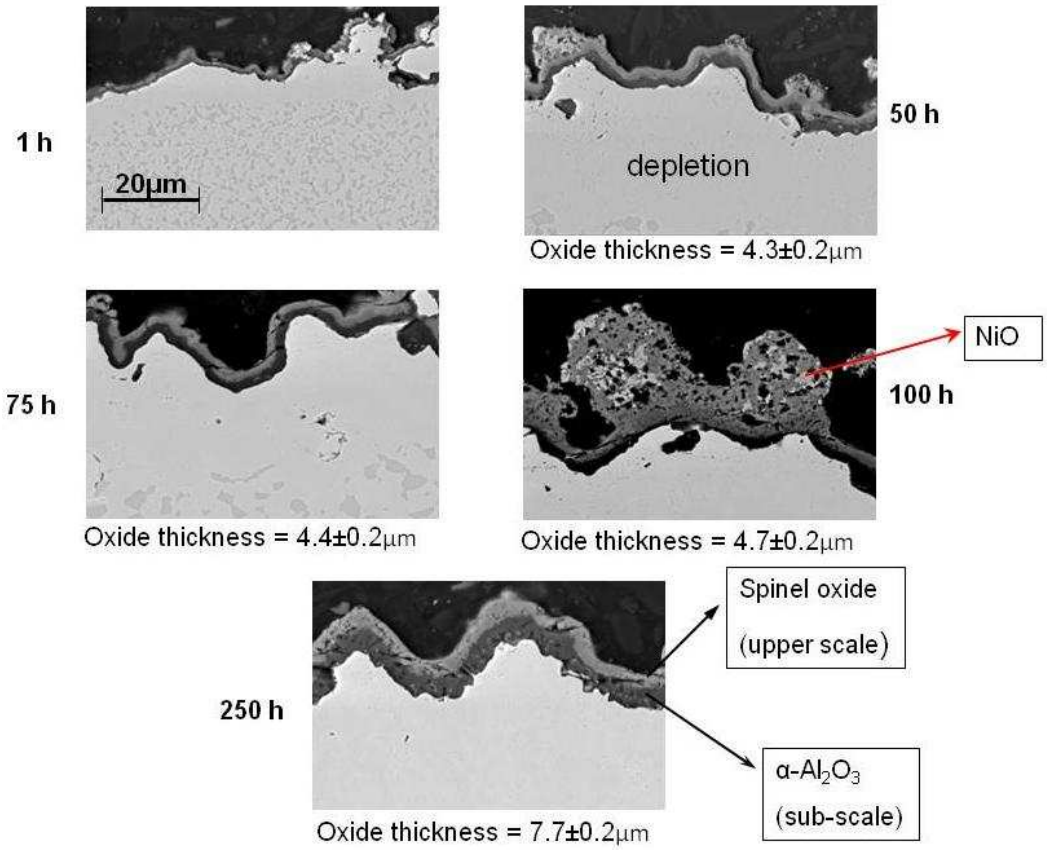

Figure 5-14. SEM micrographs of as-sprayed oxidised, at 1100°C, VPS1 coatings for different exposure times. The presence of a dual oxide layer is clear, with the upper layer being spinel oxide and the sub-scale being α-Al_2O_3. All images are in BSE mode and are at the same magnification.

The XRD spectra of the as-sprayed VPS1 coating oxidised at 1100°C for various exposure times can be found in Figure 5-15. Peaks related to alumina and spinel oxides are observed. Also, NiO peaks can be seen for duration times of 75 and 100 hours, consistent with the SEM images. However, in contrast to HVOF coatings where clear spinel peaks could be observed for the 50 hour exposure time, only small spinel peaks can be seen for the 50 hours exposure time of the as-sprayed VPS coating (compare Figure 5-2 with Figure 5-15).

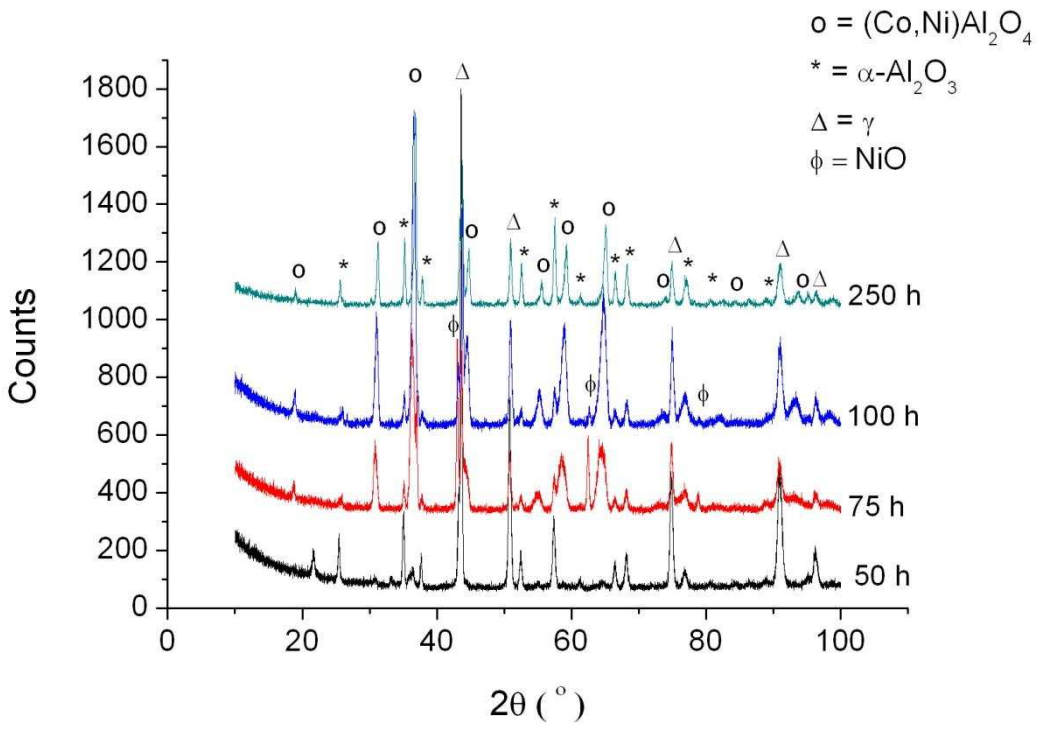

Figure 5-15. XRD pattern of as-sprayed oxidised, at 1100°C, VPS1 coating for different exposure times.

Figure 5-16 illustrates a typical microstructure of the as-sprayed VPS1 coating oxidised at 1100℃ for 100 hours. The internal oxidation of the VPS coating was less than all three HVOF coatings, especially less than that of HVOF3 (compare Figure 5-16, with Figure 5-7). As can be seen, in the as-sprayed oxidised VPS coatings, only oxide stringers can be observed in the interface between the spraying passes whereas in HVOF coatings the oxide stringers could be seen at almost all un-melted particle boundaries (compare Figure 5-7 with Figure 5-16).

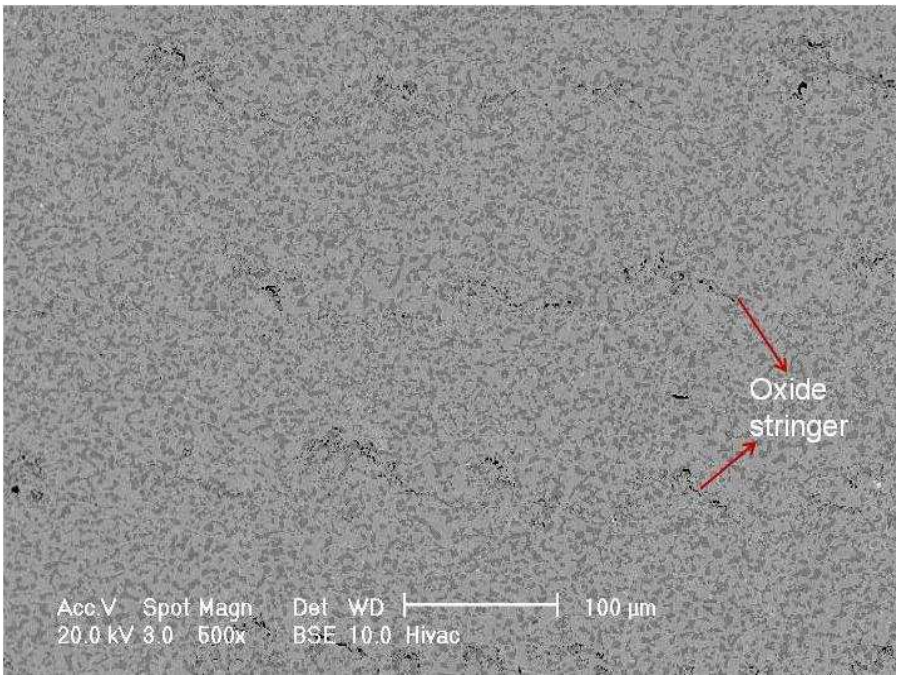

Figure 5-16.Typical SEM micrograph on the internal oxidation of as-sprayed VPS1 coating oxidised at 1100℃ for 100h. Only small amount of oxide in the interface between passes can be observed. Image is in BSE mode.

Oxidation temperature of 850 ℃

The VPS coating was oxidised at 850℃ for periods of 50 and 250 hours. Figure 5-17 illustrates the oxidised VPS1 coating. As can be seen, a very thin oxide layer exists. This oxide layer seems to be a continuous layer for the 50 hours exposed coating whereas a more fragmented oxide layer is seen for the 250 hours exposed coating. Since the oxide layer was very thin and taking into account the 2μm diameter of the electron beam, EDX analysis of this layer was not achievable. Compared to the VPS coating oxidised at 1100℃ (see Figure 5-14), a much smaller β depletion zone can be observed for the oxidised at 850℃ VPS coating.

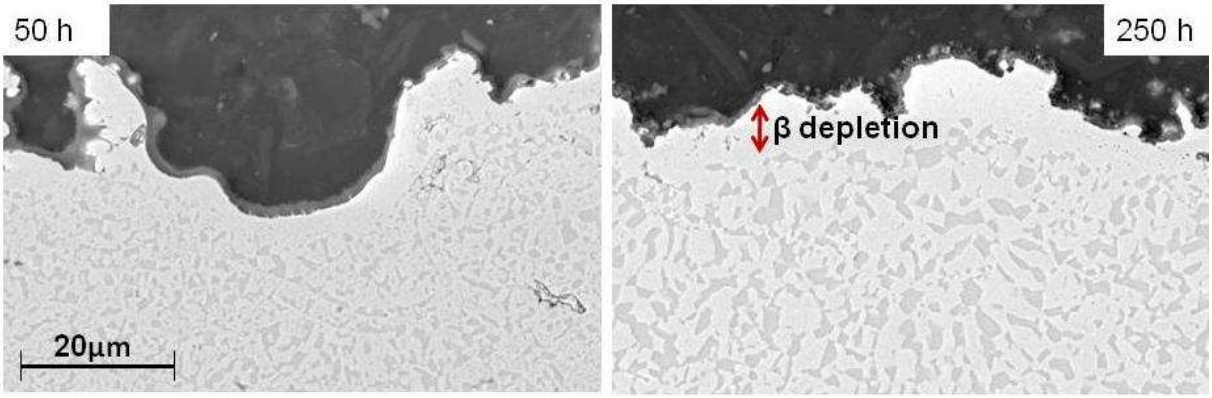

Figure 5-17. SEM micrograph of as-sprayed VPS1 coating oxidised at 850℃ for periods of 50 & 250 hours. A single oxide layer can be observed. Both images are in BSE mode and are at the same magnification.

The XRD pattern of the as-sprayed oxidised at 850℃ VPS1 coating can be seen in Figure 5-18. As can be seen, the 250 hours spectrum shows peaks related to γ, alumina and Cr_2O_3, whereas the spectrum for the 50 hours duration illustrates a greater mixture of oxides: NiO, spinel, Cr_2O_3 and alumina. Furthermore, an increase in relative peak height for the oxides, especially for alumina peaks, with increase in exposure time is clear from the XRD pattern. Where the SEM images do not show a clear oxide growth as the exposure time progresses, the XRD patterns reveal the growth of the oxide layer with increase in exposure time.

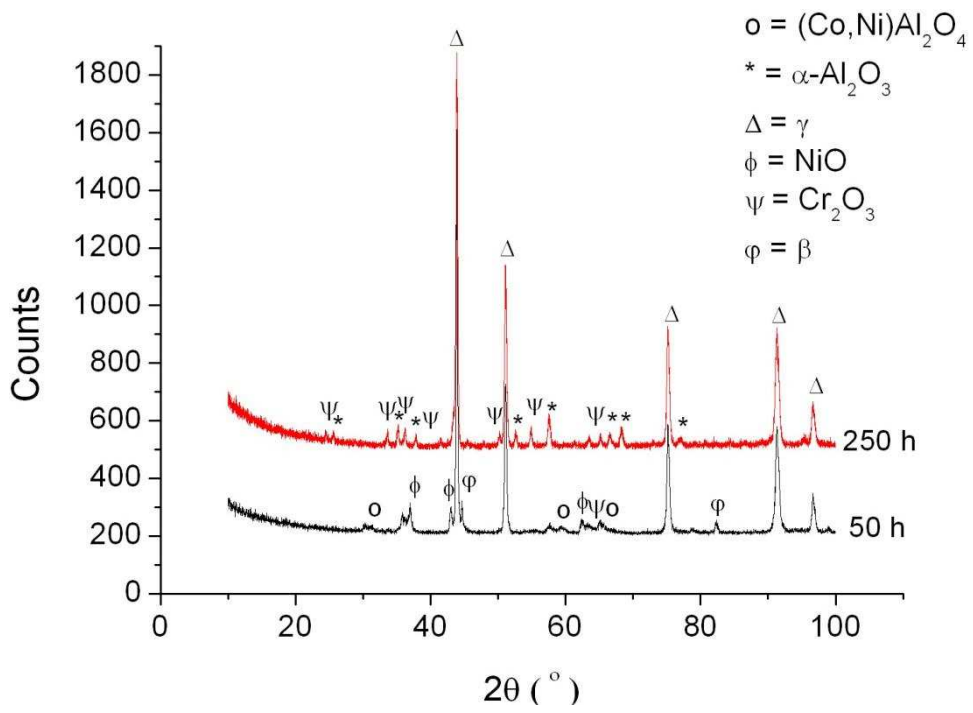

Figure 5-18. XRD spectra of as-sprayed VPS1 coating oxidised at 850 ℃ for exposure times of 50 & 250hours.

5-2- Oxidation of heat treated coatings

All samples (free standing coatings) for this part of the work were heat treated prior to oxidation tests. The heat treatment conditions are as follows:

1- Samples put in vacuum, in sealed quartz tubes;

2- Samples in tubes heated at 1100 ℃ for 3 hours;

3- Samples in tubes furnace cooled to room temperature.

5-2-1- HVOF coatings

Oxidation temperature of 1100 ℃

Figure 5-19 illustrates SEM micrographs of heat treated oxidised HVOF1 coatings for various exposure times. Unlike the as-sprayed oxidised coatings, only a single oxide layer can be observed. EDX analysis of this layer revealed high aluminium and oxygen quantities. As the exposure time increased the oxide thickness increased.

XRD analysis of the heat treated oxidised coatings confirmed the presence of alumina, however, peaks associated with spinel oxides, such as $NiAl_2O_4$ and $CoAl_2O4$, were also observed; see Figure 5-20. XRD analysis shows the presence of the spinel oxides to a much lesser extent than was seen in the as-sprayed oxidised coatings, as their peak intensities are much lower than the peak intensity for alumina, in contrast to as-sprayed oxidised coatings XRD results (see Figure 5-2). Also, it can be seen in Figure 5-20 that the spinel peaks do not tend to increase in intensity as the exposure time increases (e.g. look at spinel peaks at $2\theta°$ of ~32°, 57°, 59° and 65°), whereas the alumina peaks increase in intensity as the exposure time increases.

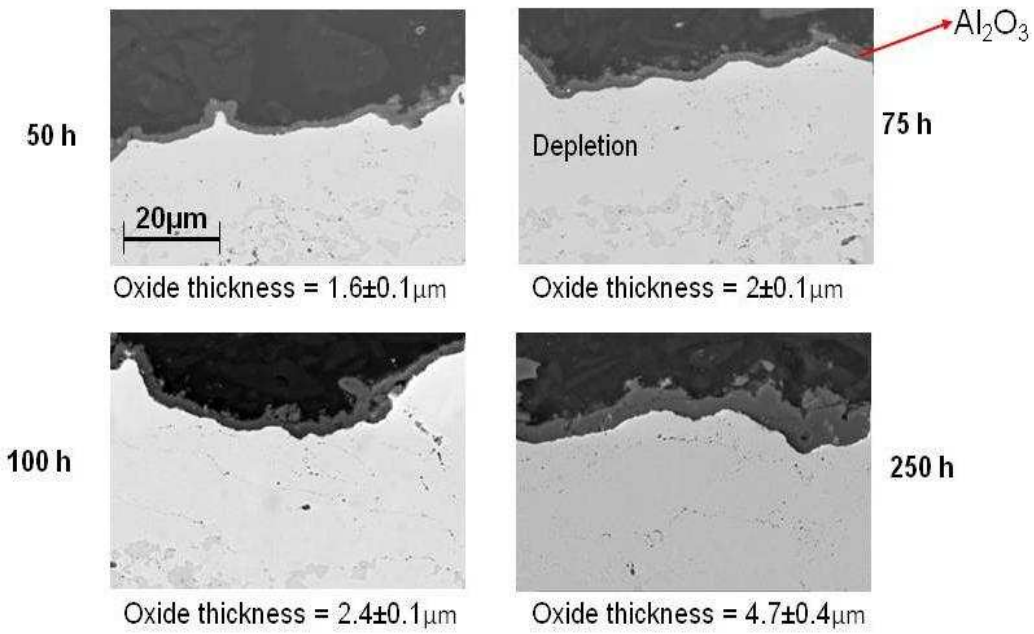

Figure 5-19. SEM micrograph of heat treated HVOF1 coating oxidised at 1100℃ for different exposure times. A single alumina scale is visible. All images are in BSE mode and are at the same magnification.

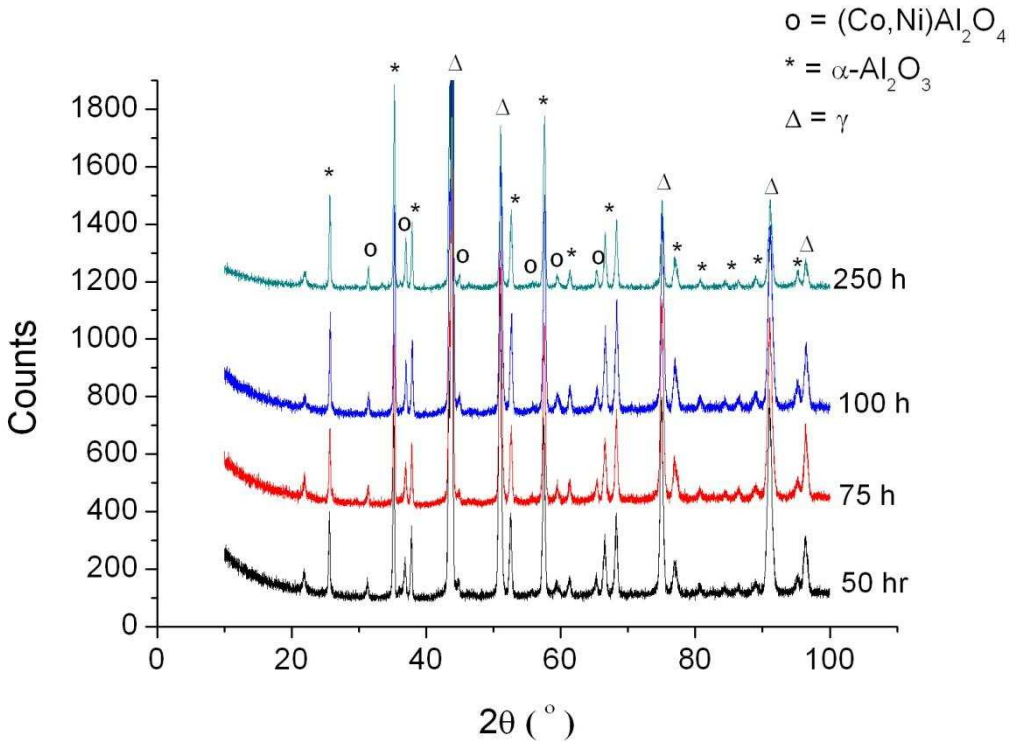

Figure 5-20. XRD spectra of heat treated oxidised at 1100℃ HVOF1 coating for various exposure times.

An average of the extent of the β depletion zone for heat treated oxidised HVOF coating for different exposure times is illustrated in Table 5-2.

Table 5-2. β depletion zone as a function of exposure time for heat treated oxidised HVOF coatings.

Exposure time (h)	β depletion zone (μm)		
	HVOF1	HVOF2	HVOF3
50	20±2	27±1	174±3
75	26±1	30±1	167±7
100	32±1	38±1	181±5
250	52±2	40±1	—

Similar behaviour for HVOF2 and HVOF3 heat treated oxidised coatings were observed. In all cases a single alumina layer was initially present, see Figure 5-21. However, a second layer was starting to form for HVOF3 coating, especially after longer exposure times, see Figure 5-22. EDX analysis of this brighter upper layer revealed that this layer is enriched in Al, O, Co and Ni. As can be seen in the case of both HVOF2 and HVOF3 as exposure time increases the oxide thickness increases.

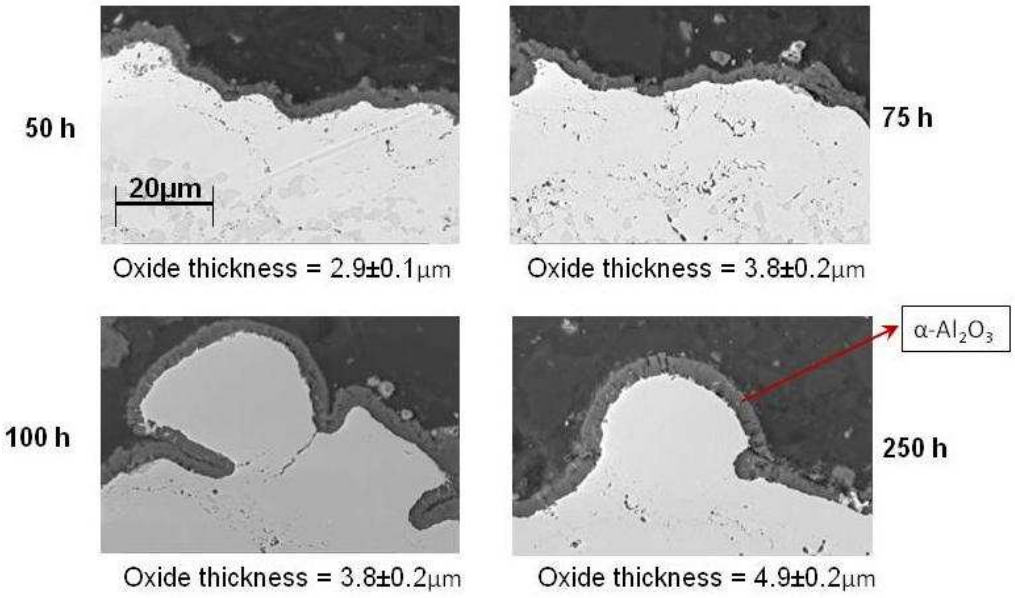

Figure 5-21. SEM micrographs of heat treated oxidised at 1100 ℃ HVOF2 coatings for various exposure times. A single dense alumina layer is visible. All images are in BSE mode and are at the same magnification.

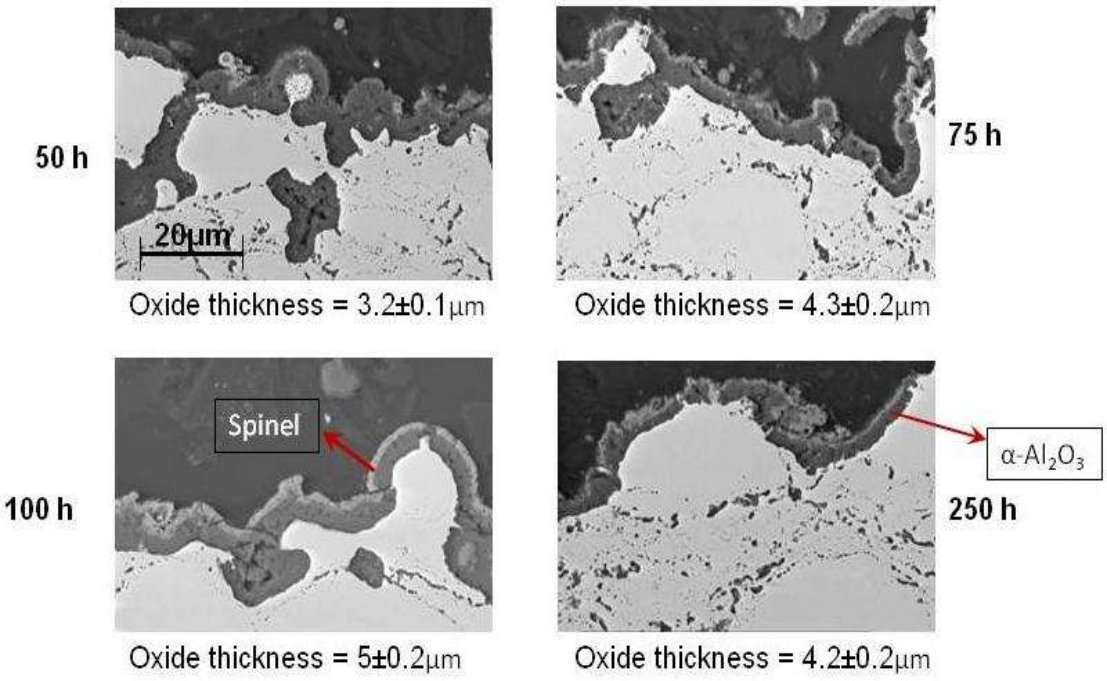

Figure 5-22. SEM micrographs of heat treated oxidised at 1100℃ HVOF3 coatings for different exposure times. As the exposure time increases a second layer is being observed which is enriched in Al, O, Co & Ni. All images are in BSE mode and are at the same magnification.

XRD patterns of heat treated oxidised HVOF2 and HVOF3 coatings are illustrated in Figure 5-23 and Figure 5-24 respectively. Although there is no sign of any spinel oxides in the SEM micrographs of HVOF2 heat treated oxidised images, the XRD spectra shows peaks related to spinel oxides such as $NiAl_2O_4$ and $CoAl_2O_4$. As can be seen, in contrast to as-sprayed oxidised coatings, the intensity for alumina peaks is much higher than the intensity of spinel peaks. However, in the case of HVOF3 coatings where a second layer is visible in the SEM images, the XRD spectra shows growth of the spinel peaks as well as of the alumina peaks, indicating growth in the spinel layer (especially for long exposure times); compare Figure 5-23 with Figure 5-24.

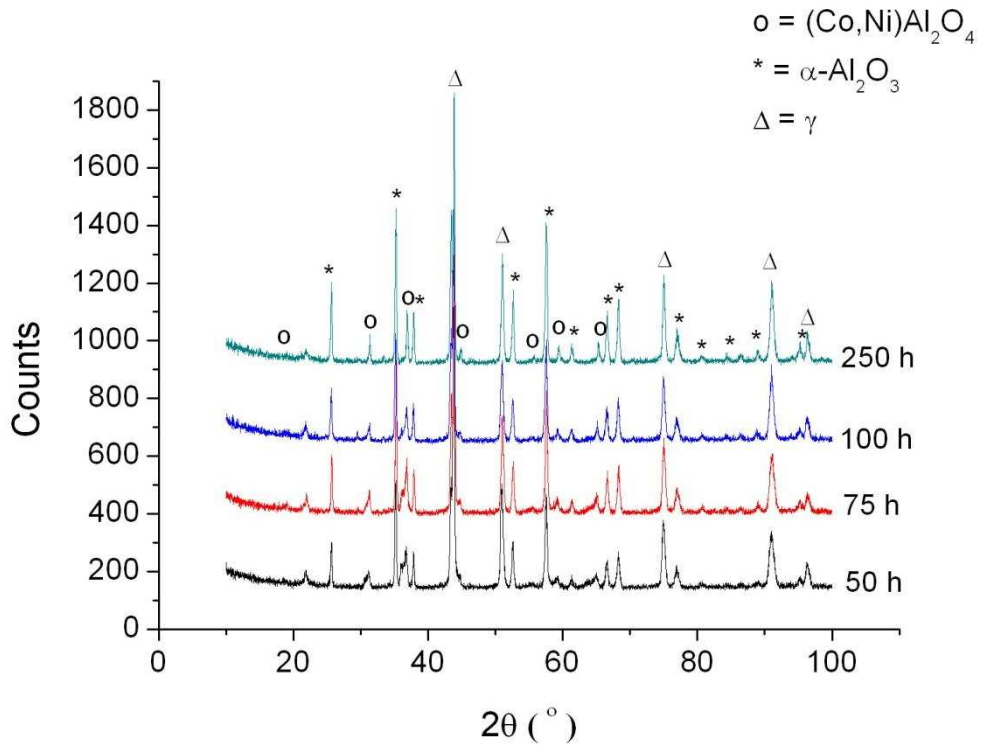

Figure 5-23. XRD spectra of heat treated oxidised at 1100 ℃, HVOF2 coatings for different exposure times.

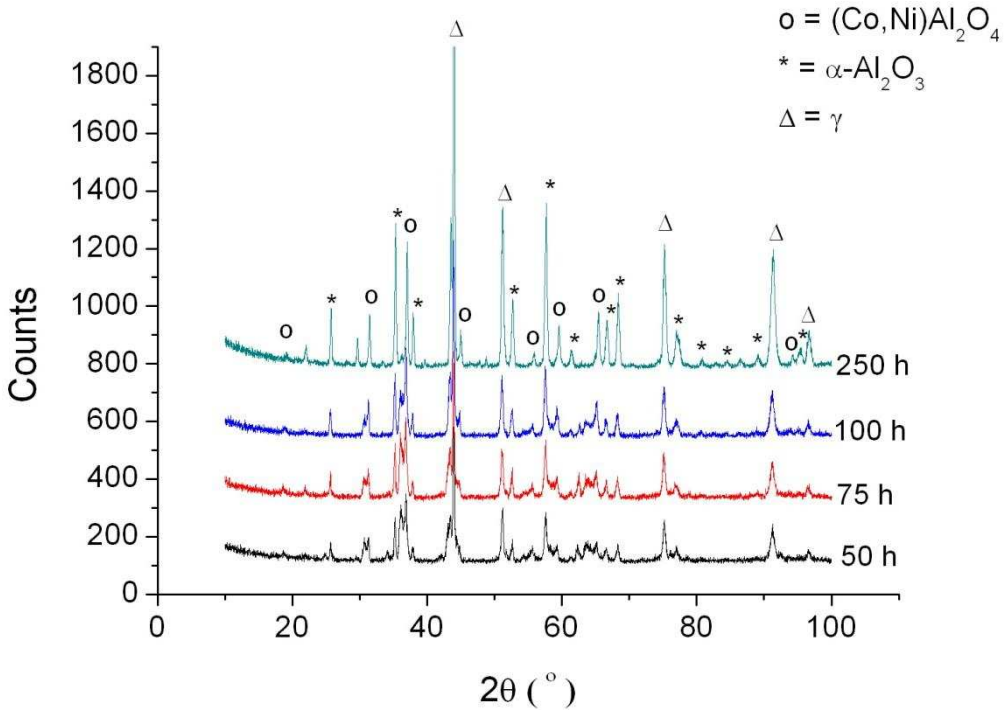

Figure 5-24. XRD spectra of heat treated oxidised at 1100 ℃, HVOF3 coatings for different exposure times.

Internal oxidation of all three heat treated oxidised HVOF coatings are illustrated in Figure 5-25. As can be seen a very high degree of internal oxidation can be observed for HVOF3 coating. Most of the β phase is consumed and as a result a large depletion area is observed.

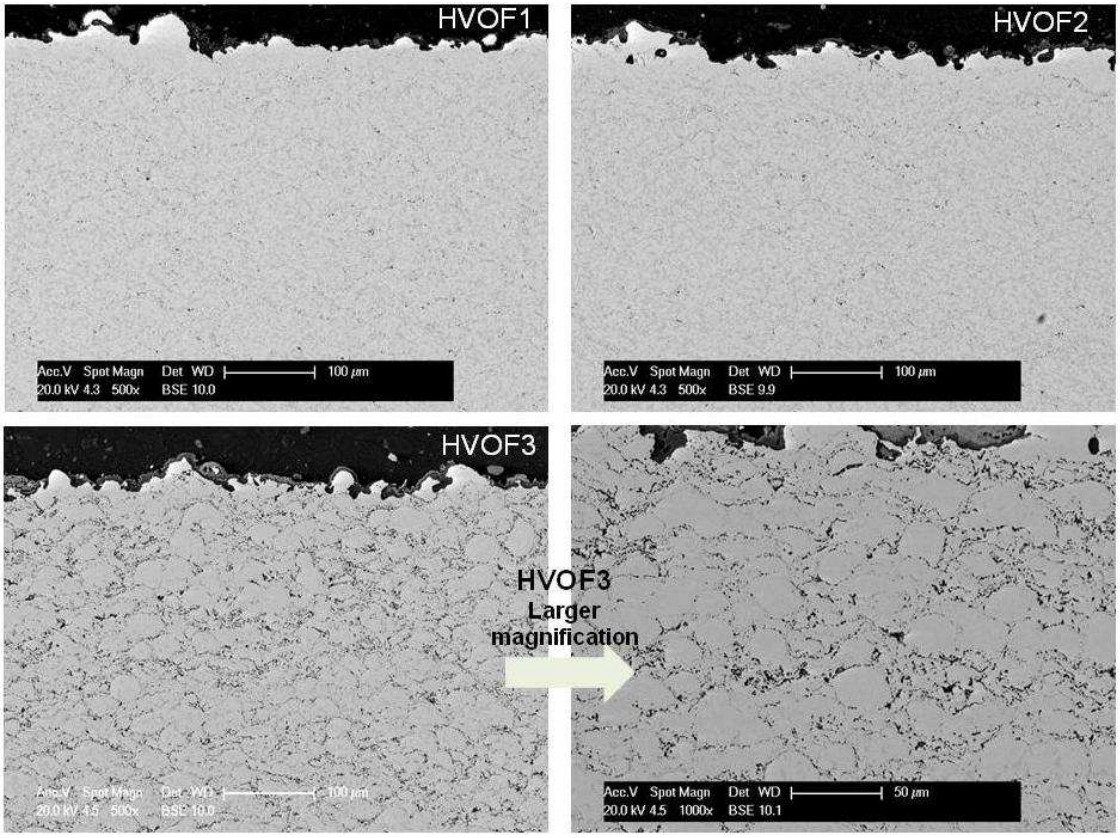

Figure 5-25. Typical SEM micrographs of internal oxidation of heat treated oxidised HVOF1, HVOF2 & HVOF3 coatings (at 1100℃ for 100h). High internal oxidation of HVOF3 coating has resulted in a large β depletion area. All images are in BSE mode.

Oxidation temperature of 850 ℃

Figure 5-29 illustrates SEM micrographs of HVOF1 coating oxidised at 850℃ for periods of 50 and 250 hours. Only a very thin oxide layer is seen. Unlike the HVOF coatings oxidised at 1100℃, where a clear difference was seen between the as-sprayed oxidised and heat treated oxidised coatings; a significant difference between the oxide layer of the as-sprayed oxidised at 850℃ and the heat treated oxidised at 850℃ HVOF coatings was not seen, compare Figure 5-26 with Figure 5-8. Again due to the very thin nature of the oxide layer, an EDX analysis was not possible. However, a clear growth in oxide layer with increase in time is visible.

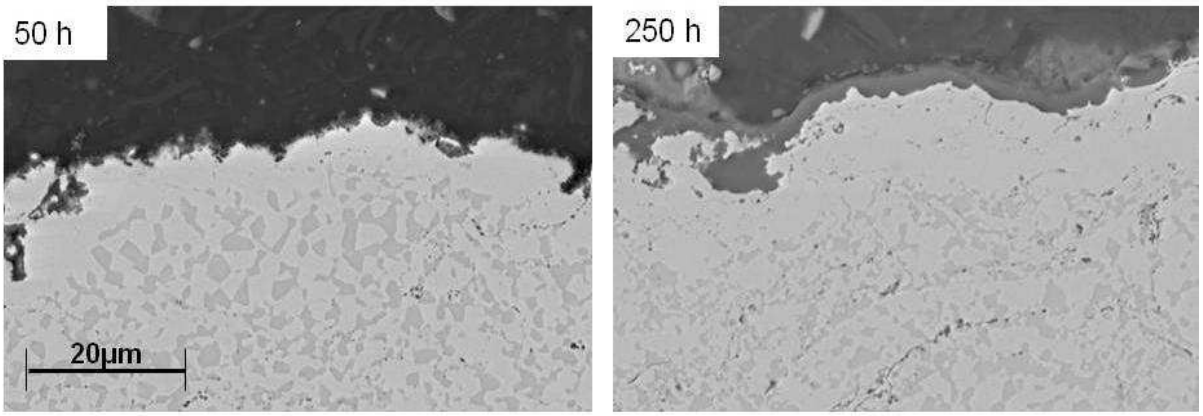

Figure 5-26. SEM micrographs of heat treated HVOF1 coating oxidised at 850℃ for periods of 50 and 250 hours. A single oxide layer is visible. All images are in BSE mode and are at the same magnification.

The XRD spectra of the HVOF1 coating oxidised at 850℃ for different exposure times can be seen in Figure 5-27. As can be seen, the XRD pattern reveals peaks mainly related to alumina and Cr_2O_3, however, some small peaks related to spinel oxides, especially for the 250h exposure, can be observed.

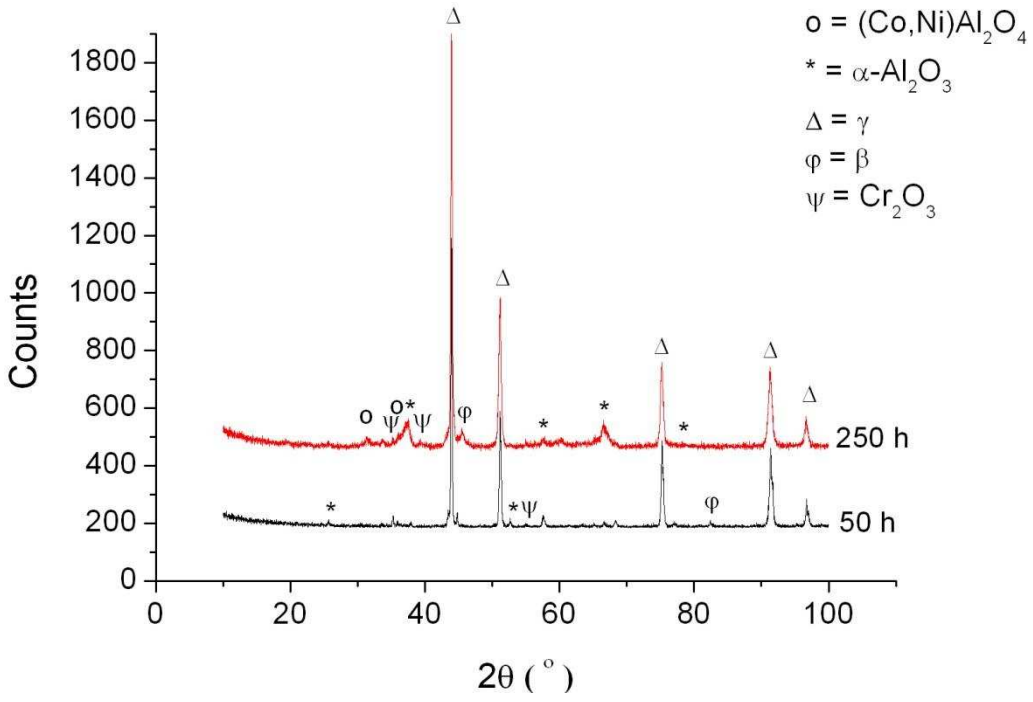

Figure 5-27. XRD spectra of HVOF1 heat treated coating oxidised at 850℃ for periods of 50 & 250 hours.

Similar behaviour was seen for HVOF2 and HVOF3 coatings which have been heat treated and oxidised at 850℃. SEM micrographs illustrated a very thin oxide layer, see Figure 5-28. XRD patterns of these coatings revealed peaks mainly related to alumina and Cr_2O_3; see Figure 5-29 and Figure 5-30. However, there were occasionally one or two peaks related to spinel oxides. If looked at in detail, it could be seen that as exposure time increase alumina peak heights increases, however, a reverse effect is seen for Cr_2O_3, i.e. with increase in exposure time the peak height for the chromium oxide seems to decrease (see Figure 5-29).

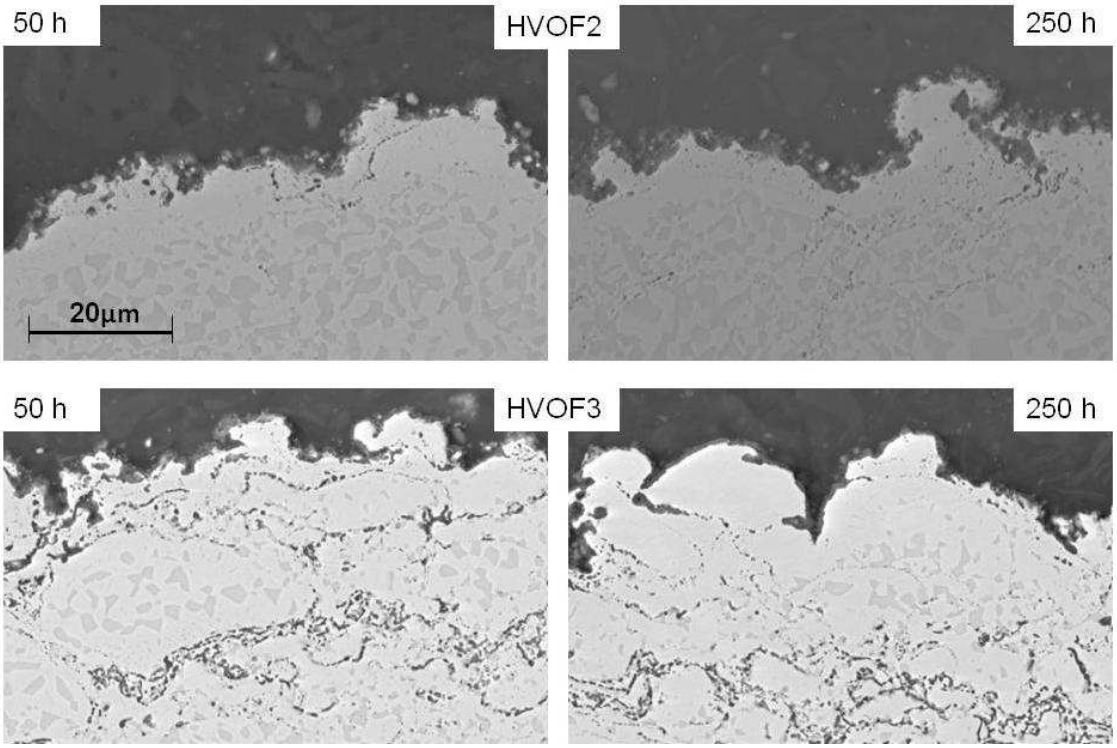

Figure 5-28. SEM micrographs of HVOF2 & HVOF3 heat treated coatings oxidised at 850 ℃ for various exposure times of 50 & 250 hours.

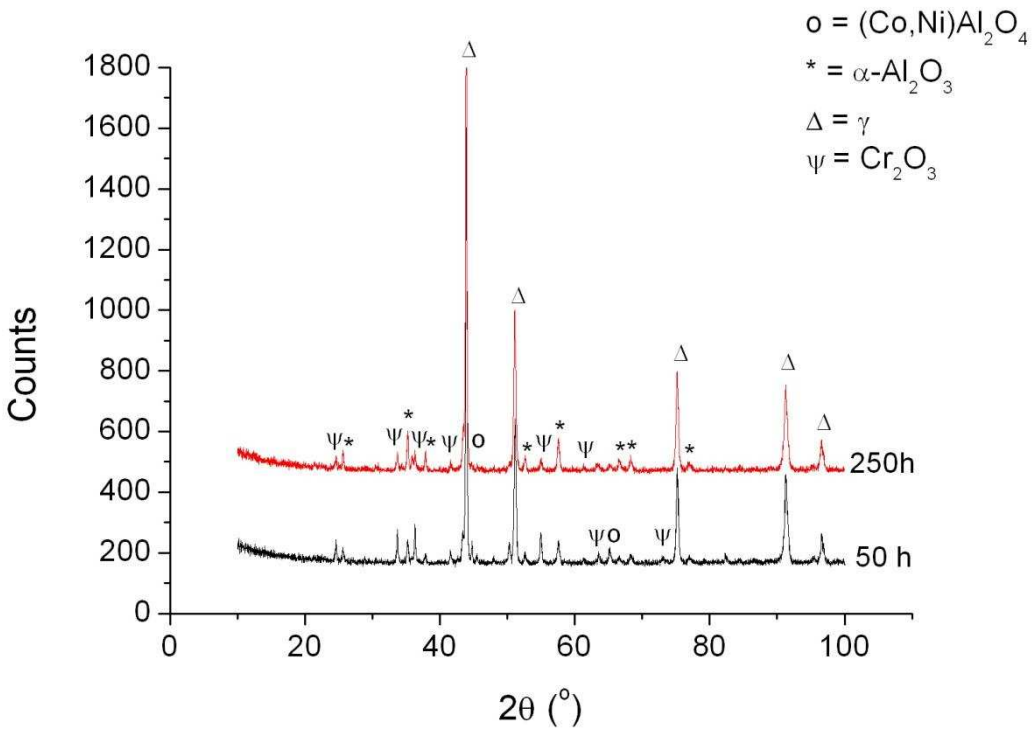

Figure 5-29. XRD pattern for HVOF2 heat treated coating oxidised at 850 ℃ for 50 & 250 hours.

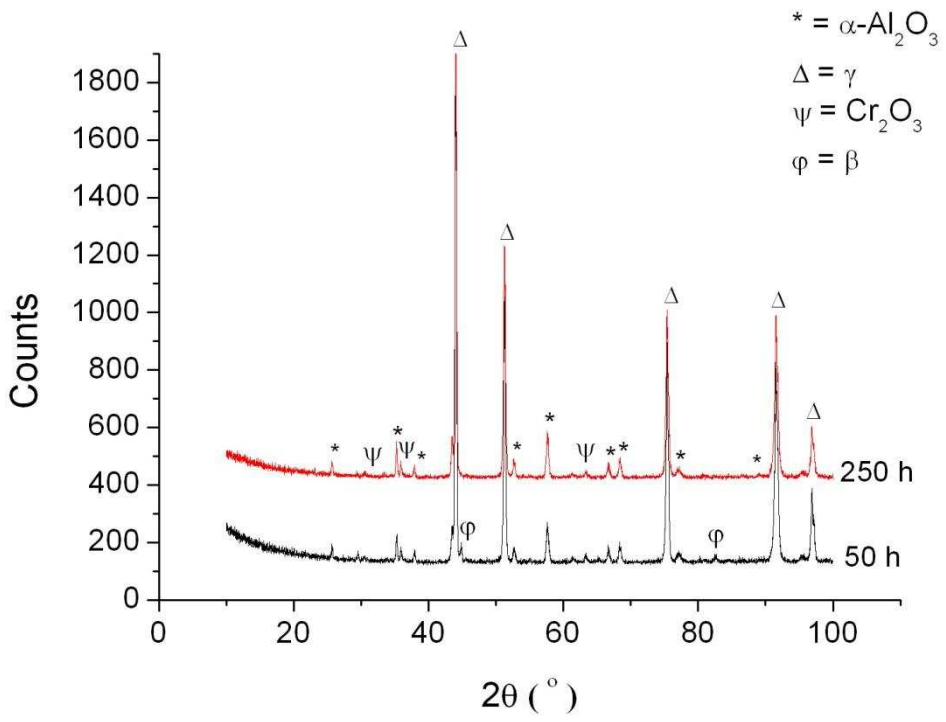

Figure 5-30. XRD pattern for HVOF3 heat treated coating oxidised at 850 ℃ for 50 & 250 hours.

5-2-2- VPS coating

Oxidation temperature of 1100°C

SEM images of heat treated oxidised VPS1 coating for various exposure times can be seen in Figure 5-31. As can be seen, similarly to HVOF heat treated oxidised coatings, only a single oxide layer is visible. EDX analysis of this layer revealed high Al and oxygen contents. As can be seen from the SEM images, as the exposure time increases the oxide thickness also increases.

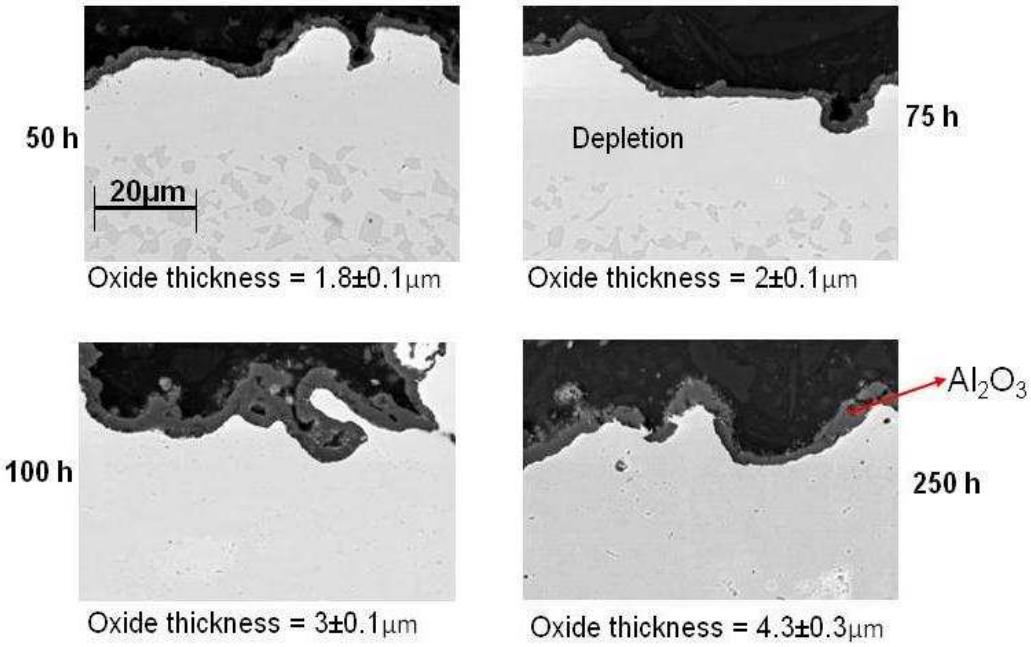

Figure 5-31. SEM micrographs of heat treated oxidised at 1100℃ VPS1 coating for various exposure times. A single alumina layer can be observed. All images are in BSE mode and are at the same magnification.

This single oxide layer was confirmed to be alumina by XRD, see Figure 5-32. However, as for HVOF heat treated oxidised coatings, although only a single oxide layer is visible in the SEM images, peaks related to spinel oxides can be seen in the XRD spectra. Once more, if looked at in more detail it can be seen that the spinel oxide peaks do not grow in intensity as much as alumina peaks, i.e. an increase in relative peak height for alumina peaks.

There are some split peaks (e.g. 100 hour exposure time pattern 2θ° of ~30° and ~36°); this is due to the fact that spinel peaks of different types have similar 2θ° values and in this case this is related to two distinct spinels, a (Co,Ni) spinel and a Cr spinel.

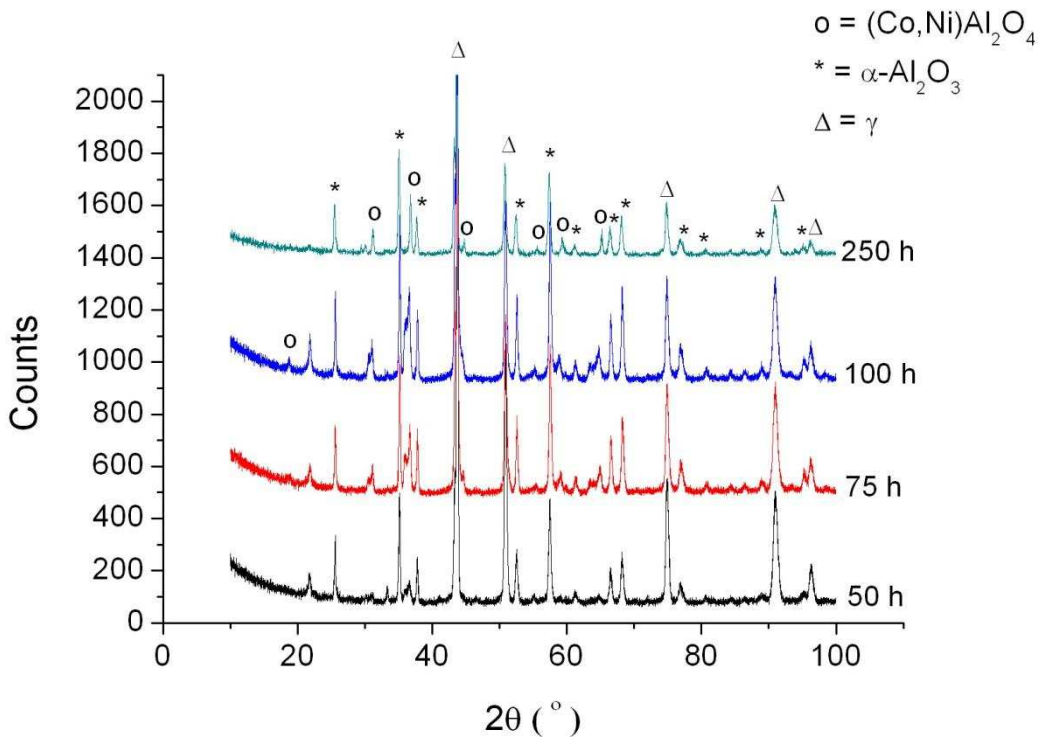

Figure 5-32. XRD spectra of heat treated oxidised at 1100℃ VPS1 coating for various exposure times.

The internal structure of the heat treated oxidised VPS1 coating can be seen in Figure 5-33, it has a similar structure to that of as-sprayed oxidised VPS1 (see Figure 5-16). There is only a small amount of oxide stringers present at the interface of different passes. The β depletion area can be observed near the surface.

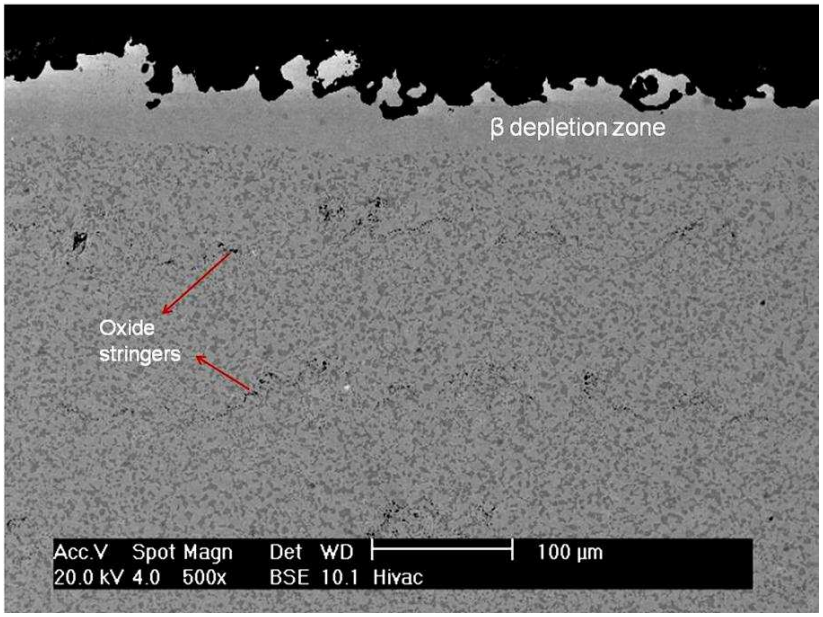

Figure 5-33. Typical SEM micrograph of heat treated oxidised at 1100℃ for 100h VPS1 coating. The only internal oxidation seen is at the interface of the passes in forms of oxide stringers. The β depletion zone is observed at the surface of the coating where the β phase has been consumed in order to form the alumina protective layer.

Oxidation temperature of 850 ℃

An SEM micrograph of the VPS1 heat treated coating oxidised at 850℃ is illustrated in Figure 5-34. Once more, a very thin oxide layer is visible at both exposure times of 50 and 250 hours. It is seen that oxides have penetrated into the coating after 250 hours exposure. XRD analysis of the coatings revealed the presence of alumina and Cr_2O_3 oxides, see Figure 5-35. However, peaks related to spinel oxides could also be seen in smaller intensities, suggesting this phase is not present in very large amounts. Compared to HVOF coatings, peaks related to NiO could also be seen showing a more complex type of oxides for VPS coating. Similar to heat treated oxidised at 850℃ HVOF coatings, the peak intensity for the chromium oxide seems to decrease as the exposure time increases from 50 to 250 hours.

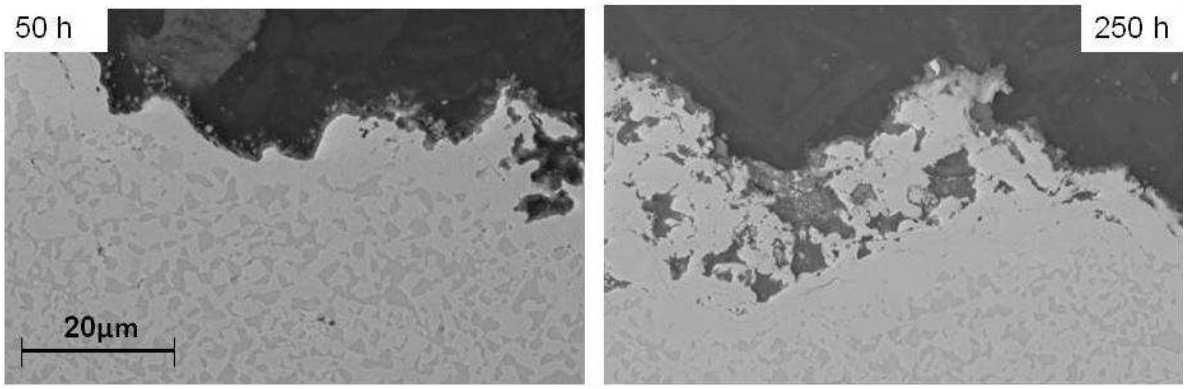

Figure 5-34. SEM micrograph of VPS heat treated coating oxidised at 850 ℃ for exposure times of 50 & 250hours.

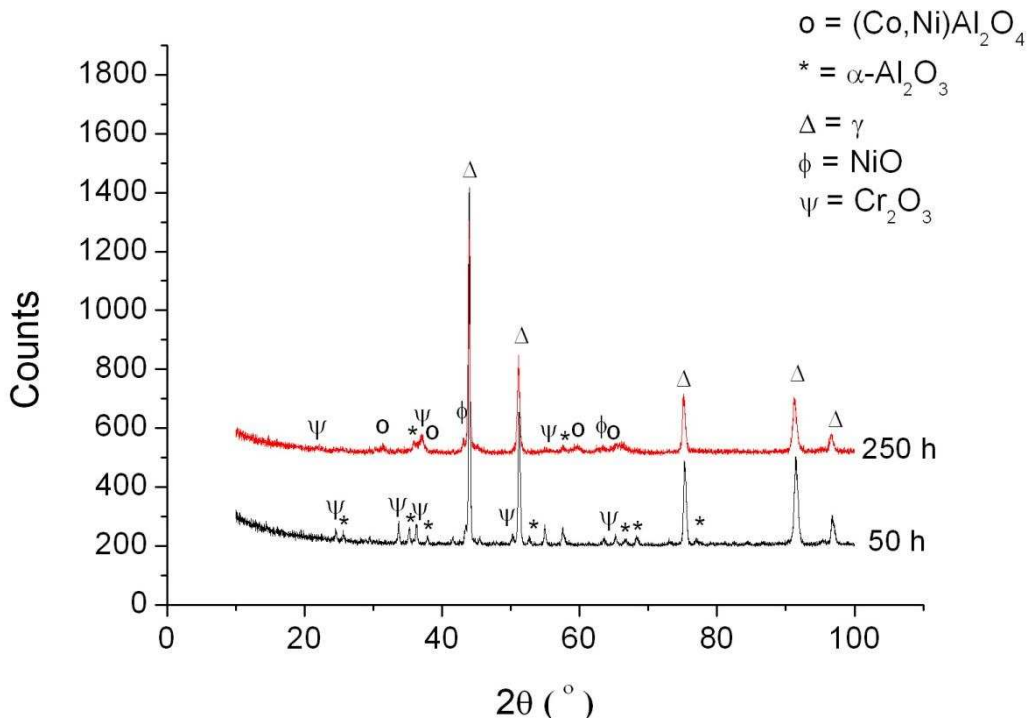

Figure 5-35. XRD spectra of VPS1 heat treated coating oxidised at 850 ℃ for various exposure times of 50 & 250 hours.

5-3- Thermogravimetric analysis (TGA)

The TGA analysis was carried out on both HVOF and VPS coatings in as-sprayed and heat treat conditions at 1100℃ in air. For more information see section 3-3-1 of chapter 3.

TGA results of HVOF1, HVOF2, HVOF3 and VPS1 as-sprayed coatings are illustrated in Figure 5-36. The K_p values calculated from the graphs are illustrated in Table 5-3. The K_p values were calculated by the method mentioned in reference [2], which takes into account the need to disregard results corresponding to transient and/or time to reach the target temperature. In this case the K_p values were determined using data from 500 minutes onwards. As can be seen for the as-sprayed coatings, HVOF3 by far has the highest oxidation rate followed by VPS1, HVOF1 and HVOF2.

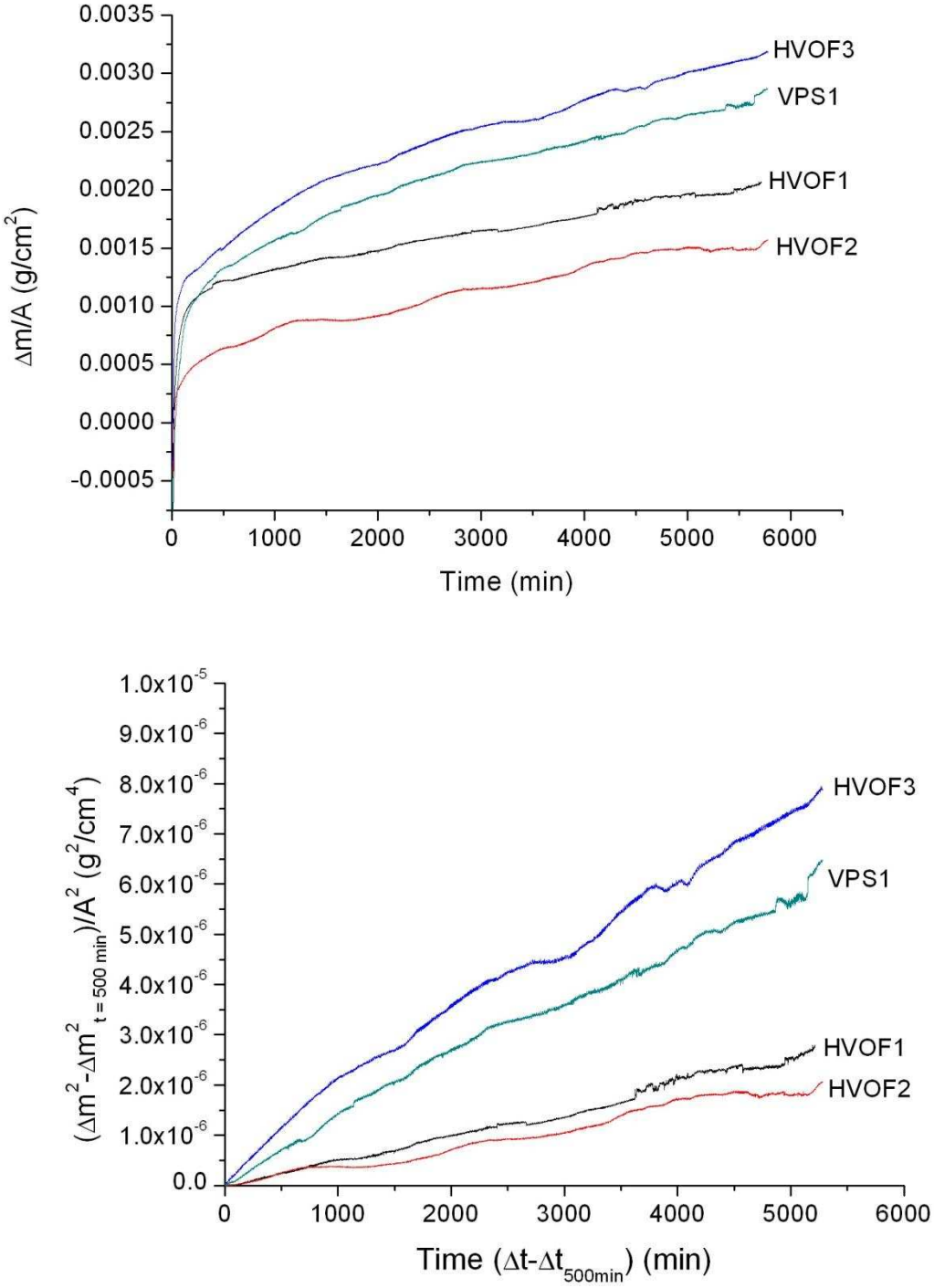

Figure 5-36. TGA graphs of HVOF1, HVOF2, HVOF3 & VPS1 as-sprayed coatings oxidised at 1100°C for 96 h.

Table 5-3. K_p values calculated from TGA graphs of as-sprayed HVOF1, HVOF2, HVOF3 & VPS1 coatings.

	HVOF1	HVOF2	HVOF3	VPS1
K_p ($g^2/cm^4/s$)	8.58×10^{-12} $R^2 = 0.990$	6.61×10^{-12} $R^2 = 0.976$	2.31×10^{-11} $R^2 = 0.993$	1.85×10^{-11} $R^2 = 0.992$

Thermogravimetric analysis of heat treated HVOF1, HVOF2, HVOF3 and VPS1 coatings carried out at 1100℃ in air is illustrated in Figure 5-37.

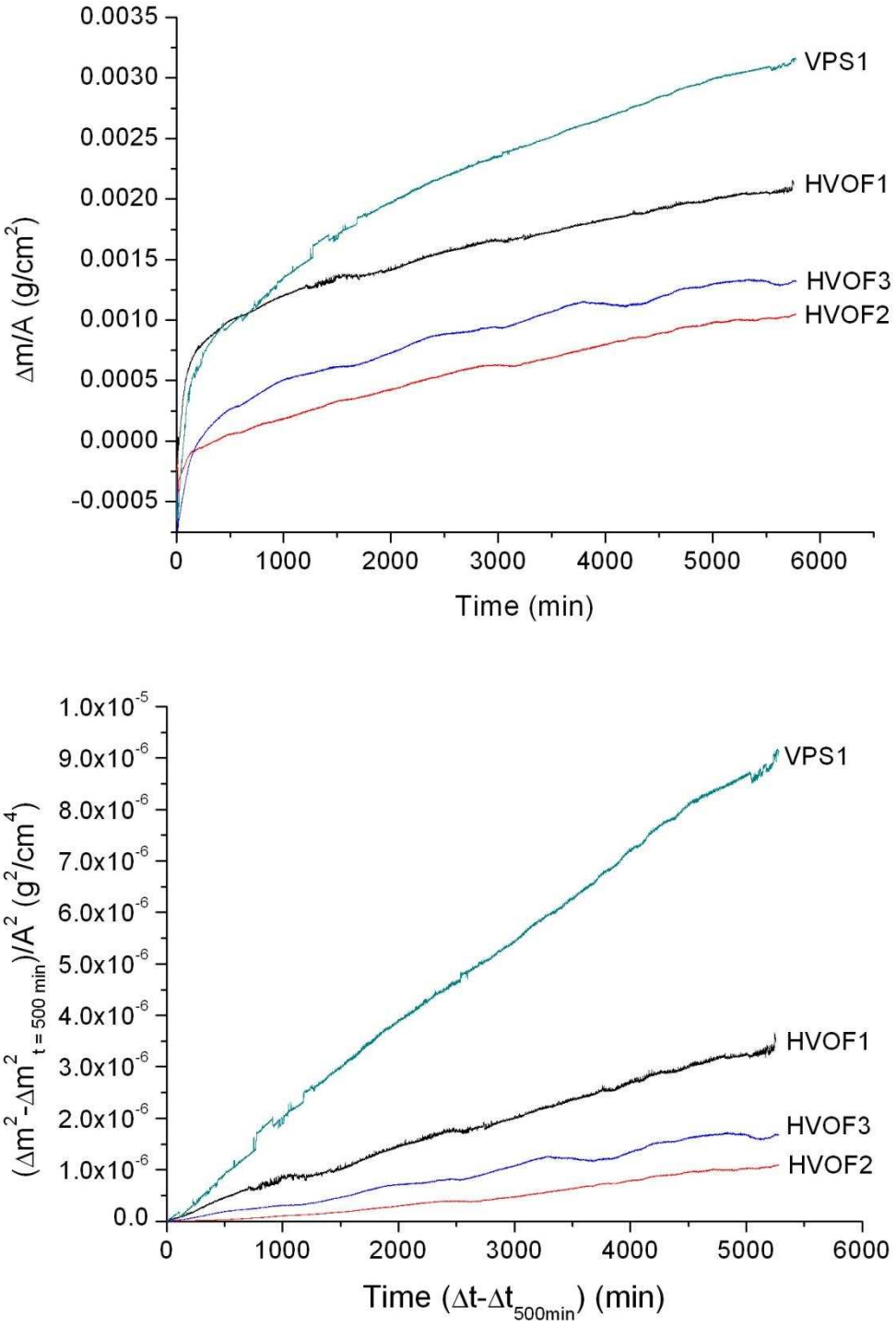

Figure 5-37. TGA graphs of heat treated HVOF1, HVOF2, HVOF3 & VPS1 coatings at 1100℃ for 96h.

Table 5-4 illustrates the K_p values calculated for the heat treated coatings. As can be seen for the heat treated oxidised samples, VPS1 has the greatest oxidation rate followed by HVOF1, HVOF3 and HVOF2 respectively. For HVOF coatings, when comparing the K_p values for heat treated oxidised coatings with the K_p values of as-sprayed oxidised, reported in Table 5-3, it can be seen that heat treatment prior to oxidation has increased the K_p for HVOF1 by 23%, whereas it has decreased the K_p for HVOF2 and HVOF3 coatings by 44% and 75% respectively. Furthermore, for the VPS coating, heat treatment prior to oxidation has increased the K_p by 55%. For a better comparison Figure 5-38 illustrates the TGA graphs for all as-sprayed and heat treated coatings.

Table 5-4. K_p values calculated from TGA graphs of heat treated HVOF1, HVOF2, HVOF3 & VPS1 coatings.

	HVOF1	HVOF2	HVOF3	VPS1
K_p ($g^2/cm^4/s$)	1.06×10^{-11} $R^2 = 0.996$	3.72×10^{-12} $R^2 = 0.980$	5.77×10^{-12} $R^2 = 0.987$	2.87×10^{-11} $R^2=0.996$

Furthermore, in order to check the K_p measured from the experimental results, oxide thickness has been calculated from the measured K_p using the calculation mentioned in section 3-3-3 of chapter 3. The calculated oxide thickness was than compared to the measured oxide thickness, from SEM images. Table 5-5 illustrates the calculated oxide thickness of both as-sprayed and heat treated HVOF and VPS coatings.

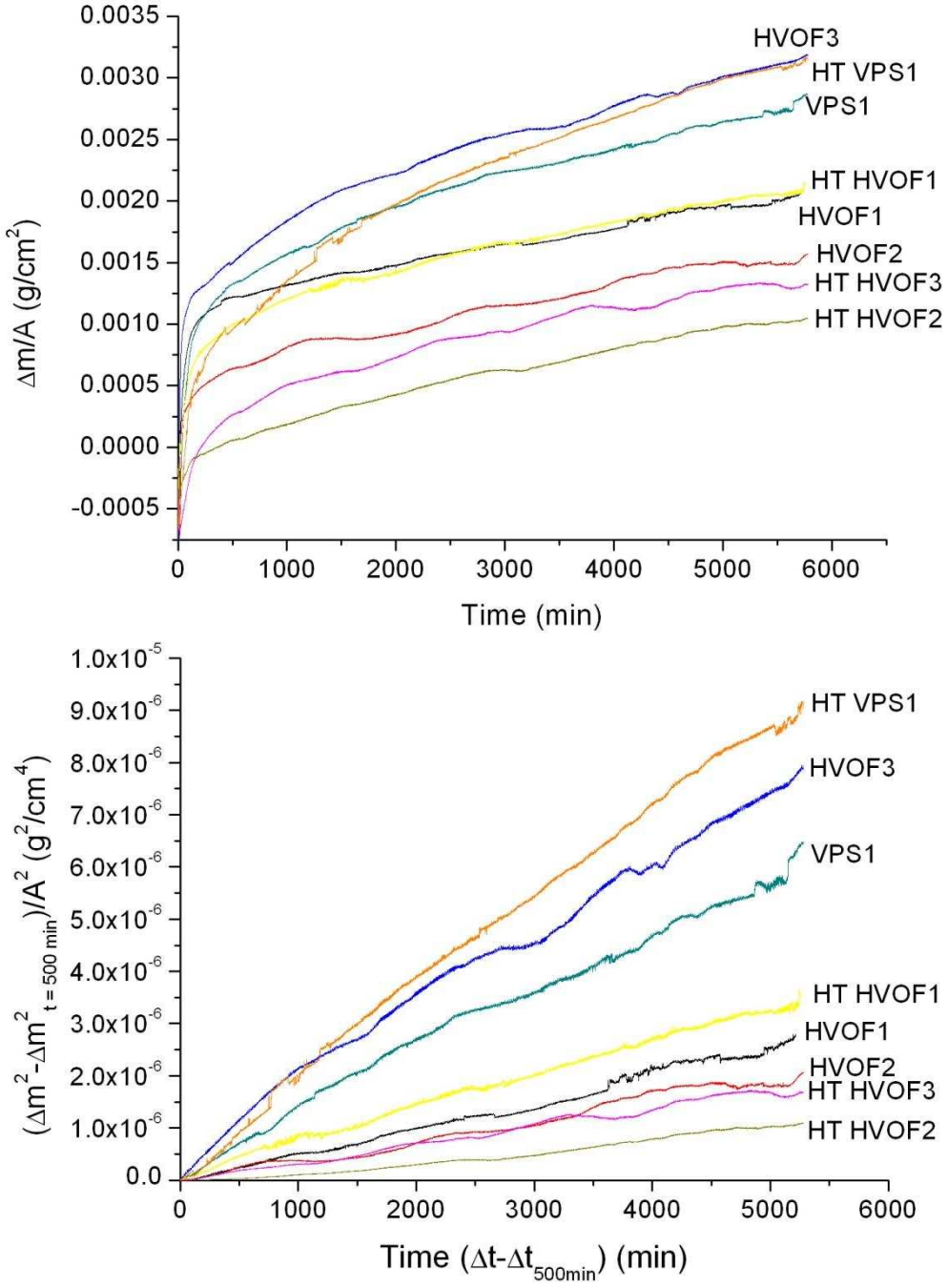

Figure 5-38. TGA graphs of as-sprayed and heat treated HVOF & VPS coatings, HT stands for heat treated.

Table 5-5. Comparison of calculated oxide thickness (from K_p) & measured oxide thickness (from SEM images) for different coatings. At least 35 measurements were carried out for each value of measured oxide thickness. Error bars are standard error in mean.

Coating type	Calculated oxide thickness (μm)	Measured oxide thickness (for 100 hour exposure, μm)
As-sprayed		
HVOF1	4.1	4.5 ± 0.3
HVOF2	3.6	5 ± 0.1
HVOF3	6.8	5.5 ± 0.1
VPS1	6.1	4.7 ± 0.2
Heat treated		
HVOF1	4.6	2.4 ± 0.1
HVOF2	2.7	3.8 ± 0.2
HVOF3	3.4	5 ± 0.3
VPS1	7.6	3 ± 0.1

A summary of the numerical results presented in this chapter is illustrated in Table 5-6.

Table 5-6. A summary of the results presented in chapter 5.

Coating type		Exposure time (h)	Oxides formed	Depletion zone (μm)	K_p $g^2/cm^4/s$ (96 h)	Oxide thickness measured (μm)	Oxide thickness calculated (μm)
as-sprayed	HVOF1	50	Spinel & alumina	24±1	8.58×10^{-12} R^2=0.990	4.6±0.2	
		75		24±1		4.7±0.2	
		100		29±2		4.5±0.3	4.1
		250		47±3		7.3±0.2	
	HVOF2	50		25±2	6.61×10^{-12} R^2=0.976	5±0.4	
		75		27±2		5.1±0.2	
		100		31±2		5±0.2	3.6
		250		37±2		7.1±0.4	
	HVOF3	50		103±3	2.31×10^{-11} R^2=0.993	4.2±0.2	
		75		127±5		4.8±0.2	
		100		164±6		5.5±0.2	6.8
		250		—		7.5±0.2	
	VPS1	50		28±1	1.85×10^{-11} R^2=0.992	4.3±0.2	
		75		32±3		4.4±0.2	
		100		36±2		4.7±0.2	6.1
		250		54±3		7.7±0.2	
Heat treated	HVOF1	50	Alumina	20±2	1.06×10^{-11} R^2=0.996	1.6±0.1	
		75		26±1		2±0.1	
		100		32±1		2.4±0.1	4.6
		250		52±2		4.7±0.4	
	HVOF2	50		27±1	3.72×10^{-12} R^2=0.980	2.9±0.1	
		75		30±1		3.8±0.2	
		100		38±1		3.8±0.2	2.7
		250		40±1		4.9±0.2	
	HVOF3	50		174±3	5.77×10^{-12} R^2=0.987	3.2±0.1	
		75	Alumina	167±7		4.3±0.2	
		100	Spinel & alumina	181±5		5±0.2	3.4
		250		—		4.2±0.2	
	VPS1	50	Alumina	16±1	2.87×10^{-11} R^2=0.996	1.8±0.1	
		75		29±2		2±0.1	
		100		41±2		3±0.1	7.6
		250		44±2		4.3±0.3	

5-4- Discussion

This section is divided into two parts. The first part provides the discussion for the behaviour of the coatings oxidised in as-sprayed and heat treated conditions. The second part discusses the TGA results obtained for the as-sprayed and heat treated HVOF and VPS coatings and the effect of heat treatment on the K_p results.

5-4-1- Oxidation following heat treatment

For as-sprayed oxidised at 1100℃ HVOF and VPS coatings a dual oxide layer was observed where the upper layer was spinel and the inner layer was alumina. SEM analysis of the internal structure of the as-sprayed oxidised coatings revealed that the HVOF3 coating had a large amount of internal oxides and had, by far, the fewest β particles as compared to other HVOF and VPS coatings, see Figure 5-7 and Figure 5-16. This is an indication of consumption of the β phase internally and hence a far shorter lifetime for this coating. Whereas for HVOF1, HVOF2 and VPS1 coatings where there is not a large degree of internal oxidation, all the β phase will be available as an Al reservoir which will enhance protection.

For heat treated and oxidised at 1100℃ coatings, in both HVOF and VPS, a single alumina layer was observed throughout the 250 hours exposure time. However, the presence of a second layer for the heat treated oxidised HVOF3 coating, after 100 hours exposure, was seen, see Figure 5-22. Furthermore, a higher degree of internal oxidation and lower amount of β phase could be seen for the HVOF3 heat treated oxidised coating. Based on the above observations, the reason for the presence of a second layer for the heat treated oxidised HVOF3 coating can be attributed to the consumption of the β phase with increase in exposure time, and hence a large

depletion zone resulting in formation and growth of oxides other than alumina, e.g. chromium oxide, spinel, etc.

While no significant differences could be seen in the SEM images of the HVOF as-sprayed oxidised and heat treated oxidised at 850℃, some differences could be observed in the XRD patterns. Similar to the oxidised at 1100℃ HVOF coatings, heat treatment seems to have prevented the growth of the spinel oxides for the heat treated oxidised compared to the as-sprayed oxidised coatings, compare Figure 5-27, Figure 5-29 and Figure 5-30 with Figure 5-9, Figure 5-12 and Figure 5-13. As can be seen in the XRD patterns, much bigger and clearer spinel peaks could be observed in the case of as-sprayed oxidised coatings, whereas for the heat treated oxidised coating, the majority of the peaks revealed corresponded to the Al and Cr oxides.

Thermodynamic stability diagrams, such as the diagram for Ni-Al-O seen in Figure 5-39, can be used to rationalise the oxide phases that form. The diagram shows the equilibria between the phases in this system, i.e. Al_2O_3, $NiAl_2O_4$, NiO and Ni-Al alloy; with the ordinate axis being oxygen activity (a_O) and the abscissa being Al activity (a_{Al}).

For the present system, a_O is maximum at the surface and decreases going into the alloy while a_{Al} is minimum at the scale surface and increases to a maximum inside the alloy.

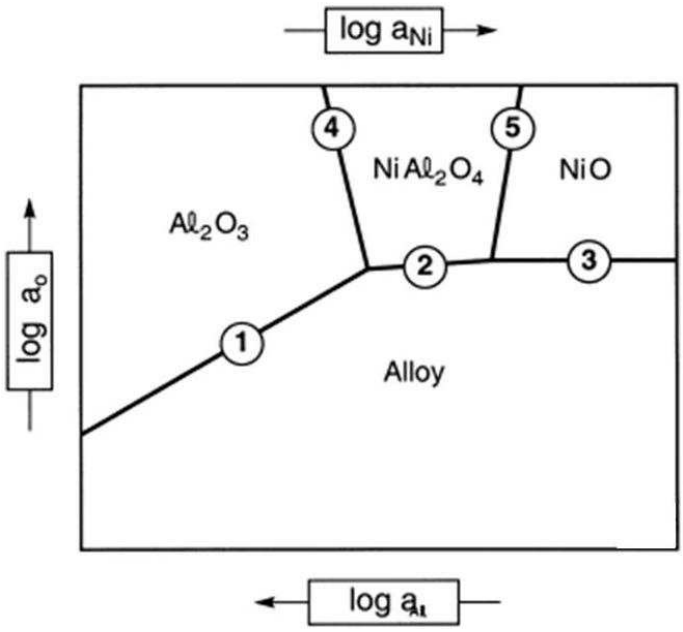

Figure 5-39. The thermodynamic stability diagram for a Ni-Al-O system [3].

The important equilibria described in Figure 5-39 are as follows [3]:

Al_2O_3-alloy equilibrium	$2Al(alloy) + 3O = Al_2O_3$	(5-1)
$NiAl_2O_4$-alloy equilibrium	$Ni(alloy) + 2Al(alloy) + 4O = NiAl_2O_4$	(5-2)
NiO-alloy equilibrium	$Ni(alloy) + O = NiO$	(5-3)
Junction of lines (1) & (2)	$3Ni(alloy) + 4Al_2O_3 = 3NiAl_2O_4 + 2Al(alloy)$	(5-4)
Junction of lines (2) & (3)	$3Ni(alloy) + NiAl_2O_4 = 4NiO + 2Al(alloy)$	(5-5)

The lines (4) and (5) involve a two phase equilibria that can be described through reactions (5-4) and (5-5), respectively expect that the activities of Al and Ni must be those in oxide phases.

Although the alloy used in this work is much more complex than the Ni-Al-O system presented in Figure 5-39, the basic concepts indicated in this diagram are still useful in the discussion of the present results.

Tang et al. [1, 4] have reported the formation of pure alumina in the beginning stage of oxidation (1 hour exposure at 1000℃) for HVOF sprayed CoNiCrAlY coatings from as-received and cryomilled powder. However, a dual oxide layer (spinel and alumina) has been observed for longer exposure times of 24 and 330 hours at 1000℃. They have discussed their observations such that at the beginning stage of oxidation (1 hour) the Al activity on the surface of the coating is high enough to form Al_2O_3 through reaction (5-1). They have mentioned that as Al is consumed in the coating surface (after 24 hours), the Al depletion near surface becomes so severe that Al activity in the surface drops lower than a certain threshold level where spinel type oxide forms (instead of alumina) as a result of outward diffusion of Cr, Ni, Co from the alloy through the previously formed alumina layer. This is while, it has been reported in [5] the main role of alumina is to inhibit continued ingress of oxygen and other elements and that the transport of reactants such as Cr, Co and Ni through Al_2O_3 is very slow compared to transport through most other oxides [6]. Also, it has been reported by Brandl et al. [7] and Prescott et al. [8] that the diffusion coefficient for Al in Al_2O_3 is higher than that of Cr, Co and Ni in alumina. So if any elements are to diffuse through Al_2O_3 after a short exposure time of 24 hours it is to be Al rather than Co, Ni, or Cr.

As seen in Figure 5-19, Figure 5-21 and Figure 5-22 in this work, the oxidation of heat treated coatings resulted in the formation of a single alumina layer. α-Al_2O_3 is thermodynamically the most stable oxide among all other possible oxides such as spinels, NiO, etc. (see Table 5-7) and hence will form at even very low oxygen partial pressures. Although the heat treatment is nominally carried out in vacuum, there is still some oxygen present. According to above (alumina being thermodynamically the most stable), it is suggested that the oxygen present is enough to form a very thin

layer of alumina and not sufficient to form any types of spinel oxides. This is what is thought to have occurred during the heat treatment of the coatings.

Table 5-7. Free energy of oxide formation from constituent oxides at 727℃ & 1227℃ [4].

Oxide	-ΔG (kJ mol^{-1})	
	727 ℃	1227 ℃
Al_2O_3	1362.4	1146.9
Cr_2O_3	861.6	731
CoO	163.3	127.7
NiO	150.7	108.4
$CoCr_2O_4$	52.6	48.9
$CoAl_2O_4$	29.1	26.9
$NiCr_2O_4$	18.6	21.1
$NiAl_2O_4$	15.3	19.9

Therefore, if what has been reported by Tang et al. [1, 4], that early stage oxidation will form an alumina layer and further oxidation (after 24 hour) will cause the diffusion of Cr, Co and Ni, from the alloy, to form a duplex alumina/spinel layer was true; oxidation of the heat treated coatings carried out in this work where an almost pure alumina layer was formed, as the result of the heat treatment, should have resulted in a dual oxide layer. However, as can be seen in Figure 5-19, Figure 5-21 and Figure 5-31, a single alumina oxide layer is observed for the heat treated oxidised HVOF and VPS coatings.

This observation, i.e. presence of a single alumina layer for heat treated oxidised coatings, can be due to the fact that the thin alumina layer formed as a result of vacuum heat treatment will act as a barrier (transport of reactants such as Cr, Co and Ni through Al_2O_3 is very slow) which separates the coating from the environment during the subsequent oxidation experiments; and as the stability diagram indicates as long as Al activity in the bond coat satisfies $a_{Al} > 10^{-17}$, reaction (5-1) dominates [3],

resulting in Al_2O_3 formation. Hence nucleation of spinel oxides is prevented and the α-Al_2O_3 grows slowly. Wherever, the alumina layer is stable oxygen activity at the interface of coating/TGO is too low to form alternative oxides.

However, as thermal exposure continues, β depletion increases, as can be seen in Table 5-2, resulting in longer distances for Al atoms to diffuse [9]. After very long exposure times, at least greater than 250 hours, where no other oxides other than alumina have been observed in this research work, when Al depletion near the surface becomes severe (known as "intrinsic chemical failure" by Ajdelsztajn et al [6]), as the Al activity decreases the oxygen activity at the coating/TGO interface increases (along line (1) in the stability diagram, Figure 5-39). Whenever the oxygen activity reaches the intersection of lines (1) and (2), see Figure 5-39, the alumina converts to spinel through reaction (5-4). Also, as the oxygen activity of the coating/TGO interface increases (as a result of decrease in a_{Al}) the solubility of Ni and Cr in the alumina layer also increase [3]. This can then result in outward diffusion of Ni and Cr from the existing alumina layer to the surface where oxygen activity is at its highest and form new oxide phases such as spinel on top of the existing alumina layer.

The discussion provided above, explains why a single alumina layer is observed for heat treated oxidised coatings and why a dual oxide layer is observed after long exposure times; as in HVOF3 heat treated oxidised coating (Figure 5-22) where an alumina layer can be seen for exposure times of up to 100 hours and upper spinel scale and an inner alumina scale is visible for higher exposure times of 100 and 250 hours. As can be seen in Table 5-2 and Figure 5-25, after 250 hours almost the entire HVOF3 coating is depleted of the Al rich phase (β phase) and hence no further alumina can form.

In contrast to heat treated oxidised coatings, oxidation of the as-sprayed coatings produced a dual oxide layer consisting of an inner layer of α-Al_2O_3 and an outer spinel layer, see Figure 5-1, Figure 5-3 and Figure 5-4. This dual oxide layer is consistent with results previously reported by other researchers [4, 10-13]. As mentioned before for an alumina scale to form, thermodynamic conditions must be such that reaction (5-1) occurs. During the vacuum heat treatment, due to the very low oxygen partial pressure no oxides other than alumina could form, see Figure 5-39. However, when as-sprayed coatings are oxidised (no prior heat treatment), the initial supply of oxygen is such that not only alumina but other oxides such as spinel and NiO also form via the following reaction, where M indicates other metallic elements.

$$2M(alloy) + O_2 = 2MO \quad (5\text{-}6)$$

Tang et al. [11] have reported that the beginning stage of oxidation (1 hour at 1000℃ for HVOF as-sprayed CoNiCrAlY coatings sprayed from a cryomilled powder) has resulted in the formation of spinel type oxides. This is in contrast to their own observation reported elsewhere [1, 4]. Furthermore, they have reported that compared to the dual oxide layer observed in the as-sprayed oxidised coating, polishing the sample prior to oxidation will result in the formation of a single alumina layer due to removal of the spinel oxides which have formed during the spraying process. This claim was made based on the fact that they have seen a single alumina layer on the top surface of the coating which has been polished while the bulk of the coating (inside of the coating) which has not been polished (and hence the oxides formed during spraying have not been removed) shows oxides other than alumina. Based on the above discussion Tang et al. [11] have claimed that the observation of a single alumina layer after surface polishing is not due to surface roughness but due to the

absence of the oxides formed during spraying. In contrast, Taylor et al. [14, 15] state that surface roughness has an effect on the oxidation behaviour of the MCrAlY coatings. They have reported that depletion rate of Al in the asperity is dependent on the geometry and the volume of each asperity; asperities with large surface area to volume ratios, associated with rough surfaces, accelerate the Al depletion (see Figure 5-40) resulting in the formation of oxides other than alumina.

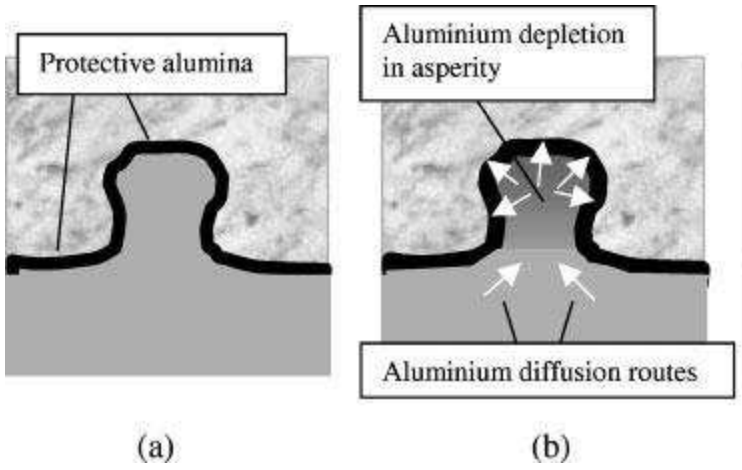

Figure 5-40. Schematic diagram describing (a) sufficient aluminium present in asperity to maintain a protective alumina layer, (b) rapid depletion and restricted replenishment, reducing Al levels within the asperity, due to higher flux of Al into the oxide layer(s) and that arriving to the asperity from the bulk of the coating [15].

The observations in this work demonstrate a mixture of alumina and spinel type oxides for short time oxidation of as-sprayed oxidised coatings, see the 1 hour exposure SEM image in Figure 5-1 and Figure 5-14.

So the reason for a dual oxide layer observed in as-sprayed oxidised coatings (see Figure 5-1, Figure 5-3 and Figure 5-4) can be discussed as follows. Due to the high oxygen activity at the coating surface at the beginning stage of oxidation, a thin layer of oxide mixtures of alumina and spinel type oxides forms. As the oxidation continues Al from the alloy reduces the MOs in the oxide mixture via the following reaction [6].

$$2Al(alloy) + 3MO = Al_2O_3 + 3M(alloy) \quad (5\text{-}7)$$

This phenomenon can result in the segregation of the alumina layer from the spinel type oxides. As the oxide layer starts to grow a gradient of oxygen will form across the oxide layer, with the top surface having the highest oxygen activity and the coating/TGO interface having the lowest oxygen activity. Since spinel oxides will form where the oxygen activity is high and alumina can also form where the oxygen activity is low, the spinel oxides will grow at the upper surface and the alumina scale will grow at the coating/TGO interface, where the oxygen activity is low (at low a_O only alumina forms). Based on the discussion above a dual oxide with an upper spinel layer and a lower alumina layer is expected for as-sprayed oxidised coatings.

The above discussion highlights the sensitivity of the oxide layer(s) to the presence of alumina in the early stages of oxidation. As explained earlier on, by using a method to only form alumina in the early stages of oxidation (such as vacuum heat treatment) further formation of spinel oxides are controlled, up to the point where the coatings runs out of Al. This control in the formation of other oxides such as spinel and NiO is beneficial as will be discussed in the following paragraph.

The morphology and the composition of the TGO layer are crucial for the performance of the coating. Although the oxidation of Al will cause growth in the volume of the coating, the growth of NiO and spinel oxides are much more damaging due to the fact that they exhibit a very high growth rate [6] which rapidly increases the volume of the coating. In fact the growth rate of NiO in air at 1100℃ is approximately three orders of magnitude larger than that of Al_2O_3 [16]. Furthermore,

NiO and spinel oxides are outward growing oxides and, where the coatings considered in this work are used as bond coats in TBCs, the growth of such oxides will causes stresses in the ceramic top coat resulting in the spallation of the top coat. While, for the alumina layer, depending on the flux of oxygen into the coating and the flux of Al towards the TGO, the growth could be an inward growth. Prescott et al. [8] have mentioned that the oxidation tends to occur by oxygen diffusion in the α-Al_2O_3 grain boundaries resulting in an inward growth for alumina. A similar behaviour has been mentioned by Evans et al. [17]. However, diffusion of Al through the alumina layer has been reported as the growth mechanism of the alumina layer by other researchers [1, 18, 19]. Furthermore, Evans [3] has mentioned that "alumina grows predominantly by inward diffusion of anions along the TGO grain boundaries but there is a contribution to K_p by outward diffusion of cations". The outward growth appears to be sensitive to cations dissolved in the alumina.

5-4-2- TGA analysis

The formation of a protective oxide scale not only depends on the chemical composition of the coating and the oxidation conditions, but also on the manufacturing process (e.g. HVOF, VPS, APS) and the microstructure of the coating [20].

One important step in studying the high temperature oxidation of any metal or alloy is to determine its overall oxidation kinetics which is commonly controlled by the diffusion of reactive species through the oxide scale. Diffusion driven oxidation kinetics usually leads to the so-called parabolic kinetics that are commonly described through a parabolic rate constant. Furthermore, what it is also of importance in the case of oxidation rate measurements is that, in cases where a dual oxide layer exists

and each layer has an effect of the other layer (e.g. in the work presented here where a dual oxide layer of alumina and spinel exists, the presence of the alumina layer will have an effect on the growth rate of the spinel layer, as it will act as a barrier to the diffusion of elements such as Co, Ni, etc and the spinel layer will act as a barrier to the diffusion of oxygen affecting further growth of the alumina layer), are the K_p values calculated valid? It has been observed that for such cases the entire coating and oxide layer(s) have been considered as one system and a K_p value for that system has been presented (rather than individual K_p values for individual oxides). Birks [21] has explained that for a Ni-Cr alloy, where a mixed oxide layer of spinel, NiO and Cr_2O_3 exists, at temperatures where a complete external layer of Cr_2O_3 forms, the oxidation rate falls to values more typical of Cr than of Ni indicating that for such system a K_p value is present which is smaller that that of Ni and bigger than that of Cr but closer to that of Cr. However, there lies the question whether it is possible to predict the thickness of the individual layers and whether the oxide layers will grow with the same ratio throughout the oxidation period.

For the coating and oxide system studied in this work, the thickness of the individual layers can be predicted if it is assumed that cation diffusion is the mechanism controlling the alumina growth. It is also essential to know the K_p value for α-Al_2O_3. The calculations used for predicting the thickness of the individual oxide layers for the coating/oxide system investigated in this work are as follows:

In the following formulas 1 is correlated to alumina, 2 is correlated to spinel and 3 is correlated to the case where both alumina and spinel oxides exist in the oxide layers.

$h_1^2 = K_{p1} \times t$

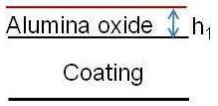

$h_2^2 = K_{p2} \times t$

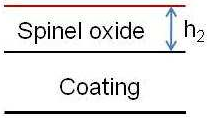

$h_3^2 = K_{p3} \times t$,
$h_3 = h_1' + h_2'$

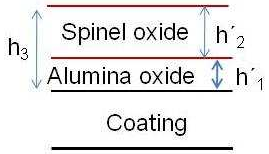

Where $K_{p1} \langle K_{p3} \langle K_{p2}$ and h_1, h_2 and h_3 are alumina, spinel and dual oxide layer (alumina+spinel) thicknesses respectively.

Based on the assumption made that cation diffusion is controlling the alumina growth;

then $h_1' \approx h_1 \Rightarrow h_2' \approx h_3 - h_1$,

Where h'_1 and h'_2 are the alumina and spinel oxide thicknesses in the dual oxide layer respectively.

By calculating h'_2 and knowing h_1 for different times it is possible to check if the h'_2/h_1 ratio is constant at different time, indicating that both oxide layers grow with the same ratio. Hence, it becomes clear once more that the initial stage of oxidation is very important, as the faster the alumina layer forms, the thinner the spinel layer becomes.

It should be noted that, experimental results (mass gain versus time graphs) for the coatings with a dual oxide layer, in this study, show a curve close to parabola. Similar

methods used in this work have been used by other researchers [22-25] in order to calculate the K_p values of materials with the existence of one or more oxide layer(s).

The TGA results indicate that oxide growth on both as-sprayed and heat-treated HVOF and VPS coatings broadly follows the expected parabolic behaviour, see Figure 5-36 and Figure 5-37. As can be seen in Table 5-3 and Table 5-4; for as-sprayed coatings, HVOF3 has the highest K_p value followed by VPS1, HVOF1 and HVOF2 respectively (i.e. for as-sprayed, K_p → HVOF3>VPS1>HVOF1>HVOF2). While for the heat treated coatings, VPS1 has the highest K_p followed by HVOF1, HVOF3 and HVOF2 (i.e. for heat treated, K_p → VPS1>HVOF1>HVOF3>HVOF2). The K_p values determined here are in line with some previously published results [18, 26-28] (for reported values see Table 2-7 in chapter 2). The reported values generally vary in the range of 10^{-12} to 10^{-14} $g^2.cm^{-4}.s^{-1}$ whereas the values reported in this work are in the range of 10^{-11} to 10^{-12} $g^2.cm^{-4}.s^{-1}$. The differences seen in the K_p values measured here with the values reported in literature could be due to several reasons such as different oxidising temperatures (much of the data in Table 2-7 refers to oxidation at temperatures lower than that used in this work), exposure times, testing conditions (e.g. polished surface, EB-remelted, etc.) and differences in the microstructure of the coatings, such as different amount of incompletely melted particles and oxide stringers.

The effect of heat treatment prior to the TGA run for HVOF1 and VPS1 is to increase K_p (from 8.58×10^{-12} for as-sprayed HVOF1 to 1.06×10^{-11} $g^2/cm^4/s$ for heat treated HVOF1 and from 1.85×10^{-11} for as-sprayed VPS1 to 2.87×10^{-11} $g^2/cm^4/s$ for heat treated VPS1), while it has decreased the K_p values for HVOF2 (from 6.61×10^{-12} for

as-sprayed to 3.72×10^{-12} $g^2/cm^4/s$ for heat treated) and HVOF3 (from 2.31×10^{-11} for as-sprayed to 5.77×10^{-12} $g^2/cm^4/s$ for heat treated).

Heat-treatment converted the single phase, γ, in the as-sprayed VPS coating to the two phase γ/β structure shared by both the as-sprayed and heat-treated HVOF coatings. If the observed change in K_p was linked to this change in structure, the heat-treatment would be expected to make the behaviour of the heat-treated coatings resemble each other more closely than the as-sprayed coatings. This is not observed, in fact the heat-treatment increases the proportional difference in the K_p values of each coating type, hence changing the VPS coating to the two phase structure is ruled out as an explanation for the difference in oxidation behaviour seen after heat-treatment.

As can be seen in SEM images in section 4-1-2 of chapter 4 (e.g. Figure 4-9 and Figure 4-11) oxide stringers are formed during spraying which can be seen in as-sprayed coatings. These oxide stringers are predominantly formed on the surface of un-melted powder particles. This is due to the fact that during spraying, the surface of in-flight powder particles is exposed to air and hence a thin oxide layer is formed on the surface/between the splats [11]. In cross sectional images these oxides are seen as stringers. The EDX analysis of these oxides suggests that they are Al and oxygen rich, i.e. alumina [29]. These oxide particles which have formed during spraying count as nuclei and favour the growth of the alumina [20, 23, 30] during permeation of oxygen through pores and interconnected boundaries between splats [29]. During the vacuum heat treatment of the coatings at 1100℃, the oxides present in the as-sprayed structure coarsen (see Figure 4-13 and Figure 4-22 in chapter 4) and transition of aluminium oxides from amorphous alumina to α-Al_2O_3 occurs [24]. As it is generally accepted that VPS coatings are essentially oxide free, due to being sprayed under

vacuum, the existence of these oxide stringers are very low in as-sprayed VPS coatings [23] and hence less coarsened oxide stringers visible after heat treatment, since there were less nuclei to start with.

Diffusion occurring during the heat-treatment heals some of the porosity present in the as-sprayed coatings via a sintering effect, as can be seen in Figure 4-20 and Figure 4-24 of chapter 4. The changes in K_p values seen for coatings can be attributed to this, as the discontinuities caused by porosity will act as barriers to diffusion, the removal or reduction in porosity levels will therefore enhance diffusion within the coating. This can result in an increased rate of supply of oxide forming elements to the surface. However, it is suggested that the oxide stringers existing in coatings are not affected by the heat-treatment, and hence are retained in the heat-treated coatings. These alumina stringers act as effective diffusion barrier layers lowering the diffusion coefficients of oxide forming elements, inhibiting oxide growth [23, 24].

The heat-treatment has its greatest effect, for reduction in porosity, on the VPS coating compared to the HVOF coatings, see Figure 4-20 and Figure 4-24. This is attributed to the different extent of coating oxidation during spraying. As mentioned before it is generally accepted that VPS coatings are essentially oxide free, due to being sprayed under vacuum [23]. In HVOF coatings on the other hand, a thin oxide layer (oxide stringer) is generated around each particle during spraying.

Hence, the increase in K_p, after heat treatment, for the VPS1 coating can be based on the discussion provided above, i.e. a large decrease in porosity content, after heat treatment, combined with minimal oxide stringers resulting in enhanced diffusion of oxide forming elements within the coating.

In the case of HVOF coatings however, as explained in chapter 4, HVOF3 has the highest degree of melting and HVOF2 has the lowest degree of melting (i.e. amount of un-melted particles → HVOF2>HVOF1>HVOF3). Oxide stringers tend to form during spraying**,** between splats and on the particle surface. The presence of alumina nuclei in the coatings can have an beneficial effect on the oxidation resistance [23]. For an un-melted particle the formation of these oxide stringers on the surface will trap the material (elements such as Co, Ni, Al, etc) within the particle and hence diffusion of the elements through the alumina diffusion barrier and to the outside of the particles dramatically drops, i.e. coherent alumina layers will make the material inside off-limits for diffusion. Figure 5-41 illustrates such behaviour. As can be seen there is still β phase available in the particles (e.g. on the top right of the image) which have a coherent alumina layer round them while, the particles surrounding has been depleted from β.

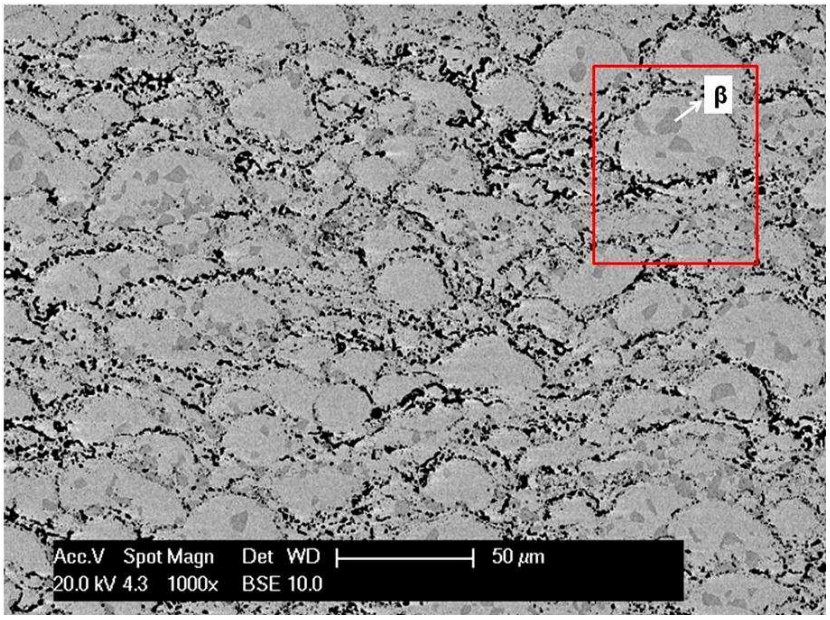

Figure 5-41. SEM micrograph of as-sprayed HVOF coating oxidised at 1100℃ for a period of 250 hours. β phase is available in the incompletely melted particles with oxide stringers (alumina) covering their surface while the surrounding of the particles is depleted from β. Image in BSE mode.

Higher amount of un-melted particles in the coating results in higher amount of trapped material. On the other hand, more extensive stringers likely to form on melted particles. However, these stringers will fracture on impact, hence no longer fully surround particles and free path ways for the diffusion of oxide forming elements exists. This is illustrated schematically in Figure 5-42.

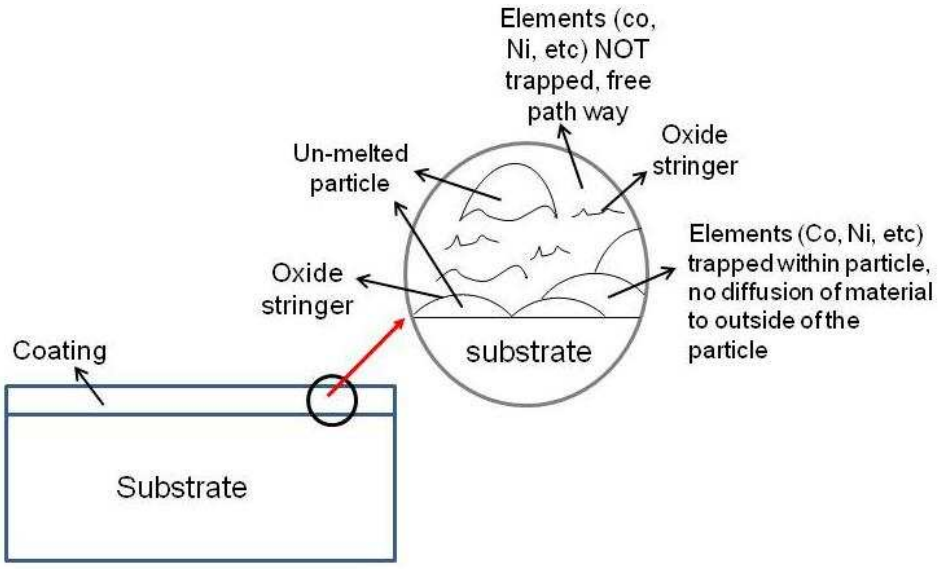

Figure 5-42. A schematic image of melted & un-melted powder particles in coating and oxide stringers acting as barriers to diffusion of oxide forming elements.

For HVOF1 coating, the heat treatment has reduced the porosity levels and hence increased the oxidation rate (K_p). Hence, for HVOF1 coating K_p is only slightly increased by heat-treatment as only some obstacles to diffusion are removed (only pores not the oxide stringers). The idea that the oxides present in the HVOF1 coating inhibit diffusion and hence result in a lower K_p also explains why the as-sprayed HVOF1 coating has a lower K_p than the oxide free as-sprayed VPS1 coating. A similar effect and explanation has been previously put forward by Brandl et al [7].

HVOF2 and HVOF3 coatings however, have behaved differently to HVOF1 and VPS1 coatings. Heat treatment has decreased their K_p values. This can also be rationalised on the basis of the above discussion. In the case of HVOF2, again heat treatment has reduced the porosity levels, but as this coating has had higher number of un-melted particles, it will have higher amount of material trapped by oxide stringers, as discussed earlier on. This is probably high enough to have a greater effect than the reduction in porosity. So, although heat treatment has reduced the porosity but due to a higher amount of trapped material, by oxide stringers, and also the coarsening of these oxide stringers as the result of heat treatment (as mentioned before) the K_p has decreased as compared to the as-sprayed samples. The idea that HVOF2 coating has more un-melted particles and hence more trapped materials also explains why the as-sprayed HVOF2 coating had a lower K_p than as-sprayed HVOF1 coating.

HVOF3 coating had the highest amount of porosity and melting among all three HVOF coatings. As can be seen in Figure 4-13 of chapter 4, a large amount of internal oxides existed in this coating (highest among all coatings). Although the existence of the internal oxides acts as barriers to the diffusion of oxide forming elements towards the surface, they act as nucleus for further growth. The existence of high porosity levels (path ways for oxygen) and high internal oxides (existing nuclei) result in further oxidation of the coating internally in addition to the surface oxidation and hence result in HVOF3 having the largest K_p value. This also explains for the total loss of Al in the HVOF3 coating in much shorter times than that of other coatings (see Figure 5-7).

The reason for reduction in K_p after heat treatment, compared to as-sprayed HVOF3 coating, can be explained as follows. Heat treatment has reduced the porosity levels

resulting in less path ways for migration of oxygen. However, since the reduction in porosity is carried out via a sintering effect and requires diffusion; and HVOF3 coating has a large amount of internal oxides (compared to all other coatings) which have coarsened due to heat treatment and act as diffusion barriers, the reduction in porosity as the result of heat treatment is not as great as other thermally sprayed coatings used in this work. Furthermore, these internal oxides also act as diffusion barriers for oxide forming elements and are not affected by heat treatment. Hence, unlike HVOF1 coating where K_p had increased after heat treatment; heat treatment has resulted in decrease of K_p for HVOF3 coating due to the smaller effect of heat treatment on the reduction of porosity and also the presence of internal oxides which act as diffusion barriers. Figure 5-43 illustrates a schematic summary of the effect of heat treatment on the K_p of HVOF coatings.

To verify the models presented in this discussion, and the effect of internal oxides and porosity on the K_p values, isothermal oxidation tests on samples with similar porosity and different oxide content are required. Richer et al. [25] have compared the isothermal oxidation (at 1000℃ for up to 100h) of CoNiCrAlY coatings, manufactured from the same feedstock powder, deposited by HVOF and cold gas dynamic spraying (CGDS). Since the CGDS process uses kinetic energy rather than thermal energy to produce coatings it is genuinely known that these coatings have very low oxide content, if any. The results presented by Richer et al. [25] showed that the CoNiCrAlY coating produced by HVOF, which typically have oxide stringers in their microstructure, had a lower K_p as compared to that produced by CGDS. This observation is consistent with the model mentioned previously.

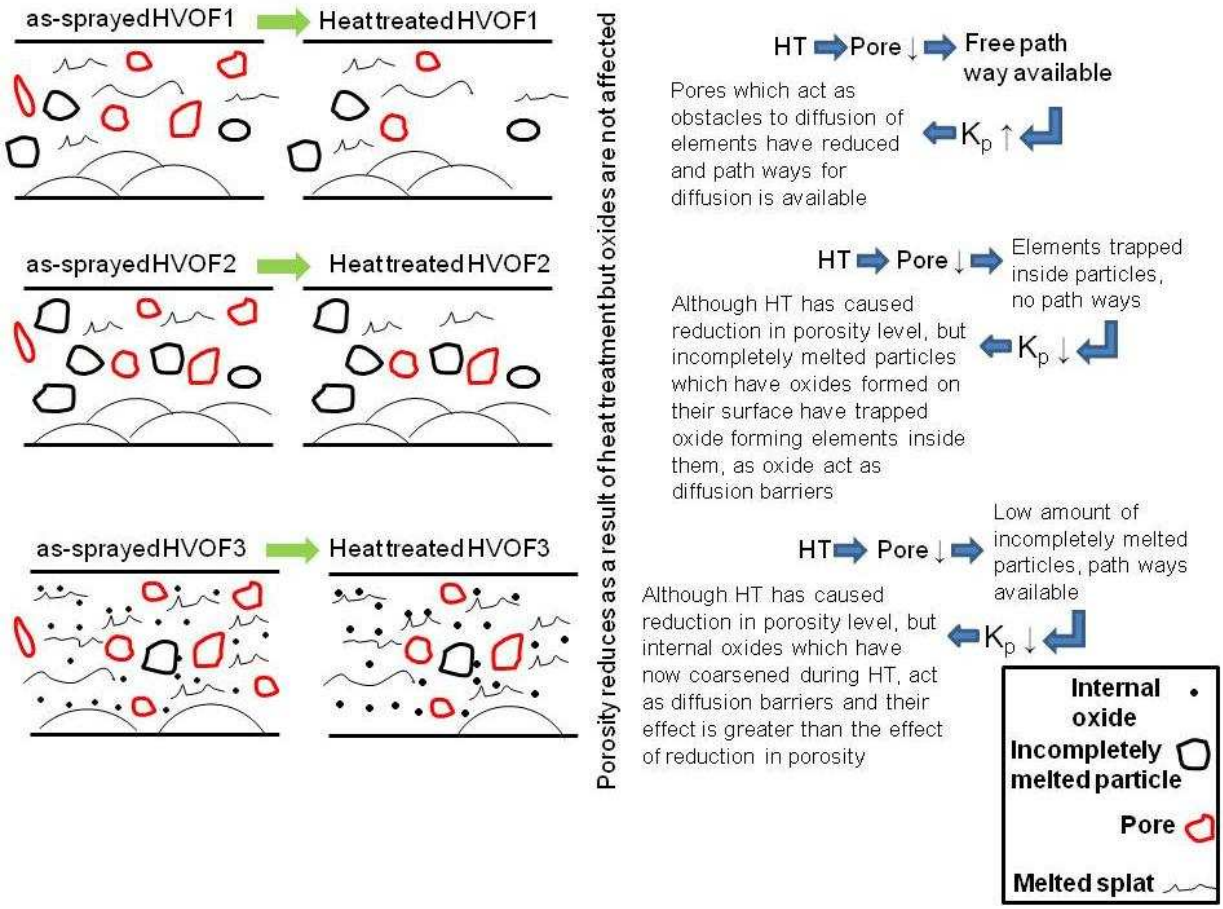

Figure 5-43. A schematic summary of the effect of heat treatment on the K_p of HVOF coatings.

However, it should be noted that the TGA tests (carried out in this work) were carried out at two different timing periods, where the TGA was broken in between these two periods. TGA tests on HVOF1 and VPS1 coatings were carried out in the first period and TGA tests on HVOF2 and HVOF3 coatings were carried out in the second period.

When looking at Figure 5-38 in more detail, it can be noticed that HTHVOF1 and HTVPS1 have higher mass gains as compared to HTHVOF3. This is while the microstructure of HTHVOF3, see Figure 5-25, seems to have been oxidised more heavily when compared to the microstructure of HTVPS1 and HTHVOF1, see Figure 5-33. However, it should be noted that the SEM micrograph of HVOF3 coating in Figure 5-25 is a mixture of oxides and pores, remained after heat treatment in

HTHVOF3. Furthermore, some pre-existing oxides from as-sprayed structure are still there which have been unaffected after heat treatment, with decrease in powder particle size the oxide content inside the coating increases [31]. The difference in the mass gain however, could be due to i) the formation of volatile CrO_3 from further oxidation of Cr_2O_3 above 900℃ [10, 30, 32, 33] in HVOF3, as the β phase has been completely depleted and hence resulted in the formation of other oxides, see Figure 5-22; and ii) due to some mismatches caused after the reinstallation of the TGA machine.

By comparing the measured oxide thickness with the oxide thickness calculated using the K_p values, it can be seen that in the majority of the cases both values are in good agreement with one another. However, discrepancies between the calculated and measured thickness can be seen. In some cases the calculated thickness is lower than the measured thickness and in some cases the calculated thickness is higher than the measured thickness. The latter case could be attributed to the loss in oxide scales during sample preparation (polishing) and the former case could be attributed to the fact that the oxides formed are porous and are not very compact. Moreover, the oxide surfaces are rough and hence this will add further errors to the thickness measurement using SEM micrographs. Furthermore, Huntz et al. [34] have reported that when diffusion is operative, deviations from the ideal parabolic growth laws occur during oxidation of metallic material. They have mentioned that one possibility consists in the evolution of the oxide grain size during oxidation which leads to a change in K_p at least at the beginning of the oxidation. They have also mentioned that in the case of compact scales experimental oxide thickness can be smaller than the thickness calculated from the TGA data in relation with a more or less pronounced anisotropic growth of the oxide.

CHAPTER 6

Conclusions

This study has investigated the microstructural and mechanical behaviour of thermally sprayed CoNiCrAlY coating using HVOF and VPS spraying techniques. It is suggested that, in contrast to VPS coatings, HVOF coatings generally retain the microstructure of the feedstock powder due to a lower flame temperature and higher particle velocity, as compared to VPS process. Comparison of the microstructure of the three HVOF coatings indicated a higher degree of melting for HVOF3 followed by HVOF1 and HVOF2, i.e. extent of melting: HVOF3>HVOF1>HVOF2.

This work illustrates the effect of annealing on the microstructure features such as porosity, γ and β volume fractions and the formation of minor phases (microstructure stability).

Annealing has caused the formation of the β phase in the VPS coating and coarsened the β phase for the HVOF coating. It is also clear that the annealing process has reduced the porosity levels for both HVOF and VPS coatings. However, it is suggested that annealing has a greater effect in the reduction of porosity for the VPS coating as compared to the HVOF coating. This is discussed to be due to the presence of oxide stringers formed on the surface of powder particles during spraying of the HVOF coatings. These oxide stringers act as obstacles to diffusion resulting in less

amount of reduction in porosity. VPS coatings, on the other hand, are believed to be oxide free as they are sprayed under vacuum and hence far fewer oxide stringers, resulting in a greater decrease in porosity as the result of annealing.

Also, it is suggested that the higher the extent of melting the higher the amount of internal oxides and oxide stringers. However, for the incompletely melted particles the presence of these oxide stringers tends to separate the particle from the surrounding material, and hence traps the constituent elements (Co, Ni, Al, etc) from diffusing outside the particle boundaries.

Furthermore, both HVOF and VPS coatings had a similar microstructure after being annealed at different temperatures for different exposure times. A γ/β microstructure is present at all annealing temperatures. However, a Cr rich phase, being identified as α-Cr, is present at coatings annealed at 800℃, 900℃ and 1000℃. This phase is not present at coatings annealed at 1100℃, indicating that the phase is not stable at this temperature and that it has dissolved in the γ phase.

This work also illustrates the effect of microstructural features such as porosity and β volume fraction on the mechanical behaviour of the coatings.

Annealing has an effect on the mechanical properties of the coatings too. It is shown that annealing increases the Young's modulus of the coatings. The higher the annealing temperature, the higher the Young's modulus. The increase in the Young's modulus as the function of annealing temperature is attributed to the decrease in porosity and also decrease in the volume fraction of the β phase.

Using the Eshelby model, a two step increase in the Young's modulus of the coatings is reported, during the increase in annealing temperatures. The first increase in the

Young's modulus, from as-sprayed to the first annealing temperature, is attributed to a large decrease in porosity level. The second increase in the Young's modulus, however, is as a result of decrease in β volume fraction.

In contrast to Young's modulus, annealing reduces the hardness of the coatings. It is believed that the presence of the well distributed fine β particles play an important role in the hardening of the coating. In fact the higher hardness values reported for the HVOF coatings, as compared to VPS, is related to the presence of the β phase. Furthermore, the reduction in hardness, as the annealing temperature increases, is associated to the growth of the β particles and also the decrease of the β volume fraction. Moreover, the stress relieving effect of the annealing process adds to the explanations of a lower hardness for the annealed coatings.

This works shows how early stages of oxidation plays an important role in the formation of a single or dual oxide layer and their relative thicknesses.

The oxidation of as-sprayed HVOF and VPS coatings carried out at 1100℃ results in the formation of a dual oxide layer with the upper brighter layer being spinel and the inner darker layer being α-Al_2O_3. The presence of such a dual layer structure is discussed to be due to the formation of a thin layer of oxide mixture at the early stages of oxidation. The progress in oxidation results in the reduction of the metallic oxides by Al via the following reaction:

$$2Al(alloy) + 3MO = Al_2O_3 + 3M(alloy)$$

This will cause in the segregation of the alumina from spinel. Since the oxygen activity is highest at the surface and spinel oxides form where the oxygen activity is

high, the spinel oxide forms as the upper layer and alumina as the inner layer, where the oxygen activity is too low for spinels to form/grow.

The oxidation of the heat treated HVOF and VPS coatings results in the formation of a single alumina layer. It is suggested that the vacuum heat treatment prior to oxidation forms a very thin alumina layer, as only alumina can form at very low oxygen partial pressures. The formation of only an alumina layer, in the early stage of oxidation, will separate the coating surface from fresh air in the subsequent oxidation and hence prevents the diffusion of other oxide forming elements. Hence, only the existing alumina layer will grow. For HVOF3 coating, however, after exposure times of approximately 100 hours, due to the internal consumption of the β phase, a large β depletion zone is resulted. Since the β depletion zone is very large and Al activity is very low, in this zone, the following reactions will take place resulting in the formation of a spinel layer.

$3Ni(alloy) + 4Al_2O_3 = 3NiAl_2O_4 + 2Al(alloy)$

$3Ni(alloy) + NiAl_2O_4 = 4NiO + 2Al(alloy)$

Hence, the oxidation behaviour not only depends on the treatments carried out prior to oxidation, but also depends on the microstructure of the coating prior to oxidation, i.e. although heat treatment causes the formation and growth of a single alumina layer in the subsequent oxidation, coatings with high degree of melting and large amount of internal oxides will behave differently.

This work also shows that both porosity and oxide stringers play a role in how heat treatment affects oxidation behaviour.

Heat treatment, also affects the oxidation rate of the coatings. This affect varies depending on the microstructure of the coatings. For VPS coatings, since there is no internal oxidation and oxide stringers, heat treatment will reduce the porosity level and hence removes any obstacles to diffusion of oxide forming elements resulting in an increase in K_p.

For HVOF coating, the reduction in porosity depends on the amount of oxide stringers present and also the number of incompletely melted particles. For HVOF1 coating, heat treatment has increased the K_p due to the decrease in porosity levels. However, as there are oxide stringers present, the reduction in porosity is not as large as for VPS coating and hence only a small increase in K_p results. For HVOF2 coating, due to the presence of a large number of incompletely melted particles, a large amount of material is trapped within the particles. Although, heat treatment reduces the porosity levels, it does not increase the K_p. This is attributed to the large amount of material trapped within the incompletely melted particles with oxide stringers covering the particle and acting as diffusion barriers, and so heat treatment actually results in reduction of the K_p.

It is suggested that sprayed coatings with high degree of melting and high amount of internal oxides (e.g. HVOF3) will have a higher oxidation rate, due to the presence of fragmented internal oxides which act as nucleus for further oxidation. Furthermore, sprayed coatings with high number of incompletely melted particles (e.g. HVOF2) result in lower oxidation rates, as the continues oxide stringers covering the incompletely melted particle surface act as obstacles to diffusion (trapping the material inside the particle) which are not removed even by heat treatment of the coatings (unlike pores which disappear by heat treatment).

Taking into account the high costs associated with VPS compared to HVOF spraying this research has demonstrated: (i) lower oxidation rates for HVOF compared to VPS, due to the beneficial effects of existing oxide stringers in the microstructure of the HVOF sprayed coating, (ii) higher strength (implied from hardness results) for HVOF coatings, due to the presence of the second phase (β phase) in the as-sprayed coatings, (iii) higher Young's modulus in a wide range of operating temperatures. As such, the HVOF process is more suitable than the VPS process for deposition of MCrAlY coatings.

Furthermore, the lower oxide thickness seen for coatings following a low pressure (vacuum) heat treatment (heat treated oxidised coatings), indicates that accommodating the costs associated with vacuum heat treatment can be of benefit, increasing the component life time. However, as mentioned in chapter 7, further work on the effect of different vacuum levels is essential.

CHAPTER 7

Future Work

Ultimately this project has shown the oxidation and microstructural behaviour of the CoNiCrAlY coatings sprayed by HVOF and VPS processes. Further investigation on the early stages of oxidation is of great importance as it was shown that it is the early stages of oxidation controlling the development and formation of a single/dual oxide layer. The effect of vacuum heat treatment has been investigated. However, no investigation on the effect of the actual extent of vacuum (pressure) during heat treatment on subsequent behaviour has been carried out. Consequently, further investigation of different extents of vacuum during heat treatment could be conducted, as vacuum generation is a costly process. Furthermore, investigation on the effect of surface roughness on oxidation behaviour is of great importance since, as mentioned in the discussions, any method of producing a thin alumina layer in the early stage of oxidation could prevent the formation of the spinel oxides. Last but not least, further investigation on the influence of pre-existing oxides on the oxidation performance of the coatings is required.

CHAPTER 8

References

[1] A.M.Y. Razak, Industrial gas turbines, performance and operability, Woodhead Pubilishing Ltd, Cambridge, 2007.

[2] W.W. Bathie, Fundamentals of gas turbines, 2nd edition, John Wiley and Sons, Inc, New York, 1996.

[3] J.R. Nicholls, Advances in surface engineering in gas turbines, 6th International Charles Parsons Turbine Conference, 2003, Dublin, pp. 803-826,

[4] T. Giampaolo, Gas turbine handbook, Principles and practices, 3rd edition, The Fairmont press, Inc, London, 2006.

[5] G.W. Meetham, The development of gas turbine materials, Applied Acience Pubilishers Ltd., London, 1981.

[6] C. Duret-Thual, R. Morbioli, and P. Steinmetz, A guide to the control of high temperature corrosion and protection of gas turbine materials, Commission of the european communities, Luxembourg, 1986.

[7] L.C. Driver, HVOF spraying of WC-Co & MCrAlY coatings for aeroengine components, PhD thesis, Department of Mechanical, Materials and Manufacturing Engineering, University of Nottingham, Nottingham, 2004.

[8] Y. Tamarin, Protective coatings for turbine blades, ASM International, Ohio, 2002.

[9] C.T. Sims, N.S. Stoloff, and W.C. Hagel, Superalloys II: high temperature materials for aerospace and industrial power, John Wiley & Sons, New York, 1987.

[10] M. Durand-Charre, The microstructure of superalloys, J.H. Davidson, Gordon and breach science publishers, 1997.

[11] B. Gunston, The development of jet and turbine aero engines, 3rd edition, Patrick Stephens Ltd., Yeovil, 2002.

[12] J.R. Nicholls, Designing oxidation resistant coatings, Journal of metals, 52 (1), pp. 28-35, 2000.

[13] C.B. Xiao, Y.F. Han, J.X. Song, and J.P. Li, Effect of NiCoCrAlYHf overlay coating on performance of Ni3Al-based alloy IC6A, Surface and Coatings Technology, 200 (9), pp. 3095-3101, 2006.

[14] A. Feuerstein, J. Knapp, T. Taylor, A. Ashary, A. Bolcavage, and N. Hitchman, Technical and economical aspects of current thermal barrier coating systems for gas turbine engines by thermal spray and EBPVD: A review, Journal of Thermal Spray Technology, 17 (2), pp. 199-213, 2008.

[15] F.T. Talboom, R.C. Elam, and L.W. Wilson, Evaluation of advanced superalloy protection systems, ReprotCR7813, Houston, NASA, 1970.

[16] N.P. Padture, M. Gell, and E.H. Jordan, Thermal barrier coatings for gas-turbine engine applications, Science, 296 pp. 280-284, 2002.

[17] A.G. Evans, D.R. Mumm, J.W. Hutchinson, G.H. Meier, and F.S. Pettit, Mechanisms controlling the durability of thermal barrier coatings, Progress in Materials Science, 46 (5), pp. 505-553, 2001.

[18] Y. Itoh, and M. Saitoh, Mechanical Properties of Overaluminized MCrAlY Coatings at Room Temperature, Journal of Engineering for Gas Turbines and Power, 127 pp. 807-813, 2005.

[19] R. Prescott, and M.J. Graham, The formation of alumina oxide scales on high-temperature alloys, Oxidation of Metals, 38 (3-4), pp. 233-254, 1992.

[20] S. Bose, High temperature coatings, Elsevier, Amsterdam, 2007.

[21] M. Kutz, Handbook of environmental degradation of materials, William Andrew Inc. , New York, 2005.

[22] W. Brandl, D. Toma, and H.J. Grabke, The characteristics of alumina scales formed on HVOF-sprayed MCrAlY coatings, Surface and Coatings Technology, 108-109 (1-3), pp. 10-15, 1998.

[23] X. Peng, and F. Wang, Morphologic investigation and growth of the alumina scale on magnetron-sputtered CoCrAlNCs with and without yttrium, Corrosion Science, 45 (10), pp. 2293-2306, 2003.

[24] J. Toscano, R. Vaen, A. Gil, M. Subanovic, D. Naumenko, L. Singheiser, and W.J. Quadakkers, Parameters affecting TGO growth and adherence on MCrAlY-bond coats for TBC's, Surface and Coatings Technology, 201 (7), pp. 3906-3910, 2006.

[25] D. Naumenko, V. Shemet, L. Singheiser, and W.J. Quadakkers, Failure mechanisms of thermal barrier coatings on MCrAlY-type bondcoats associated with the formation of the thermally grown oxide, Journal of Materials Science, 44 (7), pp. 1687-1703, 2009.

[26] T. Marrocco, Development of improved cold spray and HVOF deposited coatings, PhD thesis, Department of Mechanical, Materials and Manufacturing Engineering, University of Nottingham, Nottingham, 2008.

[27] V. Higuera, F.J. Belzunce, and J. Riba, Influence of the thermal-spray procedure on the properties of a CoNiCrAlY coating, Surface and Coatings Technology, 200 (18-19), pp. 5550-5556, 2006.

[28] H. Edris, Studies on high velocity oxy-fuel sprayed coatings of inconel 625 and Ni-Cr_3C_2, PhD thesis, Department of Mechanical, Materials and Manufacturing Engineering, University of Nottingham, Nottingham, 1997.

[29] J.R. Davis, Handbook of thermal spray technology, ASM International, USA, 2004.

[30] R. Schwetzke, and H. Kreye, Microstructure and properties of tungsten carbide coatings sprayed with various high velocity oxygen fuel spray systems, Journal of Thermal Spray Technology, 8 (3), pp. 433-439, 1999.

[31] W. Brandl, D. Toma, J. Kruger, H.J. Grabke, and G. Matthaus, The oxidation behaviour of HVOF thermal-sprayed MCrAlY coatings, Surface and Coatings Technology, 94-95 pp. 21-26, 1997.

[32] E. Lugscheider, C. Herbst, and L. Zhao, Parameter studies on high-velocity oxy-fuel spraying of MCrAlY coatings, Surface and Coatings Technology, 108-109 (1-3), pp. 16-23, 1998.

[33] T.C. Hanson, C.M. Hackett, and G.S. Settles, Independent control of HVOF particle velocity and temperature, Journal of Thermal Spray Technology, 11 (1), pp. 75-85, 2002.

[34] L.D. Zhao, C. Herbst-Dederichs, and E. Lugscheider, In-flight reactions of metallic particles during thermal spraying, Advanced Engineering Materials, 4 (12), pp. 922-924, 2002.

[35] M. Li, and P.D. Christofides, Computational study of particle in-flight behavior in the HVOF thermal spray process, Chemical Engineering Science, 61 (19), pp. 6540-6552, 2006.

[36] T. Sudaprasert, An investigation of microstructure and sliding wear in thermally sprayed WC-Co coatings, PhD thesis, Department of Mechanical, Materials and Manufacturing Engineering, University of Nottingham, Nottingham, 2002.

[37] L. Pawlowski, The science and engineering of thermal spray coatings, Second edition, John Wiley & Sons, West Sussex, 2008.

[38] D.S. Rickerby, and M.A. Matthews, Advanced surface coatings: a handbook of surface engineering, Chapman and HAll, New York, 1991.

[39] C.M. Cotell, and J.A. Sprague, Surface Engineering, ASM Handbook, Vol. 5, ASM International, 1994.

[40] P. Poza, and P.S. Grant, Microstructure evolution of vacuum plasma sprayed CoNiCrAlY coatings after heat treatment and isothermal oxidation, Surface and Coatings Technology, 201 (6), pp. 2887-2896, 2006.

[41] D. Zhang, S.J. Harris, and D.G. McCartney, Mechanical Properties and Microstructure of HVOF Sprayed Co and Ni Alloy Coatings, Thermal spray 2003: Advancing the Science & Applying the Technology pp. 829-836, 2003.

[42] J. Toscano, A. Gil, T. Huttel, E. Wessel, D. Naumenko, L. Singheiser, and W.J. Quadakkers, Temperature dependence of phase relationships in different types of MCrAlY-coatings, Surface and Coatings Technology, 202 (4-7), pp. 603-607, 2007.

[43] K. Fritscher , and Y. Lee, Investigation of an as-sprayed NiCoCrAlY overlay coating – microstructure and evolution of the coating, Materials and Corrosion, 56 (1), pp. 5-14, 2005.

[44] D.R.G. Achar, R. Munoz-Arroyo, L. Singheiser, and W.J. Quadakkers, Modelling of phase equilibria in MCrAlY coating systems, Surface and Coatings Technology, 187 (2-3), pp. 272-283, 2004.

[45] N. Czech, F. Schmitz, and W. Stamm, Microstructural analysis of the role of rehnium in advanced MCrAlY coatings, Surface & Coatings Technology, 76-77 pp. 28-33, 1995.

[46] N.S. Cheruvu, K.S. Chan, and G.R. Leverant, Cyclic Oxidation Behavior of Aluminide, Platinum Modified Aluminide, and MCrAlY Coatings on GTD-111, Journal of Engineering for Gas Turbines and Power, 122 pp. 50 - 54, 2000.

[47] R. Mobarra, A.H. Jafari, and M. Karaminezhaad, Hot corrosion behavior of MCrAlY coatings on IN738LC, Surface and Coatings Technology, 201 (6), pp. 2202-2207, 2006.

[48] R.T. Kiepura, H.F. Lampman, P. Thomas, and N.D. Wheaton, ASM Handbook, Volume 4, Heat Treating, ASM International, 1991.

[49] B.G. Mendis, B. Tryon, T.M. Pollock, and K.J. Hemker, Microstructural observations of as-prepared and thermal cycled NiCoCrAlY bond coats, Surface and Coatings Technology, 201 (7), pp. 3918-3925, 2006.

[50] R.J. Mitchell, C.M.F. Rae, and S. Tin, Grain boundary transformations during isothermal exposure of powder metallurgy nickel base superalloys for turbine disc applications, Materials Science and Technology, 21 (1), pp. 125 - 132, 2005.

[51] H. Peng, H. Guo, J. He, and S. Gong, Cyclic oxidation and diffusion barrier behaviors of oxides dispersed NiCoCrAlY coatings, Journal of Alloys and Compounds, 502 pp. 4-11-416, 2010.

[52] V. Srinivasan, N.S. Cheruvu, T.J. Carr, and C.M. O'Brien, Degradation of MCrAlY coating and substrate superalloy during long term thermal exposure, Materials and Manufacturing Processes, 10 (5), pp. 955-969, 1995.

[53] N. Briks, and G.H. Meier, Introduction to high temperature oxidation of metals, Edward Arnold Ltd, London, 1983.

[54] O. Kubaschewski, P. Habil, and B.E. Hopkins, Oxidation of metals and alloys, Butterworths Scientific London, 1953.

[55] P. Kofstad, High temperature oxidation of metals, John Wiley & Sons, New York, 1966.

[56] C.S. Giggins, and F.S. Pettit, Oxidation of Ni-Cr alloys between 800 degrees and 1200 degrees C, Transactions of the Metallurgical Society of Aime, 245 (12), pp. 2495-&, 1969.

[57] A. Ul-Hamid, A TEM study of the oxide scale development in Ni-Cr alloys, Anti-Corrosion Methods and Materials, 51 (3), pp. 216-222, 2004.

[58] C.S. Giggins, and F.S. Pettit, Oxidation of Ni-Cr-Al alloys between 1000 degrees and 1200 degrees C, Journal of the Electrochemical Society, 118 (11), pp. 1782-&, 1971.

[59] L. Zhao, M. Parco, and E. Lugscheider, High velocity oxy-fuel thermal spraying of a NiCoCrAlY alloy, Surface and Coatings Technology, 179 (2-3), pp. 272-278, 2004.

[60] K. Messaoudi, A.M. Huntz, and B. Lesage, Diffusion and growth mechanism of Al2O3 scales on ferritic Fe-Cr-Al alloys, Materials Science and Engineering A, 247 (1-2), pp. 248-262, 1998.

[61] F. Tang, L. Ajdelsztajn, G.E. Kim, V. Provenzano, and J.M. Schoenung, Effects of surface oxidation during HVOF processing on the primary stage oxidation of a CoNiCrAlY coating, Surface and Coatings Technology, 185 (2-3), pp. 228-233, 2004.

[62] F. Tang, L. Ajdelsztajn, and J.M. Schoenung, Characterization of oxide scales formed on HVOF NiCrAlY coatings with various oxygen contents introduced during thermal spraying, Scripta Materialia, 51 (1), pp. 25-29, 2004.

[63] A. Fossati, M. Di Ferdinando, A. Lavacchi, U. Bardi, C. Giolli, and A. Scrivani, Improvement of the isothermal oxidation resistance of CoNiCrAlY coating sprayed by High Velocity Oxygen-Fuel, Surface and Coatings Technology, 204 (21-22), pp. 3723-3728, 2010.

[64] M. Di Ferdinando, A. Fossati, A. Lavacchi, U. Bardi, F. Borgioli, C. Borri, C. Giolli, and A. Scrivani, Isothermal oxidation resistance comparison between air plasma sprayed, vacuum plasma sprayed and high velocity oxygen fuel sprayed CoNiCrAlY bond coats, Surface & Coatings Technology, 204 pp. 2499-2503, 2010.

[65] P. Richer, M. Yandouzi, L. Beauvais, and B. Jodoin, Oxidation Behaviour of CoNiCrAlY Bond Coats Produced by Plasma, HVOF and Cold Gas Dynamic Spraying, Surface and Coatings Technology, 204 pp. 3962-3974, 2010.

[66] W. Brandl, H.J. Grabke, D. Toma, and J. Krüger, The oxidation behaviour of sprayed MCrAlY coatings, Surface and Coatings Technology, 86-87 (Part 1), pp. 41-47, 1996.

[67] H. Choi, B. Yoon, H. Kim, and C. Lee, Isothermal oxidation of air plasma spray NiCrAlY bond coatings, Surface and Coatings Technology, 150 (2-3), pp. 297-308, 2002.

[68] A.V. Put, D. Monceau, and D. Oquab, Cyclic thermogravimetry of TBC systems, Surface & Coatings Technology, 202 (4-7), pp. 665-669, 2007.

[69] F.H. Yuan, Z.X. Chen, Z.W. Huang, Z.G. Wang, and S.J. Zhu, Oxidation behavior of thermal barrier coatings with HVOF and detonation-sprayed NiCrAlY bondcoats, Corrosion Science, 50 (6), pp. 1608-1617, 2008.

[70] N. Czech, M. Juez-Lorenzo, V. Kolarik, and W. Stamm, Influence of the surface roughness on the oxide scale formation on MCrAlY coatings studied in situ by high temperature X-ray diffraction, Surface and Coatings Technology, 108-109 (1-3), pp. 36-42, 1998.

[71] W. Brandl, G. Marginean, D. Maghet, and D. Utu, Effects of specimen treatment and surface preparation on the isothermal oxidation behaviour of the HVOF-sprayed MCrAlY coatings, Surface and Coatings Technology, 188-189 pp. 20-26, 2004.

[72] O. Trunova, T. Beck, R. Herzog, R.W. Steinbrech, and L. Singheiser, Damage mechanisms and lifetime behavior of plasma sprayed thermal barrier coating systems for gas turbines - Part 1: Experiments, Surface & Coatings Technology, 202 (20), pp. 5027-5032, 2008.

[73] U. Hermosilla, M.S.A. Karunaratne, I.A. Jones, T.H. Hyde, and R.C. Thomson, Modelling the high temperature behaviour of TBCs using sequentially coupled microstructural-mechanical FE analyses, Materials Science and Engineering: A, 513-514 pp. 302-310, 2009.

[74] U. Hermosilla, M.S.A. Karunaratne, I.A. Jones, T.H. Hyde, and R.C. Thomson, MCrAlY creep behaviour modelling by means of finite-element unit cells and self-consistent constitutive equations, Proceedings of the Institution of Mechanical Engineers Part L-Journal of Materials-Design and Applications, 223 (L1), pp. 41-51, 2009.

[75] S. Kuroda, and T.W. Clyne, The quenching stress in thermally sprayed coatings, Thin Solid Films, 200 pp. 49-66, 1991.

[76] F. Azarmi, T. Coyle, and J. Mostaghimi, Young's modulus measurement and study of the relationship between mechanical properties and microstructure of air plasma sprayed alloy 625, Surface & Coatings Technology, 203 (8), pp. 1045-1054, 2009.

[77] J.D. Eshelby, The elastic field outside an ellipsoidal inclusion, proceeding of the royal society of London series A-Mathematical and Physical sciences, 252 pp. 561-569, 1959.

[78] R.M. Spriggs, Expression for effect of porosity on elastic modulus of polycrystalline refractory materials, particularly aluminum oxide, Journal of Americal Ceramic Society, 44 pp. 628-629, 1961.

[79] D.P.H. Hasselman, On the porosity dependence of the elastic moduli of polycrystalline refractory materials, Journal of Americal Ceramic Society, 45 pp. 452-453, 1962.

[80] Z. Hashin, The elastic moduli of heterogeneous materials, Journal of Applied Mechanics, 29 pp. 143-150, 1962.

[81] J.C. Wang, Yong's modulus of porous materials, Journal of Materials Science, 19 pp. 809-814, 1984.

[82] T.W. Clyne, and P.J. Withers, An introduction to metal matrix composites, Cambridge University Press, Cambridge, 1993.

[83] J.D. Eshelby, The determination of the elastic field of an ellipsoidal inclusion, and related problems, Proceeding of the royal society of london series A-Mathematical and Physical sciences, 241 pp. 376-396, 1957.

[84] U. Hermosilla, Mechanical modelling of thermal barrier coatings at high temperatures PhD thesis, Department of Mechanical, Materials and Manufacturing Engineering, University of Nottingham, Nottingham, 2008.

[85] T.S. Price, Cold gas dynamic spraying of titanium coatings, PhD thesis, Department of Mechanical, Materials and Manufacturing Engineering, University of Nottingham, Nottingham, 2008.

[86] C.J. Li, A. Ohmori, and R. McPherson, The relationship between microstructure and Young's modulus of thermally sprayed ceramic coatings, Journal of Materials Science, 32 pp. 997-1004, 1997.

[87] T. Nakamura, G. Qian, and C.C. Berndt, Effects of pores on mechanical properties of plasma-sprayed ceramic coatings, Journal of the American Ceramic Society, 83 (3), pp. 578-584, 2000.

[88] Y.H. Zhao, G.P. Tandon, and G.J. Weng, Elastic moduli for a class of porous materials, Journal of Acta Mechanica, 76 pp. 105-130, 1989.

[89] Y.H. Zhao, and G.J. Weng, Effective elastic moduli of ribbon-reinforced composites, Journal of Applied Mechanics, 57 pp. 158-167, 1990.

[90] C. Kwakernaak, T.J. Nijdam, and W.G. Sloof, Microstructure Refinement of NiCoCrAlY Alloys by Laser Surface Melting, Metallurgical and Materials Transactions A, 37A pp. 695-703, 2006.

[91] A. Bejan, Heat Transfer, John Wiley & Sons, Inc, New York, 1993.

[92] D. Monceau, and B. Pieraggi, Determination of parabolic rate constants from a local analysis of mass-gain curves, Oxidation of Metals, 50 (5-6), pp. 477-493, 1998.

[93] E. Kimmari, and L. Kommel, Application of the continuous indentation test method for the characterization of mechanical properties of B4C/Al composites, Proceedings of the Estonian Academy of Sciences Engineering, 12 (4), pp. 399-407, 2006.

[94] A.C. Fischer-Cripps, The IBIS Handbook of Nanoindentation, Fischer-Cripps Laboratories Pty Ltd, Forestville NSW, 2009.

[95] W.C. Oliver, and G.M. Pharr, An Iimproved Technique For Determining Hardness and Elastic-Modulus Using Load and Displacement Sensing Indentation on Experiments, Journal of Materials Research, 7 (6), pp. 1564-1583, 1992.

[96] N. Ahmed, Characterisation of Different Forms of Inconel 625 for Determining the Effects of Microstructural Modifications on Electrochemical Behaviour, PhD thesis, Department of Mechanical, Materials and Manufacturing Engineering, University of Nottingham, Nottingham, 2008.

[97] Y. Itoh, M. Saitoh, and Y. Ishiwata, Characteristics of MCrAlY Coatings Sprayed by High Velocity Oxygen-Fuel Spraying System, Journal of Engineering for Gas Turbines and Power, 122 pp. 43 - 49, 2000.

[98] F. Duflos, and J.F. Stohr, Comparison of the quench rates attained in gas-atomized powders and melt-spun ribbons of Co- and Ni-base superalloys: influence on resulting microstructures, Journal of Materials Science, 17 pp. 3641-3652, 1982.

[99] M. Shibata, S. Kuroda, H. Murakami, M. Ode, M. Watanabe, and Y. Sakamoto, Comparison of microstructure and oxidation behavior of CoNiCrAlY bond coatings prepared by different thermal spray processes, 1st Asian Thermal Spray Conference (ATSC 2005), 2005, Nagoya, JAPAN, pp. 1638-1642, Nov.

[100] C. Moreau, P. Cielo, M. Lamontagne, S. Dallaire, J.C. Krapez, and M. Vardelle, Temperature evolution of plasma sprayed niobium particles impacting on substrate, Surface & Coatings Technology, 46 (2), pp. 173-187, 1991.

[101] S. Sampath, and H. Herman, Rapid Solidification and Microstructure Development during Plasma Spray Deposition, Journal of Thermal Spray Technology, 5 (4), pp. 445-456, 1996.

[102] D. Toma, W. Brandl, and U. Köster, Studies on the transient stage of oxidation of VPS and HVOF sprayed MCrAlY coatings, Surface and Coatings Technology, 120-121 pp. 8-15, 1999.

[103] C.-J. Li, and W.-Y. Li, Effect of sprayed powder particle size on the oxidation behavior of MCrAlY materials during high velocity oxygen-fuel deposition, Surface and Coatings Technology, 162 (1), pp. 31-41, 2002.

[104] J. Meng, C.C. Jia, and Q. He, Fabrication of Ni3Al by hot pressing from element powders, Rare Metals, 26 (3), pp. 222-225, 2007.

[105] P. Krukovskya, K. Tadlyaa, A. Rybnikovb, I. Kryukovb, N. Mojaiskaiab, V. Kolarikc, and M. Juez-Lorenzoc, Lifetime Modelling for MCrAlY Coatings in Industrial Gas Turbine Blades, Materials research, 7 (1), pp. 43-47, 2002.

[106] D.R.G. Achar, R. Munoz-Arroyo, L. Singheiser, and W.J. Quadakkers, Modelling of phase distributions in MCrAlY coatings and their interactions with nickel based alloys, Journal of Physics IV, France, 120 pp. 231-238, 2004.

[107] F. Azarmi, T. Coyle, and J. Mostaghimi, Young's modulus measurement and the study of the relationship between mechanical properties and microstructure of air plasma sprayed alloy 625, Surface & Coatings Technology, doi:10.1016/j.surfcoat.2008.09.035 pp., 2008.

[108] A. Scrivani, U. Bardi, L. Carrafiello, A. Lavacchi, F. Niccolai, and G. Rizzi, A comparative study of high velosity oxygen fuel, vacuum plasma, and axial plasma spray for the deposition of CoNiCrAlY bond coat alloy, Journal of Thermal Spray Technology, 12 (4), pp. 504-507, 2003.

[109] S. Floreen, G.E. Fuchs, and W.J. Yang, The metallurgy of alloy 625, Superalloys 718, 625, 706 and various derivatives, pp. 13-37, 1994.

[110] L. Qian, M. Li, Z. Zhou, H. Yang, and X. Shi, Comparison of nano-indentation hardness to microhardness, Surface & Coatings Technology, 195 pp. 264-271, 2005.

[111] W. Shen, F.-c. Wang, Q.-b. Fan, D. Hua, and Z. Ma, Proposal of new expressions for effects of splat interfaces and defects on effective properties of thermal barrier coatings, Surface and Coatings Technology, In Press, Accepted Manuscript (doi: 10.1016/j.surfcoat.2010.03.057), pp., 2010.

[112] F. Tang, L. Ajdelsztajn, and J.M. Schoenung, Effects of cryomilling on the oxidation of thermally sprayed MCrAlY, International thermal spray conference, Osaka, Japan, pp. 148-153, 2004.

[113] F. Tang, L. Ajdelsztajn, and J.M. Schoenung, Influence of Cryomilling on the Morphology and Composition of the Oxide Scales Formed on HVOF CoNiCrAlY Coatings Oxidation of Metals, 61 (3/4), pp. 219-238, 2004.

[114] L. Ajdelsztajn, J.A. Picas, G.E. Kim, F.L. Bastian, J. Schoenung, and V. Provenzano, Oxidation behavior of HVOF sprayed nanocrystalline NiCrAlY powder, Materials Science and Engineering A, 338 (1-2), pp. 33-43, 2002.

[115] W.R. Chen, X. Wu, B.R. Marple, D.R. Nagy, and P.C. Patnaik, TGO growth behaviour in TBCs with APS and HVOF bond coats, Surface and Coatings Technology, 202 pp. 2677-2683, 2008.

[116] M.C. Mayoral, J.M. Andres, M.T. Bona, V. Higuera, and F.J. Belzunce, Aluminium depletion in NiCrAlY bond coatings by hot corrosion as a function of projection system, Surface & Coatings Technology, 202 (9), pp. 1816-1824, 2008.

[117] E.A.G. Shillington, and D.R. Clarke, Spalling failure of a thermal barrier coating associated with aluminum depletion in the bond-coat, Acta Materialia, 47 (4), pp. 1297-1305, 1999.

[118] M.P. Taylor, and H.E. Evans, The influence of bond coat surface roughness and structure on the oxidation of a thermal barrier coating system. in: R. Streiff, I.G. Wright, R.C. Krutenat, M. Caillet, and A. Galerie, (Eds.), High Temperature Corrosion and Protection of Materials 5, Pts 1 and 2, 2001, pp. 711-717.

[119] M.P. Taylor, W.M. Pragnell, and H.E. Evans, The influence of bond coat surface roughness on chemical failure and delamination in TBC systems, Materials and Corrosion-Werkstoffe Und Korrosion, 59 (6), pp. 508-513, 2008.

[120] R.D. Maier, C.M. Scheuermann, and C.W. Andrews, Degradation of a 2-layer thermal barrier coating under thermal cycling, American Ceramic Society Bulletin, 60 (5), pp. 555-560, 1981.

[121] A.G. Evans, D.R. Clarke, and C.G. Levi, The influence of oxides on the performance of advanced gas turbines, Journal of the European Ceramic Society, 28 (7), pp. 1405-1419, 2008.

[122] J. Allen Haynes, E. Douglas Rigney, M.K. Ferber, and W.D. Porter, Oxidation and degradation of a plasma-sprayed thermal barrier coating system, Surface and Coatings Technology, 86-87 (Part 1), pp. 102-108, 1996.

[123] F.J. Belzunce, V. Higuera, and S. Poveda, High temperature oxidation of HFPD thermal-sprayed MCrAlY coatings, Materials Science and Engineering A, 297 (1-2), pp. 162-167, 2001.

[124] A.M. Huntz, Parabolic laws during high temperature oxidation: relations with the grain size and thickness of the oxide, Journal of Materials Science Letters, 18 (24), pp. 1981-1984, 1999.

Appendix 1

In order to calculate the volume fraction of the oxides in as-sprayed HVOF and VPS coatings the following assumptions and formulas were used.

Mass of sample (g) = Mass of metal (g) + Mass of oxide (g)

=> Mass of metal (g) = Mass of sample (g) – Mass of oxide (g)

Mass of oxide = (mass of sample × wt.% of oxide) / 100

Hence knowing the oxide weight percent in each coating (see Table 4-4) and the weight of the sample used (~0.8g), the weight of the metal can be calculated. Knowing the powder density (7.463 g/cm^3, measured using the He gas pycnometer) and the oxide density (3.96 g/cm^3, assuming all oxide is alumina) the volume of metal and oxide can be calculated as follows.

Volume metal (cm^3) = Weight metal (g) / density powder (g/cm^3)

Volume oxide (cm^3) = Weight oxide (g) / density oxide (g/cm^3)

furthermore:

Volume of sample (cm^3) = Volume of metal + Volume of oxide + Volume of pore

Assuming that the volume of pores is very small, it can be neglected and hence the oxide volume fraction can be calculated as follows.

$$\text{Oxide volume fraction} = \frac{\text{Vol}_{\text{oxide}}}{\text{Vol}_{\text{metal}} + \text{Vol}_{\text{oxide}}}$$